

Aus dem Max von Pettenkofer-Institut für Hygiene und Medizinische Mikrobiologie  
Institut der Ludwig-Maximilians-Universität München  
Vorstand: Professor Dr. med. Oliver T. Keppler



**Manipulation of SAMHD1 using lentiviral protein Vpx  
to increase sensitivity of AML cells to cytarabine**

Dissertation  
zum Erwerb des Doktorgrades der Naturwissenschaften  
an der Medizinischen Fakultät der  
Ludwig-Maximilians-Universität München

vorgelegt von  
Ramya Nair  
aus  
Kerala, Indien

Jahr  
2023



Mit Genehmigung der Medizinischen Fakultät  
der Universität München

Betreuerin: PD Dr. rer. nat. Hanna-Mari Baldauf

Zweitgutachter: PD Dr. rer. nat. Andreas Moosmann

Dekan: Prof. Dr. med. Thomas Gudermann

Tag der mündlichen Prüfung: 01. März 2024



# Table of contents

<b>Zusammenfassung</b> .....	<b>v</b>
<b>Abstract</b> .....	<b>vii</b>
<b>List of figures</b> .....	<b>ix</b>
<b>List of tables</b> .....	<b>xi</b>
<b>List of abbreviations</b> .....	<b>xiii</b>
<b>1. Introduction</b> .....	<b>1</b>
1.1 Acute Myeloid Leukemia (AML).....	1
1.1.1 Incidence, diagnosis, and prognostic factors .....	1
1.1.2 Treatment of AML: advances and challenges .....	1
1.1.3 Mechanisms of cytarabine (ara-C) resistance .....	2
1.2 The SAMHD1 protein .....	5
1.2.1 SAMHD1: Expression and regulation .....	5
1.2.2 The functions of SAMHD1 and its regulation .....	7
1.2.3 Role of SAMHD1 in cancer .....	10
1.3 The lentiviral Vpx protein .....	12
1.3.1 Lentiviruses versus retroviruses .....	12
1.3.2 Characteristics of the Vpx protein.....	13
1.3.3 SAMHD1 antagonism by Vpx .....	13
1.4 The potential Vpx delivery systems .....	15
1.4.1 Nano metal-organic frameworks (nanoMOFs) .....	16
1.4.2 Cell-penetrating peptides (CPPs) .....	18
1.4.3 Virus-like particles (VLPs) .....	20
1.5 Aims of this work .....	23
<b>2. Materials and methods</b> .....	<b>25</b>
2.1 General reagents, chemicals, and equipment.....	25
2.1.1 Chemicals .....	25
2.1.2 Drugs .....	26
2.1.3 Commercial reagents and kits.....	27
2.1.4 Buffers and solutions .....	28
2.1.5 Growth media .....	31
2.1.6 Antibiotics.....	32
2.1.7 Antibodies.....	32
2.1.8 Equipment .....	34

2.1.9	Software and web applications .....	34
2.2	Mammalian cell lines, bacteria, and nucleic acids .....	35
2.2.1	Mammalian cell lines .....	35
2.2.2	Bacteria .....	36
2.2.3	Plasmids .....	36
2.2.4	Primers and gene fragments.....	38
2.3	Cell culture .....	42
2.3.1	Mammalian cell culture and cryopreservation .....	42
2.3.2	Bacterial cell culture and cryopreservation .....	42
2.3.3	Thawing of cells.....	42
2.3.4	Isolation and cultivation of primary CD4+ T cells.....	43
2.3.5	SAMHD1 degradation and co-treatment assays.....	43
2.3.6	Resazurin cytotoxicity assay.....	44
2.4	Nucleic acid techniques.....	44
2.4.1	Preparation of chemically competent <i>E. coli</i> .....	44
2.4.2	Transformation of chemically competent <i>E. coli</i> .....	44
2.4.3	Plasmid preparation and sequencing .....	45
2.4.4	Polymerase chain reaction (PCR).....	45
2.4.5	Restriction digest and agarose gel electrophoresis .....	46
2.4.6	Gel and PCR product clean-up .....	46
2.4.7	Ligation.....	47
2.4.8	Gibson Assembly.....	47
2.4.9	RNA isolation .....	47
2.4.10	Reverse transcription and quantitative PCR (qPCR) .....	47
2.4.11	Transfection of mammalian cell lines with PEI .....	48
2.4.12	Nucleofection of primary resting CD4+ T cells .....	49
2.4.13	Generation of HEK293T cells with stable inducible expression of Vpx fusion protein.....	49
2.5	Virological techniques .....	50
2.5.1	Production of virus-like particles (VLPs) and lentiviral vectors .....	50
2.5.2	Transduction of cells with VLPs with spinoculation.....	51
2.5.3	Transduction of cells with lentiviral vectors for stable cell production.....	51
2.5.4	SG-PERT assay.....	52
2.5.5	BlaM-Vpr VLP fusion assay .....	52
2.6	Flow cytometry.....	54
2.6.1	Analysis of cells expressing fluorescent proteins.....	54
2.6.2	Staining of surface markers .....	54
2.6.3	Intracellular staining.....	54
2.6.4	Flow cytometry data analysis .....	55
2.7	Biochemical techniques.....	55

2.7.1	SDS-PAGE and western blot.....	55
2.7.2	Coomassie and silver stains.....	56
2.7.3	Bradford assay.....	57
2.7.4	Automated SDS-PAGE and western blotting with the ProteinSimple Jess system....	57
2.7.5	Protein expression and affinity purification from <i>E. coli</i> .....	58
2.7.6	Protein expression and affinity purification from HEK293T cells.....	59
2.7.7	Size exclusion chromatography (SEC).....	60
2.7.8	Assembly of GFP- and Vpx-nanoMOFs.....	61
2.7.9	Proteasome activity assay.....	62
2.7.10	<i>In vitro</i> SAMHD1 degradation assay.....	62
2.8	Fluorescence microscopy.....	62
2.9	Statistical analysis.....	63
<b>3.</b>	<b>Results.....</b>	<b>65</b>
3.1	Expression and purification of recombinant Vpx proteins.....	65
3.1.1	Bacterial expression and purification of GST-Vpx and 6xHis-T7-Vpx.....	65
3.1.2	Mammalian expression and purification of 3xFLAG-Vpx.....	68
3.1.3	Mammalian expression and purification of Vpx-HA-10xHis.....	69
3.2	Establishment of a functionality assay for purified recombinant Vpx.....	75
3.2.1	<i>In vitro</i> cell-free degradation assay was not successful.....	76
3.2.2	Cell-based degradation assay shows functionality of Vpx-HA-10xHis construct.....	78
3.3	Production and functionality of Vpx-nanoMOFs.....	80
3.3.1	Initial characterization of nanoMOFs with 6xHis-GFP.....	80
3.3.2	Vpx-nanoMOFs were taken up by THP-1 cells.....	81
3.4	Production, purification, and functionality of Vpx-CPPs.....	84
3.4.1	Commercially synthesized CPPs bound to truncated 67aa Vpx were functional.....	84
3.4.2	CPP44-HA-WT Vpx constructs purified from HEK293T cells were not functional.....	87
3.5	Production, optimization, and functionality of new generation Vpx-VLPs.....	88
3.5.1	Characterization of new generation Vpx-VLPs.....	89
3.5.2	Improvement of yield and functionality of new generation VLPs produced with HIV-1 Rev protein.....	91
3.6	Ara-C co-treatment of AML cell lines and primary cells with Vpx-VLPs.....	94
3.6.1	New generation SIVmac251 Vpx-VLPs did not improve VLP functionality.....	96
3.6.2	New generation SIVmac239 Vpx-VLP treatment slightly improved ara-C sensitivity of SAMHD1-high expressing primary AML blast.....	98
<b>4.</b>	<b>Discussion.....</b>	<b>103</b>
4.1	A functional recombinant Vpx protein could be purified from HEK293T cells.....	104
4.1.1	Proof-of-concept for the purification of Vpx-HA-10xHis proteins from HEK293T sleeping beauty cells.....	104

4.1.2	Cell-based nucleofection assay confirmed the functionality of purified Vpx-HA-10xHis .....	105
4.2	New generation SIVmac Vpx-VLPs showed superior performance compared to the other Vpx delivery systems.....	106
4.2.1	The Vpx homolog SIVmac Vpx was the most effective at improving ara-C sensitivity .....	107
4.2.2	New generation Vpx-VLPs need to be optimized to perform as well as 1 <sup>st</sup> generation Vpx-VLPs.....	109
4.2.3	Vpx-CPPs and -nanoMOFs require further optimization.....	109
4.3	Implications of Vpx-ara-C combination treatment for AML.....	111
4.4	Future directions .....	112
4.4.1	Other potential Vpx delivery systems .....	112
4.4.2	Further applications of Vpx delivery systems .....	113
4.5	Conclusion .....	114
	<b>References .....</b>	<b>115</b>
	<b>Supplementary figures.....</b>	<b>133</b>
	<b>Acknowledgements .....</b>	<b>137</b>
	<b>Affidavit .....</b>	<b>139</b>
	<b>List of publications.....</b>	<b>141</b>



## Zusammenfassung

Patienten, die an akuter myeloischer Leukämie (AML) leiden, werden in erster Linie mit den Chemotherapeutika Cytarabin (ara-C) und Daunorubicin behandelt. Die Resistenz gegen ara-C ist jedoch weiterhin eine der größten Hürden für die effiziente Behandlung von AML. Im Jahr 2017 wurde berichtet, dass eine dNTP-Hydrolase namens SAMHD1 (sterile alpha motif and HD-domain-containing protein 1) eine Rolle bei der ara-C-Resistenz in AML-Zellen spielt. SAMHD1 hydrolysiert die Triphosphatgruppe des aktiven ara-C-Metaboliten, ara-CTP, und macht ihn damit therapeutisch inaktiv. Dies macht SAMHD1 zu einem attraktiven Ziel, um AML-Zellen wieder gegen ara-C empfindlich zu machen. Eine Methode, SAMHD1 gezielt zu bekämpfen, ist die Verwendung des lentiviralen akzessorischen-Proteins Vpx, das in Simian-Immunschwäche-Viren (SIV) und humanen Immundefizienz-Viren vom Typ 2 (HIV-2) vorkommt. Vpx induziert den Abbau von SAMHD1 über den proteasomalen Komplex. Ziel dieser Arbeit war es, verschiedene Methoden zur effektiven Verabreichung von Vpx in AML-Zellen zu untersuchen, um SAMHD1 abzubauen und die Empfindlichkeit von AML-Zellen gegenüber Ara-C zu verbessern.

In dieser Arbeit wurden drei Vpx-Transportsysteme untersucht: Nano-Metallorganische Gerüste (nanoMOFs), zelldurchdringende Peptide (CPPs) und virusähnliche Partikel (VLPs). In einem ersten Schritt wurden rekombinante Vpx-Proteine (Vpx-HA-10xHis) erfolgreich aus HEK293T-Zellen gereinigt. Die Funktionalität der gereinigten Vpx-HA-10xHis-Proteine wurde durch Protein-Nukleofektion in primären CD4<sup>+</sup> T-Zellen bestätigt. Diese gereinigten funktionellen Vpx-HA-10xHis-Proteine wurden dann zur Herstellung von Vpx-nanoMOFs verwendet. Als nächstes wurde Vpx an zwei verschiedene CPPs konjugiert: CPP44 und TAT. Die CPPs wurden entweder kommerziell synthetisiert oder hausintern aufgereinigt. Die kommerziell synthetisierten CPPs wurden aufgrund von Größenbeschränkungen bei der Peptidsynthese an eine verkürzte 67-Aminosäure-Version von Vpx (67aa Vpx) gebunden. Für die hausinterne Aufreinigung wurde WT-Vpx verwendet, das mit den CPPs konjugiert war. Für die VLPs wurden modifizierte Vpx-VLPs der neuen Generation verwendet, die nur wesentliche Strukturproteine und verschiedene Vpx-Homologe enthielten. Diese drei Vpx-Transportsysteme wurden dann anhand von vier Kriterien bewertet: (1) einfache Herstellung, (2) Fähigkeit SAMHD1 abzubauen, (3) Fähigkeit, die Empfindlichkeit gegenüber ara-C in AML-Zelllinien *in vitro*, und (4) in primären AML-Blasten *ex vivo* zu verbessern.

Auf der Grundlage der Ergebnisse dieser Arbeit war die neue Generation von Vpx-VLPs, die Vpx vom Makaken SIV (SIVmac) enthielten, das leistungsfähigste Vpx-Transportsystem. Die SIVmac-Vpx-VLPs konnten in hoher Ausbeute hergestellt werden, induzierten den SAMHD1-Abbau und verbesserten die Ara-C-Empfindlichkeit sowohl in AML-Zelllinien als auch in primären AML-Blasten. Kommerziell synthetisierte 67aa Vpx-CPPs waren ebenfalls in der Lage SAMHD1-Degradation zu induzieren und die Empfindlichkeit gegenüber ara-C in der AML-Zelllinie THP-1 zu verbessern. Sie waren jedoch weniger wirksam als Vpx-VLPs und es waren hohe Konzentrationen von CPPs (25 µM) erforderlich. Vpx-nanoMOFs waren nicht in der Lage SAMHD1 zu degradieren, obwohl das Vpx-HA-10xHis-Protein effektiv an die nano-MOFs adsorbiert werden konnte.

Zusammenfassend konnte ich zeigen, dass Vpx mit Hilfe von VLPs und CPPs das Potenzial hat SAMHD1 in AML-Zellen zu degradieren und ihre Empfindlichkeit gegenüber dem

Chemotherapeutikum Ara-C zu erhöhen. Letztlich könnten durch die Kombination von Vpx-Transportsystemen und Chemotherapeutika, wie zum Beispiel Ara-C, nicht nur AML-Patienten profitieren, die auf eine Behandlung mit Ara-C nicht reagieren, sondern auch Patienten, die an anderen Krankheiten leiden, bei denen sich die Degradation von SAMHD1 als vorteilhaft erwiesen hat.

## Abstract

Individuals suffering from a type of deadly blood cancer called acute myeloid leukemia (AML) are primarily treated with the front-line chemotherapeutic drugs cytarabine (ara-C) and daunorubicin. However, ara-C drug resistance continues to be one of the major hurdles for the efficient treatment of AML. In 2017, it was reported that a dNTP hydrolase called sterile alpha motif and HD-domain-containing protein 1 (SAMHD1) plays a role in ara-C resistance in AML cells. SAMHD1 hydrolyzes the triphosphate group of the active ara-C metabolite, ara-CTP, rendering it therapeutically inactive. This makes SAMHD1 an attractive target to re-sensitize AML cells to ara-C. One method of targeting SAMHD1 is using the lentiviral accessory protein Vpx, which is found in simian immunodeficiency viruses (SIV) and type 2 human immunodeficiency viruses (HIV-2). Vpx induces SAMHD1 degradation via the proteasomal complex. The aim of this work was to evaluate different methods to effectively deliver Vpx into AML cells to deplete SAMHD1 and improve ara-C sensitivity.

Three Vpx delivery systems were investigated in this work: nano metal-organic frameworks (nano-MOFs), cell-penetrating peptides (CPPs), and virus-like particles (VLPs). As an initial step, recombinant Vpx proteins (Vpx-HA-10xHis) were successfully purified from HEK293T cells. The functionality of the purified Vpx-HA-10xHis proteins was confirmed via protein nucleofection in primary resting CD4+ T cells. These purified functional Vpx-HA-10xHis proteins were then used to generate Vpx-nanoMOFs. Next, Vpx was conjugated to two different CPPs: CPP44 and TAT. The CPPs were either commercially synthesized or purified in-house. The commercially synthesized CPPs were bound to a truncated 67 amino acid version of Vpx (67aa Vpx) due to size limitations for peptide synthesis. Full length WT Vpx conjugated to the CPPs were used for the in-house purification. For the VLPs, modified new generation Vpx-VLPs containing only essential structural proteins and various Vpx homologs were generated. These three Vpx delivery systems were then evaluated based on four criteria: (1) ease of production, (2) ability to induce SAMHD1 degradation, (3) ability to improve ara-C sensitivity in AML cell lines *in vitro*, and (4) in primary AML blasts *ex vivo*.

Based on the results of this work, the new generation Vpx-VLPs incorporating Vpx from SIV macaque (SIVmac) were identified as the best performing Vpx delivery system. The SIVmac Vpx-VLPs could be generated in high yields, induced SAMHD1 degradation and improved ara-C sensitivity in both AML cell lines and primary AML blasts. Commercially synthesized 67aa Vpx-CPPs were also able to induce SAMHD1 degradation and improve ara-C sensitivity in the AML cell line, THP-1. However, they were less effective than Vpx-VLPs and high concentrations of CPPs (25  $\mu$ M) were required. Vpx-nanoMOFs were unable to induce SAMHD1 degradation, although the Vpx-HA-10xHis protein could be effectively adsorbed onto the nanoMOFs.

In conclusion, I demonstrated the potential of delivering Vpx using VLPs and CPPs to induce SAMHD1 degradation in AML cells and enhance their sensitivity to the chemotherapeutic drug ara-C. Ultimately, the combination of Vpx delivery systems and chemotherapeutic drugs like ara-C could not only benefit AML patients who do not respond to ara-C treatment, but also patients suffering from other diseases where SAMHD1 depletion has been shown to be beneficial.



## List of figures

Figure 1: Illustration of the metabolism and mechanism of action of ara-C.....	3
Figure 2: Illustration of SAMHD1's role in AML treatment response to ara-C. ....	11
Figure 3: Vpx antagonism of SAMHD1 and the residues involved in interactions with SAMHD1 and DCAF1. ....	14
Figure 4: Vpx delivery systems investigated in this work.....	16
Figure 5: Comparison of lentivirus and its VLP derivative. ....	21
Figure 6: The four major parts of this work. ....	23
Figure 7: Schematic representation of generating stable inducible Vpx-expressing HEK293T cells. ....	50
Figure 8: BlaM-Vpr VLP fusion assay.....	53
Figure 9: An example of the gating strategy implemented for the analysis of flow cytometry data. ....	55
Figure 10: Exemplary output gel image and graph generated by Jess.....	58
Figure 11: Schematic representation of the various plasmids used, encoding the different tagged Vpx proteins for the purification of recombinant Vpx from the <i>E. coli</i> Rossetta2 strain. ....	65
Figure 12: SEC purification and functionality of recombinant Vpx proteins. ....	67
Figure 13: Expression and purification of 3xFLAG-Vpx from HEK293T cells.....	69
Figure 14: The Vpx-HA-10xHis constructs were functional in primary resting CD4+ T cells. ....	70
Figure 15: Initial establishment of lysis and purification conditions for Vpx-HA-10xHis from HEK293T cells. ....	71
Figure 16: SEC improved purity of Vpx-HA-10xHis protein after IMAC purification. ....	73
Figure 17: Purification of Vpx-HA-10xHis from HEK293T sleeping beauty cells. ....	74
Figure 18: Proteasome activity of THP-1 lysates determined using Suc-LLVY-AMC substrate. ....	76
Figure 19: Impact of lysis buffer composition and imidazole on THP-1 lysate proteasome activity. ....	77
Figure 20: <i>In vitro</i> degradation assay with purified recombinant Vpx. ....	78
Figure 21: Purified WT Vpx-HA-10xHis proteins degraded SAMHD1 in primary resting CD4+ T cells. ....	79
Figure 22: Binding and THP-1 uptake of 6xHis-GFP-nanoMOFs. ....	81
Figure 23: Vpx-HA-10xHis bound to MIL88A nanoMOF were taken up by THP-1 cells but did not induce SAMHD1 degradation.....	82
Figure 24: Endosomal entrapment of Vpx in THP-1 cells after uptake of Vpx-bound MIL88A nanoMOF. ....	83
Figure 25: Endosomal escape enhancer treatment of Vpx-MIL88A-treated THP-1 cells did not improve functionality.....	84
Figure 26: CPP-HA-67aa Vpx synthesized from Eurogentec were taken up and induced SAMHD1 degradation in THP-1 cells. ....	85
Figure 27: CPP-HA-67aa Vpx synthesized from Davids Biotechnologie were taken up and induced SAMHD1 degradation in THP-1 cells but precipitated in medium.....	86
Figure 28: CPP-HA-67aa Vpx synthesized from Davids Biotechnologie improved ara-C sensitivity in THP-1 cells. ....	87

Figure 29: CPP44-HA-WT Vpx could be purified from HEK293T cells but were not functional. .88	
Figure 30: New generation pSIV3+ 3xFLAG-Vpx/Vpr constructs were generated and expressed in HEK293T cells.....90	90
Figure 31: Low yield and functionality of new generation SIVmac239 Vpx-VLP. ....91	91
Figure 32: Improvement of yield and functionality of new generation VLPs after using HIV-1 Rev protein. ....93	93
Figure 33: SAMHD1 expression and VSV-G susceptibility of AML cell lines.....94	94
Figure 34: New generation Vpx-VLPs improved ara-C sensitivity of AML cell lines. ....96	96
Figure 35: New generation SIVmac251 Vpx-VLPs were not functionally superior to new generation SIVmac239 Vpx-VLPs. ....98	98
Figure 36: Characterization of primary AML blasts with flow cytometry.....99	99
Figure 37: The new generation SIVmac239 Vpx-VLPs only slightly improved ara-C sensitivity of SAMHD1-high expressing primary AML blasts. .... 101	101
Figure 38: Role of Vpx delivery systems on ara-C metabolism in AML cells. .... 103	103

## List of tables

Table 1: List of chemicals.....	25
Table 2: List of drugs. ....	26
Table 3: List of commercial reagents and kits.....	27
Table 4: List and components of self-made buffers and solutions. ....	28
Table 5: List of mammalian and bacterial growth media. ....	31
Table 6: List of antibiotics.....	32
Table 7: List of antibodies used for western blot (WB), flow cytometry (FC), immunofluorescence (IF) and automated WB (Jess).....	32
Table 8: List of equipment. ....	34
Table 9: List of software and web applications used in this work.....	34
Table 10: List of cell lines.....	35
Table 11: List of bacteria.....	36
Table 12: List of mammalian and bacterial expression plasmids.....	36
Table 13: List of primers. ....	38
Table 14: Volume of reagents used in PCR reaction using Phusion® DNA polymerase.....	46
Table 15: Typical thermocycler run conditions for Phusion® DNA polymerase PCR.....	46
Table 16: qPCR run conditions in the QuantStudio™ 3 Real-Time PCR instruments.....	48
Table 17: Amount of plasmids used for the production of VLPs and lentiviral vectors from one 145 mm <sup>2</sup> dish of HEK293T cells. ....	51
Table 18: Components of 12% and 15% SDS-polyacrylamide gels.....	56
Table 19: SEC run and fractionation conditions.....	61
Table 20: List of nanoMOFs provided and their components.....	62
Table 21: Lysis buffer compositions for initial lysis test shown in Figure 15A and B. ....	70
Table 22: Summary of studies which reported recombinant Vpx interaction with SAMHD1. ....	75
Table 23: Composition of lysis buffers used in THP-1 lysate proteasome activity assay.....	77
Table 24: Summary of key take-aways obtained for each Vpx delivery system. ....	107





## List of abbreviations

ara-C	Cytarabine
ABC	ATP binding cassette
ABCB1	ABC transporter B1
ABCC10	ABC transporter C10
ABCC11	ABC transporter C11
AGS	Aicardi-Goutières syndrome
AKT	Serine threonine kinase
ALL	Acute lymphoblastic leukemia
AML	Acute myeloid leukemia
APOBEC	Apolipoprotein B mRNA editing enzyme catalytic subunit
APS	Ammonium persulfate
ARD1	Acetyltransferase arrest-defection protein 1
ART	Anti-retroviral therapy
ATP	Adenosine triphosphate
ATR	Ataxia-telangiectasia mutated and Rad3-related
AZT	Azidothymidine
BFP	Blue fluorescence protein
BSA	Bovine serum albumin
CD	Cluster of differentiation
CDA	Cytidine deaminase
CDK	Cyclin-dependent kinases
cDNA	Complementary DANN
cGAS	Cyclic GMP-AMP synthase
CHAPS	3-((3-cholamidopropyl) dimethylammonio)-1-propanesulfonate
Chk1	Checkpoint kinase 1
CHO	Chinese hamster ovary cells
CLL	Chronic lymphoblastic leukemia
CMV	Cytomegalovirus
Co-IP	Co-immunoprecipitation
CPP	Cell penetrating peptide
CRL4	Cullin-4 RING ubiquitin ligase complex
CTCL	Cutaneous T-cell lymphoma
CtIP	CtBP-interacting protein
CUL4	Cullin-4
CV	Column volume

dATP	Deoxyadenosine triphosphate
dC	Deoxycytidine
DC	Dendritic cells
DCAF1	DDB1 and CUL4 associated factor 1
dCK	Deoxycytidine kinase
dCMP	Deoxycytidine monophosphate
DCTD	Deoxycytidylate deaminase
dCTP	Deoxycytidine triphosphate
DDB1	DNA damage binding protein 1
DDM	Dodecylmaltoside
dGTP	Deoxyguanosine triphosphate
DMEM	Dulbecco's modified eagle medium
DMSO	Dimethylsulfoxide
DNA	Deoxyribonucleic acid
DNMT	DNA methyltransferase
dNTP	Deoxynucleoside triphosphate
DTT	Dithiothreitol
dTTP	Deoxythymidine triphosphate
EBV	Epstein-Barr virus
EDTA	Ethylenediaminetetraacetic acid
EGF	Epidermal growth factor
EIAV	Equine infectious anemia virus
EP28	Epidermal growth factor receptor pathway substrate no. 8
FAB	The French-American-British classification
FC	Flow cytometry
FCS	Fetal calf serum
FDA	Food and Drug Administration
FLT3	Fms-like tyrosine kinase 3
FRET	Fluorescence resonance energy transfer
FSC	Forward scatter
FT	Flow-through
GFP	Green fluorescence protein
GO	Gemtuzumab ozogamicin
GST	Glutathione S-transferases
HA	Haemagglutinin
HBV	Hepatitis B virus
HCMV	Human Cytomegalovirus

hENT1	Human equilibrative nucleoside transporter 1
HIV	Human immunodeficiency virus
HMA	Hypomethylating agents
HPV	Human papilloma viruses
HRP	Horseradish peroxidase
HSV-1	Herpes simplex virus 1
HU	Hydroxyurea
HUSH	Human silencing hub
IDH	Isocitrate dehydrogenase
IF	Immunofluorescence
IFN	Interferon
IL	Interleukin
IMAC	Immobilized metal affinity
IMDM	Iscoves modified dulbecco's medium
IPTG	Isopropyl $\beta$ -d-1-thiogalactopyranoside
IRES	Internal ribosome entry site
IRF3	Interferon regulatory factor 3
L-PEI	Linear polyethylenimine
LINE-1	Long interspersed element 1
LPS	Lipopolysaccharide
LTR	Long terminal repeats
MAPK	Mitogen-activated protein kinase
MCL1	Induced myeloid leukemia cell differentiation protein
MDM	Monocyte-derived macrophages
MDR	Multidrug resistance
MDS	Myelodysplastic syndrome
MFI	Mean fluorescence intensity
MIL	Material from Institute Lavoisier
MLV	Murine leukemia virus
MOF	Metal-organic frameworks
MOPS	3-morpholinopropane-1-sulfonic acid
mTOR	Mammalian target of rapamycin
MudPIT	Multi-dimensional protein identification technology
NLS	Nuclear localization signal
NT5C2	5' nucleotidase cytosolic II
NTA	Nitrilotriacetic acid
Nup153	Nucleoporin 153

OD <sub>600</sub>	Optical density at 600 nm wavelength
PBS	Phosphate-buffered saline
PCP	Porous coordination polymers
PEG	Polyethylene glycol
PFA	Paraformaldehyde
PI3K	Phosphatidylinositol 3-kinase
PIC	Protease inhibitor complex
PIM	Proviral integration site for Moloney murine leukemia virus
PMAP	pH-dependent membrane active peptides
PMSF	Phenylmethylsulfonyl fluoride
PTM	Post-translational modifications
qPCR	Quantitative polymerase chain reaction
RBX1	E3 ubiquitin-protein ligase 1
RFI	Relative fluorescence intensity
RFU	Relative fluorescence units
RNA	Ribonucleic acid
RNP	Ribonucleoprotein
RPMI	Roswell Park Memorial Institute medium
RNR	Ribonucleotide reductase
RRE	Rev responsive element
RT	Reverse transcriptase
SAMDH1	The sterile alpha motif (SAM) and histidine-aspartate (HD) domains-containing protein 1
SB	Sleeping beauty
SDS-PAGE	Sodium dodecyl sulfate – polyacrylamide gel electrophoresis
SEC	Size exclusion chromatography
SERINC5	Serine incorporator 5
SG-PERT	SYBR Green I-based real-time PCR-enhanced reverse transcriptase
siRNA	Short interfering RNA
SIV	Simian immunodeficiency virus
<i>SLC29A1</i>	Solute carrier family 29 member 1
SSC	Side scatter
STING	Stimulator of interferon genes
SUMO	Small Ubiquitin-like Modifier
SV40	Simian virus 40
T-PLL	T-cell prolymphocytic leukemia
TAE	Tris-acetate-EDTA

TAT	Trans-Activator of Transcription
TBS	Tris-buffered saline
TEMED	Tetramethylethylenediamine
TEV	Tobacco etch virus
TLR3	Toll-like receptor 3
VAI	Adenoviral Virus Associated I RNA
VAII	Adenoviral Virus Associated II RNA
VLP	Virus-like particle
VSV-G	Vesicular stomatitis virus glycoprotein
WB	Western blot
WT	Wild-type
ZIF	Zeolitic imidazole framework



## 1. Introduction

### 1.1 Acute Myeloid Leukemia (AML)

#### 1.1.1 Incidence, diagnosis, and prognostic factors

In the United States, 4.3 out of 100,000 people on average are diagnosed with a type of blood cancer called acute myeloid leukemia (AML)<sup>1,2</sup>. AML is an aggressive disease characterized by the abnormal proliferation of cells of the myeloid lineage<sup>3</sup>, which normally give rise to red blood cells and white blood cells of the innate immune system<sup>4</sup>. AML primarily affects individuals around the age of 68 and is the most common type of acute leukemia among adults<sup>5</sup>. It is also the deadliest form of acute leukemia, since only 24% of patients survive 5 years after diagnosis<sup>1</sup>. AML differs from its chronic counterparts (chronic myeloid and lymphoblastic leukemia) in that it develops rapidly as opposed to the gradual development of the chronic leukemias<sup>6</sup>.

An individual affected by AML might present symptoms such as fatigue, bleeding, and infections caused by reduced amounts of mature white blood cells<sup>7</sup>. Upon examination of peripheral blood and blood smears, AML is diagnosed by the observation of abnormally high amounts of immature myeloid progenitor cells, or blast cells<sup>8</sup>. These cells are undifferentiated and quickly proliferating, causing them to be the dominant cell type in the bone marrow<sup>8</sup>. AML develops through the accumulation of genetic aberrations resulting in hematological disorders such as myelodysplastic syndrome (MDS), or after chemotherapy or radiation therapy as a secondary cancer (therapy-related AML, or tAML)<sup>9</sup>.

Certain factors, both patient-specific and disease-specific, predict the prognosis of patients diagnosed with AML and help healthcare providers decide on the best treatment options<sup>10</sup>. This is known as risk stratification. Patient-specific factors include age, comorbidities, and performance status, while disease-specific factors include karyotype and genetic abnormalities<sup>10</sup>. For instance, younger patients generally tend to respond better to treatment than older patients<sup>10</sup>. This is because older patients are more likely to have comorbidities which make them more sensitive to the toxic side-effects of the drugs<sup>11</sup>. Additionally, patients with mutated *TP53* gene, which encodes the tumor suppressor protein p53, have an adverse prognosis compared to patients without the mutation<sup>10</sup>. Loss-of-function mutations of the pro-apoptotic p53 protein contribute to uncontrolled cell division and survival<sup>12</sup>. As more research is done on AML biology, more factors are included into the list to guide healthcare providers towards treatment options most beneficial to individual patients<sup>13</sup>.

#### 1.1.2 Treatment of AML: advances and challenges

AML is a highly heterogenous disease. Within individuals, the blast cells vary significantly in terms of their genetic signature and karyotype, making effective treatment very challenging<sup>14</sup>. Over the last decades, one treatment has been the front-line option for many patients. This is the 7+3 chemotherapy treatment scheme consisting of 7 days of a nucleoside analogue cytarabine (ara-C) and 3 days of a topoisomerase inhibitor daunorubicin<sup>15</sup>. However, due to the poor outcomes, especially in elderly patients, and the high toxicity of the treatment, there has been considerable effort to develop better

therapeutic options for AML patients<sup>16</sup>. As a result, several new drugs have been approved by the Food and Drug Administration (FDA) for treatment of AML since 2017<sup>17,18</sup>. These new drugs are primarily targeted therapies. Targeted therapy, as opposed to chemotherapy, refers to the use of small molecule inhibitors which specifically target certain proteins and pathways that are mutated or altered in the leukemic cells of patients<sup>19</sup>. The 7+3 treatment scheme is still the treatment of choice for patients who are fit for intensive chemotherapy<sup>20</sup>. Nevertheless, the targeted therapies allow patients in specific subgroups to benefit from increased efficiency and reduced toxicity<sup>20</sup>. For example, Fms-like tyrosine kinase 3 (*FLT3*) inhibitors such as midostaurin are given to AML patients who have specific mutations in the *FLT3* gene (e.g., *FLT3-ITD* or *FLT3-TKD*), and isocitrate dehydrogenase (*IDH*) inhibitors such as ivosidenib are given to *IDH*-mutated AML patients<sup>18</sup>. Mutations in the *FLT3* gene gives rise to a constitutively active tyrosine kinase receptor which contributes to the expression of genes involved in survival and proliferation<sup>21</sup>. Whereas, mutations in the *IDH* gene contributes to increased deoxyribonucleic acid (DNA) damage and reduced differentiation as a result of an active *IDH* metabolic enzyme, which is involved in the Krebs cycle<sup>21</sup>. Mutations in both genes are frequent among AML patients, and are known to be important contributors of AML development<sup>21</sup>. Besides the targeted therapeutics, which are given to specific subsets of patients, some low intensity chemotherapeutic drugs are also approved for AML treatment for those who are ineligible for targeted therapy or intensive chemotherapy. These include the B-cell lymphoma 2 (Bcl-2) inhibitor venetoclax, the anti-CD33 antibody-drug conjugate gemtuzumab ozogamicin (GO), as well as a liposomal formulation of cytarabine and daunorubicin CPX-351<sup>18</sup>. Many of these new therapeutic agents are used in combination with either hypomethylating agents (HMA) such as decitabine and azacytidine or with ara-C (in low-doses for unfit patients) as they have shown better efficiency than monotherapy<sup>20</sup>. For more detailed insights into these new therapies, I recommend the review by Short N. J. *et al.*<sup>22</sup>.

Despite the availability of new therapeutic options, some patients still undergo incomplete remission and relapse. A major reason for this is drug resistance, and research on deciphering and combating resistance mechanisms are currently underway<sup>23</sup>. In the case of venetoclax, the increased expression of the anti-apoptotic induced myeloid leukemia cell differentiation protein (MCL1) leads to drug resistance<sup>24,25</sup>. With this knowledge, combination therapies with venetoclax and MCL1 inhibitors have shown superior responses compared to monotherapy<sup>25</sup>. Resistance has also been reported for targeted therapies such as the *FLT3* inhibitor midostaurin<sup>26</sup>. Since ara-C is still a major drug used in combating AML for both fit and unfit patients (low-dose ara-C), resistance mechanisms against ara-C have been extensively studied. The next subsection will discuss such ara-C resistance mechanisms and strategies to combat them.

### 1.1.3 Mechanisms of cytarabine (ara-C) resistance

Ara-C is an analog of the nucleoside cytidine. The structure of ara-C differs from deoxycytidine (dC) just by an additional -OH moiety at the 2' carbon position (Figure 1A)<sup>27</sup>. Ara-C first enters the cell either through diffusion, if the concentration is high enough, or using the transport molecule human equilibrative nucleoside transporter 1 (hENT1)<sup>28,29</sup>. It then gets triphosphorylated to ara-CTP via a phosphorylation cascade involving different kinases<sup>28</sup>. Ara-CTP, resembling deoxycytidine triphos-



phate (dCTP), then gets incorporated into the DNA during replication, stops elongation and terminates DNA synthesis (Figure 1B)<sup>27</sup>. Figure 1C summarizes the pathway taken by ara-C from entering the AML cells to causing cell death.

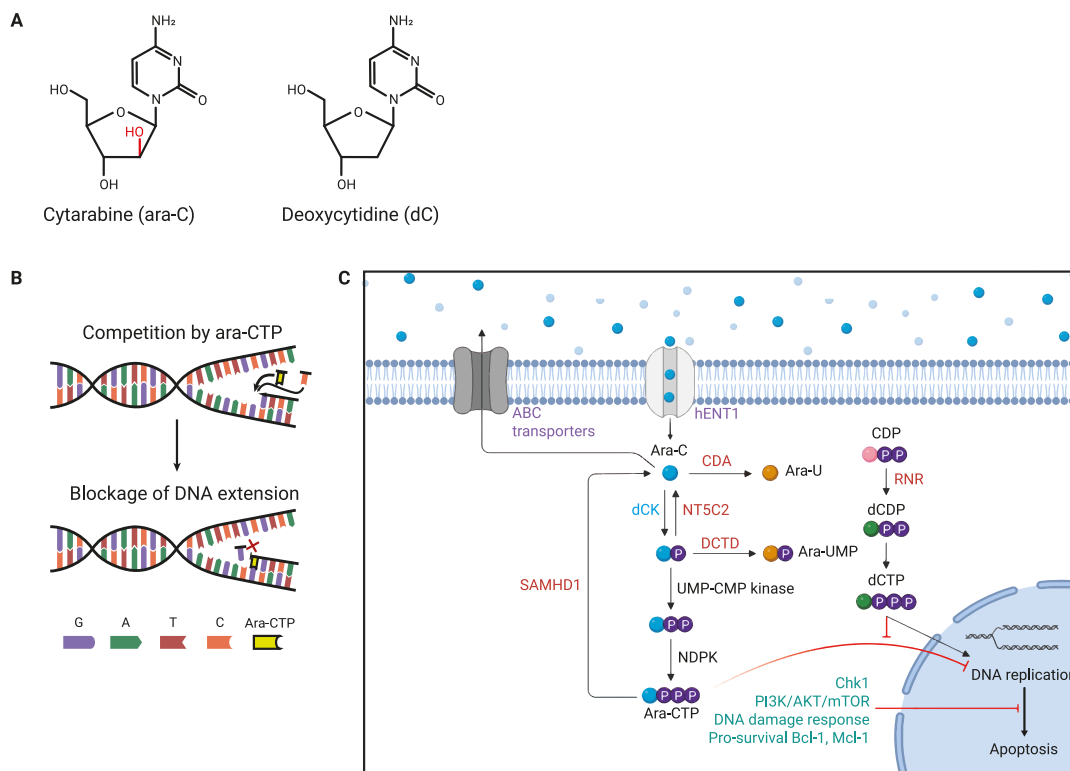


Figure 1: Illustration of the metabolism and mechanism of action of ara-C.

**A** Ara-C and dC only differ in structure by one -OH group (in red) on the 2' carbon position. **B** The active form of ara-C, ara-CTP, gets incorporated into DNA during replication and prevents DNA extension, leading to replication fork stalling and subsequent DNA damage and apoptosis. **C** Ara-C enters the AML cell through the transporter hENT1 and undergoes a phosphorylation cascade to convert to ara-CTP. Throughout this process, several proteins are involved, which either promote (blue text) or interfere (red text) with the production of ara-CTP. The uptake and expulsion of ara-C is also a factor involved in ara-C resistance (purple text). Finally, the induction of apoptosis by ara-CTP can be hindered by the aberrations in molecules involved in cell cycle progression, survival, and DNA damage response (green text).

Several mechanisms of ara-C resistance have been identified in AML cells (Figure 1C). These can be divided into three categories: (1) reduction of ara-C influx or increase of efflux, (2) inhibition of ara-C-induced apoptosis, and (3) reduction of ara-C activation to ara-CTP.

**Mechanism (1):** The first hurdle for ara-C is not only entering the cells, but also staying in the cells. As mentioned earlier, the main transporter responsible for ara-C entry into the cells is hENT1, encoded by the gene solute carrier family 29 member 1 (*SLC29A1*). Studies have shown that patients with higher expression levels of hENT1 are more responsive to ara-C treatment and have better overall survival rates compared to patients with lower hENT1 expression levels<sup>30–32</sup>. In contrast, higher expression of efflux pumps such as the ATP-binding cassette (ABC) transporters C10 and C11 (*ABCC10* and *11*) have been associated with ara-C resistance and reduced survival in AML patients<sup>33,34</sup>.

In an effort to counteract these mechanisms, several strategies have been proposed. One is the use of elacytarabine to circumvent the need for hENT1 for drug uptake. Elacytarabine is able to diffuse through the cell membrane due to the addition of a lipophilic ester side chain to ara-C<sup>35</sup>. The newly approved CPX-351, which is a liposomal formulation of ara-C and daunorubicin, is also able to enter AML cells independent of the hENT1 transport molecule, allowing a better uptake of the drugs<sup>36</sup>. In the case of the increased efflux of drugs resulting in resistance, it has recently been reported that midostaurin, an FLT3 inhibitor, also suppresses the action of ABC transporter ABCB1, thereby reversing resistance towards daunorubicin<sup>37</sup>. Sorafenib, which also targets FLT3, has been shown to inhibit the ara-C transporter ABCC10, resulting in the accumulation of ara-C in AML cells and ara-CTP-induced cell death<sup>38</sup>. Interestingly, yet another FLT3 inhibitor tandutinib has been found to inhibit ABCC10<sup>39</sup>, suggesting the potential combination of further FLT3 inhibitors with ara-C to increase its efficiency even in patients who do not harbor FLT3 mutations.

**Mechanism (2):** Ara-C completes its cytotoxic function via the induction of apoptosis in the AML cells. Therefore, aberrations in the cell's ability to induce apoptosis can be a hurdle for ara-C-mediated cytotoxicity<sup>40,41</sup>. One of the pathways extensively studied to be involved in the response to drugs like ara-C is the phosphatidylinositol 3-kinase (PI3K)/ serine threonine kinase (AKT)/ mammalian target of rapamycin (mTOR) pathway<sup>42–44</sup>. Inhibitors of members of this pathway have been reported to enhance the cytotoxic effects of ara-C, reinforcing the role of this pathway in ara-C resistance<sup>43,45–47</sup>. Besides the PI3K/AKT/mTOR pathway, molecules that are involved in DNA damage response and cell cycle checkpoints also play a role in ara-C resistance. An example of a cell cycle checkpoint molecule is the checkpoint kinase 1 (Chk1), which controls cell cycle arrest to facilitate DNA damage repair<sup>48,49</sup>. Since chemotherapeutic drugs rely on extensive DNA damage to induce cell death<sup>50</sup>, Chk1 reduces their toxicity by allowing DNA damage repair to occur<sup>48,49</sup>. An example of a DNA damage response molecule is a sensor like ataxia-telangiectasia mutated and Rad3-related (ATR), which acts upstream of Chk1 by recognizing DNA damage and activating the damage repair pathway<sup>51</sup>. Inhibitors of both molecules, Chk1 and ATR, have been shown to act synergistically with ara-C, enhancing its cytotoxic effects<sup>48,49,51</sup>. In addition to Chk1 and ATR, inhibition of other molecules involved in the DNA damage response and cell cycle checkpoint pathways such as cyclin-dependent kinases (CDKs) have been reported to increase the sensitivity of AML cells to ara-C<sup>52</sup>. A recent publication has also observed enhanced cytotoxicity of ara-C when combined with the novel Bcl-2 inhibitor venetoclax and an anti-malaria drug artesunate<sup>53</sup>. The two additional drugs, venetoclax and artesunate, inhibit the activity of pro-survival proteins Bcl-2 and Mcl-1 and allow apoptosis to proceed following ara-C treatment<sup>53</sup>. Other strategies to lift the block caused by anti-apoptotic proteins include the usage of pro-apoptotic BH3 mimetics, which can inhibit pro-survival proteins and facilitate ara-C-induced cytotoxicity<sup>54</sup>. All these examples further support the strategy to combine different targets to best leverage the efficiency of ara-C.

**Mechanism (3):** The formation of ara-CTP is critical for the induction of cytotoxicity by ara-C. Since ara-C is a nucleoside analog, it undergoes a similar metabolism to be converted to ara-CTP as the canonical nucleosides. As shown in Figure 1C, the first rate-limiting step in the conversion of ara-C to ara-CTP involves the enzymes deoxycytidine kinase (dCK) and 5' nucleotidase cytosolic II (NT5C2). dCK promotes the production of ara-CTP, while NT5C2 acts in an opposite way to dCK to prevent the eventual conversion to ara-CTP<sup>55</sup>. The expression levels of these two enzymes are not

only proportional to the accumulation of ara-CTP in AML cell lines and patient samples, but are also predictive of the prognosis of AML patients<sup>55–57</sup>. Several studies have shown that reduced expression or lower activity of dCK correlates with a reduced accumulation of ara-CTP and subsequently ara-C resistance<sup>52,55,58–60</sup>. Meanwhile, high NT5C2 expression correlates with poorer prognosis<sup>57</sup>. Interestingly, when patient samples were analyzed at diagnosis and relapse, higher NT5C2 and lower dCK expressions were found in relapse samples after ara-C treatment compared to samples at diagnosis, providing further support for the roles of dCK and NT5C2 in ara-C response<sup>61</sup>.

In order to counteract the lack of dCK activity in resistant cells, Levin *et al.* have reported the use of hydroxyurea (HU) and azidothymidine (AZT), which are cytotoxic to ara-C-resistant cells and do not depend on dCK for activation<sup>62</sup>. HU is a ribonucleotide reductase (RNR) inhibitor. RNRs are involved in the *de novo* nucleotide synthesis pathway. They have also been implicated as a resistance factor against ara-C in AML cells by producing more dCTP to compete with ara-CTP during DNA replication<sup>63</sup>. In addition, HU has also been described to activate dCK<sup>64</sup>. To this extent, the synergistic effects of combining RNR inhibitors and ara-C treatment in phase I trials have been reported with promising outcomes<sup>65,66</sup>.

NT5C2 inhibition is also another strategy to increase the conversion of ara-C to ara-CMP and subsequently to ara-CTP. There has been some reports in acute lymphoblastic leukemia, where NT5C2 inhibition led to increased sensitivity to other nucleoside analog drugs such as thiopurine<sup>67,68</sup>. However, to my knowledge, studies that investigate NT5C2 inhibition in the context of AML are lacking.

In addition to dCK and NT5C2, cytidine deaminase (CDA) and deoxycytidylate deaminase (DCTD) are two enzymes responsible for the deamination of dC and deoxycytidine monophosphate (dCMP), respectively, that contribute to the reduction of ara-CTP levels. These two enzymes are less studied compared to dCK and NT5C2. Nevertheless, their increased expression levels have been correlated with reduced ara-C response in older studies<sup>29,69,70</sup>. Contrastingly, low CDA levels have been implicated with increased off-target toxicity of ara-C treatment, arguing against reducing CDA levels for AML treatment<sup>71,72</sup>.

Another important contributor to ara-C resistance is SAMHD1, which is the focus of this thesis. Further in this work, strategies to combat SAMHD1-induced ara-C resistance will be pursued. More details about SAMHD1, its mediation of ara-C resistance, and its antagonism are provided in the upcoming subsections.

## 1.2 The SAMHD1 protein

### 1.2.1 SAMHD1: Expression and regulation

The sterile alpha motif (SAM) and histidine-aspartate (HD) domains-containing protein 1 (SAMHD1) is a 626 amino acid protein and is around 72 kDa in size. Although considered as a deoxynucleoside triphosphate hydrolase (dNTP hydrolase), SAMHD1 also possess functions beyond its hydrolase activities<sup>73</sup>, which will be discussed further in subsection 1.2.2.

The two major domains of SAMHD1 are the SAM and HD domains. The SAM domain is mainly involved in protein-protein interactions<sup>74–76</sup> whereas the HD domain contains the catalytically active site<sup>76,77</sup>. Apart from these two major domains, SAMHD1 also possesses a nuclear localization signal (NLS) at its N-terminus, and regulatory sites at its C-terminus<sup>73</sup>. Due to its NLS, SAMHD1 primarily localizes to the nucleus<sup>78,79</sup>. However, several studies have reported cytoplasmic localization of SAMHD1 as well<sup>80–82</sup>, indicating perhaps functional differences between nuclear and cytoplasmic SAMHD1<sup>80</sup>.

Based on immunohistochemical staining of human tissues, SAMHD1 is expressed in all tissues, albeit at varying levels<sup>83</sup>. In general, highly proliferative cells tend to have lower levels of SAMHD1<sup>84</sup>. SAMHD1 is also present in all hematopoietic cells, but shows the highest expression in cells of the myeloid lineage, as well as resting CD4+ T cells<sup>83</sup>. The expression of SAMHD1 can be regulated via two main ways: epigenetically and transcriptionally.

Epigenetically, the gene expression of *Sambd1* is regulated via methylation of its promoter. Methylation of promoters occurs at CpG islands, which are regions of the promoter with a large amount of cytidine and adjacent guanosine (CpG) nucleotides<sup>85</sup>. A methyl group is added to the cytidine nucleotide, eventually inhibiting gene expression<sup>85</sup>. Highly methylated *Sambd1* promoters have been found in the cell lines Jurkat and Sup-T1, which is reversible upon treatment with DNA methyltransferase (DNMT) inhibitors<sup>86</sup>. Comparison of Jurkat and Sup-T1 cells with the AML cell line THP-1 have revealed low promoter methylation in THP-1 cells, which are also unresponsive to DNMT inhibition<sup>86</sup>.

Another factor influencing SAMHD1 expression is the transcription of the *Sambd1* gene. Since the identification of SAMHD1 as an ortholog of the murine interferon-induced gene *Mg11*<sup>87</sup>, the ability of interferons to induce the expression of SAMHD1 has been demonstrated in some cells. Induction with type I interferons leads to the increase in SAMHD1 expression in the cell lines HEK293T and HeLa but not in primary dendritic cells (DCs) or CD4+ T cells<sup>88</sup>. These results are supported by a later study by Riess *et al.*, which has reported no response of primary DCs and macrophages to type I and II interferon stimulation, although in primary monocytes an increase in SAMHD1 expression was observed<sup>89</sup>. In their study, the increase in SAMHD1 in primary monocytes is a result of a down-regulation of interfering microRNAs (miRNA), miR-181a and miR-30a<sup>89</sup>. This down-regulation of miRNA is induced by interferon gamma (IFN $\gamma$ )<sup>89</sup>. These miRNAs have been shown to be responsible for down-regulating SAMHD1 by binding to its mRNA<sup>90,91</sup>. Therefore, the differences in SAMHD1 expression induction in different cell types might be caused by the interferon-induced down-regulation of *Sambd1* mRNA-targeting miRNA in monocytes, but not in primary DCs and macrophages<sup>89</sup>. In addition to interferons, cytokines like interleukin (IL)-12 and IL-18 have also been shown to increase *Sambd1* mRNA levels in primary monocyte-derived macrophages<sup>92</sup>. Interferon regulatory factor 3 (IRF3), a downstream effector of the toll-like receptor 3 (TLR3) pathway, has been reported to directly increase SAMHD1 expression by binding to the *Sambd1* promoter<sup>93</sup>. Interestingly, IRF3 is known to induce type I interferon production, further strengthening the link between SAMHD1 and interferon responses<sup>94</sup>.

Besides the regulation of the expression of SAMHD1 via epigenetic and transcriptional modulation, the stability and activity of the SAMHD1 protein is also regulated via post-translational modifications

(PTMs), including phosphorylation, acetylation, small ubiquitin-like modifier (SUMO)-ylation and ubiquitination. Since these modifications are closely related to SAMHD1 functions, they will be further explored in the following subsection.

## 1.2.2 The functions of SAMHD1 and its regulation

As previously mentioned, the primary role of SAMHD1 is the hydrolysis of dNTPs, which is conducted by the HD domain of the protein. However, several additional functions of SAMHD1 have also been identified. In this subsection, the various functions of SAMHD1 will be explored and some insights into how these functions are modulated via PTMs will be provided.

The functions of SAMHD1 can be divided into the following four groups:

1. dNTP homeostasis and cell cycle progression
2. Innate immunity
3. DNA damage response
4. Retrotransposon modulation

### 1.2.2.1 dNTP homeostasis and cell cycle progression

The proper maintenance of dNTP pools is crucial not only for cell survival and replication, but also for the integrity of the genome<sup>95</sup>. Two main pathways contribute to the level of dNTPs in the cell: the *de novo* synthesis pathway, and the salvage pathway<sup>96</sup>. SAMHD1 is involved in the salvage pathway, in contrast to RNRs, which are involved in the *de novo* synthesis pathway (as mentioned in subsection 1.1.3). Mechanistically, SAMHD1 hydrolyses dNTPs into unphosphorylated nucleosides and triphosphates<sup>97</sup>. The dNTP hydrolase activity of SAMHD1 varies based on the cell cycle stage the cell is in. The change in activity is controlled by PTMs. For instance, during G1-phase, the SAMHD1 dNTP hydrolase activity is increased via the acetylation of the lysing residue at position 405 (K405)<sup>98</sup>. The acetyltransferase arrest-defection protein 1 (ARD1) is responsible for this acetylation<sup>98</sup>. The subsequent reduced dNTP pool allows for the transition into S-phase<sup>98</sup>, as a high dNTP pool has been reported to slow entry into S-phase in yeast cells<sup>99</sup>. *In vitro* studies using *Sambd1* knock-out cells have also revealed that cells without SAMHD1 are arrested in the G1-phase with an increased dNTP pool<sup>100</sup>. During the S-phase, phosphorylation of the threonine residue at position 592 (T592) by cyclin-dependent kinases (CDKs), especially CDK2, has been reported to reduce the dNTP hydrolase activity of SAMHD1, followed by an increased dNTP pool to allow for DNA replication<sup>101</sup>. In contrast to the studies showing reduced dNTP hydrolase activity upon T592 phosphorylation<sup>102–104</sup>, a recent study by Batalis *et al.* has reported that a phosphomimetic mutant, T592E SAMHD1, is an active dNTP hydrolase<sup>80</sup>, in agreement with other studies as well<sup>105,106</sup>. This phosphomimetic mutant prevents S- to G2-phase transition and reduces proliferation of the cells<sup>80</sup>. Batalis *et al.* have attributed this observation to the retention of the phosphomimetic mutant in the nucleus, in contrast to the cytosolic and nuclear distribution of wild-type SAMHD1<sup>80</sup>. All in all, these studies show that the dNTP hydrolase activity of SAMHD1 is tightly controlled via PTMs to maintain the right dNTP levels needed at the various stages of the cell cycle.

### 1.2.2.2 Innate Immunity

Next to dNTP homeostasis, SAMHD1's role in innate immune responses has been extensively studied. The involvement of SAMHD1 in the autoinflammatory disease Aicardi-Goutières syndrome (AGS), as well as its induction by interferons and cytokines (as mentioned in subsection 1.2.1), reveal a connection of SAMHD1 to the immune system. AGS is a childhood disease characterized by increased production of interferon alpha (IFN- $\alpha$ ), mimicking an immune response to a viral infection<sup>78</sup>. In AGS patients, mutations in SAMHD1 leading to lower protein levels have been identified<sup>78</sup>. Depletion of SAMHD1 results in an increased dNTP pool, which subsequently causes genomic instability and activation of type I interferon via DNA damage signaling<sup>107</sup>.

In addition to AGS, SAMHD1's involvement in restricting viral replication has also been extensively studied. SAMHD1 is reported to restrict the replication of several retroviruses such as type 1 human immunodeficiency virus (HIV-1)<sup>81,108,109</sup>, equine infectious anemia virus (EIAV)<sup>76,110</sup>, and murine leukemia virus (MLV)<sup>76,110</sup>, as well as herpesviruses such as herpes simplex virus 1 (HSV-1)<sup>111-113</sup>, Epstein-Barr virus (EBV)<sup>114,115</sup> and human cytomegalovirus (HCMV)<sup>116,117</sup>. The primary mechanism of restriction against retroviruses is the inhibition of reverse transcription of the viral RNA into complementary DNA (cDNA) via the viral reverse transcriptase (RT) enzyme<sup>118</sup>. SAMHD1 lowers the dNTP pool to levels below what is required for proper activity of the viral RT<sup>118</sup>. Similarly, in the case of herpesviruses with DNA genomes, the decrease in dNTP levels caused by SAMHD1 prevents viral DNA replication by reducing the availability of nucleotides that are required for the activity of the viral polymerases<sup>111,113</sup>.

In order to counteract the restriction by SAMHD1, viruses have evolved several mechanisms. SAMHD1 phosphorylation at T592 has been shown to abolish its anti-viral activity<sup>105,106,119</sup>. In a study by Zhang *et al.* using EBV as a herpesvirus model, they have identified viral kinases that phosphorylate SAMHD1<sup>115</sup>. This phosphorylation has been reported to abolish restriction by SAMHD1 due to the inability of SAMHD1 to hydrolyze dCTP and deoxythymidine triphosphate (dTTP), allowing viral replication to proceed<sup>115</sup>. This phosphorylation of SAMHD1 is also induced by HCMV kinase pUL97<sup>116</sup>. Another PTM involved in herpesvirus restriction is SUMOylation. A recent study by Saida *et al.* has shown that SUMOylation of SAMHD1 at lysine residues at positions 469, 595 and 622 leads to an increase in restriction of EBV replication<sup>114</sup>. Their study also provides evidence for multiple layers of regulation of the viral restriction activity of SAMHD1. They show that SUMOylated SAMHD1 can also be phosphorylated at T592, whereas the phosphorylation of mutants unable to be SUMOylated is hindered<sup>114</sup>. SUMOylation of SAMHD1 seems to be important for the anti-HIV-1 activity, regardless of the phosphorylation status of SAMHD1<sup>120</sup>. This means that in the absence of SUMOylation of SAMHD1, dephosphorylation of SAMHD1 at T592 cannot recover its anti-viral activity<sup>120</sup>.

In addition to phosphorylation and SUMOylation, ubiquitination of SAMHD1 and its subsequent degradation is also a mechanism used by viruses to evade SAMHD1's anti-viral activity. Recently, there has been reports of HCMV making use of proteasomal degradation of SAMHD1 to counteract its anti-viral activity<sup>116,121</sup>. The exact mechanism, however, is not well understood. Nonetheless, a well-studied example of the virus-induced SAMHD1 degradation is the viral protein Vpx found in

lentiviruses<sup>108,122,123</sup>. Since the antagonism of SAMHD1 by Vpx is the basis of this work, more details into this interaction will be provided in section 1.3.

### 1.2.2.3 DNA damage response

Aside from its dNTP hydrolase-dependent functions, SAMHD1 has also been implicated in DNA damage responses<sup>124,125</sup>. In particular, SAMHD1 has been shown to interact with the endonuclease CtBP-interacting protein (CtIP), promoting repair of double stranded breaks via homologous recombination<sup>124</sup>. A recent study by Felip *et al.* has reported that SAMHD1 deficiency sensitizes several solid cancers, such as lung, ovarian and breast cancers, to DNA damage inducers<sup>125</sup>. They have also observed that low SAMHD1 expression in these cancers predicts longer survival of patients<sup>125</sup>.

In addition to interacting with damage response proteins, the dNTP hydrolase activity of SAMHD1 promotes DNA repair<sup>126,127</sup>. By lowering the dNTP levels, SAMHD1 prevents unwanted insertions at damage sites during repair<sup>126</sup>. In line with this, depletion of SAMHD1 causes instability of the genome through an increased frequency of insertions at the sites of repair due to increased dNTP levels<sup>126,127</sup>. Based on these observations, Akimova *et al.* hypothesize that SAMHD1 functions as a tumor-suppressor, and that reduced SAMHD1 levels lead to cancer progression. A deeper look into SAMHD1's role in cancer will be provided in subsection 1.2.3.

### 1.2.2.4 Retrotransposon regulation

Several studies have reported a role of SAMHD1 in the regulation of retroelements. Retroelements are parts of our DNA that contain the remains of ancient retroviral genomes that were integrated into host germline cells and passed down generations<sup>128</sup>. These elements have the ability to replicate and insert themselves into different genomic regions by a process called retrotransposition<sup>129</sup>. One such retrotransposon is called the long interspersed element 1 (LINE-1), which encodes an RNA-binding protein, an endonuclease and a reverse transcriptase<sup>129</sup>. Upon transcription, the LINE-1 mRNA translocates into the cytoplasm, where the mRNA is translated. The proteins encoded by LINE-1 and the mRNA form a ribonucleoprotein (RNP) complex which reenters the nucleus and subsequently integrates into the genome.

Zhao *et al.* have reported that LINE-1 is repressed by SAMHD1<sup>130</sup>. Interestingly, they have shown that the LINE-1 repression is independent of the dNTP hydrolase activity of SAMHD1<sup>130</sup>. Further studies have also confirmed SAMHD1's involvement in LINE-1 repression, however, the exact mechanism of repression is still unclear<sup>131,132</sup>. Essentially, the ability of SAMHD1 to repress retroelements further underscores its role in innate immunity, as well as cancer. In fact, several cancer-related mutations of SAMHD1 have been implicated in the de-repression of LINE-1 retroelements<sup>133</sup>, leading to genomic instability as a result of increased insertions of the retrotransposon<sup>134</sup>.

In summary, SAMHD1 is heavily involved in several key pathways involved in cell cycle progression, innate immunity, as well as genomic stability. The involvement in these pathways makes SAMHD1 an attractive candidate to investigate in the context of cancer, since disruptions of these pathways are implicated in cancer progression. The following subsection will discuss both the detrimental and the beneficial roles played by SAMHD1 in the context of cancer, as already alluded to above.

### 1.2.3 Role of SAMHD1 in cancer

SAMHD1's several functions mentioned in subsection 1.2.2 suggest its possible involvement in cancer progression. Indeed, changes in SAMHD1 protein levels and regulation of its activity have been implicated in several cancers. Mutations leading to reduced dNTP hydrolase activity, or increased methylation of *Samhd1* promoters causing reduced expression, have been observed in solid cancers such as lung and colon cancer, as well as in hematological malignancies such as chronic lymphoblastic leukemia (CLL), cutaneous T-cell lymphoma (CTCL), and T-cell prolymphocytic leukemia (T-PLL). A comprehensive summary of all the SAMHD1 mutations and their association with different cancers are provided in the recent review by Schott *et al.*<sup>135</sup>. In brief, lower SAMHD1 levels are hypothesized to aid cancer progression through the increase in mutations, increase in cell proliferation, and contribution to a pro-tumor microenvironment<sup>135</sup>.

Contrastingly, lower SAMHD1 levels could be beneficial in terms of therapy response. As mentioned in subsection 1.2.2.3, low SAMHD1 levels have been shown to increase sensitivity of several solid cancers to DNA damage inducers<sup>125</sup>. Although not yet experimentally investigated, low SAMHD1 levels may also be beneficial in enhancing anti-tumor immunity through the activation of the cyclic GMP-AMP synthase - stimulator of interferon genes (cGAS-STING) pathway<sup>136</sup>. The cGAS-STING pathway recognizes single-stranded DNA fragments and activates type-I interferon production<sup>137</sup>, which is potent against tumors<sup>138</sup>. Furthermore, an increase in genomic instability has also been shown to be a positive prognosis factor for immunotherapy<sup>139</sup>. Since reduction of SAMHD1 levels leads to genomic instability, cancers with lower SAMHD1 levels might be more sensitive to immunotherapy. This could be due to the increase in tumor-specific neo-antigens generated by the increase in mutation rate or, as mentioned above, by activating the cGAS-STING pathway<sup>140</sup>. This hypothesis, however, needs to be experimentally validated.

The role of SAMHD1 in the sensitivity of cancer cells to nucleoside analogs, however, has been extensively studied. Nucleoside analogs are commonly used in cancer treatment as they interfere with DNA replication to eventually induce cell death<sup>141</sup>. Since SAMHD1's primary role is to hydrolyze dNTPs, it is conceivable that nucleoside analogs, which have close structural similarities to dNTPs, also serve as substrates for SAMHD1 hydrolysis. Indeed, a study by Knecht *et al.* has evaluated the ability of SAMHD1 to hydrolyze a range of nucleoside analogs and has reported that the triphosphorylated forms of the drugs clofarabine, fludarabine and ara-C are all recognized as SAMHD1 substrates<sup>142</sup>. They have also tested the drug sensitivity of THP-1 cells, an AML cell line highly expressing SAMHD1, and have found that high SAMHD1 levels correlate with reduced sensitivity of the cells to the drugs<sup>142</sup>. In support of this, reducing SAMHD1 levels significantly restore drug-sensitivity of the cells<sup>142</sup>. In addition to the three drugs mentioned earlier, the activities of other nucleoside analogs such as nelarabine, decitabine, vidarabine and trifluridine have also been shown to be negatively influenced by SAMHD1<sup>143</sup>. The influence of SAMHD1 on the cytotoxicity of these drugs has been shown in the context of acute lymphoblastic leukemia (ALL)<sup>144</sup>, as well as AML<sup>145,146</sup>. More details into the role of SAMHD1 in AML will be provided next.



## 1.2.3.1 Role of SAMHD1 in AML

In 2017, Schneider *et al.* have provided evidence for the role of SAMHD1 in AML treatment response<sup>145</sup>. Based on retrospective analysis of an AML patient cohort, the authors show that AML patients with high SAMHD1 levels respond poorly to ara-C treatment and have poorer overall survival rates compared to low SAMHD1 expressers<sup>145</sup>. This observation has also been reported in a later study by Rassidakis *et al.*, who have investigated the impact of SAMHD1 on high-dose ara-C treatment regimen<sup>147</sup>. In addition to ara-C, response to the HMA decitabine, also used in AML treatment, is also influenced by SAMHD1 levels<sup>146</sup>.

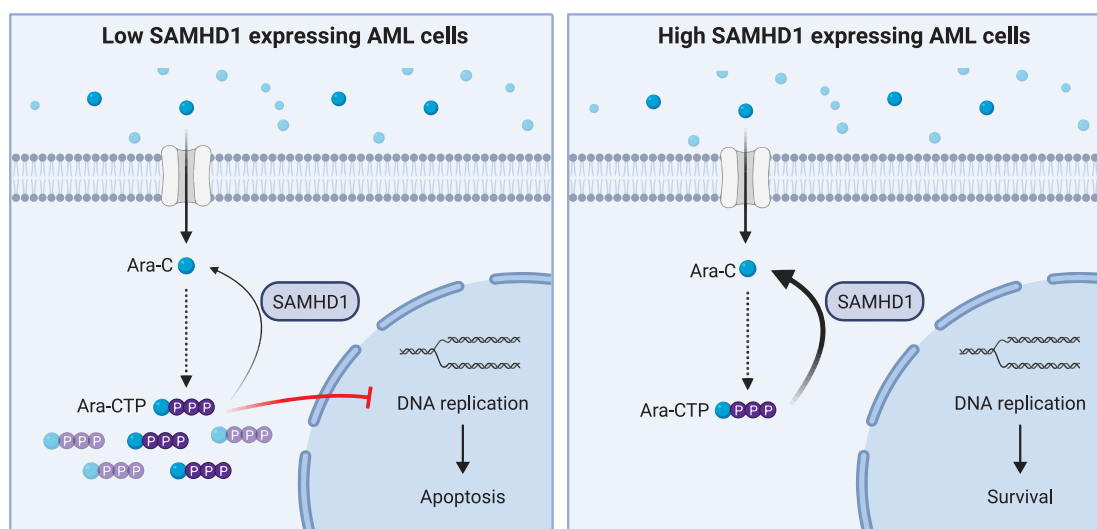


Figure 2: Illustration of SAMHD1's role in AML treatment response to ara-C.

Low SAMHD1 levels allows the accumulation of ara-CTP and subsequent cytotoxicity (left). High expression of SAMHD1 reduces the levels of ara-CTP, resulting in the survival of the AML cells (right).

Since ara-CTP closely resembles dCTP, it is recognized as a substrate by the dNTP hydrolase SAMHD1, which reduces ara-CTP levels in the cells by hydrolyzing it back to the inactive ara-C (Figure 2)<sup>145</sup>. As already discussed in detail in subsection 1.1.3, this reduction in ara-CTP levels then restricts the cytotoxic activity of ara-CTP leading to survival of AML cells (Figure 2). Reducing *Samhd1* expression or degrading the SAMHD1 protein significantly increases the sensitivity of both AML cell lines and patient-derived AML blasts to ara-C treatment<sup>145</sup>. In addition, mice transplanted with *Samhd1* knock-out AML cells show better survival compared to mice transplanted with AML cells expressing wild-type (WT) SAMHD1<sup>145</sup>. A recent study by Rothenburger *et al.* has reported the same phenomenon in ALL cells<sup>144</sup>. In their study, they have found high SAMHD1 expression to negatively influence treatment response to the guanine analog nelarabine<sup>144</sup>. Based on these observations, the authors conclude that SAMHD1 serves as a predictive biomarker for not only ara-C response, but also decitabine and nelarabine response<sup>144-146</sup>.

Since high SAMHD1 expression is a cause for concern regarding treatment efficiency of several nucleoside analogs and the HMA decitabine, several investigations have been made to identify ways to reduce SAMHD1 levels which could synergize with ara-C to improve treatment efficiency. One such strategy is to use RNR inhibitors (RNRi) which reduce the activity of SAMHD1 dNTP hydrolase by

lowering the levels of dNTPs required to activate SAMHD1<sup>148</sup>. A study has also identified several small molecule inhibitors of SAMHD1's dNTP hydrolase activity via a high-throughput assay<sup>149</sup>. Another strategy is to use Vpx (as previously mentioned in subsection 1.2.2.2), which is found in Simian Immunodeficiency Viruses (SIV) and type-2 HIV (HIV-2) strains. In the work by Schneider *et al.* and Oellerich *et al.*, Vpx containing virus-like particles (VLPs) are used as one of the strategies alongside small interfering RNAs (siRNAs) to reduce levels of SAMHD1 in the AML cells<sup>145,146</sup>. Using Vpx to manipulate the cellular levels of the SAMHD1 protein is the strategy that this work will be focusing on. Therefore, more information on Vpx and its antagonism of SAMHD1 will be provided in the upcoming section.

## 1.3 The lentiviral Vpx protein

### 1.3.1 Lentiviruses versus retroviruses

Lentiviruses are a part of the retrovirus family of RNA viruses. On one hand, retroviruses generally have a simple genomic organization encoding structural proteins such as the capsid and matrix proteins via the *gag* gene, the RT enzyme, protease and integrase via the *pol* gene, and an envelope protein via the *env* gene<sup>150</sup>. Lentiviruses, on the other hand, encode in addition to *gag*, *pol* and *env*, the regulatory proteins Tat, Rev, the accessory proteins Vif, Vpr, Vpu, Nef, and in some strains, Vpx<sup>151</sup>. Lentiviruses differ from retroviruses in that lentiviruses can infect both dividing and non-dividing cells, whereas retroviruses can only infect actively dividing cells<sup>152</sup>. The murine leukemia virus (MLV) is an example for a retrovirus, whereas HIV and SIV are considered lentiviruses.

In both lentiviral and retroviral life cycles, the RT enzyme is responsible for reverse transcribing the viral RNA genome into its cDNA. For retroviruses, which require dividing cells to replicate, the cDNA is then transported into the nucleus during the mitotic phase and subsequently integrated into the genome of the host cell<sup>153</sup>. Lentiviruses, however, can actively transport viral cDNA into the nucleus, enabling them to integrate viral cDNA into the host genome without the requirement of active cell division<sup>153,154</sup>.

The successful replication of lentiviruses in cells is restricted by several cellular proteins, one of which is SAMHD1, as described in subsection 1.2.2.2. SAMHD1 prevents the reverse transcription of viral RNA to cDNA by reducing the dNTP pool required for the RT to synthesize the viral cDNA<sup>118</sup>. Other restriction factors of lentiviral replication include serine incorporator 5 (SERINC5), apolipoprotein B mRNA editing enzyme catalytic subunit 3G (APOBEC3G), and tetherin, among others. The review by Boso & Kozak provides a detailed overview of known restriction factors and their functions<sup>155</sup>. In order to counteract the restriction by the host cells, lentiviruses have evolved antagonists of the restriction factors. For example, the accessory proteins Vpu (HIV-1) and Nef (SIV) antagonize tetherin, which prevents the release of virus particles from the cells after replication<sup>156</sup>. The Vif accessory protein counteracts APOBEC3G, a cytidine deaminase which facilitates the production of defective viral particles and also block RT<sup>157,158</sup>. SERINC5, which prevents lentiviral infection of cells after getting incorporated into the envelope of viral particles, is targeted by the accessory protein Nef<sup>159</sup>. Finally, the restriction factor SAMHD1 is targeted for degradation by the accessory protein Vpx<sup>108,123</sup>, or in some cases Vpr<sup>160</sup>.

### 1.3.2 Characteristics of the Vpx protein

Vpx is an accessory protein commonly found in lentiviruses such as SIV and HIV-2, but not in the more prevalent HIV-1. Vpx and the accessory protein Vpr share a high sequence similarity. Vpx was hypothesized to be a result of a duplication event of the *Vpr* gene that arose as a result of an evolutionary arms race between the viruses and SAMHD1<sup>160,161</sup>. The Vpx protein is relatively small, with a size of around 12-16 kDa<sup>162</sup>. The Vpx structure consists of 3 helices, a zinc-binding motif, and a poly-proline motif<sup>163</sup>. The zinc-binding motif contains histidines at positions 39 and 82 (H39 and H82), as well as cysteines at positions 87 and 89 (C87 and C89) of the sooty mangabey SIV strain (SIVsm), as an example<sup>163</sup>. This motif influences the stability of the Vpx protein by bridging the 1<sup>st</sup> and 3<sup>rd</sup> helices<sup>163</sup>. The poly-proline motif, which is highly conserved among HIV-2 and SIV strains, influences the expression levels of Vpx. A comprehensive study by Miyake *et al.* in 2014 has revealed that the number of prolines and their location on the Vpx protein determine the extent of dependency on the motif for expression<sup>164</sup>. Vpx is loaded into virus particles through its interaction with the Gag p6 protein<sup>165</sup> and it has been reported that the SIVsm Vpx residues 66, 69, 71, 74 and 75 are important for this interaction<sup>166</sup>. Vpx has also been shown to have a half-life of 30 hrs in HeLa cells (based on SIV macaque Vpx)<sup>167</sup>.

Vpx localizes to the nucleus despite not possessing a canonical nuclear localization signal. The residues 64-82 seem to be responsible for the nuclear localization of Vpx<sup>166,168,169</sup>. Due to its ability to enter the nucleus, Vpx has been reported to aid in the nuclear import of the viral pre-integration complex (consisting of viral cDNA and viral proteins)<sup>170</sup>. This import is dependent on the interaction with nucleoporin 153 (Nup153) protein<sup>171</sup> and is regulated by the phosphorylation of Vpx protein by the mitogen-activated protein kinase (MAPK)<sup>172</sup>.

In addition to aiding in the nuclear import of the viral pre-integration complex, additional functions of Vpx have also been investigated. As mentioned earlier, APOBEC3G is a restriction factor that is counteracted by the Vif protein. Another member of the APOBEC family, APOBEC3A, has also been shown to restrict lentiviral infection in a similar manner to APOBEC3G<sup>173</sup>. It has been reported that Vpx interacts with and induces proteasomal degradation of APOBEC3A<sup>158,174</sup>. The human silencing hub (HUSH) complex is another target of Vpx. The HUSH complex is involved in the repression of retrotransposons by maintaining the trimethylation mark at histone H3 lysine 9 (H3K9me3)<sup>175</sup>. In 2018, two groups have reported that Vpx is able to induce degradation of the HUSH complex via proteasomal degradation<sup>176,177</sup>. The antagonism of both APOBEC3A and HUSH complex takes place in a manner similar to that of SAMHD1, which will be described in subsection 1.3.3 next.

### 1.3.3 SAMHD1 antagonism by Vpx

The primary function of Vpx is to antagonize SAMHD1. Vpx induces SAMHD1 degradation in a species-specific manner, with some Vpx homologs having a broader specificity compared to others<sup>160</sup>. For example, Vpx from the SIV red-capped mangabey strain (SIVrcm) can only degrade SAMHD1 from red-capped mangabeys and not SAMHD1 from other species<sup>160</sup>. In contrast, Vpx from SIV macaque (SIVmac) is able to degrade SAMHD1 from a wide range of species, including human SAMHD1<sup>160</sup>. Interestingly, Vpr from two SIV lineages are also able to degrade human SAMHD1:

SIV De Brazza's monkeys (SIVdeb) and SIV mustached monkeys (SIVmus)<sup>160</sup>. Among the HIV-2 viruses, Vpx from the strains Rod9 and 7312a degrade human SAMHD1 but Rod9 Vpx has a much higher species specificity, only being able to degrade human and De Brazza's SAMHD1, compared to 7312a Vpx<sup>160</sup>.

The mechanism of Vpx antagonism of SAMHD1 is illustrated in Figure 3A<sup>178</sup>. Vpx hijacks the cellular cullin-4 RING ubiquitin ligase complex (CRL4), consisting of the proteins DNA damage binding protein 1 (DDB1), Cullin-4A (CUL4A), and E3 ubiquitin-protein ligase 1 (RBX1), via the direct interaction with DDB1 and CUL4A associated factor 1 (DCAF1)<sup>178</sup>. The main residue on Vpx responsible for this interaction is glutamine at position 76 (Q76)<sup>163</sup>. On the DCAF1 molecule, the residues asparagine at position 1135 and tryptophan at position 1156 are critical<sup>163</sup>. Vpx also directly interacts with SAMHD1 via its tryptophan at position 24 (W24)<sup>163</sup>. A summary of the various residues involved in the antagonism of SAMHD1 is provided in Figure 3B, based on the review by Schaller *et al.* and work done by Schwefel *et al.*<sup>163,179</sup>.

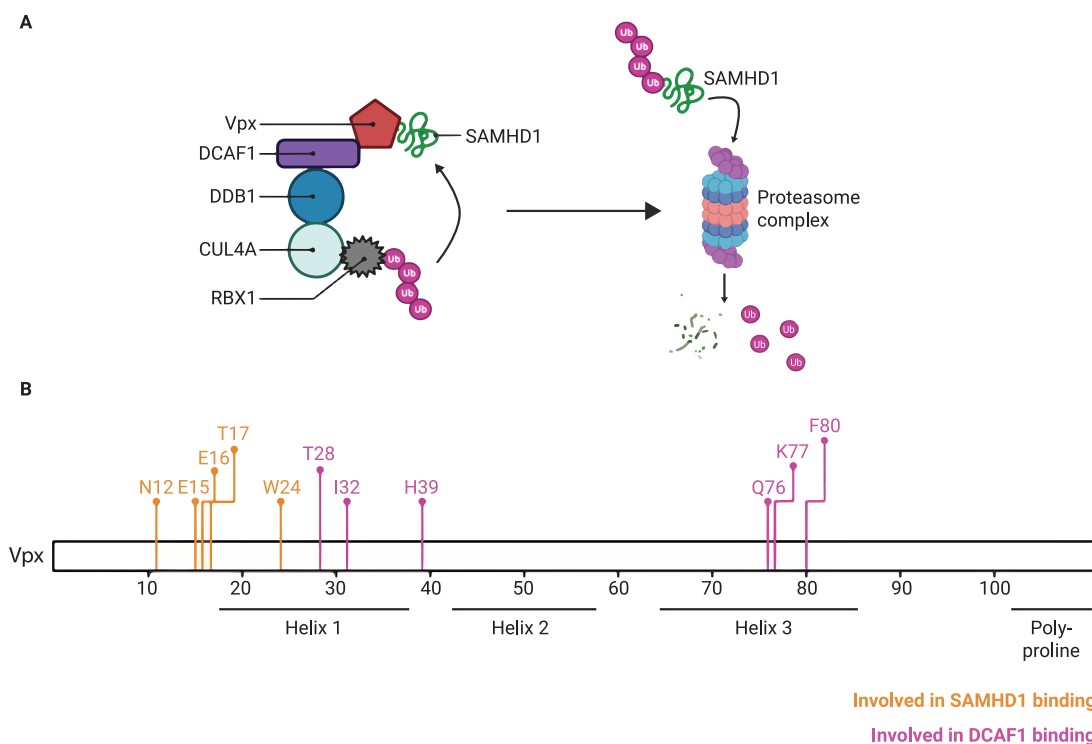


Figure 3: Vpx antagonism of SAMHD1 and the residues involved in interactions with SAMHD1 and DCAF1.

**A** Illustration showing the interaction of SAMHD1 with the proteasome complex consisting of DCAF1, DDB1, CUL4A and RBX1, which brings SAMHD1 in close proximity to RBX1, followed by its ubiquitination and subsequent proteasomal degradation. Illustration is modified after Schaller *et al.*<sup>179</sup>. Ub: ubiquitin **B** The Vpx residues involved in binding both SAMHD1 (orange) and DCAF1 (pink) are annotated, as well as the location of the helices and the poly-proline tail of the Vpx protein. The illustration is based on Schaller *et al.* and Schwefel *et al.*<sup>163,179</sup>.

Through their interactions with Vpx, the ubiquitin ligase RBX1 and SAMHD1 get into close proximity, allowing the ubiquitination of SAMHD1 and its subsequent degradation via the proteasome complex<sup>163,179</sup> (Figure 3A). In terms of the location of the antagonism, most studies agree that Vpx

induces SAMHD1 degradation in the nucleus<sup>79,122,180,181</sup>. However, some studies report that SAMHD1 is exported into the cytoplasm for degradation<sup>161,167</sup>. The reasons for the discrepancies are unclear, although different experimental set-ups and the Vpx homologs used may be contributing factors.

The induction of SAMHD1 degradation by Vpx occurs within 4 to 8 hrs of transduction with Vpx-containing VLPs<sup>182</sup>. SAMHD1 levels remain low for one week and start rising again from day 7 onwards after Vpx-VLP treatment<sup>183</sup>. Hollenbaugh *et al.* have also analyzed the dNTP levels after Vpx-mediated SAMHD1 degradation and have found that only deoxyadenosine triphosphate (dATP) and deoxyguanosine triphosphate (dGTP) levels peak after 24 hrs and decline to base levels 5 days after Vpx-VLP treatment<sup>183</sup>. They report no significant differences in dCTP and dTTP levels after Vpx-VLP treatment<sup>183</sup>.

The induction of SAMHD1 degradation by Vpx has been reported to be regulated by the phosphorylation of serine residue 13 (S13), based on experiments using HIV-2 Vpx<sup>184</sup>. This phosphorylation is mediated by the proviral integration site for Moloney murine leukemia virus (PIM) kinases 1 and 3<sup>184</sup>. Both, mutation of Vpx at the S13 site to alanine (S13A) and knock-down of PIM kinases using short hairpin RNA (shRNA), attenuated the SAMHD1 degradation capacity of Vpx<sup>184</sup>. Interestingly, serine 13 is highly conserved among human SAMHD1 degradation-competent Vpx but not in degradation-incompetent Vpx from SIVrcm and SIV mandrill (SIVmnd-2)<sup>163</sup>, reiterating the role of S13 phosphorylation for inducing SAMHD1 degradation.

The ability of Vpx to induce the degradation of SAMHD1, which is involved in the resistance of AML cells to ara-C (see subsection 1.2.3.1), prompted the investigation into effectively delivering Vpx into AML cells. With an effective Vpx delivery system, SAMHD1 levels in AML cells can be temporarily reduced to allow ara-C to induce cytotoxicity. In the next section, three different delivery systems will be discussed, which will be investigated in this work to deliver Vpx into AML cells.

## 1.4 The potential Vpx delivery systems

In this work, three main carriers will be investigated for the delivery of Vpx into AML cells: two chemical carriers, namely nano metal-organic frameworks (nanoMOFs) and cell-penetrating peptides (CPPs), and a virus-based carrier using VLPs (Figure 4). An introduction into each of these delivery systems will be provided in the following subsections.

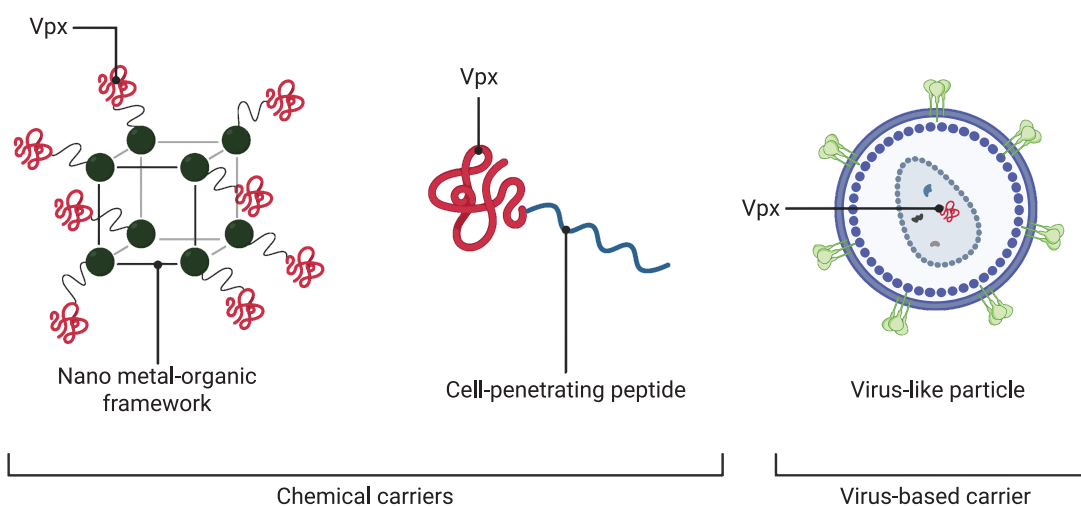


Figure 4: Vpx delivery systems investigated in this work.

Nano metal-organic frameworks (nanoMOFs), cell-penetrating peptides (CPPs) and virus-like particles (VLPs) carrying Vpx will be evaluated for their ability to effectively deliver Vpx into AML cells to induce SAMHD1 degradation, and subsequently ara-C cytotoxicity.

#### 1.4.1 Nano metal-organic frameworks (nanoMOFs)

Metal-organic frameworks (MOFs) are a class of porous coordination polymers (PCPs) that are assembled using metal ions and organic linkers<sup>185</sup>. They are known for their high porosity and surface area, as well as versatility<sup>186</sup>. Because of the possibilities of combining different metal ions with different organic linkers, a wide range of MOFs can be generated with varying physical and chemical characteristics<sup>186</sup>. Although MOF applications for storage and separation of gases have been extensively studied, they have been attracting attention for biological applications, such as imaging and drug delivery, as well<sup>185</sup>.

For use in biological settings, MOFs are reduced in size to nano-scale (nanoMOFs) to be able to effectively deliver molecules into cells<sup>185,187,188</sup>. In addition to size, the metal and organic components of the nanoMOFs used for biological applications must be carefully selected to avoid toxicity<sup>189</sup>. Metals like cobalt and nickel might not be suitable compared to iron, zinc and calcium, which exhibit lower toxicity<sup>190</sup>. Since MOFs are so versatile, the metal and organic linkers can be easily exchanged to make them more biocompatible. MOFs can be functionalized with biological molecules via three main ways: adsorption onto surface, encapsulation in its pores, or via covalent binding to either the metal or organic linker<sup>185</sup>. These functionalized MOFs have thus far been used in delivery of small molecule drugs, bioimaging, biosensing, as well as catalysis<sup>191</sup>.

##### 1.4.1.1 Biological applications of nanoMOFs

Since the application of nanoMOFs in biological settings is relatively new, only one nanoMOF has so far entered clinical trials for the treatment of tumors with radiation (Identifier: NCT03444714). This phase I clinical trial is based on the study by Lu *et al.*, where they report that a nanoMOF loaded with an immune checkpoint inhibitor molecule is able to reduce tumor burden in mice upon irradiation<sup>192</sup>. In addition, several nanoMOFs have shown both *in vitro* and *in vivo* functionality as drug<sup>193,194</sup> and imaging dye<sup>195,196</sup> delivery systems. The delivery of macromolecules, such as proteins and nucleic

acids, by nanoMOFs has also been investigated. For example, the delivery of plasmid DNA encapsulated in zeolitic imidazole framework-8 (ZIF-8) nanoMOFs has been shown to be highly efficient *in vitro* and cost-effective compared to traditional transfection methods<sup>197</sup>. NanoMOFs called Material from Institute Lavoisier (MIL)-101 have also been used to co-deliver short interfering RNA (siRNA) targeting multidrug resistance (MDR) genes with selenium/ruthenium nanoparticles into drug-resistant MCF-7 cells, leading to their cell death<sup>198</sup>. Tumor burden is also reduced *in vivo* upon treatment with the loaded MOF, providing evidence for the rationale of using nanoMOFs to deliver both siRNA and therapeutic agents for the effective treatment of cancer<sup>198</sup>.

For this work, the delivery of proteins by nanoMOF is of interest. This presents unique challenges because proteins are large and more sensitive to environmental conditions than small molecules and nucleic acids to maintain their functionality<sup>199,200</sup>. Nevertheless, several groups have successfully delivered proteins like cytochrome c, insulin, glucose oxidase, bovine serum albumin (BSA), green fluorescence protein (GFP) and Cas9, among others, into cells<sup>201</sup>. ZIF-8 is the most frequently investigated nanoMOF for the *in vitro* and *in vivo* delivery of proteins, either by adsorption onto their surface, encapsulation in pores, or via co-assembly of both MOFs and protein (i.e., one-pot coprecipitation)<sup>201</sup>. Other nanoMOFs like zirconium fumarate (Zr-fum)<sup>202</sup> and MIL<sup>203</sup> have also been investigated for their delivery of proteins, showing promise.

### 1.4.1.2 Challenges of nanoMOF-based delivery systems

Despite the successful applications mentioned above for drug and macromolecule delivery using nanoMOFs, several challenges exist that limit the expansion of its usage. One of these challenges is the effective release of the cargo carried by the nanoMOFs<sup>185,199</sup>. NanoMOFs are taken up by cells primarily via endocytosis<sup>199</sup>. Linnane *et al.* provide an excellent overview of the mechanisms of nanoMOF uptake by cells<sup>199</sup>. In summary, nanoMOFs are taken up either by pinocytosis or phagocytosis, where the nanoMOFs eventually end up in endosomes. This is followed either by their release into the cytoplasm or their degradation in the lysosomes or excretion through exosomes<sup>199</sup>. The efficiency of uptake of the nanoMOFs and release of cargo is influenced by many factors. The nanoMOF-intrinsic factors include size, shape, the charge, and modifications on its surface<sup>199,204</sup>. Strategies to improve the uptake of nanoMOFs are being investigated, including altering their size. For example, the study by Orellana-Tavra *et al.* compares two nanoMOFs of different sizes and reports that the larger particle, despite using different endocytosis pathways, is better able to avoid lysosomal degradation compared to the smaller particle<sup>205</sup>. Another study has reported that the addition of polyethylene glycol (PEG) improves uptake of the MOF UiO-66 loaded with a chemotherapeutic drug and its release inside the cell<sup>206</sup>.

Another challenge of using nanoMOFs as delivery tools is targeted delivery. For use in cancer therapy, it is important to consider targeting options of drug carriers to prevent any unwanted off-target effects<sup>207</sup>. Surface modification of nanoMOFs is one strategy to facilitate targeted delivery of cargo. The comprehensive study by Abánades Lázaro *et al.* shows that cancer cell lines HeLa and MCF-7 specifically take up UiO-66 nanoMOFs bound with folic acid on its surface, compared to the immortalized HEK293T cell line and primary lymphocytes from healthy donors<sup>208</sup>. In addition, they also show that the addition of PEG to its surface enhanced the delivery of nanoMOFs loaded with the

drug dichloroacetate by circumventing lysosomal degradation and, thereby, enabling effective drug release<sup>208</sup>.

Despite these challenges, the usage of nanoMOFs as drug delivery systems is gaining attention with increasing investigations into its optimization for therapeutic applications. Based on the promising evidence so far on the delivery of therapeutics, and their immense versatility, it is certainly worth investigating the use of nanoMOFs for the delivery of the Vpx protein.

#### 1.4.2 Cell-penetrating peptides (CPPs)

Cell-penetrating peptides (CPPs), as the name suggests, are peptides not exceeding 30 amino acids that are able to transverse the semi-permeable cell membrane without causing any damage to the cell<sup>209</sup>. This makes them very attractive carriers of impermeable biological molecules to facilitate their cellular delivery<sup>209</sup>. CPPs are categorized based on their amino acid characteristics. Amphipathic CPPs contain both hydrophobic and hydrophilic amino acids whereas non-amphipathic or cationic CPPs comprise positively charged amino acids<sup>210</sup>. The most studied cationic CPPs include naturally derived penetratin, the trans-activator of transcription (TAT) peptide derived from HIV-1 Tat protein, VP22 peptide of herpes simplex virus 1 (HSV-1), and the synthetic poly-arginine peptides. Amphipathic CPPs include the chimeric transportan, the synthetic Pep-1 and chimeric MPG<sup>211</sup>. Some of these CPPs are also commercially available, like TAT, penetratin, MPG and Pep-1<sup>210</sup>.

Due to the different chemical properties of CPPs, their internalization into cells varies and is dependent also on the concentration of peptide used. CPPs enter the cells via a combination of two main pathways: (1) direct translocation via micelle or pore formation, and (2) endocytosis<sup>212,213</sup>. The study by Duchardt *et al.* suggests that cationic CPPs enter the cells largely via direct translocation when present at high concentrations<sup>213</sup>. At lower concentrations, cationic CPPs are taken up via endocytosis<sup>214</sup>. However, this observation has not been reproduced in studies using other cationic CPPs such as poly-arginine or poly-lysine peptides<sup>215</sup>. In the case of amphipathic CPPs, their ability to form alpha helices or beta sheets have been reported to positively influence their uptake by cells<sup>216</sup> and even at low concentrations are able to directly transverse the cell membrane<sup>214</sup>. The uptake of the cationic CPPs like TAT and penetratin have been shown to be dependent on glycosaminoglycans on the cell surface<sup>217</sup>. However, since the uptake of CPPs is influenced not only by their chemical properties but also by other factors, including the type of cell, concentration, and type and size of cargo, it is hard to generalize a pattern of uptake<sup>212</sup>.

##### 1.4.2.1 Biological applications of CPPs

Like the nanoMOFs, CPPs have also been investigated for their use as delivery systems owing to their ability to easily penetrate cells. Cargo are loaded onto CPPs either covalently or non-covalently<sup>218</sup>. Many different CPPs with varying chemical and physical properties have been successfully used in the delivery of cargo such as small molecule drugs<sup>219,220</sup>, proteins<sup>221,222</sup>, peptides<sup>223</sup>, nucleic acids<sup>224,225</sup>, and even nanoparticles<sup>226</sup>. Interestingly, several CPPs have also been investigated to be used in leukemia therapy. For example, a CPP consisting of TAT and a nuclear localization signal obtained from the epidermal growth factor receptor pathway substrate no. 8 (EP28) successfully induce cell death of AML cells *in vitro* and inhibit leukemia progression *in vivo*<sup>227</sup>. Another study has



also utilized TAT as the CPP to facilitate the delivery of a short fragment of ASH2L, a protein involved in histone methylation, into AML cells to reduce histone methylation, increase sensitivity of AML cells to epigenetic modifier inhibitors, and inhibit the growth of AML cell lines<sup>228</sup>. The recent review by Matijaas & Neundorff presents an overview of CPPs used in other malignancies<sup>229</sup>. Some CPPs have even entered clinical trials over the last decade, being used to deliver therapeutics or imaging agents for tumors, hearing loss, Crohn's disease and inflammation, as summarized in the reviews by Xie *et al.*<sup>230</sup> and Matijass & Neundorff<sup>229</sup>. Despite their investigation in clinical trials, no CPP has been approved for clinical use thus far. Like the nanoMOFs, CPPs also face several challenges which need to be addressed in order to be successful.

### 1.4.2.2 Challenges of CPP-based delivery systems

The successful application of CPP-based delivery of therapeutics encounter challenges such as toxicity, instability, non-specificity and cargo release efficiency<sup>230,231</sup>. In terms of toxicity, a metabolomic study by Kilk *et al.* has compared five different CPPs for their toxic effects on the Chinese hamster ovarian (CHO) cell line, and has reported considerable toxicity for the transportan CPP<sup>232</sup>. In addition, due to the inherent non-specificity of CPPs, its ability to transport cargo into all kinds of cells might induce off-target toxicity<sup>233</sup>, as it has been observed in the study by Schwarze *et al.*<sup>234</sup>. Instability of CPPs is also a concern for effective treatment since CPPs are highly prone to degradation by proteases<sup>231,235</sup>. This has been demonstrated in a study by Elmquist & Langel, using a CPP called pVEC (derivative of murine vascular endothelial cadherin) which is readily degraded in medium containing serum compared to incubation in phosphate buffer<sup>236</sup>. A later study by the same group also reports degradation of the CPP penetratin to a higher degree than the CPPs transportan and TP10 (a transportan derivative)<sup>237</sup>.

Once CPPs reach their target cells, the cargo needs to be effectively released and reach their target site inside the cell to carry out their function. This effective release of cargo is another roadblock for the successful application of CPP-based therapies. CPPs taken up through endocytosis could end up getting trapped in the endosomes. A 2019 study by Patel *et al.* has investigated the uptake and endosomal escape efficiency of several CPPs covalently bound to GFP cargo<sup>238</sup>. They report that the uptake is heavily dependent on the cell type and the CPP and that the GFP cargo is frequently trapped in endosomes<sup>238</sup>.

In order to address these challenges, several strategies have been investigated. To address the issue of non-specificity, "smart" strategies to control the activation of CPPs have been developed<sup>239</sup>. This constitutes modifying the CPP itself or the use of carriers to target the CPPs to tumor sites, for instance. The investigated strategies entail the specific activation of CPPs via tumor-specific proteases, leveraging pH changes, or using external stimulus-sensitive CPPs<sup>239</sup>. In addition to the aforementioned strategies, tumor-homing peptides have also been identified, which specifically interact with cell surface receptors that are expressed on tumor cells<sup>240</sup>. A tumor-homing peptide relevant to this work is CPP44, which has been shown to specifically target AML cells and primary AML blasts without high uptake in healthy blood cells<sup>241</sup>, serving as an attractive CPP candidate for the delivery of Vpx.

Improving stability of the CPPs is achieved by modifying the physical and chemical properties of the CPPs. For example, using D-isoforms instead of L-isoform of amino acids or by modifying residues at the N-terminus of the CPPs<sup>242</sup>. More examples for improving stability are provided in the in-depth review by Fominaya, Bravo & Rebollo<sup>242</sup>.

Enhancing cellular uptake and cargo release is very complex due to the number of factors that influence this process. A comprehensive study by Mueller *et al.* has compared the uptake of 22 CPPs in various cell lines<sup>243</sup>. They report that the uptake efficiency varies based on the CPP and the cell line<sup>243</sup>. The efficiency is further complicated by changes in properties of the CPPs when a cargo is bound to it. Nevertheless, several studies have attempted to improve the uptake and cargo release efficiency of CPPs. One study by Patel *et al.* has reported that cyclizing the CPPs or fusing them with the influenza virus glycoprotein haemagglutinin (HA) increases the uptake of the CPPs conjugated to GFP<sup>238</sup>. However, no improvement in cargo release has been observed<sup>238</sup>. Nevertheless, multiple strategies have been investigated to improve cargo release by escaping the endosomes. Examples include fusion with pH-dependent membrane active peptides (PMAPs), using light to trigger the lysis of endosomes, or using multivalent CPPs<sup>244</sup>. These strategies are discussed in greater detail in the review by Erazo-Oliveras *et al.*<sup>244</sup>.

CPPs, like the nanoMOFs discussed in the previous subsection, offer many advantages as delivery systems. These advantages include the ability of CPPs to non-invasively transverse membranes with low general immunogenicity and inherent toxicity. Despite the challenges mentioned above, the availability of strategies to address the challenges make it worthwhile to pursue CPPs as a potential delivery system to carry Vpx to AML cells.

### 1.4.3 Virus-like particles (VLPs)

The final delivery system which will be investigated in this work is VLPs. VLPs are nano-scaled particles that resemble viruses, but are not infectious as they lack genetic material<sup>245</sup>. An illustration of the difference between an infectious virus and a VLP is shown in Figure 5, using lentiviruses as an example. VLPs can be generated from many different viruses such as rotavirus<sup>246</sup>, poliovirus<sup>247</sup>, lentivirus<sup>248</sup>, retrovirus<sup>249</sup>, coronavirus<sup>250</sup>, flavivirus<sup>251</sup>, papillomavirus<sup>252</sup> and adenovirus<sup>253</sup>. They therefore possess different physical characteristics. For example, they can either be enveloped or non-enveloped depending on their production method and the virus they are derived from<sup>254</sup>. VLPs are produced by self-assembly of viral structural proteins in producer cells and can be engineered to encapsulate biological or imaging material in their cavity<sup>255</sup>. Among mammalian cells, CHO and HEK293T cells are regularly used for VLP production<sup>256</sup>. Mammalian cells have the advantage that they have the capability to generate highly complex VLPs with envelopes and also retain post-translational modifications of the viral proteins which might be needed for effective VLP production<sup>256</sup>. For the purpose of this work, lentivirus-based VLPs will be discussed.

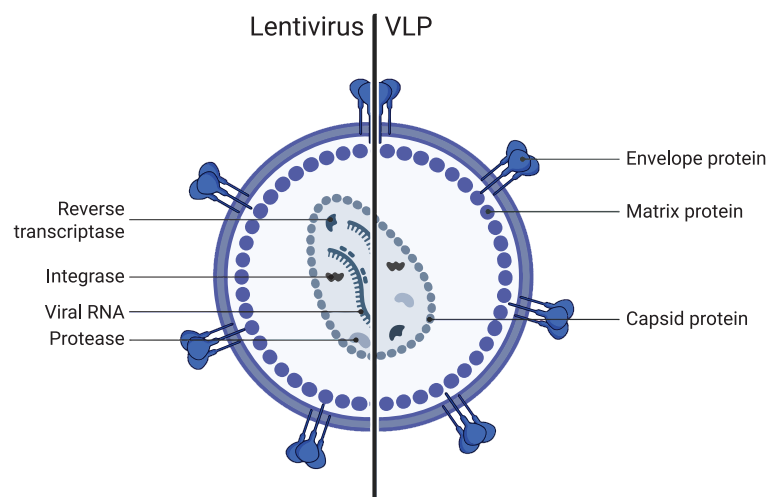


Figure 5: Comparison of lentivirus and its VLP derivative.

Lentivirus-based VLPs are structurally similar to lentiviruses but differ in the presence of the viral RNA. VLPs do not contain any genetic material and are therefore not infectious.

#### 1.4.3.1 Lentiviral VLPs as vaccines and nanocarriers

The usage as vaccines is the most investigated application of VLPs. A number of VLPs have already been approved by the FDA as vaccine candidates and many others are under clinical trial, as summarized by Nooraei *et al.*<sup>254</sup>. VLPs are very attractive as vaccine candidates due to their immunogenicity and safety. Since they resemble viral particles and are not infectious, they can be used to train the immune system to recognize their parent virus and induce both T cell and antibody responses<sup>245</sup>. Due to this, VLPs have demonstrated success through FDA-approved vaccines such as Gardasil, and Cervarix which are VLP vaccines against human papilloma viruses (HPV), and PreHevBrio which is a VLP vaccine against hepatitis B virus (HBV)<sup>257</sup>.

Besides their usage as vaccines, VLPs are very attractive as carriers of biological cargo due to their biocompatibility, their inherent ability to enter cells, and the ease of engineering their surfaces for targeted delivery<sup>258</sup>. There are several methods to package cargo into VLPs. One way is to disassemble the VLPs after purification and mix the dissociated proteins with the desired cargo under controlled conditions for reassembly<sup>259</sup>. This method allows for the encapsulation of cargo without the need to chemically modify it, however this process is not efficient<sup>260</sup>. Another encapsulation method involves modifying the cargo or the structural component of the VLPs such that they interact with each other<sup>261,262</sup>. This allows for effective loading of the VLPs but could result in loss of functionality of the cargo as a consequence of the modifications<sup>260</sup>. Further methods of cargo loading into VLPs are discussed in the reviews by He *et al.*<sup>263</sup> and Chung *et al.*<sup>255</sup>. With these methods, VLPs carrying cargo such as drugs and nucleic acids have been investigated for use in tumor therapy and antimicrobial therapy (with bacteriophages)<sup>254</sup>. Doxorubicin is the most studied drug cargo to be delivered with VLPs<sup>255</sup>. The delivery of proteins and peptides, however, is more complicated due to the risk of functionality loss from modifications to enhance VLP encapsulation<sup>255,260</sup>. Nevertheless, Kaczmarczyk *et al.* have reported the successful delivery of several functional proteins via fusion with the retroviral Gag polyprotein<sup>264</sup>. The Gag polyprotein is an important and the only component needed to generate VLPs as it consists of all structural proteins required<sup>265</sup>. Another study by Voelkel *et al.*

has also shown the successful delivery of F1p, a DNA recombinase, by fusion with the Gag protein<sup>266</sup>. The release of F1p from the Gag protein is facilitated by proteolysis<sup>266</sup>. A more recent example of Gag fusion proteins for cargo loading is provided by Banskota *et al.*, who have engineered MLV-based VLPs with enhanced cargo loading capacities by fusing the ribonucleoprotein cargo to MLV Gag<sup>267</sup>. These studies provide evidence for the potential of VLPs not only as vaccines or for the delivery of nucleic acids and drugs, but also for the successful delivery of complex macromolecules like proteins.

### 1.4.3.2 Challenges of VLP-based delivery systems

This subsection will only discuss the challenges faced by VLPs in terms of the delivery of cargo, and not in terms of their role as vaccines. As a cargo delivery system, the immunogenicity of VLPs can be a big drawback, since VLPs may be cleared by the immune system before they reach their target cells<sup>263</sup>. PEGylation is recognized as one of the most frequently used strategies to prolong the circulation of delivery systems in the blood stream<sup>268</sup>. Another method of preventing immune clearance of VLPs is the addition of “self-peptides” on their surface, such as human CD47, which has been shown to reduce the phagocytosis of nanobeads *in vivo*<sup>269</sup>. However, since VLPs have been mostly investigated for their application as vaccines, more investigations into strategies to mask the immunogenicity of VLPs need to be done<sup>260</sup>.

Another challenge, in common with CPPs and nanoMOFs, is the targeting of the VLPs. Luckily, the surface of the VLPs can be modified to specifically recognize target cells, such as tumor cells<sup>260,270</sup>. For example, a simian virus 40 (SV40)-based VLP is specifically taken up by epithelial carcinoma cells expressing epidermal growth factor (EGF) receptor, through the incorporation of the EGF molecule on the VLP surface<sup>271</sup>. This allows for specific endocytosis of the VLP and subsequent release of the mCherry fluorescent cargo<sup>271</sup>. The VLPs can also be pseudotyped with envelope glycoproteins from other viruses to change their cell tropism<sup>270</sup>. The study by Banskota *et al.*, for example, uses engineered envelope glycoproteins such as FuG-B2, which is a combination of rabies virus glycoprotein and the cytoplasmic domain of the vesicular stomatitis virus glycoprotein (VSV-G), to specifically target murine neuron cells<sup>267</sup>. Their study also shows the broad cell tropism of their VSV-G-pseudotyped VLPs, releasing cargo in a wide range of cells<sup>267</sup>. VSV-G can also be modified to alter cell specificity, as reviewed by Hastie *et al.*, making it a very versatile glycoprotein to be used for pseudotyping VLPs<sup>272</sup>.

The release of cargo is a further consideration for the successful application of VLPs as delivery systems. Viruses in general are naturally adapted to release their cargo in the cells<sup>273</sup>. Similarly, VLPs can enter cells via endocytosis and escape the endosomes to release their cargo<sup>273</sup>. In the case of non-viral cargo, however, effective release of the cargo from the VLPs can be a challenge. To this end, strategies involving environment-triggered release of cargo have been investigated. For instance, Thong *et al.* have used VLPs that can release its cargo upon thermal activation at 43°C<sup>274</sup>. In addition, Hu & Steinmetz report controlled and pH-dependent release of doxorubicin cargo from VLPs<sup>275</sup>. VLPs can also be purposefully designed to have chemical properties that allow them to disassemble under the specific conditions of endosomes for cargo release<sup>262,276</sup>. This strategy has been employed in MS2-based VLPs, which are derived from MS2 bacteriophages, where the authors show how mutations in the capsid protein can promote disassembly under the acidic conditions of endosomes<sup>276</sup>.

A VLP-based system is well-suited for the delivery of Vpx. Since Vpx is a lentiviral protein, it is naturally encapsulated into the lentivirus-based VLPs without the need for modification, due to its inherent Gag-binding ability. It is also efficiently released from the VLPs inside the cells, similar to its release during a natural infection cycle. These properties provide the rationale for investigating VLPs to deliver Vpx for the treatment of AML.

In summary, all three delivery systems discussed in this section (nanoMOFs, CPPs and VLPs) have their own unique properties that may be leveraged for the delivery of the Vpx protein. Even though each come with their own and shared challenges, it is still worthwhile to investigate their potential to deliver Vpx and induce SAMHD1 degradation.

## 1.5 Aims of this work

This work aims to lay the foundation for a Vpx-ara-C combination therapy for the treatment of AML. Thereby, the delivery systems, described in section 1.4, containing Vpx will be generated and evaluated for superior SAMHD1-degradation capacity, as well as the ability to improve ara-C sensitivity in AML cells. Figure 6 illustrates the four major parts of this work and will be used as a guide for the results and discussions, described in Chapter 3 and Chapter 4, respectively.

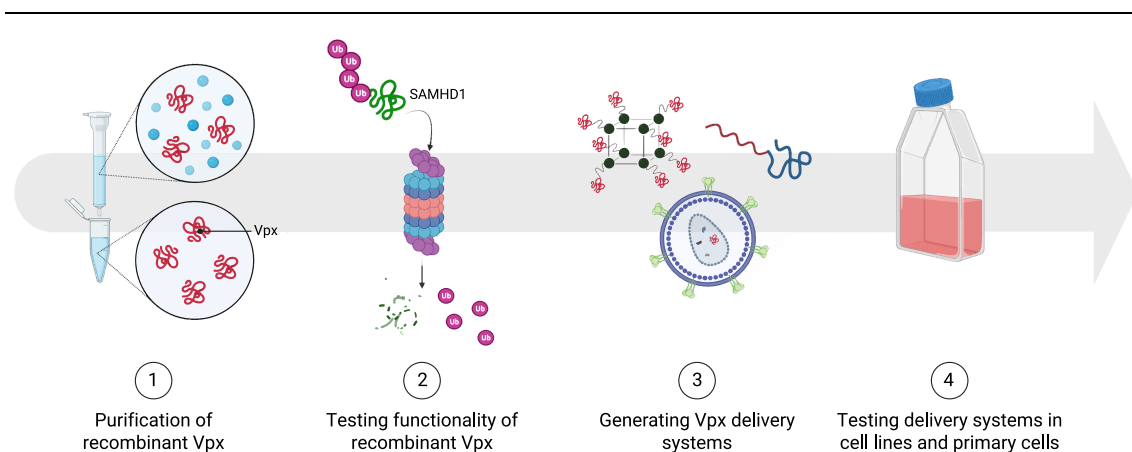


Figure 6: The four major parts of this work.

This illustration describes the four major phases which will be discussed in this thesis. The results obtained in this work will be discussed based on this framework.

- Part 1. The first part is the purification of recombinant Vpx. This purified Vpx will be used for the generation of nanoMOFs, and the purification strategy will also be used for the generation of CPPs, in part 3.
- Part 2. Before generating the delivery systems, the function of the purified Vpx needs to be confirmed in part 2. Since purified Vpx proteins from previous publications have never been utilized in cellular assays to show SAMHD1 degradation, this work will provide a proof-of-concept that a purified Vpx protein is functional in cellular assays.

- Part 3. In addition to the generation of nanoMOFs and CPPs, Vpx-VLPs will also be generated in part 3 of this work. The publication of Schneider *et al.* has reported a proof-of-concept using Vpx-VLPs to improve treatment response in AML cells. In this work, the VLPs will be modified to contain only the Vpx protein, without any accessory proteins that may cause side-effects in the AML cells. Once all the delivery systems are generated, they will be evaluated for their ability to reduce SAMHD1 levels in AML cell lines.
- Part 4. Finally, once the delivery systems are evaluated for their SAMHD1-degradation capacities, they will then be investigated for their ability to improve ara-C cytotoxicity in AML cell lines and in primary AML blasts.

Based on these results, some conclusions and recommended future directions will be provided on the use of Vpx-based ara-C combination therapies for AML treatment.

## 2. Materials and methods

### 2.1 General reagents, chemicals, and equipment

#### 2.1.1 Chemicals

Table 1: List of chemicals.

Chemical	Supplier	Catalog number
20% SDS solution	AppliChem	A0675
3-morpholinopropane-1-sulfonic acid (MOPS)	Carl Roth	6979.3
37% Formaldehyde	Carl Roth	7398.1
40% Acrylamide	Thermo Fisher Scientific	HC2040
99% Ethanol	Fisher Chemical	E/0600DF/17
Acetic acid	Carl Roth	3738.1
Albumin Fraction V	Carl Roth	8076.2
Ammonium persulfate (APS)	Thermo Fisher Scientific	HC2005
Ammonium sulfate	Merck	1217
ATP disodium salt	Sigma-Aldrich	A3377
Calcium chloride (CaCl <sub>2</sub> )	Carl Roth	A119.1
3-((3-cholamidopropyl) dimethylammonio)-1-propanesulfonate (CHAPS)	Carl Roth	1479.1
Dimethylsulfoxide (DMSO)	Carl Roth	4720.2
Dithiothreitol (DTT)	Carl Roth	6908.3
Ethylenediaminetetraacetic acid (EDTA)	ChemSolute	2216.1000
Glycerol	TH. Geyer	2050.1011
Glycine	AppliChem	A1067-1KG
HEPES sodium salt	Carl Roth	7020.2
Hydrochloric acid (HCl)	Carl Roth	P074.3
Imidazole	Carl Roth	X998.2
Isopropanol/ 2-propanol	Sigma-Aldrich	33539-2.5L-M
Isopropyl $\beta$ -d-1-thiogalactopyranoside (IPTG)	Glentham Life Sciences	CG2102
L-Glutathione reduced	Sigma-Aldrich	G4251-10G
Linear polyethylenimine (L-PEI)	Polysciences	23966-1
Magnesium chloride (MgCl <sub>2</sub> )	Carl Roth	KK36.1

Manganese chloride (MnCl <sub>2</sub> )	Carl Roth	4320.1
Methanol	TH. Geyer	1437.2511
Milk powder	Carl Roth	T154.3
NP-40	AppliChem	A1694.500
Paraformaldehyde (PFA)	AppliChem	A3813.1000
Phenylmethylsulfonyl fluoride (PMSF)	Carl Roth	6367.1
Poly-L-lysine solution (0.1%)	Sigma-Aldrich	P4832
RNase-free water	Sigma-Aldrich	W4502
SDS pellets	Carl Roth	CN30.3
Silver nitrate 5% solution	Carl Roth	N053.1
Sodium azide (NaN <sub>3</sub> )	Carl Roth	4221.3
Sodium carbonate (Na <sub>2</sub> CO <sub>3</sub> )	Carl Roth	P028.1
Sodium chloride (NaCl)	Carl Roth	9265.2
Sodium hydroxide (NaOH)	Carl Roth	P031.2
Sodium thiosulfate	Carl Roth	217263-250G
Sucrose	Carl Roth	4621.1
Tetramethylethylenediamine (TEMED)	Thermo Fisher Scientific	HC2006
Triton X-100	Carl Roth	3051.2
TRIZMA base (Tris)	Sigma-Aldrich	T1503
Tween-20	Carl Roth	9127.1
Zinc chloride (ZnCl <sub>2</sub> )	Carl Roth	Z0152-100G

### 2.1.2 Drugs

Table 2: List of drugs.

<b>Drug name</b>	<b>Supplier</b>	<b>Catalog number</b>
Cytarabine (Ara-C)	Tocris	4520
Daunorubicin	Selleckem	S3035
Decitabine	Selleckem	S1200
MG132	Sigma-Aldrich	474787-10MG



**2.1.3 Commercial reagents and kits**

Table 3: List of commercial reagents and kits.

<b>Name</b>	<b>Supplier</b>	<b>Catalog number</b>
<i>Reagents</i>		
10x Phosphate-buffered saline (PBS) powder	Sigma-Aldrich	P38135
4x Laemmli sample buffer	BioRad	1610747
50x Tris-acetate-EDTA (TAE) buffer	Carl Roth	CL86.2
Agarose	Omnilab	A2114
BD Phosflow Perm Buffer III	BD	558050
Biocoll separating solution	Biochrom	L6115
Clarity™ Western ECL Substrate	BioRad	1705061
cComplete EDTA-free Protease inhibitor cocktail	Sigma-Aldrich	11873580001
Enterokinase	New England BioLabs	P8070
Fetal calf serum (FCS)	Sigma-Aldrich	F7524
Gibson Assembly® Master Mix	NEB	E2611S
His-GFP	Thermo Fisher Scientific	A42611
HisPur Cobalt resin	Thermo Fisher Scientific	89964
Hoechst 33342 Solution	Thermo Fisher Scientific	62249
M2 Anti-FLAG resin	Sigma-Aldrich	A2220
MS2 RNA	Sigma-Aldrich	10165948001
Ni-nitrilotriacetic acid (NTA) Agarose	Qiagen	30210
NucleoZOL	Macherey-Nagel	740404.200
PageRuler™ Plus prestained protein ladder	Thermo Fisher Scientific	26619
ProLong™ Gold Antifade Mountant	Thermo Fisher Scientific	P36930
Quick Start Bovine Serum Albumin Standard Set	BioRad	5000207
Quick Start™ Bradford 1x Dye Reagent	BioRad	5000205
RiboLock RNase inhibitor	Thermo Fisher Scientific	EO0382
RosetteSep™ Human CD4+ T cell Enrichment Cocktail	Stemcell Technologies	15062
SmartLadder 200-10000bp	Eurogentec	MW-1700-10
SuperSignal™ West Femto Maximum Sensitivity Substrate	Thermo Fischer Scientific	34095
Suc-LLVY-AMC substrate	Enzo Life Sciences	BML-P802-0005

SYBR <sup>TM</sup> Safe DNA gel stain	Thermo Fisher Scientific	S33102
Trypan blue	Sigma-Aldrich	T8154
TurboFect <sup>TM</sup> transfection reagent	Thermo Fisher Scientific	R0531
Zombie Green <sup>TM</sup> Fixable Viability kit	BioLegend	423111
<i>Commercial Kits</i>		
GenElute <sup>TM</sup> Plasmid Miniprep kit	Sigma-Aldrich	PLN350-1KT
LiveBLAzer <sup>TM</sup> FRET-B/G Loading Kit with CCF2-AM	Thermo Fisher Scientific	K1032
MycoAlert <sup>TM</sup> Mycoplasma Detection kit.	Lonza	LT07-318
Nucleobond <sup>®</sup> Xtra Midi kit	Macherey-Nagel	740410.100
NucleoSpin <sup>TM</sup> Gel and PCR Clean-up kit	Macherey-Nagel	740609.250
P3 Primary cell nucleofection kit	Lonza	V4XP-3032
TaqMan <sup>®</sup> Gene Expression Assay – SAMHD1	Thermo Fisher Scientific	Hs00210019_m1
TaqMan <sup>®</sup> RNase P Control Reagents Kit	Thermo Fisher Scientific	4316844

#### 2.1.4 Buffers and solutions

Table 4: List and components of self-made buffers and solutions.

<b>Buffer/ Solution</b>	<b>Components</b>	<b>Application</b>
Flow cytometry (FC) stain buffer	PBS 1% FCS 0.09% NaN <sub>3</sub> Sterile-filtered	Flow cytometry intracellular staining
FC stain buffer with EDTA	FC stain buffer 2mM EDTA	Flow cytometry intracellular staining of primary AML blasts
Hunt lysis buffer	20 mM Tris-HCl pH 8.0 100 mM NaCl 1 mM EDTA 0.5% NP-40	Lysis of cells for SDS-PAGE

French press lysis buffer	50 mM Tris-HCl pH 7.5 150 mM NaCl 1 mM MgCl <sub>2</sub> 5 mM DTT 1 mM PMSF 1 µg/mL DNase	For the lysis of bacterial cells via french press homogenization
Sonication lysis buffer	50 mM Tris-HCl pH 7.5 100 mM NaCl 1% Triton X-100 1 mM DTT 1 mM PMSF 1.54 µM Aproptinin 10 µg/mL trypsin-inhibitor	For the lysis of bacterial cells via sonication
Glutathione S-transferases (GST) elution buffer	50 mM Tris base 10 mM reduced glutathione 1 mM DTT pH adjusted to 8 with HCl	For purification of GST-Vpx from bacterial cell lysate
Ni-NTA wash buffer	50 mM Sodium phosphate 300 mM NaCl 20 mM Imidazole pH adjusted to 7.5 with HCl	For purification of 6xHis-T7-Vpx from bacterial cell lysate
Ni-NTA elution buffer	50 mM Sodium phosphate 300 mM NaCl 250 mM Imidazole pH adjusted to 7.5 with HCl	
Size exclusion chromatography (SEC) protein storage buffer (Bacterial purification)	25 mM Tris-HCl, pH 7.5 150 mM NaCl 10% Glycerol 0.02% NaN <sub>3</sub> 5 mM DTT	Used during SEC as protein storage buffer after protein purification from bacterial cells
SEC protein storage buffer (Mammalian purification)	20 mM HEPES, pH 7.5 150 mM NaCl 10% Glycerol 1 mM DTT	Used during SEC as protein storage buffer after protein purification from mammalian cells
10x Tris-Glycine running buffer	250 mM Tris base 0.1% SDS 1.92 M Glycine	Electrophoresis buffer for SDS-PAGE
10x Tris-Glycine transfer buffer	250 mM Tris base 1.92 M Glycine	Transfer buffer for western blotting

## 2 Materials and methods

10x Tris-buffered saline (TBS)	500 mM Tris base 1.5 M NaCl pH adjusted to 7.5 with HCl	Nitrocellulose membrane and FLAG resin wash buffer stock
1x TBS-T	1x TBS 0.1% Tween-20	Nitrocellulose membrane wash buffer
Antibody solution	1x TBS-T 0.5% BSA 0.05% NaN <sub>3</sub> Sterile-filtered	Diluent for primary anti- bodies used for im- munoblotting
25% (w/v) sucrose	125 g sucrose PBS to 500 mL Sterile-filtered	Purification of VLPs and lentiviral vectors from cell supernatant
2x SG-PERT <sup>†</sup> reaction buffer	1x SG-PERT <sup>†</sup> Dilution buffer 10 mM MgCl <sub>2</sub> 0.2 mg/mL BSA 0.4 mM each dNTP 1 μM forward primer 1 μM reverse primer 8 ng MS2 RNA 1x SYBR™ Green I Master Mix	Dilution, lysis, and RT- PCR assay of lentiviral vectors and VLPs
2x SG-PERT lysis buffer	50 mM Potassium chloride (KCl) 100 mM Tris-HCl pH 7.4 40% Glycerol 1% Triton X-100	
10x SG-PERT dilution buffer	50 mM Ammonium sulfate 200 mM KCl 200 mM Tris-HCl pH 8	
CCF2 staining solution	2 μL CCF2 dye* 10 μL Probenecid 8 μL Solution B* 1 mL CO <sub>2</sub> -independent medium	Staining cells after virion fusion assay
Adherent cell freezing medium	70% DMEM unsupplemented 10% DMSO 20% FCS	For cryopreservation of HEK293T and HeLa cells
Suspension cell freezing me- dium	70% IMDM unsupplemented 10% DMSO 20% FCS	For cryopreservation of all suspension cells

TfbI	30.57 mM Potassium acetate 79.47 mM MnCl <sub>2</sub> 100.6 mM KCl 16 mM CaCl <sub>2</sub> 15% Glycerol pH adjusted to 5.8 with HCl	For preparation of chemically competent <i>E. coli</i> StbIII cells
TfbII	9.56 mM MOPS buffer 76 mM CaCl <sub>2</sub> 10.06 mM KCl 15% Glycerol pH adjusted to 7 with potassium hydroxide	
Silver stain fixation solution	40% Ethanol 10% Acetic acid	For silver staining of SDS polyacrylamide gels
Sensitization solution	0.02% Sodium thiosulfate	
Silver staining solution	0.1% Silver nitrate 0.02% Formaldehyde	
Development solution	3% Na <sub>2</sub> CO <sub>3</sub> 0.05% Formaldehyde	

*\*Part of LiveBLAzer™ FRET-B/G Loading Kit with CCF2-AM*

### 2.1.5 Growth media

Table 5: List of mammalian and bacterial growth media.

Media	Supplier	Catalog number
<i>Mammalian growth media</i>		
Dulbecco's modified eagle medium (DMEM)*	Thermo Fisher Scientific	31966047
Iscoves modified dulbecco's medium (IMDM)*	Sigma-Aldrich	I6529-500ML
Roswell Park Memorial Institute (RPMI) 1640 Medium*	Thermo Fisher Scientific	61870044
CO <sub>2</sub> -independent medium	Thermo Fisher Scientific	18045054

<i>Bacterial growth media</i>		
LB medium	TH-Geyer	8885.0500
LB agar	TH-Geyer	8822
TB medium	TH-Geyer	8049
SOB medium	Carl Roth	AE27.1

\*DMEM, IMDM and RPMI were supplemented with 10% heat-inactivated fetal calf serum, 100 units/mL penicillin and 0.1 mg/mL streptomycin before usage as cell growth media. They will be henceforth referred to as supplemented media.

### 2.1.6 Antibiotics

Table 6: List of antibiotics.

Antibiotic	Supplier	Catalog number	Working concentration
Ampicillin sodium salt	Carl Roth	K029.2	0.1 mg/mL
Carbenicillin sodium salt	Carl Roth	6344.3	0.1 mg/mL
Kanamycin sulfate	Carl Roth	T832.1	0.05 mg/mL
Puromycin dihydrogen chloride	Carl Roth	0240.3	Empirically determined for each cell line (0.1 µg/mL – 40 µg/mL)
Penicillin/ Streptomycin (Pen/Strep)	Sigma-Aldrich	P0781	100 units/mL penicillin and 0.1 mg/mL streptomycin

### 2.1.7 Antibodies

Table 7: List of antibodies used for western blot (WB), flow cytometry (FC), immunofluorescence (IF) and automated WB (Jess).

Antibody target	Species	Conjugate	Supplier (Catalog Number)	Application	Dilution
<i>Primary antibodies</i>					
SAMHD1	Rabbit	None	Proteintech (12586-1-AP)	WB	1:1000
				FC	1:100
SAMHD1	Mouse	None	See note 1	Jess	1:200

2 Materials and methods

		None	BioLegend (901513)	WB	1:1000
HA.11-tag	Mouse	BV421	BioLegend (682405)	FC	1:100
		AlexaFluor® 488	BioLegend (901509)	IF	1:1000
Vinculin	Mouse	None	Sigma-Aldrich <i>See note 1</i>	WB Jess	1:2000 1:2000
$\gamma$ -Tubulin	Mouse	None	Sigma-Aldrich	WB	1:500
SIV capsid protein p27	Mouse	None	<i>See note 1</i>	WB	1:100
HIV capsid pro- tein p24	Mouse	None	<i>See note 1</i>	WB	1:200
DDB1	Rabbit	None	Proteintech	WB	1:1000
B23	Rabbit	None	Proteintech (60096-1-IG)	WB	1:1000
	Mouse	None	Sigma-Aldrich (F3165-.2MG)	WB	1:1000
FLAG-tag	Rat	APC	BioLegend (637308)	FC	1:100
His-tag	Mouse	None	Dianova (DIA- 900-M)	WB	1:500
GST-tag	Goat	None	Cytiva Life Sci- ences (27457701)	WB	1:1000
CD33	Mouse	PE	BioLegend (303403)	FC	1:20
CD34	Mouse	FTTC	BioLegend (343603)	FC	1:20
CD45	Mouse	V450	BD (560368)	FC	1:20
<i>Secondary antibodies</i>					
Rabbit IgG	Goat	HRP	Jackson Immu- noresearch	WB	1:10,000
		AlexaFluor® 660	Thermo Fisher Scientific	FC	1:200
Mouse IgG	Goat	HRP	Jackson Immu- noresearch	WB	1:10,000

Goat IgG	Rabbit	HRP	Jackson Immuno- research	WB	1:10,000
----------	--------	-----	-----------------------------	----	----------

**Note 1:** Antibody received from the research group of Prof. Oliver T. Keppler as supernatant of hybridoma cells

### 2.1.8 Equipment

Table 8: List of equipment.

Equipment name	Supplier
Äkta Pure ( <i>see note 2</i> )	Cytiva
Bandelin Sonorex Super	Bandelin
BD FACSLytic	BD
BioSpectrometer	Eppendorf
Branson Ultrasonics™ Sonifier ( <i>see note 3</i> )	Fisher Scientific
CFX96 Touch Real-Time PCR Detection System	BioRad
CLARIOstar	BMG
Concentrator Plus	Eppendorf
Fisherbrand™ Model 120 Sonic Dismembrator	Fisher Scientific
Jess	Biotechne (Protein Simple)
Mastercycler Nexus X2	Eppendorf
NanoDrop One Spectrophotometer	Thermo Fisher Scientific
QuantStudio™ 3 Real-Time PCR System	Applied Biosystems
Sorvall mTX150 Micro-Ultracentrifuge	Thermo Fisher Scientific
Sorvall wX+ Ultra Series Ultracentrifuge	Thermo Fisher Scientific
Table-top centrifuges	Eppendorf
UVP UVsolo touch	Analytic Jena
Vilber Fusion FX	Vilber

**Note 2:** The Äkta Pure machine was kindly provided by the research group Höpfner, Gene Center Munich

**Note 3:** The sonifier was kindly provided by the research group Hornung, Gene Center Munich

### 2.1.9 Software and web applications

Table 9: List of software and web applications used in this work.

Software/ Web app	Company	Version
Adobe Illustrator	Adobe	2022
Benchling	Benchling	-
BioRad CFXMaestro™	BioRad	1.1
BioRender	BioRender	-
FlowJo	FlowJo, LLC	10.7.1
GraphPad Prism	GraphPad	7, 8 and 9



ImageJ (Fiji)	NIH	2.0
Imaris Viewer	Oxford Instruments	9.9.1
NEB Tm Calculator	NEB	1.15.0
NEBioCalculator	NEB	1.15.0
Nikon NIS-Elements	Nikon	5.11.01
QuantStudio™ Design & Analysis Software	Applied Biosystems	1.4.3
SnapGene	SnapGene	6.1

## 2.2 Mammalian cell lines, bacteria, and nucleic acids

### 2.2.1 Mammalian cell lines

Table 10: List of cell lines.

Cell line name	Description	Source
THP-1	Acute monocytic leukemia	Cinatl Lab
HEL	Erythroleukemia, FAB M6 classification	Frankfurt, Germany
THP-1 SAMHD1 +/+	THP-1 parental cells used as controls for SAMHD1 knock-out	
THP-1 SAMHD1 -/-	SAMHD1 knocked-out THP-1 cells	
HEL WT SAMHD1	HEL cells overexpressing WT SAMHD1	
MonoMac6	Acute myeloid leukemia, FAB M5 classification	
OCI-AML2	Acute myeloid leukemia, FAB M4 classification	
OCI-AML3	Acute myeloid leukemia, FAB M4 classification	
HL60	Acute promyelocytic leukemia, FAB M2 classification	
HEK293T	Immortalized human endothelial kidney cells	DSMZ
HeLa	Immortalized cervical cancer cells from Henrietta Lacks (1951)	DSMZ
Jurkat	Acute T cell leukemia cells	Cinatl Lab Frankfurt, Germany

### 2.2.2 Bacteria

Table 11: List of bacteria.

<b>Bacteria name</b>	<b>Description</b>	<b>Source</b>
<i>E. coli</i> StbIII	Chemically competent <i>E. coli</i> for plasmid preparation	NEB
<i>E. coli</i> Rosetta2	Chemically competent <i>E. coli</i> for protein expression, encoding rare tRNA	Novagen
<i>E. coli</i> BL21	Chemically competent <i>E. coli</i> for protein expression	NEB

### 2.2.3 Plasmids

Table 12: List of mammalian and bacterial expression plasmids.

<b>Plasmid name</b>	<b>Description</b>	<b>Purpose</b>
<i>Mammalian expression plasmids</i>		
pCDNA3.1+	Plasmid backbone with CMV promoter and ampicillin resistance	Overexpression of protein-of-interest in mammalian cells
pCMV HIV-1 Rev	Encodes HIV-1 Rev protein	Enhancement of new generation VLP yield
pCMV BlaM-Vpr	Encodes the Vpr protein fused to beta-lactamase (BlaM)	Expression of the BlaM-Vpr fusion protein for the production of BlaM-Vpr-VLPs
pWPI	Lentiviral transfer vector encoding protein-of-interest and puromycin resistance gene separated by an internal ribosome entry site (IRES) sequence and flanked by 5' and 3' long terminal repeats (LTR)	Production of lentiviral vectors encoding protein-of-interest
pMD2.G	Encodes VSV-G envelope protein via the CMV promoter	Used to pseudotype lentiviral vectors and VLPs with the VSV-G envelope protein
pPAX2	Lentiviral packaging vector encoding HIV-1 Gag and Pol	Production of lentiviral vectors
pAdVantage	Vector encoding adenoviral Virus Associated I and II RNA (VAI and VAII RNA)	Used during lentiviral vector production to enhance translation of viral proteins

pSIV3+ SIVmac251 X+	Encodes SIVmac251 Gag, Pol, Vif, Nef, Rev, Tat, and Vpx	Used for production of 1 <sup>st</sup> generation VLPs containing all regulatory and accessory proteins
pSIV3+ SIVmac251 R+	Encodes SIVmac251 Gag, Pol, Vif, Nef, Rev, Tat, and Vpr	
pSIV3+ SIVmac239 Vpx	Encodes SIVmac251 Gag, Pol, and 3xFLAG-tagged SIVmac239 Vpx	Used for production of new generation VLPs carrying the various 3xFLAG-tagged Vpx or Vpr constructs without additional regulatory or accessory proteins
pSIV3+ SIVmnd-2 Vpx	Encodes SIVmac251 Gag, Pol, and 3xFLAG-tagged SIVmnd-2 Vpx	
pSIV3+ SIVdeb Vpr	Encodes SIVmac251 Gag, Pol, and 3xFlag-tagged SIVdeb Vpr	
pSIV3+ SIVmus Vpr	Encodes SIVmac251 Gag, Pol, and 3xFlag-tagged SIVmus Vpr	
pSIV3+ HIV-2 7312a Vpx	Encodes SIVmac251 Gag, Pol, and 3xFlag-tagged HIV-2 7312a Vpx	
pSIV3+ HIV-2 Rod9 Vpx	Encodes SIVmac251 Gag, Pol, and 3xFlag-tagged HIV-2 Rod9 Vpx	
pSIV3+ HIV-1 Vpr	Encodes SIVmac251 Gag, Pol, and 3xFlag-tagged HIV-1 Vpr	
pSIV3+ delta	Encodes only SIVmac251 Gag and Pol	
pSIV3+ SIVmac239 P64Q Vpx	Encodes SIVmac251 Gag, Pol, and 3xFlag-tagged SIVmac239 P64Q Vpx mutant	
pSIV3+ SIVmac239 I75M Vpx	Encodes SIVmac251 Gag, Pol, and 3xFlag-tagged SIVmac239 I75M Vpx mutant	
pSIV3+ SIVmac251 Vpx	Encodes SIVmac251 Gag, Pol, and 3xFlag-tagged SIVmac251 Vpx	
pSIV3+ SIVmac251 Vpx untagged	Encodes SIVmac251 Gag, Pol, and an untagged SIVmac251 Vpx	
<i>Bacterial expression plasmids</i>		
pGEX-2T GST-Vpx	Encodes a GST-Vpx fusion protein	Expression and purification of GST-Vpx from <i>E. coli</i>
pGEX6P GST-6xHis-Vpx	Encodes a GST-6xHis-Vpx fusion protein with a PreScission Protease cleavage site between the GST and 6xHis tags	Expression and purification of GST-6xHis-Vpx from <i>E. coli</i>

pET28a 6xHis-T7-Vpx	Encodes a 6xHis-T7-Vpx fusion protein	Expression and purification of 6xHis-T7-Vpx from <i>E. coli</i>
pUC57-Kan CPP44-HA-Vpx	Encodes CPP44-HA-WT Vpx protein, synthesized by Genewiz	Used for subcloning of 3xFLAG-CPP44-HA-Vpx into mammalian expression plasmid for expression and purification from HEK293T cells
pUC57-Kan TAT-HA-Vpx	Encodes TAT-HA-WT Vpx protein, synthesized by Genewiz	Used for subcloning of 3xFLAG-TAT-HA-Vpx into mammalian expression plasmid for expression and purification from HEK293T cells

#### 2.2.4 Primers and gene fragments

Primers were designed using SnapGene and were obtained from Eurogentec. Melting temperatures of each primer were obtained using NEB Tm Calculator.

Table 13: List of primers.

Pseudo-nym	Primer name	Sequence (5' to 3')	Restriction enzymes	Purpose
R1	pET_Vpx_fwd	CGGAATTCATGTCAGATC CCAGGGAG	EcoRI	Cloning of SIVmac Vpx into pET28a(+) vector
R2	pET_Vpx_rev	CGGTCGACTTATGCTAGT CCTGGAGGG	Sall	
R3	pcDNA_His-Vpx_fwd	CGAAGCTTATGGGCAGC AGCCATCAT	HindIII	Cloning of 6xHis-T7-SIVmac Vpx into pcDNA3.1(+) vector
R4	pcDNA_His-Vpx_rev	CGTCTAGATTATGCTAGT CCTGGAGGG	XbaI	
R5	pcDNA_6xHis-T7-Vpx 67aa_fwd	CGGAATTCGAGTGGCTG AACAGAACC	EcoRI	Cloning of 6xHis-T7-SIVmac 67 amino acid truncated Vpx into pcDNA3.1(+) vector
R6	pcDNA_6xHis-T7-Vpx 67aa_rev	CGTCTAGATTAGCATCTG CAGCCCTTCTT	XbaI	
R7	pcDNA_6xHis-T7-Vpx 49aa_fwd_flank	CGGAATTCGAGTGGCTG AACAGAACCG	EcoRI	Cloning of 6xHis-T7-SIVmac 49 amino acid truncated

2 *Materials and methods*

R8	pcDNA_6xHis-T7-Vpx 49aa_rev_int	GGGCAGGTGGTTCACGG	-	Vpx into pcDNA3.1(+) vector
R9	pcDNA_6xHis-T7-Vpx 49aa_fwd_int	CCGTGAACCACCTGCCC CAGGGCATGAGCCCCAG	-	
R10	pcDNA_6xHis-T7-Vpx 49aa_rev_flank	CGTCTAGATTAGCATCTG CAGCCCTTCTTG	XbaI	
R11	pGEX_6xHis-Vpx_fwd	CGGGATCCGGGCACCAC CACCACCACCACGGG ATGTCAGATCCCAGGGA G	BamHI	Cloning of 6xHis-SIVmac Vpx or 3xFLAG-SIVmac Vpx into pGEX-6P vector
R12	pGEX_3xFLAG-Vpx_fwd	CGGGATCCGGGGACTAC AAGGACCACGACGGC GGGATGTCAGATCCCAG GGAG	BamHI	
R13	pGEX_Vpx_rev	CGGAATTCCTTATGCTAGT CCTGGAGGG	EcoRI	
R14	pcDNA_6xHis-T7-Vpx 67aa_fwd_ATG	CGGAATTCATGGAGTGG CTGAACAGAACAG	EcoRI	Addition of ATG start codon to pcDNA3.1 6xHis- 67aa Vpx and 6xHis- 49aa Vpx
R15	pcDNA_6xHis-T7-Vpx 49aa_fwd_flank_ATG	CGGAATTCATGGAGTGG CTGAACAGAACCG	EcoRI	
R16	pCDH_SAMHD1-T2A-Vpx_fwd	CGATGCATATGGGCAGC AGCCATCAT	NsiI	Cloning of Vpx after T2A self-cleavage site into pCDH SAMHD1-T2A-BFP vector
R17	pCDH_SAMHD1-T2A-Vpx_rev	CGGTCGACTTATGCTAGT CCTGGAGGG	Sall	
R18	pSIV3+_6xHis-Vpx_fwd	CGGCTTAGCCACCATGG GCAGCAGCCATCAT	BlnI	Cloning of 6xHis-SIVmac Vpx into pSIV3(+) vector
R19	pSIV3+_6xHis-Vpx_rev	CGCTCGAGTTATGCTAGT CCTGGAGGG	XhoI	
R20	pWPI_6xHis-Vpx_fwd	CGACGCGTATGGGCAGC AGCCATCAT	MluI	Cloning of 6xHis-SIVmac Vpx into pWPI vector
R21	pWPI_6xHis-Vpx_rev	CGACTAGTTTATGCTAGT CCTGGAGGG	SpeI	

R22	pSIV3+_Hibit_3 xFLAG_rev	GAGATCTTCTTGAACAGC CGCCATCCAGACACTGCT CCCTTGTCGTCGTCGTC	-	Insertion of Hibit se- quence between 3xFLAG and Vpx
R23	pSIV3+_Hibit_ Vpx_fwd	GTCTGGATGGCGGCTGT TCAAGAAGATCTCTGGG GCGGCCGCTATGA	-	sequences in pSIV3(+) vector
R24	pSIV3+_pol 3' end_fwd	AGGCTAGAGAGGTGGCA TAG	-	
R25	pSIV3+_Vpx 3' end_rev	CGGTAATGTTGGACATG AGCC	-	
R26	pWPI_3xFLAG- Vpx_rev	GACTAGTTTAGGCCAG GCCAGGAG	SpeI	Cloning of 3xFLAG- Vpx (WT and Q76A) into pWPI vector
R27	pWPI_3xFLAG- Vpx_fwd	CGGATCCATGGACTAC AAGGACCACGA	BamHI	
R28	pcDNA_Vpx- HA-10xHis_rev	CCGTCTAGATTAATGGTG ATGGTGGTGATGGTG	XbaI	Cloning of Vpx-HA- 10xHis (WT and Q76A) into pcDNA3.1(+) vector
R29	pcDNA_Vpx- HA-10xHis_fwd	CCCAAGCTTGCCACCATG AGCGACCC	HindIII	
MS2- fwd	SG-PERT MS2 cDNA_fwd	TCCTGCTCAACTTCCTGT CGAG	-	Used for the amplifi- cation of MS2
MS2-rev	SG-PERT MS2 cDNA_rev	CACAGGTCAAACCTCCTA GGAATG	-	cDNA in the SG- PERT assay <sup>277</sup>

#### 2.2.4.1 Gene Fragments

Gene fragments not exceeding 500 base pairs were used for Gibson assembly cloning. Codon optimization was performed using Thermo Fisher GeneArt software and the gene fragments were obtained from IDT technologies as gBlocks. The following lists the gene fragments used in this study:

G1: codon-optimized WT Vpx-HA-TEV-10xHis (For cloning pWPI and pcDNA WT Vpx-HA-10xHis)

5' –

GTTTAAACCTGCAGGCGCGCCGGATCCGCCACCATGAGCGACCCAGAGAGAGAATCCCTCCTGGCAAT  
AGCGGCGAGGAAACAATCGGCGAGGCCTTCGAGTGGCTGAACAGAACCGTGGAAGAGATCAACCGCGA  
GGCCGTGAACCATCTGCCTCGCGAGCTGATCTTCCAAGTGTGGCAGAGAAGCTGGGAGTACTGGCACG  
ATGAGCAGGGCATGAGCCCCAGCTACGTGAAGTACAGATACCTGTGCCTGATCCAGAAAAGCCCTGTTCA  
TGCCTGCAAGAAAGGCTGCAGATGCCTCGGCCAAGGACATGGTGCTGGTGGATGGCGACCTGGACCT  
CCTCCACCTCCACCACCTGGACTTGTGGTGGCGGAGGCAGCTACCCCTACGATGTGCCAGACTACGCCG  
AGAACCTGTACTTCCAAGGCCACCACCATCATCACCACCATCACCATCACTGAACTAGTAAACTACGGGCT  
GCAGGAATCCGCC – 3'

G2: codon-optimized Q76A Vpx-HA-TEV-10xHis (For cloning pWPI and pcDNA Q76A Vpx-HA-10xHis)

5' –

GTTTAAACCTGCAGGCGCGCCGGATCCGCCACCATGAGCGACCCAGAGAGAGAATCCCTCCTGGCAAT  
AGCGGCGAGGAAACAATCGGCGAGGCCTTCGAGTGGCTGAACAGAACCGTGGAAGAGATCAACCGCGA  
GGCCGTGAACCATCTGCCTCGCGAGCTGATCTTCCAAGTGTGGCAGAGAAGCTGGGAGTACTGGCAGC  
ATGAGCAGGGCATGAGCCCCAGCTACGTGAAGTACAGATACCTGTGCCTGATCGCCAAGGCTCTGTTCA  
TGCACTGCAAGAAAGGCTGCCGGTGTCTCGGAGAAGGACATGGTGCTGGTGGATGGCGACCTGGACCT  
CCTCCACCTCCACCACCTGGACTTGTGTGGTGGCGGAGGCAGCTACCCTTACGATGTGCCAGACTACGCCG  
AGAACCTGTACTTCCAAGGCCACCACCATCATCACCACCATCACCATCACTGAACTAGTAAACTACGGGCT  
GCAGGAATTCCGCC – 3'

G3: CPP44-HA-Vpx (amino acids 1-50) (For cloning pWPI and pcDNA CPP44-HA-Vpx-10xHis)

5' –

AAACCTGCAGGTCAACAGCAGCTTAGCACGCGTGCCACCATGAAGAGGGCCACCATGCGGTTCCGGTAC  
ACCTGGAATCCCATGAAGTACCCTTACGACGTGCCCGACTACGCCATGAGCGACCCAGAGAGAGAATC  
CCTCCTGGCAATAGCGGCGAGGAAACAATCGGCGAGGCCTTCGAGTGGCTGAACAGAACCGTGGAAGA  
GATCAACCGCGAGGCCGTGAACCATCTGCCTCGCGAGCTGATCTTCCAAGTGTGGCAG – 3'

G4: TAT-HA-Vpx (amino acids 1-50) (For cloning pWPI and pcDNA TAT-HA-Vpx-10xHis)

5' –

AAACCTGCAGGTCAACAGCAGCTTAGCACGCGTGCCACCATGTACGGCCGGAAGAAGCGGCGGCAGCG  
GAGAAGATACCCCTTACGACGTGCCCGACTACGCCATGAGCGACCCAGAGAGAGAATCCCTCCTGGCAA  
TAGCGGCGAGGAAACAATCGGCGAGGCCTTCGAGTGGCTGAACAGAACCGTGGAAGAGATCAACCGCG  
AGGCCGTGAACCATCTGCCTCGCGAGCTGATCTTCCAAGTGTGGCAG – 3'

G5: WT Vpx (amino acids 50-112)-TEV-10xHis (Used in combination with G3 or G4 to clone pWPI and pcDNA CPP44- or TAT-HA-WT Vpx-10xHis, respectively)

5' –

GCTGATCTTCCAAGTGTGGCAGAGAAGCTGGGAGTACTGGCACGATGAGCAGGGCATGAGCCAGAGCT  
ACGTGAAGTACAGATACCTGTGCCTGATGCAGAAAGCCCTGTTTCATGCACTGCAAGAAAGGCTGCAGAT  
GCCTCGGCGAAGGACATGGTGCTGGTGGATGGCGACCTGGACCTCCTCCACCTCCACCACCTGGACTTG  
CTGGTGGCGGAGGAAGCGAGAACCTGTACTTCCAAGGCCACCACCATCATCACCACCATCACCATCACTG  
AACTAGTAAACTACGGGCTGCAGGAATTCCG – 3'

G6: Q76A Vpx (amino acids 50-112)-TEV-10xHis (Used in combination with G3 or G4 to clone pWPI and pcDNA CPP44- or TAT-HA-Q76A Vpx-10xHis, respectively)

5' –

GCTGATCTTCCAAGTGTGGCAGAGAAGCTGGGAGTACTGGCACGATGAGCAGGGCATGAGCCAGAGCT  
ACGTGAAGTACAGATACCTGTGCCTGATGGCCAAAGCCCTGTTTCATGCACTGCAAGAAAGGCTGCAGAT  
GCCTCGGCGAAGGACATGGTGCTGGTGGATGGCGACCTGGACCTCCTCCACCTCCACCACCTGGACTTG  
CTGGTGGCGGAGGAAGCGAGAACCTGTACTTCCAAGGCCACCACCATCATCACCACCATCACCATCACTG  
AACTAGTAAACTACGGGCTGCAGGAATTCCG – 3'

## 2.3 Cell culture

### 2.3.1 Mammalian cell culture and cryopreservation

Mammalian cells (listed in Table 10) were regularly split to maintain cell viability. All suspension cell lines were cultured in supplemented IMDM, while all adherent cell lines were cultured in supplemented DMEM. Refer to subsection 2.1.5 for information on supplemented media. All cells were incubated at 37°C and 5% CO<sub>2</sub>.

Adherent cells were split once they reached a confluency of approximately 90%. The medium was aspirated, and cells were detached from the plate after incubation with Trypsin-EDTA for 5 mins. Trypsin was inactivated by the addition of fresh supplemented DMEM. An appropriate volume of cells was transferred to a fresh tissue culture-treated plate and incubated until needed. The adherent cells were cultivated for a maximum of 30 passages and then discarded.

Suspension cells were split by simply replacing appropriate volumes of cells with fresh supplemented IMDM and maintaining cell density at approximately 1x10<sup>6</sup> cells/mL.

All cell lines were routinely tested for mycoplasma contamination using the MycoAlert™ Mycoplasma Detection kit.

For cryopreservation of mammalian cells, approximately 2x10<sup>6</sup> cells/mL of cells were washed in PBS, resuspended in an appropriate volume of freezing medium (see Table 4 for components) and transferred to cryotubes (Sarstedt). Cells in the freezing medium were then placed in a Mr. Frosty freezing container at -80°C overnight to allow for slow freezing of cells at a rate of 1°C per minute. The following day, the frozen cells were transferred to liquid nitrogen tanks for long-term storage.

Primary AML blast cells were cultivated in the laboratories of Prof. Dr. Marion Subklewe at the Gene Center, LMU Munich, with the approval of the ethics committee of LMU Munich, Germany (project number: 216-08). Aliquots of the cultivated cells were obtained to be used in flow cytometric analysis (see section 2.6) and for the BlaM-Vpr fusion assay (see subsection 2.5.5).

### 2.3.2 Bacterial cell culture and cryopreservation

Bacterial cells were either cultured in liquid LB or TB medium, or on solid LB agar plates containing the appropriate antibiotics, where applicable, and incubated at 37°C. Liquid cultures were grown in either 15 mL conical tubes with loosened lids, or in baffled Erlenmeyer flasks.

For the cryopreservation of bacterial liquid cultures, equal volumes of an overnight bacterial culture and sterile-filtered 50% glycerol were mixed in 1.5 mL Eppendorf tubes. The glycerol stocks were then stored at -80°C.

### 2.3.3 Thawing of cells

Mammalian cryopreserved cells were quickly thawed in a 37°C water bath and transferred to 9 mL of appropriate medium in a 15 mL conical tube. Cells were pelleted at 500 x g for 5 mins, then



resuspended in the appropriate medium and transferred to a culture plate or flask. The cells were then incubated as per usual at 37°C and 5% CO<sub>2</sub>.

Bacterial cryopreserved cells were removed from the freezer in a cool rack to maintain the frozen state of the cells. A pipette tip was used to scrape off frozen cells from the Eppendorf tubes into a 15 mL conical tube containing LB or TB medium with the appropriate antibiotics, and resuspended. The cells were then incubated as per usual at 37°C.

#### **2.3.4 Isolation and cultivation of primary CD4+ T cells**

Blood from healthy human donors were provided by the University Hospital of Munich, Department of Immunohematology, Infection Screening and Blood Bank (ATMZH) with approval from the ethics committee of LMU Munich, Germany (project number: 17-202-UE).

The RosetteSep™ Human CD4+ T cell Enrichment Cocktail was used to isolate the CD4+ T cells from blood by negative selection, according to the manufacturer's instructions. Briefly, 1 mL of the cocktail was added to 20 mL of blood, mixed, and incubated for 20 mins at room temperature. Non-CD4 recognizing antibodies and anti-glycophorin A antibodies in the cocktail recognize cells without CD4 surface expression and red blood cells, respectively. The blood was further diluted with PBS to a final volume of 30 mL, and overlaid onto 15 mL Biocoll separating solution to separate CD4+ T cells from the remaining blood cells. The tube was then centrifuged at 700 x g for 35 mins at room temperature, with slow acceleration and deceleration. During centrifugation, the antibody-cell complexes run through the Biocoll layer, while the CD4+ T cells remain between the plasma and Biocoll layers. The CD4+ T cell layer was then carefully transferred to a fresh 50 mL conical tube, washed twice in PBS at 500 x g for 5 mins, and finally resuspended in supplemented RPMI medium at a cell density of 2x10<sup>6</sup> cells/mL. The primary resting CD4+ T cells were cultured for a maximum of 7 days from isolation without the addition of any cytokines.

#### **2.3.5 SAMHD1 degradation and co-treatment assays**

Vpx delivery systems used in this thesis were routinely characterized for their SAMHD1 degradation capability and subsequently, their ability to improve cytotoxicity of ara-C. The Vpx delivery systems were Vpx-VLPs, Vpx-CPPs and Vpx-nanoMOFs. In order to determine SAMHD1 degradation capabilities, 1x10<sup>5</sup> THP-1 cells in a final volume of 200 µL were treated with the delivery systems in a flat-bottom 96-well plate. For treatment using Vpx-VLPs, refer to subsection 2.5.2. Varying amounts of Vpx-CPPs and Vpx-nanoMOFs were added to the THP-1 cells and incubated to 24 hrs. Thereafter, the treated THP-1 cells were intracellularly stained for SAMHD1 and subjected to flow cytometric analysis. Reduction in the fluorescence intensity of SAMHD1 served as an indicator of a functional Vpx delivery system. For more information on the flow cytometric procedure and analysis, see section 2.6.

For co-treatment assays, 1x10<sup>4</sup> cells per well in a final volume of 100 µL of various cell lines and primary cells were first pre-treated with Vpx delivery systems for 24 hrs. After pre-treatment, 1:4 serial dilutions of ara-C were added to the cells and treated for 96 hrs. Thereafter, the resazurin cytotoxicity assay was performed (see subsection 2.3.6). The calculated percentage of viable cells was

plotted against the drug concentration to determine the absolute inhibitory drug concentration at which 50% of the cells were killed ( $IC_{50}$ ), using the GraphPad Prism software.

### 2.3.6 Resazurin cytotoxicity assay

The viability of suspension cells after drug treatment, with or without Vpx delivery systems, was determined by the resazurin cytotoxicity assay. Resazurin is a blue, cell-permeable compound with low fluorescence. Upon entry into viable cells which produce NADH<sup>+</sup>, resazurin is reduced to a pink compound resorufin. By measuring the absorbance of resazurin and resorufin at the optical densities of 600 nm and 570 nm, respectively, the viability can be calculated (Equation (1)). Wells with only media without cells were included as negative controls to account for background fluorescence.  $A_{570nm}$  and  $A_{600nm}$  in Equation (1) refers to the absorbance at the indicated wavelengths after subtracting background absorbance from negative control wells.

$$\% \text{ viable cells} = \frac{A_{570nm} - A_{600nm} \text{ of treated wells}}{A_{570nm} - A_{600nm} \text{ of untreated wells}} \times 100\% \quad (1)$$

For this assay, 10  $\mu$ L of resazurin dye was added to each well containing 100  $\mu$ L of cells and incubated for 5 hrs at 37°C and 5% CO<sub>2</sub>. Cells which were not treated with drugs or delivery systems were used as positive control. Absorbance was measured using the CLARIOstar Plus microplate reader.

## 2.4 Nucleic acid techniques

### 2.4.1 Preparation of chemically competent *E. coli*

*E. coli* StbIII cells (NEB) were made chemically competent using CaCl<sub>2</sub>. For this, *E. coli* StbIII cells from NEB were streaked onto a LB agar plate without any antibiotics and incubated overnight at 37°C. The following day, a single colony was picked, transferred to a 15 mL tube containing 10 mL of 10-beta/Stable Outgrowth Medium (NEB), and incubated overnight again at 37°C. The next day, 3 mL of the preculture were added to 200 mL of SOB medium and grown at 37°C until an optical density at 600 nm wavelength ( $OD_{600}$ ) of 0.5 was reached. The cells were then distributed to four 50mL falcon tubes and pelleted with 3500 x g at 4°C for 10 mins. The pellets were then resuspended in 10 mL TfbI buffer per tube. After incubating on ice for 10 mins, the cells were pelleted with 3500 x g at 4°C for 12 mins. The pellets were then resuspended in 2.5 mL TfbII buffer per tube and incubated on ice for 10 mins. The competent cells were then distributed into 50  $\mu$ L aliquots in 0.5 mL tubes and stored at -80°C. See Table 4 for the recipes of TfbI and TfbII buffers.

### 2.4.2 Transformation of chemically competent *E. coli*

Chemically competent *E. coli* StbIII cells (NEB) were transformed with plasmids for their amplification and isolation. 100 ng of plasmid or 20  $\mu$ L of ligation product were added to 50  $\mu$ L thawed chemically competent *E. coli* and incubated on ice for 2 mins. The cells were then heat-shocked for exactly 30 seconds at 42°C and incubated on ice again for 2 mins. Finally, 100  $\mu$ L of SOC medium

were added to the transformed cells and plated onto LB agar plates containing the appropriate antibiotics (see Table 6 for antibiotic concentrations). The plates were incubated at 37°C overnight for selection of successfully transformed colonies. The following day, single colonies were picked and cultivated overnight in 5 mL of TB medium containing the appropriate antibiotics. These overnight cultures were then further used for plasmid preparation (see subsection 2.4.3) and subsequent downstream applications.

### 2.4.3 Plasmid preparation and sequencing

Plasmids were isolated from *E. coli* StblII cells either using the GenElute™ Plasmid Miniprep kit or the Nucleobond® Xtra Midi kit for small-scale and large-scale preparation of plasmids, respectively. 1 mL of bacterial culture in TB medium was used for the small-scale preparation and between 300 – 1000 mL of bacterial culture in TB medium were used for the large-scale preparation. Bacterial cultures were grown at 37°C under constant shaking at 180 rpm overnight.

For large-scale plasmid preparation, after incubation, cells were pelleted by centrifugation at 3400 x g for 25 mins at 4°C in 500 mL conical centrifugation tubes. Pelleted cells were then further processed for plasmid isolation according to manufacturer's instructions. Purified plasmids were reconstituted in appropriate volumes of nuclease-free water overnight at 4°C. Plasmid concentration was then measured using the Nanodrop One Spectrophotometer, diluted to 1 µg/µL concentration, and kept at -20°C for long-term storage or 4°C for short-term storage.

For small-scale plasmid preparation, manufacturer's instructions were followed. Purified plasmids were reconstituted in 100 µL of nuclease-free water. Plasmid concentration was checked, as described above.

In order to verify the sequences, the plasmids were sent for Sanger sequencing, provided by Eurofins Genomics. The obtained sequences were analysed using SnapGene or Benchling. Standard primers provided by Eurofins Genomics were used for sequencing.

### 2.4.4 Polymerase chain reaction (PCR)

PCR was generally performed for cloning purposes. Desired DNA sequences were amplified from 10 ng of template plasmids using the high-fidelity Phusion® DNA polymerase (NEB) and the appropriate primer pairs (see Table 13 for list of primers). Table 14 shows the volumes of reagents used in a typical PCR reaction with a final volume of 20 µL. Primer melting temperatures were obtained using NEB Tm Calculator according to the polymerase used. The PCR reactions were then carried out in an Eppendorf Thermocycler. Table 15 shows the typical PCR run conditions used with the Phusion® DNA polymerase.

Table 14: Volume of reagents used in PCR reaction using Phusion® DNA polymerase.

Reagent (Stock concentration)	Volume ( $\mu\text{L}$ )	Final concentration
Plasmid template	Dependent on concentration (10 ng)	
5x Phusion® HF buffer	2	1x
dNTPs (10 mM)	0.4	200 $\mu\text{M}$
Forward primer (10 $\mu\text{M}$ )	1	0.5 $\mu\text{M}$
Reverse primer (10 $\mu\text{M}$ )	1	0.5 $\mu\text{M}$
Phusion® DNA polymerase	0.2	
Nuclease-free water	To 20 $\mu\text{L}$	

Table 15: Typical thermocycler run conditions for Phusion® DNA polymerase PCR.

Step	Temperature ( $^{\circ}\text{C}$ )	Time (sec)	
Initial denaturation	98	30	
Denaturation	98	10	
Annealing	Determined by calculation	30	30 cycles
Elongation	72	30*	
Final extension	72	600	
Hold	10		

\*Elongation time is dependent on size of amplicon. In general, 30 seconds were used for 1 kb of amplicon.

#### 2.4.5 Restriction digest and agarose gel electrophoresis

Plasmids and PCR products were digested with restriction enzymes for the purpose of cloning or for confirming the identity of plasmids after preparation. In general, 1  $\mu\text{g}$  of plasmid or PCR product was digested with 1  $\mu\text{L}$  of restriction enzymes in 1x CutSmart buffer at the recommended digestion temperature for the enzymes for 60 mins in a final volume of 50  $\mu\text{L}$ . The digested nucleic acids were loaded onto 1% (w/v) agarose gels containing 1x SYBR™ Safe DNA gel stain and electrophoresis was performed at a constant voltage of 80 V for 60 mins. Thereafter, the gels were imaged using the UVP UVsolo touch gel documentation system. For cloning purposes, the desired fragments of digested plasmids were cut from the agarose gel on a UV transilluminator.

#### 2.4.6 Gel and PCR product clean-up

Cut agarose gel fragments of digested plasmids and PCR products were cleaned up for further downstream applications using the NucleoSpin™ Gel and PCR Clean-up kit, according to manufacturer's instructions. The cleaned fragments and PCR products were reconstituted in 30  $\mu\text{L}$  nuclease-free water and stored at 4 $^{\circ}\text{C}$  until further downstream processing.

### 2.4.7 Ligation

Digested and cleaned PCR products and plasmid fragments were ligated using T4 DNA ligase. The plasmid fragment (vector) and PCR product (insert) were mixed with 1 µg of T4 DNA ligase in a final volume of 20 µL. A 3:1 ratio of insert to vector was generally used and their corresponding volumes were determined using the NEBioCalculator based on their length. The mixture was incubated overnight at 16°C and used for transformation of *E. coli* (see subsection 2.4.2) and subsequent clone selection.

### 2.4.8 Gibson Assembly

Gibson assembly cloning allows for the ligation of several DNA fragments with overlapping end regions, without the need for generating sticky overhangs with restriction enzymes. For this reaction, 100 ng of plasmid backbone was mixed with 50 fmol of synthesized DNA fragments (gBlocks, see subsection 2.2.4.1 for sequences) and 1x Gibson Assembly Master Mix in a final volume of 20 µL. The mixture was incubated at 50°C for 1 hr, followed by transformation of *E. coli* (see subsection 2.4.2) and subsequent clone selection.

### 2.4.9 RNA isolation

Total RNA (mRNA) was isolated from cell lines using the NucleoZOL reagent, according to manufacturer's instructions. In general, approximately 5 to 10 million cells were used for total RNA isolation. Briefly, the cells were washed in PBS and resuspended in 500 µL NucleoZOL per 5 million cells. Thereafter, the DNA and protein contaminants were removed by centrifugation, and the supernatant containing RNA was transferred to a fresh tube. Total RNA was then precipitated using isopropanol and pelleted by centrifugation. The isolated RNA pellet was reconstituted in RNase-free water, and concentration was measured on the NanoDrop One Spectrophotometer. The purified RNA was then stored at -80°C or used directly for reverse transcription (see subsection 2.4.10).

### 2.4.10 Reverse transcription and quantitative PCR (qPCR)

Purified RNA was converted to cDNA using the High-Capacity RNA-to-cDNA™ kit, according to manufacturer's instructions. Briefly, 1 µg of RNA was mixed with the buffer and enzyme mix provided by the kit. The reaction was performed on a thermocycler set to an incubation at 37°C for 60 mins, followed by an inactivation at 95°C for 5 mins and storage at 4°C. The prepared cDNAs were either directly used for qPCR reaction or stored at -20°C.

The qPCR reaction was performed on the QuantStudio™ 3 Real-Time PCR System. TaqMan® Gene Expression assays (20X reagent) containing gene-specific primers for SAMHD1 and a FAM dye-conjugated probe, and TaqMan RNase P Control Reagents kit (20X reagent) with a VIC dye-conjugated probe (endogenous control) were used together with the TaqMan® Fast Advanced Master Mix (2X reagent) for the qPCR reactions, according to manufacturer's instructions. Briefly, 2 µL of cDNA template was mixed with the master mix and the Gene Expression assay or RNase P control Reagents kit to a final volume of 20 µL per well in a white-walled 96-well qPCR reaction plate. The qPCR run

conditions are shown in Table 16, based on the manufacturer’s instructions (TaqMan® Fast Advanced Master Mix User Guide).

Table 16: qPCR run conditions in the QuantStudio™ 3 Real-Time PCR instruments.

Step	Incubation temperature (°C)	Incubation time	Cycles
UNG incubation	50	2 mins	1 cycle
Polymerase activation	95	2 mins	
Denaturation	95	1 sec	40 cycles
Annealing and extension	60	20 secs	

Following the qPCR run, the real time data was analyzed on the QuantStudio™ Design & Analysis Software. The comparative  $C_t$  method was used to analyze the gene expression levels (Equation (2)).  $C_t$  refers to the cycle number at which the fluorescence signal crosses the background threshold.  $\Delta C_t$  normalizes the  $C_t$  value of the gene-of-interest and the  $C_t$  value of the endogenous control gene, which is RNaseP.

$$\Delta C_t = \text{Average } C_t (\text{gene-of-interest}) - \text{Average } C_t (\text{endogenous control}) \quad (2)$$

In order to calculate fold changes in expression, the  $\Delta C_t$  values were further normalized to the  $\Delta C_t$  value of a reference sample ( $\Delta\Delta C_t$ ). Generally, samples from the THP-1 cell line were used as references, unless otherwise stated (Equations (3) and (4)).

$$\Delta\Delta C_t = \Delta C_t (\text{Sample 1}) - \Delta C_t (\text{THP-1}) \quad (3)$$

$$\text{Fold change in expression} = 2^{-\Delta\Delta C_t} \quad (4)$$

#### 2.4.11 Transfection of mammalian cell lines with PEI

Plasmid DNA was transfected into mammalian cell lines using L-PEI as the transfection reagent. One day before transfection, HEK293T cells were seeded onto the appropriate tissue culture dishes such that they reached 80-90% confluency the following day. For the transfection of HEK293T cells in 12-well plates, a total of 3  $\mu\text{g}$  of plasmid and 9  $\mu\text{L}$  of L-PEI in a total volume of 100  $\mu\text{L}$  unsupplemented DMEM medium was prepared per well. The DNA-PEI mix was incubated at room temperature for 20 mins and subsequently added dropwise to each well. For the transfection of HEK293T cells in 145  $\text{mm}^2$  dishes, a total of 36.9  $\mu\text{g}$  of plasmid and 110  $\mu\text{L}$  of PEI in a total volume of 2.46 mL unsupplemented DMEM medium was prepared per dish. In this case, the DNA-PEI mix was incubated for 45 mins at room temperature before adding 2.5 mL dropwise to each dish. The cells were then incubated for 24 to 48 hrs at 37°C and 5%  $\text{CO}_2$ , before harvesting for downstream applications.

#### 2.4.12 Nucleofection of primary resting CD4+ T cells

Plasmid DNA or purified proteins were introduced to primary resting CD4+ T cells via nucleofection, which is an electroporation-based method of transfection, in contrast to using chemical reagents like PEI. Nucleofection was performed using the P3 Primary cell nucleofection kit from Lonza in a 16-well cuvette format.

For plasmid nucleofection,  $1 \times 10^6$  cells were used per reaction. The appropriate number of freshly isolated primary resting CD4+ T cells (see subsection 2.3.4) were transferred to 1.5 mL Eppendorf tubes and washed twice in PBS. In the meantime, 40  $\mu$ L of unsupplemented RPMI medium were pre-warmed to 37°C in each well of a 96-well plate. 1  $\mu$ g of plasmid DNA was added to 0.2 mL Eppendorf tubes. The washed cell pellets were resuspended in 20  $\mu$ L of nucleofection solution (supplemented), transferred to the tubes containing plasmid DNA, and resuspended. 20  $\mu$ L of the cells/DNA mixture was transferred to each well of a 16-well cuvette and nucleofected following the program EO-115. Following nucleofection, the cells were transferred to the 40  $\mu$ L of pre-warmed unsupplemented RPMI in the 96-well plate and incubated at 37°C and 5% CO<sub>2</sub> for 15 mins. Subsequently, 160  $\mu$ L of supplemented RPMI medium were added to the cells and incubated at 37°C and 5% CO<sub>2</sub> for 24 hrs before analysis via flow cytometry (see section 2.6).

The protocol for protein nucleofection is based on the publication by Albanese, Ruhle, and team<sup>278</sup>. Briefly,  $2 \times 10^6$  CD4+ T cells were used for each reaction. 100  $\mu$ L of unsupplemented RPMI medium were pre-warmed in each well of a 24-well plate. 10  $\mu$ L of purified protein were transferred to 0.2 mL Eppendorf tubes. Washed CD4+ T cells were then resuspended in 20  $\mu$ L supplemented nucleofection solution, as described above. The cells were then mixed with the proteins and 20  $\mu$ L of the mixture was transferred to each well of the 16-well cuvette. The cells were nucleofected using the program EH-100. Nucleofected cells were then transferred to the 100  $\mu$ L of pre-warmed unsupplemented RPMI medium and incubated at 37°C and 5% CO<sub>2</sub> for 15 mins. Subsequently, 400  $\mu$ L of supplemented RPMI medium were added to the cells and incubated at 37°C and 5% CO<sub>2</sub> for 24 hrs before analysis via flow cytometry (see section 2.6). For MG132 treatment, 10  $\mu$ M of MG132 dissolved in DMSO were added to the 400  $\mu$ L of supplemented RPMI medium before adding to nucleofected cells. 0.1% DMSO-treated cells were included as control.

#### 2.4.13 Generation of HEK293T cells with stable inducible expression of Vpx fusion protein

HEK293T cells stably expressing Vpx fusion proteins were generated for the purpose of protein purification. Unlike lentiviral transduction (described in subsection 2.5.3) which generated a stable cell line that continuously expressed the Vpx fusion protein, the sleeping beauty system was used to generate stable cells with an inducible expression of the fusion protein<sup>279</sup>. Figure 7 shows a graphical representation of the sleeping beauty inducible expression system. Using this system, HEK293T cells encoding WT and Q76A Vpx-HA-10xHis fusion proteins were kindly generated by Alejandro Salinas-Illarena, Max von Pettenkofer Institute. Briefly, HEK293T cells in 100 mm<sup>2</sup> tissue culture dishes were co-transfected with 10  $\mu$ g total of the pSBtet-Vpx-HA-10xHis (either WT or Q76A Vpx) and SB100X transposase vectors (Figure 7A), as described in the publication by Kowarz, Löshcer and Marschalek<sup>279</sup>. 24 hrs after transfection, the cells were subjected to selection with 1  $\mu$ g/mL puromycin

(Figure 7B). Expression of blue fluorescence protein (BFP) was checked by flow cytometry after a week of selection to ensure that the DNA fragment has been inserted. The stable cells were later maintained in 10  $\mu\text{g}/\text{mL}$  puromycin. For the induction of fusion protein expression, 2  $\mu\text{g}/\text{mL}$  of doxycycline were added to the cells and incubated for 24 – 48 hrs (Figure 7B). The induction of Vpx fusion protein expression was confirmed by flow cytometry using the anti-HA.11 antibody conjugated to AlexaFluor® 488 (see Table 7 for antibody dilution).

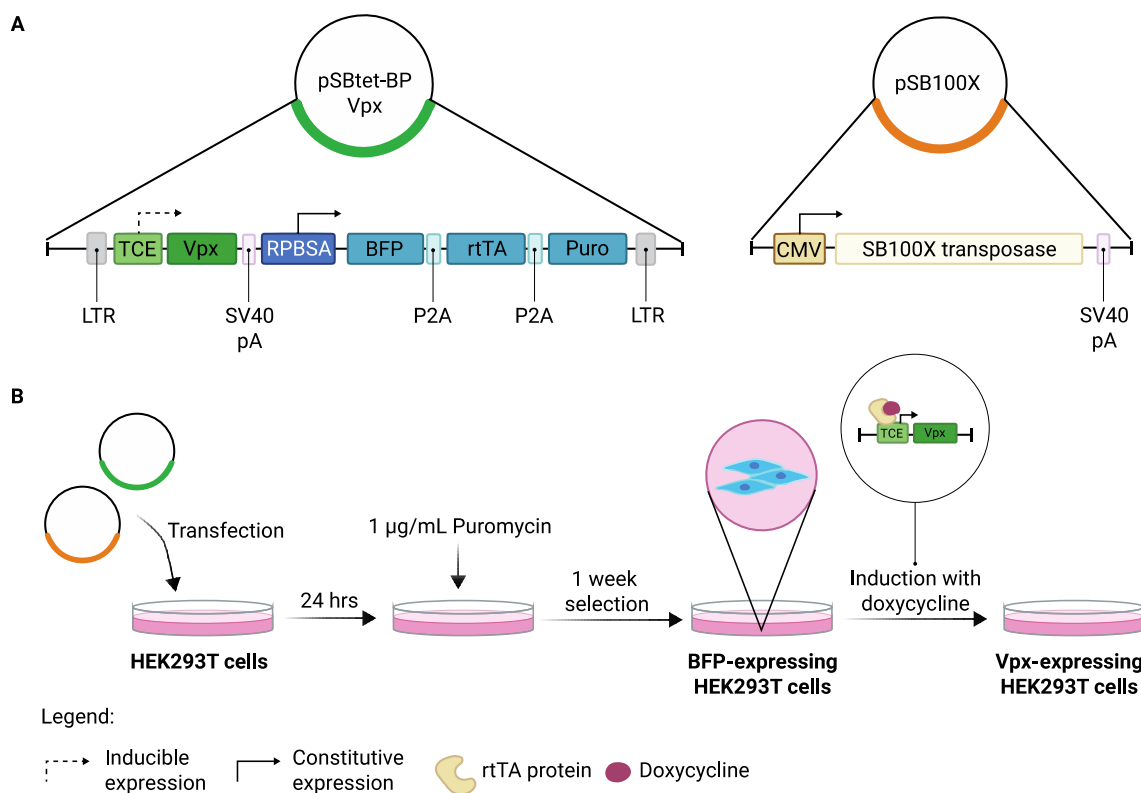


Figure 7: Schematic representation of generating stable inducible Vpx-expressing HEK293T cells<sup>280</sup>.

**A** The pSBtet-BP plasmid contains an LTR-flanked gene fragment encoding the BFP protein, a reverse Tetracycline trans activator (rtTA), and puromycin resistance under the control of a synthetic RPBSA promoter, as well as the Vpx fusion protein under the control of an inducible TCE promoter, which combines a tetracycline response element and a minimal CMV promoter. The pSB100X promoter encodes the transposase which then facilitates the insertion of the LTR-flanked gene fragment into the genome. Illustration modified from Kowarz, Löshcer and Marschalek<sup>279</sup>. **B** Illustration of the transfection, puromycin selection, and induction of Vpx expression of HEK293T cells. Doxycycline binds the rtTA, which then interacts with the TCE promoter, allowing for expression of the Vpx fusion protein.

## 2.5 Virological techniques

### 2.5.1 Production of virus-like particles (VLPs) and lentiviral vectors

VLPs and lentiviral vectors were produced by transient transfection of HEK293T cells with the appropriate plasmids using L-PEI, as described in subsection 2.4.11. The amount of plasmid used is shown in Table 17. 48 to 72 hrs after transfection, the cell supernatant containing the viruses was collected and filtered through 0.45  $\mu\text{m}$  vacuum filters. The filtered supernatant was either stored overnight at 4°C or immediately processed for virus harvest and concentration.



Table 17: Amount of plasmids used for the production of VLPs and lentiviral vectors from one 145 mm<sup>2</sup> dish of HEK293T cells.

<b>Vector</b>	<b>Amount (μg) of vector for Vpx-VLPs</b>	<b>Amount (μg) of vector for lentiviral vectors</b>	<b>Amount (μg) of vector for BlaM-Vpr-VLP</b>
pSIV3+	26.25	-	-
Transfer vector pWPI	-	17.5	-
pCMV HIV-1 Rev	3.55	-	-
pCMV BlaM-Vpr	-	-	8.3
Packaging vector pPAX2	-	11.4	12.5
Glycoprotein vector pMD2.G	7.08	6.2	4.125
pAdVantage	-	1.8	-

For harvesting and concentrating the VLPs and lentiviral vectors, open-top polyallomer ultracentrifugation tubes (Seton Scientific) were filled with 6 mL of 25% sucrose solution and 28 mL of the filtered supernatant were carefully overlaid onto the sucrose solution. Ultracentrifugation was performed at a speed of approximately 110,000 x g for 2 hrs at 4°C under vacuum. Subsequently, the supernatant was discarded and 50 μL of PBS were added per ultracentrifugation tube. After an incubation period of at least 30 mins at 4°C, the pellet was thoroughly resuspended. The concentrated VLPs and lentiviral vectors were then pooled, aliquoted and stored at -80°C. The activity of RT was measured to estimate the amount of VLPs and lentiviral vectors obtained. This is because RT activity is proportional to amount of RT input from the VLPs and lentiviral vectors<sup>277</sup>. This RT activity was determined by the SG-PERT assay (see subsection 2.5.4).

### 2.5.2 Transduction of cells with VLPs with spinoculation

In order to enhance the transduction efficiency of VLPs in suspension cells, spinoculation was performed. Once the VLPs were added to cells, they were subjected to centrifugation at 1200 x g for 90 mins at 37°C. Subsequently, the spinoculated cells were further incubated at 37°C and 5% CO<sub>2</sub> for 24 hrs.

### 2.5.3 Transduction of cells with lentiviral vectors for stable cell production

HEK293T cells were transduced with lentiviral vectors containing the coding sequence of proteins-of-interest, and a puromycin resistance cassette, for the production and selection of cells stably expressing the protein-of-interest. For this, 1.5x10<sup>5</sup> HEK293T cells were seeded onto each well of a 12-well plate and transduced with varying amounts of lentiviral vectors for 48 hrs. Thereafter, the selection of cells stably expressing the protein-of-interest was performed by treating the transduced cells with a pre-determined concentration of puromycin for at least 2 weeks. The optimal puromycin

concentration, which is the lowest concentration at which all non-transduced cells were killed, was determined empirically. After selection in puromycin-containing medium, protein expression levels were determined by flow cytometry (see section 2.6) or SDS-PAGE and Western Blot (see subsection 2.7.1). Once expression was confirmed, the cells were cryopreserved and further cultivated in medium without puromycin. After at least two weeks in culture, the supernatant of the cells was analyzed for residual lentiviral vectors by SG-PERT (see subsection 2.5.4) to ensure absence of any viral component and biosafety level 1 assignment. The expression of the protein-of-interest was also routinely checked by flow cytometry after cultivation in medium without puromycin.

#### **2.5.4 SG-PERT assay**

The SYBR Green I-based real-time PCR-enhanced reverse transcriptase (SG-PERT) assay was used to quantify lentiviral vectors and VLPs based on the activity of RT found in the viral particles<sup>277</sup>. The following SG-PERT protocol is based on the publication by Vermeire and team<sup>277</sup>. The MS2 RNA was used as the mRNA template which was then reverse transcribed into cDNA by the viral RT. The amount of cDNA produced is proportional to the amount of RT. The amount of cDNA was quantified in real-time using MS2-specific primers (see Table 13 for sequence) and a SYBR Green probe included in the SG-PERT reaction buffer. A standard series with known RT activity was also included with every SG-PERT assay for the absolute quantification of RT activity in the lentiviral vectors and VLPs. First, the lentiviral vectors, VLPs, and standards were diluted in SG-PERT dilution buffer, then lysed in the lysis buffer for 20 mins at room temperature. Then, the lysed samples were mixed at a 1:1 ratio with the reaction buffer on 96-well qPCR plate to a final volume of 20  $\mu$ L (BioRad). See Table 4 for all SG-PERT buffer recipes. Finally, the assay was run on the BioRad CFX96 machine and the results were analyzed using the CFX Maestro software. A threshold for the relative fluorescence intensity (RFI) was automatically set by the software based on the amplification curve, and the  $C_t$  values, as explained in subsection 2.4.10, were identified. Subsequently, a standard curve was generated using the known RT activity of the standard series and  $C_t$  values and the RT activity of the unknown samples were interpolated from the standard curve. The resulting values were represented as pRT units per  $\mu$ L (pRTU/ $\mu$ L). Samples were usually diluted 1:100 or 1:1000 in dilution buffer to ensure that the values fall within the standard range. Additionally, SG-PERT was also used to check for residual viral particles after the production of stable cell lines (see subsection 2.5.3). In this case, undiluted cell supernatants were used as samples.

#### **2.5.5 BlaM-Vpr VLP fusion assay**

A virion fusion assay was performed to determine the efficiency of fusion of viral envelope protein with the host cell receptor, providing insights into the susceptibility of different cells to recognition by the envelope protein<sup>281</sup>. For this assay, VLPs pseudotyped with VSV-G envelope protein encapsulating the accessory protein Vpr fused with beta-lactamase (BlaM-Vpr) were produced (see subsection 2.5.1). Suspension cell lines and primary AML blasts were seeded in U-bottom 96-well plates at a density of  $2 \times 10^5$  cells per well in 200  $\mu$ L of the appropriate medium. An aliquot of the culture medium for the primary AML blasts was obtained from the laboratories of Prof. Dr. Marion Subklewe. BlaM-Vpr VLPs were then added to each well, corresponding to  $1 \times 10^{10}$  pRTU/ $\mu$ L based

on SG-PERT values. Spinoculation was performed as described in subsection 2.5.2, and the transduced cells were further incubated for 2.5 hrs at 37°C and 5% CO<sub>2</sub>. Subsequently, the cells were pelleted, and supernatant was carefully aspirated. The transduced cells were then stained with a CCF2 staining solution (see Table 4 for components) and incubated overnight at room temperature in the dark, wrapped in wet tissue to maintain high humidity. Non-transduced cells, which were stained with CCF2, were used as a negative control. The fusion efficiency was then calculated based on the cleavage of CCF2 at the beta-lactam ring by BlaM-Vpr, which was released into the cytoplasm upon virion fusion (Figure 8A). This cleavage causes the emission spectrum of CCF2 to shift from 520 nm to 450 nm (Figure 8A), which was then detected by flow cytometry (see section 2.6) (Figure 8B).

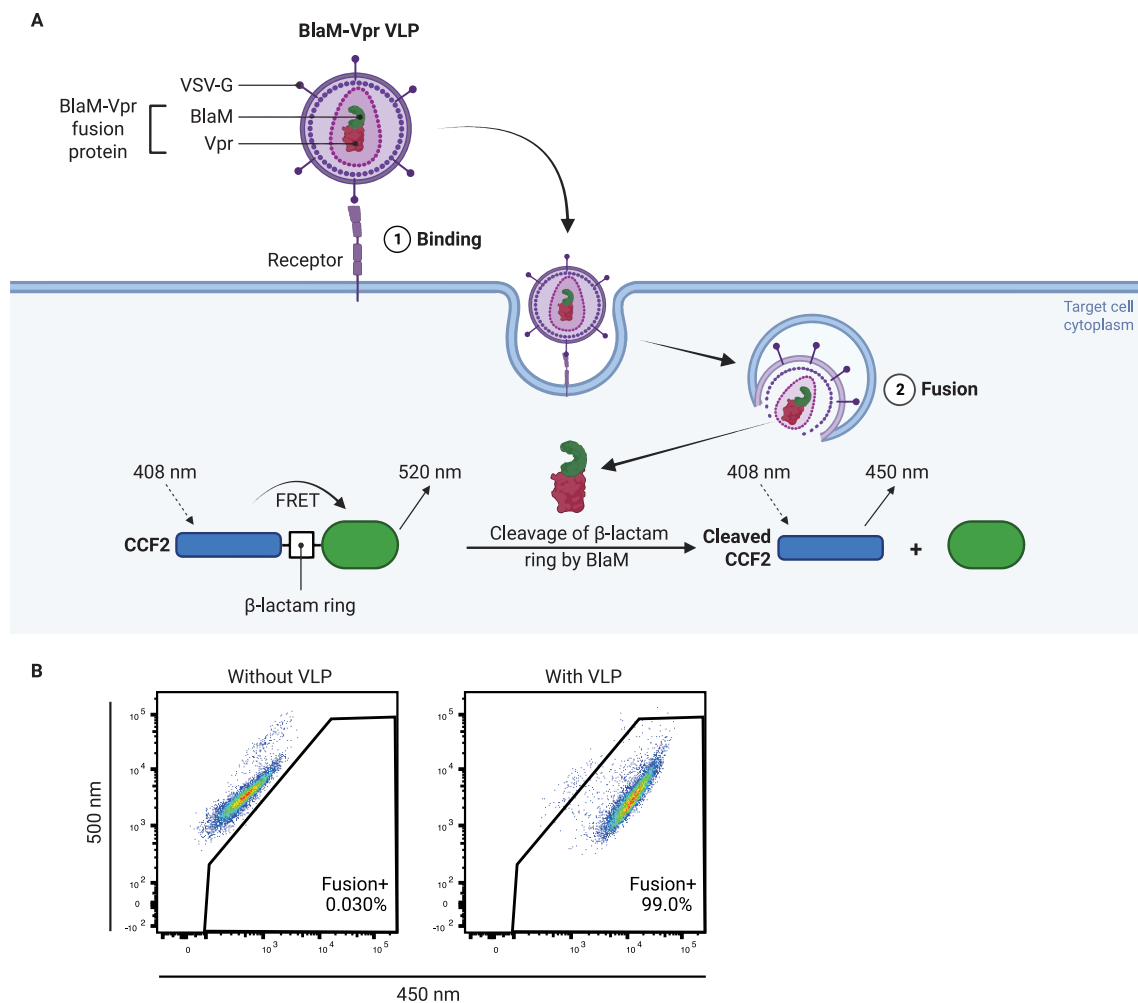


Figure 8: BlaM-Vpr VLP fusion assay.

**A** Schematic representation of VLP fusion and cleavage reaction of the  $\beta$ -lactam ring by BlaM, leading to the shift of emission spectrum of CCF2 from 520 nm to 450 nm. FRET: fluorescence resonance energy transfer. **B** An example of the emission shift seen during flow cytometry.

## 2.6 Flow cytometry

Flow cytometry was routinely used in this work to detect and analyze levels of both surface and intracellular proteins in each cell of a single-cell suspension. In the following subsections, the general procedures for preparing cells for flow cytometry and its analysis will be detailed.

### 2.6.1 Analysis of cells expressing fluorescent proteins

For the analysis of cells expressing fluorescent proteins or fusion proteins, between  $10^5$  and  $10^6$  cells resuspended in 100  $\mu\text{L}$  PBS were fixed with 100  $\mu\text{L}$  of 4% PFA solution for 10 mins at room temperature. The PFA was then removed via centrifugation at  $1000 \times g$  for 5 mins and the cells were resuspended in 180-200  $\mu\text{L}$  PBS and used directly for flow cytometric analysis with the BD FACSLyric instrument. On occasion, the fixed cells were also stored at  $4^\circ\text{C}$  for a maximum of 3 days before analysis.

### 2.6.2 Staining of surface markers

For the analysis of cells without fluorescent proteins, proteins-of-interest needed to be stained with fluorophore-conjugated antibodies before flow cytometric analysis. The staining of surface markers was routinely performed for the characterization of primary AML blasts. The surface markers CD33, CD34 and CD45 were stained with a 1:20 dilution each of anti-CD33-PE, anti-CD34-FITC, and anti-CD45-V450, respectively. 50  $\mu\text{L}$  of antibodies diluted in FC stain buffer with EDTA were added to the cells and incubated for 30 mins at  $4^\circ\text{C}$ , in the dark. Subsequently, the cells were washed once in 150  $\mu\text{L}$  of FACS stain buffer, resuspended in 100  $\mu\text{L}$  FC stain buffer with EDTA and fixed, as described in subsection 2.6.1. After fixation, the cells were subjected to further intracellular staining for the detection of SAMHD1 protein (see subsection 2.6.3).

### 2.6.3 Intracellular staining

For intracellular staining, cells were fixed, as described above in subsection 2.6.1, and subsequently permeabilized on ice for 2 mins using 100  $\mu\text{L}$  of the BD Perm Buffer III, which contains methanol as the permeabilization agent. The permeabilized cells were then thoroughly washed twice in 150  $\mu\text{L}$  FC stain buffer (see Table 4 for recipe). The cells were then stained with either a fluorophore-conjugated or a non-conjugated antibody against a protein-of-interest. 50  $\mu\text{L}$  of the antibodies, diluted in FC stain buffer, were then added to the cells, and incubated for 45 mins at room temperature protected from light. If a non-conjugated antibody was used, a second staining step with a fluorophore-conjugated secondary antibody was necessary, as in the case of SAMHD1 detection. In this case, the cells were first washed in 150  $\mu\text{L}$  FC stain buffer and incubated with 50  $\mu\text{L}$  of secondary antibody for 45 mins at room temperature, protected from light. The various antibodies and their dilutions used are shown in Table 7. After the final staining step, the cells were washed again in 150  $\mu\text{L}$  FC stain buffer and resuspended in 180-200  $\mu\text{L}$  FC stain buffer for flow cytometric analysis. A viability stain was also included regularly to identify living cells. For this, 50  $\mu\text{L}$  of Zombie Green<sup>TM</sup> fixable viability dye (in DMSO) diluted 1:1000 in PBS was added to the cells prior to cell fixation and incubated for 15 mins at room temperature in the dark. The cells were then fixed as per usual.

## 2.6.4 Flow cytometry data analysis

Samples processed as described in subsections 2.6.1 – 2.6.3, were subjected to flow cytometry using the BD FACSLyric instrument. Assays were generated based on cell properties and fluorophores used, and the acquisition criteria were set to 10,000 single living cells or 60 seconds acquisition time on a high flow rate. See Figure 9 for an example of the implemented gating strategy for single living cells. The data obtained was analyzed using the FlowJo software.

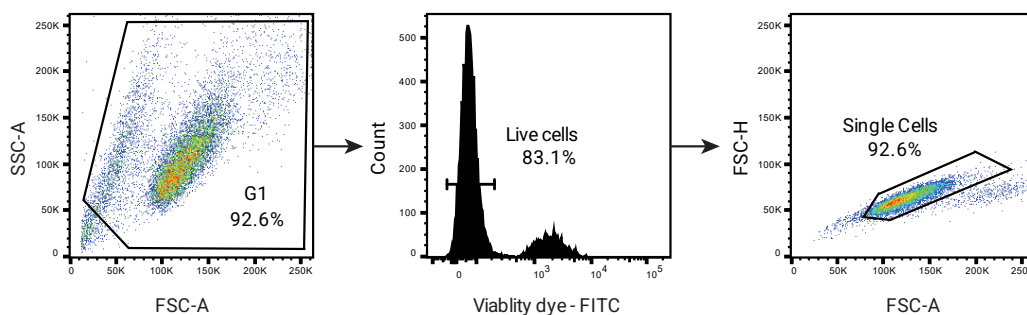


Figure 9: An example of the gating strategy implemented for the analysis of flow cytometry data.

The “G1” gate excluded small debris, the “Live cells” gate selected living cells which did not take up the viability dye, and the “Single cells” gating selected single cells from doublets. FSC-A: forward scatter area, SSC-A: side scatter area, FSC-H: forward scatter height. Forward scatter measures the size of the cells, while side scatter measures the cell granularity. Large granular cells, such as monocytes and macrophages, have high FSC-A and SSC-A values. Small cells, like lymphocytes, have a small FSC-A and SSC-A value. Doublet cells contribute to a larger FSC-A while maintaining FSC-H.

## 2.7 Biochemical techniques

### 2.7.1 SDS-PAGE and western blot

Sodium dodecyl sulfate – polyacrylamide gel electrophoresis (SDS-PAGE) is a technique used to separate denatured proteins based on their molecular weight. Gels with varying resolving polyacrylamide concentrations were freshly prepared before gel electrophoresis, according to the manufacturer’s instructions (Thermo Fischer Scientific, SureCast system). In general, a 12% resolving polyacrylamide gel was used to detect most proteins between 10 kDa and 150 kDa. For the detection of Vpx proteins only, a 15% resolving polyacrylamide gel was used for better resolution of the lower molecular weight proteins. The components for both 12% and 15% resolving SDS-polyacrylamide gels, as well as the 4% stacking gel, are shown in Table 18. 10-, 12- and 15-well combs were used during the gel preparation for the loading of 25  $\mu$ L, 20  $\mu$ L, and 15  $\mu$ L of protein sample per well, respectively. Protein samples used for SDS-PAGE originated from various sources. If no further downstream application of the protein was required, total protein samples were prepared by lysing cells in the Hunt lysis buffer (see Table 4 for components). Briefly, at least  $10^5$  cells were harvested, washed once in PBS and resuspended in 30-100  $\mu$ L of Hunt lysis buffer, depending on the amount of cells used for lysis. The resuspended pellets were then lysed by three freeze-thaw cycles in liquid nitrogen or dry ice. The lysed cells were subsequently centrifuged at 21,000 x g for 30 mins at 4°C and the supernatant was transferred to a fresh Eppendorf tube. The total protein concentration of

the supernatant was determined using the Bradford assay (see subsection 2.7.3). Three parts of total protein between 10-20  $\mu\text{g}$  were mixed with one part of 4x Laemmli buffer, boiled for 5 mins at 95°C, and loaded onto each well of an SDS-polyacrylamide gel. 5  $\mu\text{L}$  of the PageRuler™ Plus Prestained Protein Ladder were used as a protein ladder. The gels were then run at a constant voltage of 80V for 30 mins, followed by 100V for 70 mins or until the blue dye in the Laemmli buffer reached the bottom of the gel.

Table 18: Components of 12% and 15% SDS-polyacrylamide gels.

Components	Resolving gel		4% Stacking gel
	12% gel	15% gel	
40% acrylamide	2.4 mL	3 mL	300 $\mu\text{L}$
Resolving buffer	2 mL	2 mL	-
Stacking buffer	-	-	750 $\mu\text{L}$
10% (w/v) APS	80 $\mu\text{L}$	80 $\mu\text{L}$	30 $\mu\text{L}$
TEMED	8 $\mu\text{L}$	8 $\mu\text{L}$	3 $\mu\text{L}$
ddH <sub>2</sub> O	3.5 mL	2.9 mL	1.92 mL

After gel electrophoresis, the separated proteins were transferred onto a 0.45  $\mu\text{m}$  nitrocellulose membrane at a constant voltage of 10V for 1 hr in 1x Tris-Glycine transfer buffer containing 20% methanol. Following transfer, the membranes were blocked in a 5% milk solution dissolved in TBS-T for at least 30 mins. The blocked membranes were then incubated in primary antibodies diluted in antibody solution at 4°C for 24-72 hrs. Subsequently, membranes were washed at least five times in TBS-T and incubated in secondary horseradish peroxidase (HRP)-conjugated antibodies diluted in 5% milk in TBS-T for at least 1 hr at room temperature. All antibodies and their dilutions used for immunoblotting are listed in Table 7. Membranes were finally washed again at least five times in TBS-T and stained with the Clarity™ Western ECL Kit. For low abundance proteins, the SuperSignal™ West Femto Maximum Sensitivity Substrate kit was used for staining the membranes. Images were obtained using the Vilber Fusion FX device and software. Band intensities of the protein-of-interest and housekeeping genes were obtained using the ImageJ software for semi-quantification. See Table 4 for recipes of all buffers used.

### 2.7.2 Coomassie and silver stains

In some cases, after SDS-PAGE, the gels were subjected to either Coomassie stain or silver stain to visualize total protein separated on the gel. This was usually done after protein purification to determine protein purity and as a quality control of the purification procedure.

For Coomassie staining of the gels, the InstantBlue® Coomassie Protein Stain was used. After SDS-PAGE, the gel was removed from the plates, transferred to a tray, and rinsed in deionized water. The rinsed gel was then submerged in an appropriate volume of the staining solution and incubated for at least 15 mins on constant shaking. Only the proteins separated on the gel were stained blue and the gel could be immediately photographed without further processing. No de-staining was required.

For silver staining of the gels, the gels were first rinsed in deionized water after SDS-PAGE, followed by fixation in the silver stain fixation solution for 1 hr, under constant shaking. Next, the gel was washed in deionized water for at least 30 mins, with regular exchange of the water, and sensitized for 1 min with the sensitization solution. The gel was then rinsed three times in deionized water and incubated in silver staining solution for 20 mins, under constant shaking. The gel was then rinsed again, and then transferred to a fresh tray. The gel in the fresh tray was rinsed again for 1 min in deionized water and then incubated in development solution until the protein bands were visible. The gel was then washed in deionized water and photographed. See Table 4 for solution recipes.

### **2.7.3 Bradford assay**

Total protein concentrations were obtained using the Bradford assay. 5  $\mu$ L of known concentrations of BSA, ranging from concentrations of 2 mg/mL to 0.125 mg/mL, and diluted total protein obtained from lysed cells were added to each well of a flat-bottom 96-well plate. 250  $\mu$ L of Quick Start Bradford 1x dye reagent were added to each well and incubated for 5 mins in the dark at room temperature. Subsequently, the absorbance of the dye was measured using the CLARIOStar plate reader at wavelengths 595 nm and 690 nm. A standard curve was generated using the MARS software based on a linear regression fit of the blank-corrected absorbance plotted against the known BSA concentration. Concentrations of the protein samples were then interpolated from the standard curve.

### **2.7.4 Automated SDS-PAGE and western blotting with the ProteinSimple Jess system**

The ProteinSimple Jess system allows for the all-in-one automated gel electrophoresis, western blotting, and visualization of proteins-of-interest with very low amounts of protein needed. The Jess system requires the usage of specific separation modules, which comes with varying number of wells and range of molecular weights. A detection module for the staining and visualization of the separated proteins is also required. In this work, the 13-well 12-230 kDa separation module, the total protein detection module, and the anti-mouse detection module were used. The preparation of the protein samples, the separation modules and detection modules were all performed according to the manufacturer's instructions. The data output included a gel view, as well as graphical view for quantification of proteins. An example of the output images is shown in Figure 10.

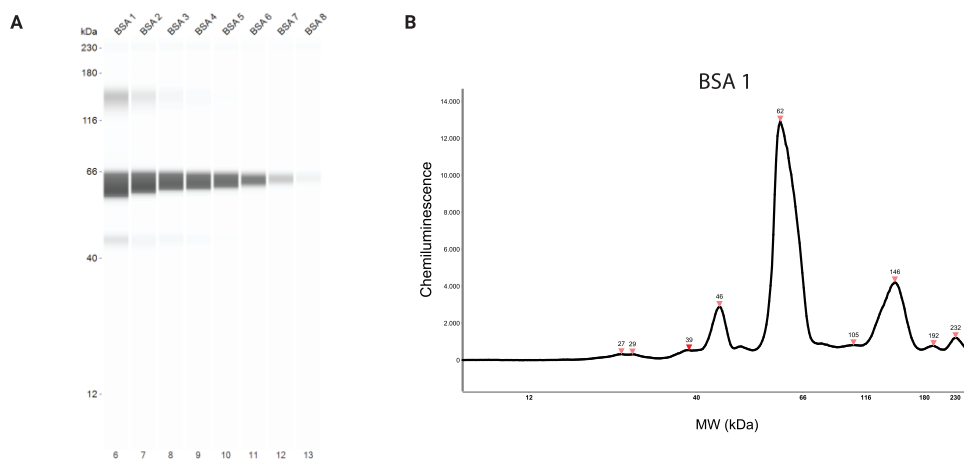


Figure 10: Exemplary output gel image and graph generated by Jess.

**A** An example of a gel image generated by Jess loaded with a dilution series of BSA protein ranging from 2 mg/mL (BSA 1) to 0.125 mg/mL (BSA 8) concentration. **B** An example of the graphical output by Jess showing the chemiluminescence signal produced by each peak, representing the different sized proteins. The graph shown is representative of the BSA protein with a concentration of 2 mg/mL (BSA 1).

### 2.7.5 Protein expression and affinity purification from *E. coli*

*E. coli* BL21 and Rosetta2 strains were used for expression and purification of various fusion Vpx proteins. pGEX-2T-GST-Vpx, pGEX-6P-GST-6xHis-Vpx, and pET28a-6xHis-T7-Vpx were transformed into the *E. coli* strains, as described in subsection 2.4.2. Sequence-verified single colonies were cryopreserved.

The initial growth, expression induction and lysis conditions were similar among the purifications of the different fusion proteins and will therefore be summarized in this paragraph. Two days before purification, *E. coli* expressing the various Vpx fusion proteins were pre-cultured in 50 mL LB medium containing the appropriate antibiotic at 37°C overnight. The following day, 10 mL of the pre-culture were added to 1 L of LB medium containing the appropriate antibiotic and grown at 37°C until an OD<sub>600</sub> of 0.5 was reached. Subsequently, 0.1 mM IPTG was added to the culture and incubated at 20°C overnight to induce the expression of the fusion Vpx proteins. The induction conditions (OD<sub>600</sub> and IPTG concentration) were determined based on several rounds of optimization. On the day of purification, the bacterial culture was pelleted by centrifugation at 3400 x g for 45 mins at 4°C. The bacterial pellet was resuspended in 50 mL french press lysis buffer or sonication lysis buffer (see Table 4 for recipe). For french press lysis, cells were lysed using the french press homogenizer at 12,000 – 15,000 psi pressure for 3 rounds. For sonication lysis, cells were lysed using the Branson Ultrasonics™ Sonifier at 40% duty, and an intensity of 4 for 3 rounds of 30 seconds each, with 1 min interval between rounds at 4°C. After lysis, the total protein supernatant was isolated after centrifugation at 21,000 x g for 30 mins at 4°C. The supernatant was filtered through a 0.22 µm filter and used for purification. An aliquot of the supernatant was collected for SDS-PAGE analysis as the input fraction.

For purification of GST-Vpx and GST-6xHis-Vpx proteins, the optimal OD<sub>600</sub> for induction was 0.5. The glutathione sepharose 4B resin was used to capture the GST fusion proteins. In general, 4



mL of 50% slurry in PBS were used for 4 L of bacteria. All steps were performed at 4°C. Gravity flow purification was performed by transferring the slurry onto an empty PD-10 column with a filter. The slurry was washed and equilibrated in PBS, followed by incubation with the filtered supernatant for 15 mins by end-over-end rotation. After incubation, the bottom cap of the column was opened to allow for unbound proteins to flow through. A fraction of the flow-through was collected for SDS-PAGE analyses. The resin was then washed thoroughly with PBS. Aliquots of each washing step were also collected for SDS-PAGE analyses. In the case of the GST-Vpx fusion protein, the protein was eluted with 7 mL of GST elution buffer (see Table 4 for recipe). An aliquot of the eluted proteins was collected for SDS-PAGE analyses. The remaining eluted proteins were concentrated to approximately 1 mL using the Amicon® Ultra centrifugal filters with a molecular weight cutoff of 3 kDa for size exclusion chromatography (see subsection 2.7.7).

In the case of the GST-6xHis-Vpx fusion protein purification, the GST tag was cleaved off using the PreScission Protease. After washing the resin with bound GST-6xHis-Vpx in PBS, the resin was equilibrated in 10 mL of the PreScission Protease cleavage buffer (see Table 4 for recipe). 80 µL of PreScission Protease were dissolved in 1.92 mL of cleavage buffer, which were then added to the resin with the bottom cap closed, and incubated for 4 hrs at 4°C. Subsequently, the flow-through was collected, which contained the cleaved 6xHis-Vpx protein. The cleavage of the GST-6xHis-Vpx was confirmed via immunoblotting against the His-tag.

For the purification of 6xHis-T7-Vpx, the Ni-NTA agarose was used for the capture of the 6xHis tag. 1 mL of the 50% resin slurry was transferred to an empty PD-10 column and equilibrated with the french press lysis buffer. After adding the supernatant containing fusion protein to the resin and allowing unbound proteins to flow-through, the resin was washed twice in Ni-NTA wash buffer, followed by elution in 4 mL of Ni-NTA elution buffer. All buffer recipes are listed in Table 4. The eluted protein was concentrated for size exclusion chromatography, as described above.

### **2.7.6 Protein expression and affinity purification from HEK293T cells**

The mammalian cell line HEK293T was used for the expression and affinity purification of the Vpx fusion proteins, Vpx-HA-10xHis, 3xFLAG-Vpx, as well as CPP44-HA-Vpx-10xHis and 3xFLAG-CPP44-HA-Vpx. The Vpx fusion proteins were either transiently expressed by HEK293T cell transfection, as described in subsection 2.4.11, or stably expressed. The stable expression of the fusion proteins was achieved either by lentiviral vector transduction (see subsection 2.5.3) or using the sleeping beauty system (see subsection 2.4.13). 24 -48 hrs after transfection or induction of fusion protein expression with doxycycline, the HEK293T cells were harvested and washed twice in PBS, under centrifugation at 500 x g for 5 mins. The washed cells were then resuspended in 1 mL of appropriate lysis buffer per 145 mm<sup>2</sup> dish of HEK293T cells. If detergent lysis was performed, the cells were incubated on an end-over-end rotator for 1 hr in the cold room. If sonication was performed, the cells were sonicated using the Fisherbrand™ Model 120 Sonic Dismembrator at 70% amplitude, 30 seconds ON/OFF pulsing for a total of 1 min on ice. The lysed cells were cleared by centrifugation at 21,000 x g for 30 mins at 4°C. The supernatant containing the proteins were filtered through a 0.45 µm filter and was ready for purification. Subsection 3.1.3 will go into more detail on the optimization process of the lysis and the subsequent purification steps for the Vpx-HA-10xHis proteins.

For the purification of 3xFLAG-tagged Vpx proteins, the M2 anti-FLAG resin was used according to manufacturer's instructions. HEK293T cells expressing 3xFLAG-Vpx were lysed in buffer containing 50 mM Tris-HCl (pH 7.5), 150 mM NaCl, 1% Triton X-100, 20 mM ZnCl<sub>2</sub>, and 1x protease inhibitor complex. 400  $\mu$ L of the M2 anti-FLAG resin were transferred to an empty PD-10 column and washed thoroughly with TBS buffer. The clarified supernatant of the lysed cells was then added to the column and incubated with the resin for 1 hr in the cold room on the end-over-end rotator. The unbound proteins were allowed to flow-through the column and the resin was then washed thoroughly with TBS. For elution, 1 bed volume of 100  $\mu$ g/mL of 3xFLAG peptide was diluted in TBS and added to the resin, incubated for approximately 5 mins, and collected. The elution process was repeated four times and the eluate was pooled and concentrated to 200 – 500  $\mu$ L, as described in subsection 2.7.5. For the purification of the 3xFLAG-tagged CPP44 fusion proteins, the 3xFLAG tag was cleaved off using enterokinase. After concentration, the purified proteins were incubated in about 100 U of enterokinase overnight at 4°C. The cleavage efficiency was confirmed by immunoblotting for the HA tag.

For the purification of Vpx-HA-10xHis fusion proteins, either Ni-NTA resin or Co-NTA resin was used. An appropriate amount of resin was transferred to an empty PD-10 column and washed with equilibration buffer (20 mM HEPES pH 7.5, 150 mM NaCl, 5 mM imidazole, and 1 mM DTT). The clarified supernatant was added to the resin and incubated as described above for the 3xFLAG-Vpx purification. After which, the resin was first washed with 10 bed volumes of a high salt buffer (20 mM HEPES pH 7.5, 500 mM NaCl, 10 mM imidazole, and 1 mM DTT), followed by the equilibration buffer containing 10 mM imidazole. The elution was performed three times with 1 bed volume of the elution buffer (20 mM HEPES pH 7.5, 150 mM NaCl, 250 mM imidazole, and 1 mM DTT). The eluate was pooled and concentrated to 200 – 500  $\mu$ L, as described in subsection 2.7.5. For the purification of CPP44-HA-Vpx-10xHis proteins, the same purification procedure as Vpx-HA-10xHis was applied, with the exception of using HEPES buffer at a pH of 8.5 instead of 7.5.

### **2.7.7 Size exclusion chromatography (SEC)**

SEC was performed to further purify proteins after affinity purification. The Superdex 200 10/300 GL increase column was used. The Äkta chromatography systems were used with kind permission from the research group of Prof. Dr. Karl-Peter Hopfner at the Gene Center, LMU Munich. In general, 500  $\mu$ L – 1 mL of purified proteins were subjected to SEC. For this, the Superdex column was first equilibrated in the appropriate protein storage buffers (see Table 4 for recipes). Following equilibration, the purified protein was injected into the system via a tuberculin syringe. The run and fractionation conditions are stated in Table 19. After fractionation, the fractions containing proteins were identified using the chromatogram. The relevant fractions were pooled and analyzed on SDS polyacrylamide gels, which were then stained with Coomassie (see subsection 2.7.2) to confirm the presence of the protein-of-interest. Following SEC, the Superdex column was washed with 1 M sodium hydroxide, followed by MilliQ water and finally, 20% ethanol, in which the column was stored. All buffers used for the SEC were sterile filtered through a 0.22  $\mu$ m filter before usage.

Table 19: SEC run and fractionation conditions.

Parameter	Condition
Flowrate	0.5 mL/min
Column volume (CV)	23.562 mL
Column equilibration volume	2 CV
Isocratic elution volume	1.2 CV
Elution format	96-well deep-well plate 500 $\mu$ L – 1 mL fractions

### 2.7.8 Assembly of GFP- and Vpx-nanoMOFs

Nano metal-organic frameworks (nanoMOFs) were synthesized by Nagore Barroso García from the research group of Dr. Stefan Wuttke at the Basque Center for Materials, Applications and Nanostructures (BCMaterials), Spain. The nanoMOFs provided are summarized in Table 20. Before loading the Vpx onto the nanoMOFs, they were first pelleted to remove the ethanol, in which the nanoMOFs were stored. After drying the nanoMOFs, they were then resuspended in a reaction buffer (20 mM HEPES, pH 7.5, 150 mM NaCl, 15% glycerol, and 1 mM DTT) to a final concentration of 5 mg/mL. In order to ensure homogenous resuspension of the nanoMOFs, they were sonicated for 10 mins on the Bandelin Sonorex Super ultrasonic bath, at 4°C. For 6xHis-GFP binding, 1.5  $\mu$ g of 6xHis-GFP reconstituted in the reaction buffer were mixed with 5  $\mu$ g of homogenous nanoMOF solution in a 1.5 mL Eppendorf tube. The mix was incubated for 15 mins at room temperature, shaking constantly at 600 rpm. Subsequently, the GFP-loaded nanoMOFs were pelleted at 10,000 x g for 10 mins and the supernatant was transferred to a fresh tube. 5  $\mu$ L of the supernatant, containing unbound 6xHis-GFP, were diluted with 95  $\mu$ L reaction buffer and GFP signal was measured using the CLARIOstar plate reader. 6xHis-GFP incubated without nanoMOF was used as control (GFP control). The percentage of bound GFP was measured using Equations (5) and (6).  $A$  refers to the fluorescence signal of GFP.

$$A_{bound\ GFP} = A_{GFP\ control} - A_{unbound\ GFP} \quad (5)$$

$$\% bound\ GFP = \left( \frac{A_{bound\ GFP}}{A_{GFP\ control}} \right) \times 100\% \quad (6)$$

Uptake of 6xHis-GFP-bound nanoMOFs by THP-1 cells was performed by incubating 20  $\mu$ L of the 6xHis-GFP-nanoMOF mixture with  $1 \times 10^5$  THP-1 cells in flat-bottom 96-well plates directly after the 15-minute self-assembly process for 24 hrs. Uptake of GFP was then measured via flow cytometry.

For the binding of purified Vpx proteins onto nanoMOFs, 25  $\mu$ g of the resuspended nanoMOFs were transferred to fresh 1.5 mL Eppendorf tubes and 20  $\mu$ L of purified Vpx-HA-10xHis proteins were added. The mixture was incubated for 15 mins at room temperature, shaking constantly at 600 rpm. Subsequently, the Vpx-loaded nanoMOFs were pelleted and the supernatant was transferred to a fresh tube to check for binding of Vpx via SDS-PAGE (see subsection 2.7.1) and Coomassie stain (see subsection 2.7.2). The pelleted nanoMOFs were then resuspended in supplemented IMDM medium and added to cells for the SAMHD1 degradation assay (see subsection 2.3.5). Uptake of Vpx and degradation of SAMHD1 was determined by flow cytometry (see section 2.6).

Table 20: List of nanoMOFs provided and their components.

NanoMOF	Metal component	Organic component
MIL88A	Fe <sup>3+</sup>	Fumaric acid
ZIF-8	Zn <sup>2+</sup>	Methylimidazole
Zr-fumarate	Zr <sup>4+</sup>	Fumaric acid

### 2.7.9 Proteasome activity assay

In order to determine the presence of proteasomal degradation activity in total protein lysates, the proteasome activity assay was performed<sup>282</sup>. THP-1 cells were lysed in buffer containing 50 mM HEPES, pH 7.5, 10 mM NaCl, 5 mM MgCl<sub>2</sub>, 250 mM sucrose, and 5 mM DTT, unless otherwise stated, and total proteins were isolated by centrifugation of cell lysates at top speed for 30 mins at 4°C. Various amounts of total proteins were mixed with 100 µM of Suc-LLVY-AMC substrate, 250 mM sucrose and 2 mM ATP for 1 hr at 37°C in a black-walled flat-bottom 96-well plate. Pre-incubation of the THP-1 lysates with 40 µM of MG132 for 2 hrs at 37°C was performed to inhibit the proteasome activity. Degradation of Suc-LLVY-AMC and the release of the fluorophore AMC was measured on the CLARIOstar plate reader at 460 nm wavelength. The higher the fluorescence, the higher the proteasome activity in the total protein. Reactions containing Suc-LLVY-AMC substrate without the lysate, and lysate without substrate were used as controls.

### 2.7.10 *In vitro* SAMHD1 degradation assay

The *in vitro* SAMHD1 degradation assay was established to confirm the functionality of purified Vpx fusion proteins. In general, the assay involved the combination of total proteins obtained from THP-1 cells and the purified Vpx protein in the presence of ATP to allow for the proteasomal degradation of SAMHD1 provided by the THP-1 lysate. For this, 10 µg of total protein from THP-1 cells were added to 30 µL of purified protein and 2 mM ATP in 100 µL final volume of the lysis/ reaction buffer (50 mM HEPES, pH 7.5, 10 mM NaCl, 5 mM MgCl<sub>2</sub>, 250 mM sucrose, and 5 mM DTT). The reaction was performed at 37°C for 6 hrs under constant shaking at 300 rpm. Once the reaction was over, 30 µL were removed and used for SDS-PAGE and western blot analysis, staining for SAMHD1, Vpx (using HA or FLAG) and γ-tubulin (see subsection 2.7.1).

## 2.8 Fluorescence microscopy

Intracellular proteins were stained with fluorophore-conjugated antibodies and analyzed on a fluorescence microscope to determine their intracellular localization. THP-1 cells treated with Vpx delivery systems had to first be adhered onto glass slides before they could be stained for microscopy. For this, 13 mm glass cover slips were placed in each well of a 12-well plate. The cover slips were then treated with 1 mL of poly-L-lysine for 10 mins at room temperature. The treated cover slips were then left to dry. 100 µL of suspension cells washed in PBS were then added to the dried cover slips and incubated at room temperature for 1 hr. Subsequently, the cover slips were transferred onto parafilm-wrapped plate lid and carefully washed in 100 µL PBS. The cells were then fixed with 4% PFA for 15 mins at room temperature, followed by permeabilization with 0.1% Triton X-100 for 5

mins. The permeabilized cells were blocked in 2% BSA containing PBS for 30 mins before staining with fluorophore-conjugated antibodies for 1 hr at room temperature in the dark. See Table 7 for antibody dilutions. The cells were then washed in PBS and stained with Hoechst 33342 solution diluted to a concentration of 1  $\mu\text{g}/\text{mL}$  in PBS for 15 mins. The stained cells were then mounted onto glass slides using the ProLong™ Gold Antifade Mountant and left to dry overnight. The cells were analyzed on the Nikon CSU-W1 confocal microscope. Microscopy images were taken using the Nikon NIS-Elements software and analyzed using the Imaris Viewer software.

## 2.9 Statistical analysis

Means, standard error of means (s.e.m.), and statistical significance of differences between means of three or more samples were calculated using one-way ANOVA and Tukey's multiple comparisons test. Statistical significance of difference between means of two samples was calculated using unpaired t-test. All statistical calculations were performed with the GraphPad Prism 9 software. P values in graphs are indicated as asterisks: \*:  $p < 0.05$ , \*\*:  $p < 0.01$ , \*\*\*:  $p < 0.001$ . Non-significant differences are indicated with "ns".



### 3. Results

#### 3.1 Expression and purification of recombinant Vpx proteins

##### 3.1.1 Bacterial expression and purification of GST-Vpx and 6xHis-T7-Vpx

The first part of this work focused on the production of a functional recombinant Vpx protein which would be packaged into different Vpx delivery systems. Bacterial purification is the most widely used and cost-effective method for protein purification. Due to this, the purification of several tagged Vpx proteins using the *E. coli* Rossetta2 strain were attempted. Figure 11 shows the various tagged Vpx proteins in their respective bacterial expression backbone vectors used in this work. The pGEX-2T-GST-Vpx bacterial expression plasmid, encoding Vpx from SIVsmm PBj1.9, was generously provided by the laboratory of Dr. Egbert Flory<sup>174</sup>. The pET28a 6xHis-T7-Vpx and pGEX-6P GST-6xHis-Vpx plasmids encoded Vpx from the SIVmac251 stain and were cloned in-house.

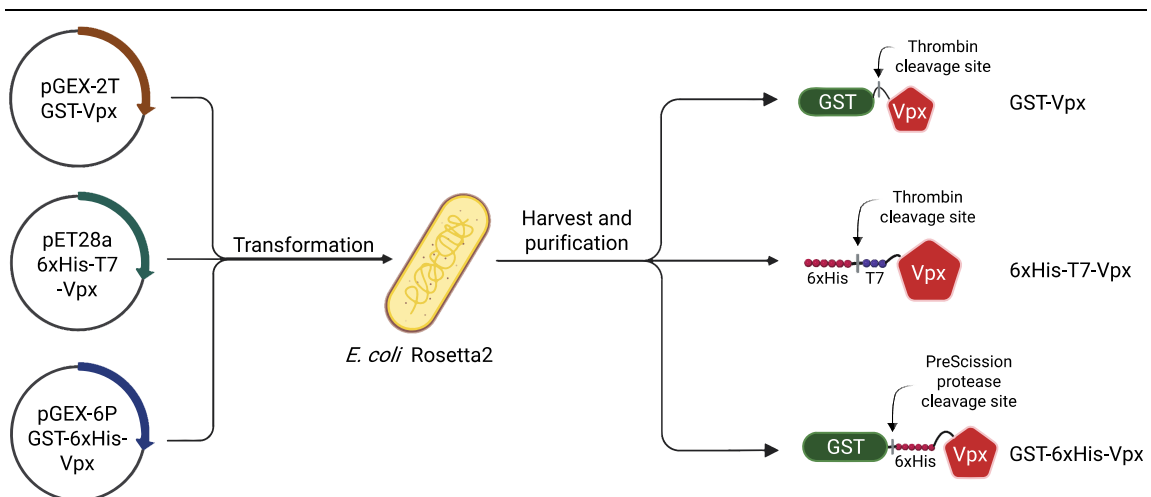


Figure 11: Schematic representation of the various plasmids used, encoding the different tagged Vpx proteins for the purification of recombinant Vpx from the *E. coli* Rossetta2 strain.

GST-Vpx was purified, based on previous published Vpx purifications<sup>283</sup>, using affinity chromatography over glutathione sepharose resin and subjected to SEC for further purification (Figure 12A). After optimization of the lysis method (Supplementary Figure 1), high amounts of recombinant GST-Vpx with high purity were obtained, as shown by the presence of only two peaks in the SEC histogram (Figure 12A). The influence of the added tags on the ability of Vpx to induce SAMHD1 degradation was assessed by nucleofecting primary resting CD4<sup>+</sup> T cells with mammalian expression plasmids (i.e., pcDNA) encoding the tagged Vpx proteins and measuring the SAMHD1 signal by flow cytometry (Figure 12D). Adding a GST-tag impaired the ability of Vpx to induce SAMHD1 degradation, while a C-terminal 6x poly-histidine (6xHis)-T7 tag did not (Figure 12D). This is possibly due to the large size of the GST-tag (26 kDa) compared to Vpx (12 kDa). Therefore, the 6xHis-T7 tagged Vpx was purified via immobilized metal affinity chromatography (IMAC) nickel-loaded resin and subjected to SEC (Figure 12B). This alternative purification strategy, unfortunately, was unsuccessful

due to the insolubility of the construct (Supplementary Figure 2), high impurity and low yield of the protein (Figure 12B).

Since the 6xHis-tagged Vpx retained its ability to induce SAMHD1 degradation (Figure 12D) and the GST-tagged Vpx could be purified with high purity (Figure 12A), a cleavable GST-6xHis-tagged Vpx was generated containing a PreScission Protease cleavage site between the GST and 6xHis tags. The 6xHis tag attached to the Vpx protein was necessary for visualization of the Vpx protein in downstream experiments since no reliable Vpx-specific antibodies exist. The GST-6xHis-Vpx proteins were first bound to the glutathione sepharose resin, then the GST tag was cleaved on-column using PreScission Protease. The GST-cleaved 6xHis-Vpx proteins were then isolated and subjected to SEC (Figure 12C). The purification of the GST-6xHis-Vpx was equally unsuccessful as the 6xHis-T7-Vpx purification due to the formation of aggregates, low purity, and low yield (Figure 12C). In summary, despite the successful purification of the non-functional GST-Vpx construct, none of the attempted purifications produced Vpx proteins in high yields and high purity, as would have been expected from bacterial purifications, even after SEC.

One drawback of bacterial purification is the contamination of purified proteins with the bacterial endotoxin lipopolysaccharide (LPS), which can activate immune cells as an unwanted side-effect<sup>284</sup>. Since the final goal of the thesis is to treat primary AML blasts with delivery systems containing purified recombinant Vpx, and due to the lack of success from the bacterial purifications, we decided to switch to mammalian cells for Vpx purification.



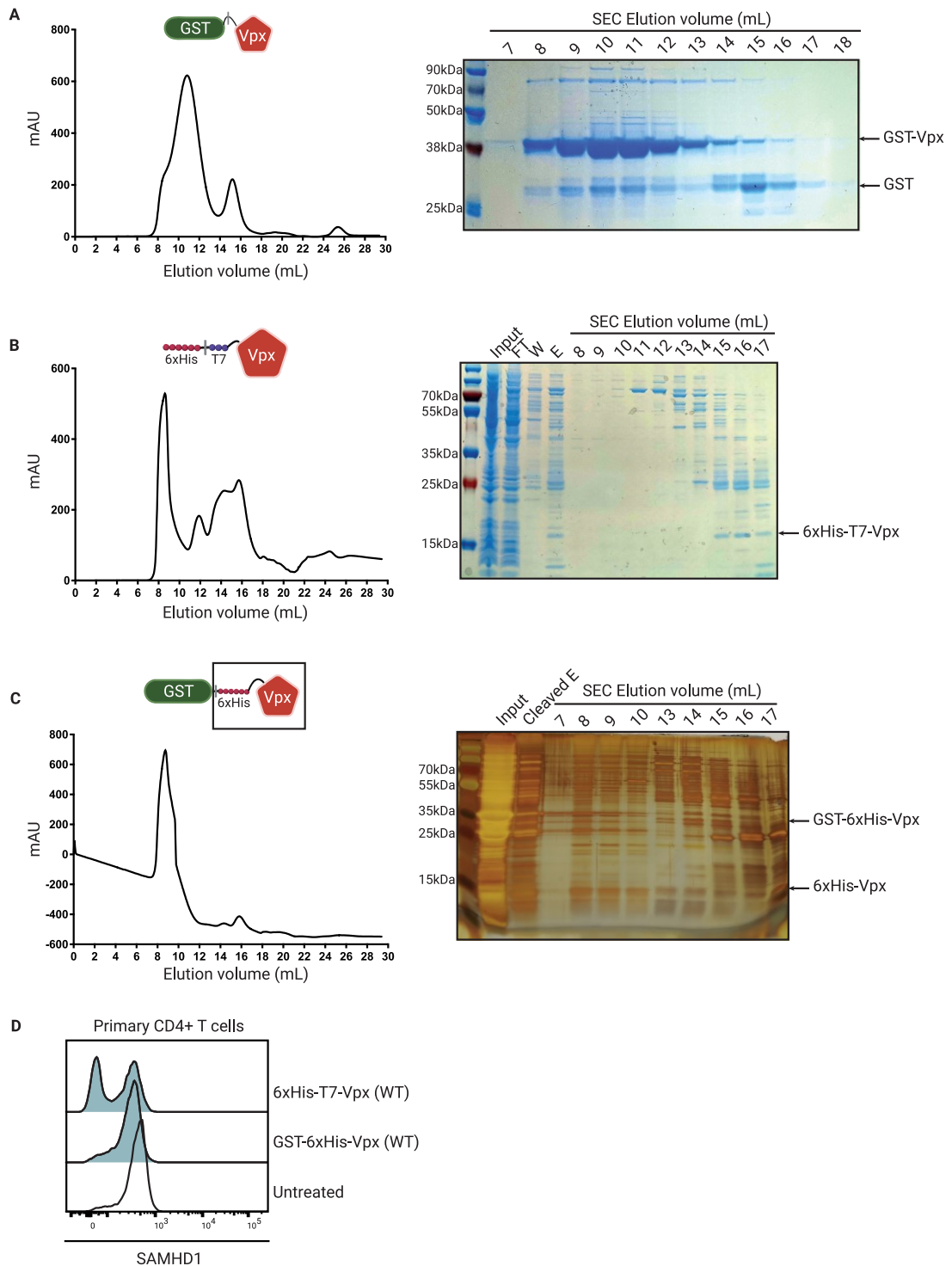


Figure 12: SEC purification and functionality of recombinant Vpx proteins.

Affinity-purified recombinant Vpx proteins were subjected to SEC. The absorption at wavelength 280 nm (mAU) of proteins at different elution volumes after SEC is shown for GST-Vpx (**A**), 6xHis-T7-Vpx (**B**), and cleaved GST-6xHis-Vpx (**C**). Selected elution volume fractions were separated on an SDS-polyacrylamide gel and stained either with InstantBlue Coomassie stain (**A** and **B**) or with silver staining (**C**). **D** Intracellular SAMHD1 staining of primary resting CD4+ T cells nucleofected with pcDNA plasmids encoding either 6xHis-T7-Vpx or GST-6xHis-Vpx. The histogram shown here represents live and single gated cells. The gating strategy is shown in Figure 9. Untreated CD4+ T cells were used as control.

### 3.1.2 Mammalian expression and purification of 3xFLAG-Vpx

Using mammalian cells for protein purification is usually preferred when the target proteins are complex with multiple subunits, require PTMs, or are insoluble in bacterial cells<sup>285</sup>. The most commonly used mammalian cell line for purification of proteins is the CHO cell line and the most used human cell line is the HEK293 cell line<sup>286</sup>. Due to the established protocols available in our laboratory for the efficient gene delivery and growth conditions for the HEK293T cell line, they were used as the host system to purify recombinant Vpx. Vpx from the SIVmac239 strain was used for the mammalian purifications.

Initially, a 3xFLAG-tagged Vpx purification was tested. The ability of 3xFLAG-Vpx to induce SAMHD1 degradation was confirmed based on the reduced SAMHD1 signal observed after nucleofecting primary resting CD4+ T cells with pcDNA 3xFLAG-Vpx plasmids (Figure 13A). For purification, adherent HEK293T cells were transfected with pcDNA plasmids encoding the 3xFLAG-Vpx construct via PEI transfection (Figure 13B). Subsequently, the cells were harvested, lysed and the 3xFLAG-Vpx proteins were purified over an anti-FLAG resin via affinity purification. The 3xFLAG-Vpx proteins were eluted via competitive binding using 3xFLAG peptide. The affinity purified 3xFLAG-Vpx proteins were subjected to SEC for further purification (Figure 13C). The presence of many peaks in the SEC histogram indicated low purity (Figure 13C). In addition, the low absorption at 280 nm (mAU) of the fraction containing the 3xFLAG-Vpx protein showed that the yield was very low (Figure 13C). This was also confirmed by the low intensity, albeit pure, band visible on the silver-stained gel of the elution fractions (Figure 13D).

The low yield of the 3xFLAG-Vpx construct might have been due to the insufficient amount of 3xFLAG peptides used during the elution. However, increasing the peptide amount did not result in increased yield (data not shown) and was not economically viable as the 3xFLAG peptides as well as the anti-FLAG resins were costly. For these reasons, Vpx purification using a different tag was investigated.

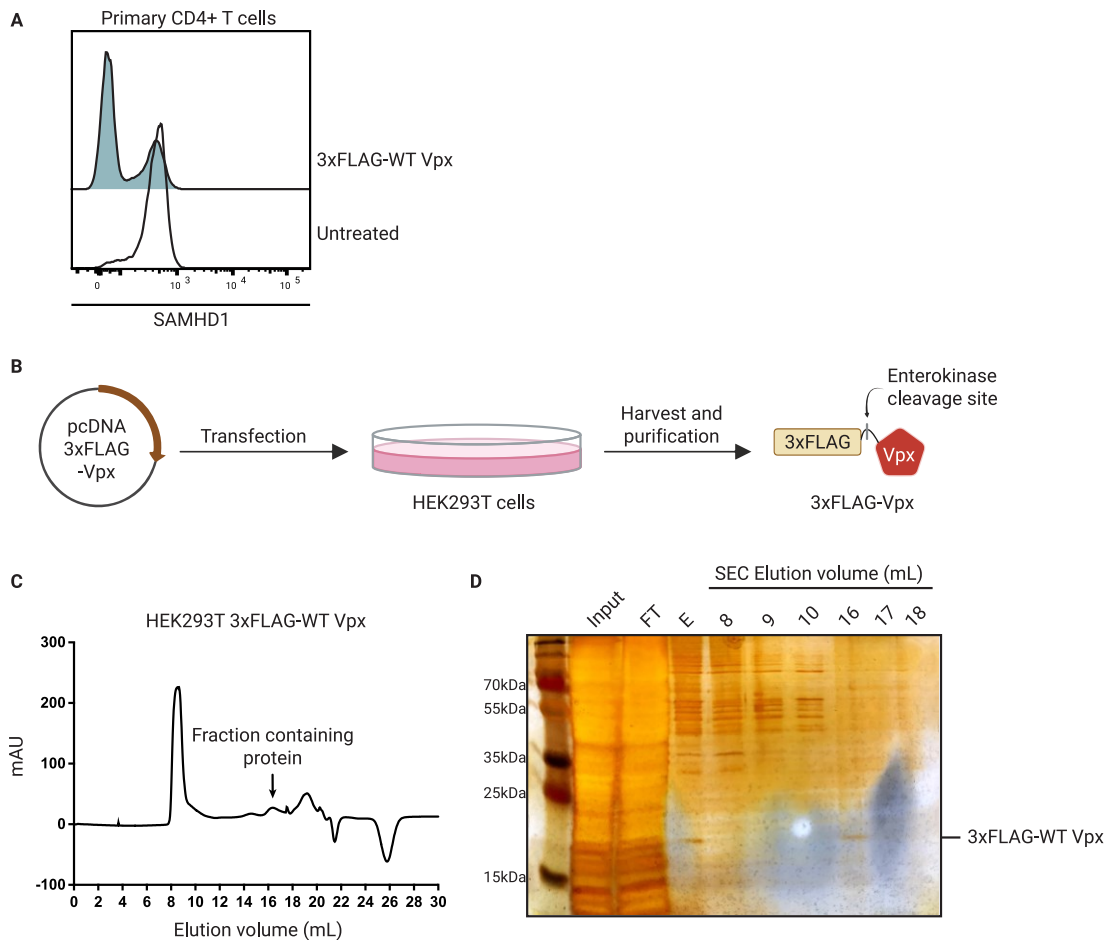


Figure 13: Expression and purification of 3xFLAG-Vpx from HEK293T cells.

3xFLAG-Vpx proteins were evaluated for their SAMHD1 degradation functionality and purified from HEK293T cells. **A** Primary resting CD4+ T cells were nucleofected with pcDNA 3xFLAG-Vpx and intracellularly stained for SAMHD1. The histogram shown here represents live and single gated cells. **B** Schematic representation of 3xFLAG-Vpx purification from HEK293T cells. **C** Affinity-purified 3xFLAG-Vpx was subjected to SEC. The absorption at wavelength 280 nm (mAU) of proteins at different elution volumes after SEC is shown. The fraction containing the 3xFLAG-Vpx protein is indicated with the arrow. **D** Selected elution volume fractions were separated on an SDS-polyacrylamide gel and stained with silver staining. FT: flow-through, E: eluate.

### 3.1.3 Mammalian expression and purification of Vpx-HA-10xHis<sub>7</sub>

Since the His tag is a widely used tag for protein purification and due to the low cost of the IMAC resins and elution reagents, a Vpx-HA-10xHis construct was developed. The 10xHis tag could be cleaved via a tobacco etch virus (TEV) protease, leaving the HA tag behind as a visual surrogate for Vpx (Figure 14A). The SAMHD1 degradation functionality of the Vpx-HA-10xHis construct was also confirmed, as previously described, using primary resting CD4+ T cell nucleofection (Figure 14B and C). The Q76A Vpx-HA-10xHis mutant, which is unable to induce SAMHD1 degradation<sup>163</sup>, was used as control.

<sup>7</sup> Some of the results presented in this subsection have been adapted and published in Nair *et al.*<sup>280</sup>, and indicated in the figure legends, where applicable. Work done by co-authors is indicated in footnotes and figure legends.

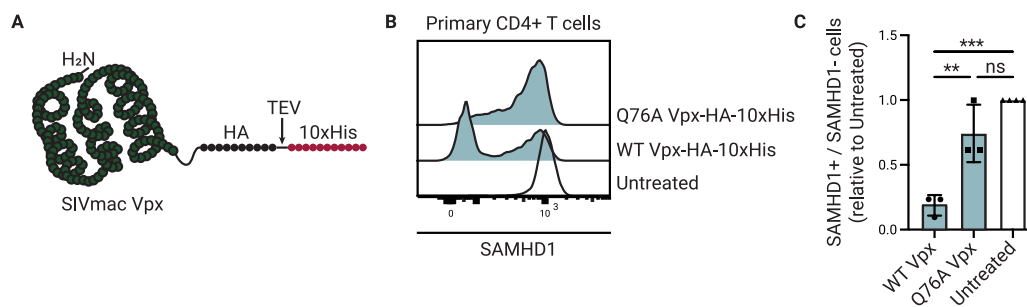


Figure 14: The Vpx-HA-10xHis constructs were functional in primary resting CD4+ T cells.

Primary resting CD4+ T cells were nucleofected with pcDNA WT or Q76A Vpx-HA-10xHis. **A** Schematic representation of the Vpx-HA-10xHis expression construct, indicating the location of the HA and 10xHis tags, and the TEV cleavage site at the C-terminus of the Vpx protein. **B** Representative histogram of nucleofected primary resting CD4+ T cells intracellularly stained for SAMHD1. The histogram shown here represents live and single gated cells. **C** Ratio of SAMHD1+ to SAMHD1- cells from nucleofected primary resting CD4+ T cells, as shown in **B**, were calculated, and normalized to untreated control. Error bars represent the standard error of mean (s.e.m.) from three independent biological replicates. One-way ANOVA was used for statistical analysis: \*\*,  $p < 0.01$ , \*\*\*,  $p < 0.001$ , ns:  $p > 0.05$ . (This figure is modified and published in Nair *et al.*<sup>280</sup>)

### 3.1.3.1 Establishment of an optimal Vpx-HA-10xHis purification workflow

Due to the lack of success of the previous purification attempts, a step-by-step optimization workflow was performed for the harvest and purification of the Vpx-HA-10xHis constructs. In the first step, several cell lysis conditions were investigated. Figure 15A shows the experimental set-up for the initial lysis buffer test. HEK293T cells were transfected with pcDNA encoding either WT or Q76A Vpx-HA-10xHis and incubated for 48 hrs. The cells were then harvested and lysed using the various lysis buffers indicated in Table 21. The total protein was isolated from the lysate by centrifugation and 2  $\mu$ L from each lysis condition were blotted onto a dry nitrocellulose membrane, blocked, and incubated with anti-HA.11 antibody to detect the HA signal from the Vpx-HA-10xHis construct. Untransfected HEK293T cells, lysed using lysis buffer 1, served as negative control. Lysis buffer containing Tween-20 (lysis buffer 2) was not as efficient as the remaining buffers to release Vpx-HA-10xHis from the cells, evidenced by the weaker HA signal seen in Figure 15B.

Table 21: Lysis buffer compositions for initial lysis test shown in Figure 15A and B.

Lysis buffer	Composition	NaCl	Detergent	pH
1			2% NP-40	
2			2% Tween-20	7.5
3	20 mM HEPES	150 mM	2% Triton X-100	
4	10% Glycerol			8
5	1x PIC		2% NP-40	7
6		250 mM		7.5
7		500 mM		

PIC: Protease inhibitor complex

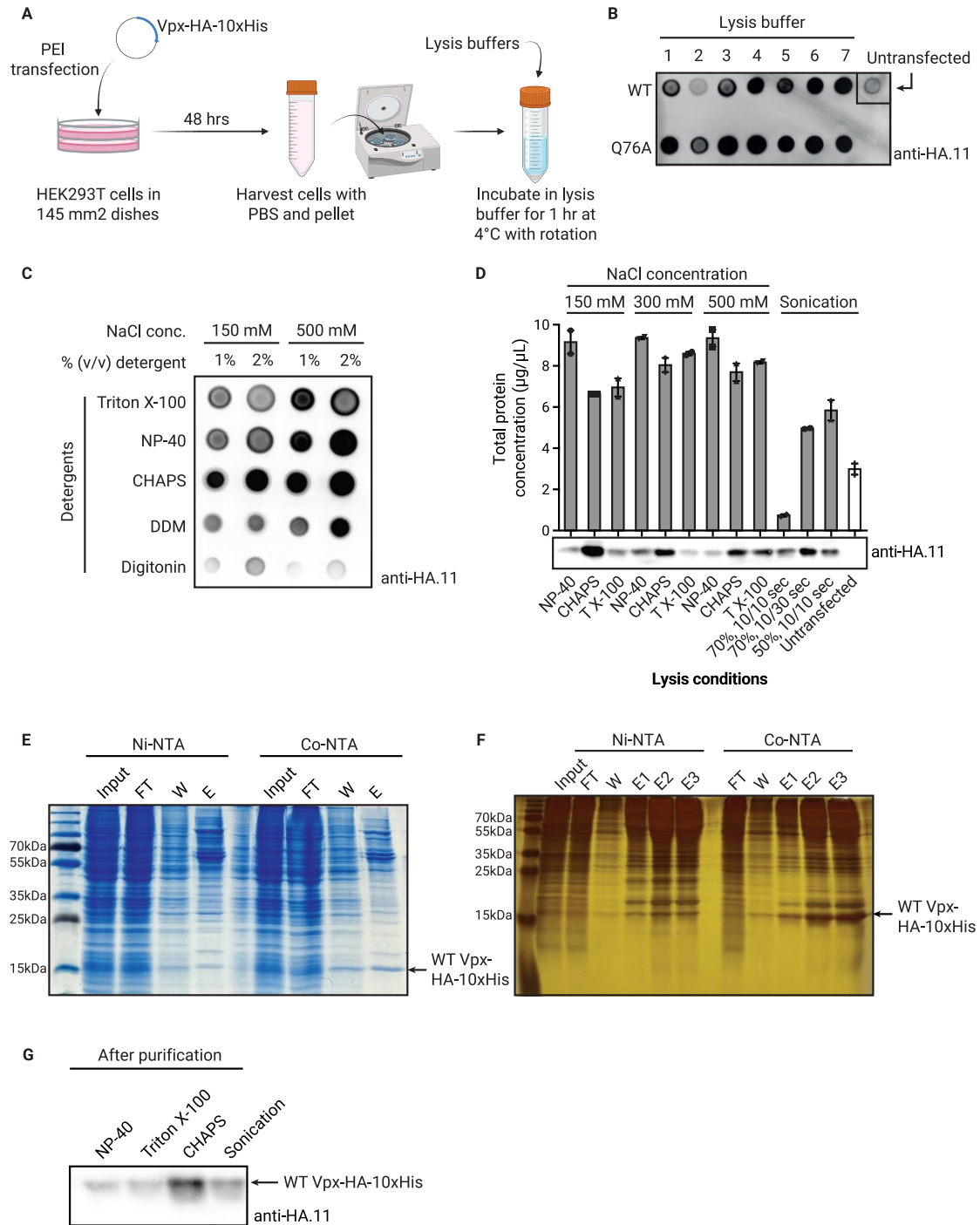


Figure 15: Initial establishment of lysis and purification conditions for Vpx-HA-10xHis from HEK293T cells. HEK293T cells transiently expressing Vpx-HA-10xHis were lysed under various conditions and used for purification of Vpx-HA-10xHis proteins. **A** Workflow of the initial lysis buffer test to purify Vpx-HA-10xHis proteins. The lysis buffer compositions are provided in Table 21. **B** Dot blot of total protein from lysed transfected and untransfected HEK293T cells from **A** immunoblotted against the HA tag. **C** Dot blot of total protein from HEK293T cells transfected with WT Vpx-HA-10xHis lysed with buffers containing the various detergents and salt (NaCl) concentrations indicated, immunoblotted against the HA tag. **D** Same as in **C**, including sonicated samples with total protein concentration measured via Bradford. Equal volumes of total protein were loaded on an SDS-polyacrylamide gel and immunoblotted against the HA tag. T X-100: Triton X-100, sonicated samples: indicated are the percentage amplitude and the ON/OFF pulse length. (Continued on next page)

**E** and **F** Aliquots from the different Vpx fusion protein purification steps from HEK293T cells either using Ni-NTA or Co-NTA resin were loaded on SDS-polyacrylamide gels and stained either using InstantBlue Coomassie stain (**E**) or silver staining (**F**). FT: flow-through, W: wash, E: eluate. **G** HA tag immunoblot of eluates of affinity purified WT Vpx-HA-10xHis after lysis with buffers containing the various detergents indicated. (Parts of this figure are modified and published in Nair *et al.*<sup>280</sup>)

In the next attempt, lysis buffers with a larger panel of detergents and two different salt (NaCl) concentrations were tested. Figure 15C shows that the CHAPS, NP-40, and Triton X-100 were the best detergents for lysis at 2% concentration, whereas digitonin and dodecylmaltoside (DDM) were not as effective at lysis. Another method of lysis is mechanical rupture, for instance via sonication. The release of the Vpx-HA-10xHis proteins from cells using detergent-based and sonication-based lysis was compared next (Figure 15D). Detergent lysis was again conducted under different salt concentrations at 2% detergent concentration. After lysis, equal volume of total protein was loaded onto an SDS-polyacrylamide gel. The separated proteins were then immunoblotted against the HA tag. In addition, the total protein concentration was also measured to evaluate the efficiency of lysis. Based on the HA blot and the total protein amount shown in Figure 15D, the CHAPS detergent with 150 mM salt concentration showed a high lysis efficiency (high total protein concentration) and the highest release of the Vpx-HA-10xHis protein (strong HA band intensity) compared to all other lysis conditions.

After identifying the optimal lysis conditions, the right IMAC resin for the affinity purification via the His tag was determined. His-tagged proteins are purified through the binding of the histidine amino acids to the metal ions on IMAC resins. Different bivalent metal ions can be utilized in IMAC resins for the binding of His-tagged proteins. Nickel ( $\text{Ni}^{2+}$ ) and cobalt ( $\text{Co}^{2+}$ ) are the most commonly used metal ions in IMAC resins and they possess different binding capacities to the histidine amino acids<sup>287</sup>.  $\text{Ni}^{2+}$ , which was used for the purification of bacterial 6xHis-T7-Vpx mentioned in subsection 3.1.1, has a high binding affinity towards histidine compared to  $\text{Co}^{2+}$ . However, due to the high affinity,  $\text{Ni}^{2+}$  binds impurities that contain histidine amino acids to a larger extent than  $\text{Co}^{2+}$ . In this work,  $\text{Ni}^{2+}$  and  $\text{Co}^{2+}$  immobilized onto NTA matrix were compared for their ability to bind the Vpx-HA-10xHis protein. The purity was also investigated after elution of the protein via competitive binding of IMAC with imidazole (imidazole binds metal ions in IMAC resins). Figure 15E and F show the total protein obtained from the different steps of the purification process separated on SDS-polyacrylamide gels, either stained with InstantBlue Coomassie stain (Figure 15E) or silver stain (Figure 15F). Comparing the elution fractions for both Ni-NTA and Co-NTA resins, more Vpx-HA-10xHis protein with higher purity was yielded from the Co-NTA purification compared to Ni-NTA. Finally, combining the detergent and sonication lysis conditions and purification via the Co-NTA resin, the CHAPS detergent lysis still gave the best yields (Figure 15G). Despite the better purity achieved with the Co-NTA resins, impurities were still present in the eluate. The addition of 10 mM imidazole to the wash buffer removed some impurities without significant loss of the Vpx protein (Supplementary Figure 3). However, despite the large number of impurities present after IMAC purification (Figure 16A), an additional SEC step improved the purity of the Vpx-HA-10xHis eluate significantly (Figure 16B).

In conclusion, through this stepwise optimization, lysing cells using the CHAPS lysis buffer and purification of the Vpx-HA-10xHis fusion proteins via the Co-NTA resins followed by SEC were revealed to be optimal.

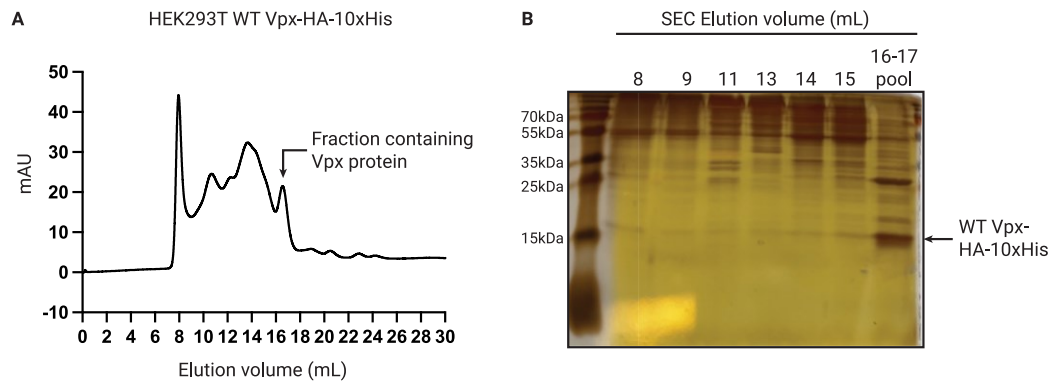


Figure 16: SEC improved purity of Vpx-HA-10xHis protein after IMAC purification.

IMAC-purified Vpx-HA-10xHis was subjected to SEC. **A** The absorption at wavelength 280 nm (mAU) of proteins at different elution volumes after SEC is shown. The fraction containing the Vpx-HA-10xHis protein is indicated with the arrow. **B** Selected elution volume fractions were separated on an SDS-polyacrylamide gel and stained either with silver staining.

### 3.1.3.2 Generation of Vpx-HA-10xHis-expressing sleeping beauty HEK293T cells

Thus far, the purifications were performed on HEK293T cells transfected with pcDNA plasmid encoding the Vpx-HA-10xHis fusion proteins. Consequently, large amounts of plasmids will be required to increase the scale of production. To avoid the need to constantly purify plasmids, HEK293T cells stably expressing the Vpx-HA-10xHis fusion proteins were generated. Since Vpx reduces SAMHD1 levels and SAMHD1 is involved in cell cycle progression (see subsection 1.2.2.1), a constitutive Vpx expression might not be beneficial for the cells. Therefore, an inducible promoter was used to control the expression of the *Vpx-HA-10xHis* genes in the cells, which could be activated by the addition of the drug doxycycline (Figure 7)<sup>2</sup>. These so-called sleeping beauty cells were generated by transfecting HEK293T cells with 2 plasmids: one containing the gene-of-interest (i.e., *Vpx-HA-10xHis*) and the other containing a transposase (Figure 7 and subsection 2.4.1.3). Cells that have successfully integrated the genes-of-interest into their genome constitutively express BFP and possess puromycin resistance, as illustrated in Figure 7. After one week of selection with 1 µg/mL puromycin, the proteins levels of BFP and both WT and Q76A Vpx-HA-10xHis upon doxycycline induction were measured via flow cytometry (Figure 17A). Both WT and Q76A Vpx-HA-10xHis constructs, represented by the HA signal, were expressed in at least 85% (BFP+HA+) of the sleeping beauty cells after induction with 1 µg/mL doxycycline (Figure 17A).

<sup>2</sup> These cells were generated by Alejandro Salinas-Illarena at the Max von Pettenkofer Institute

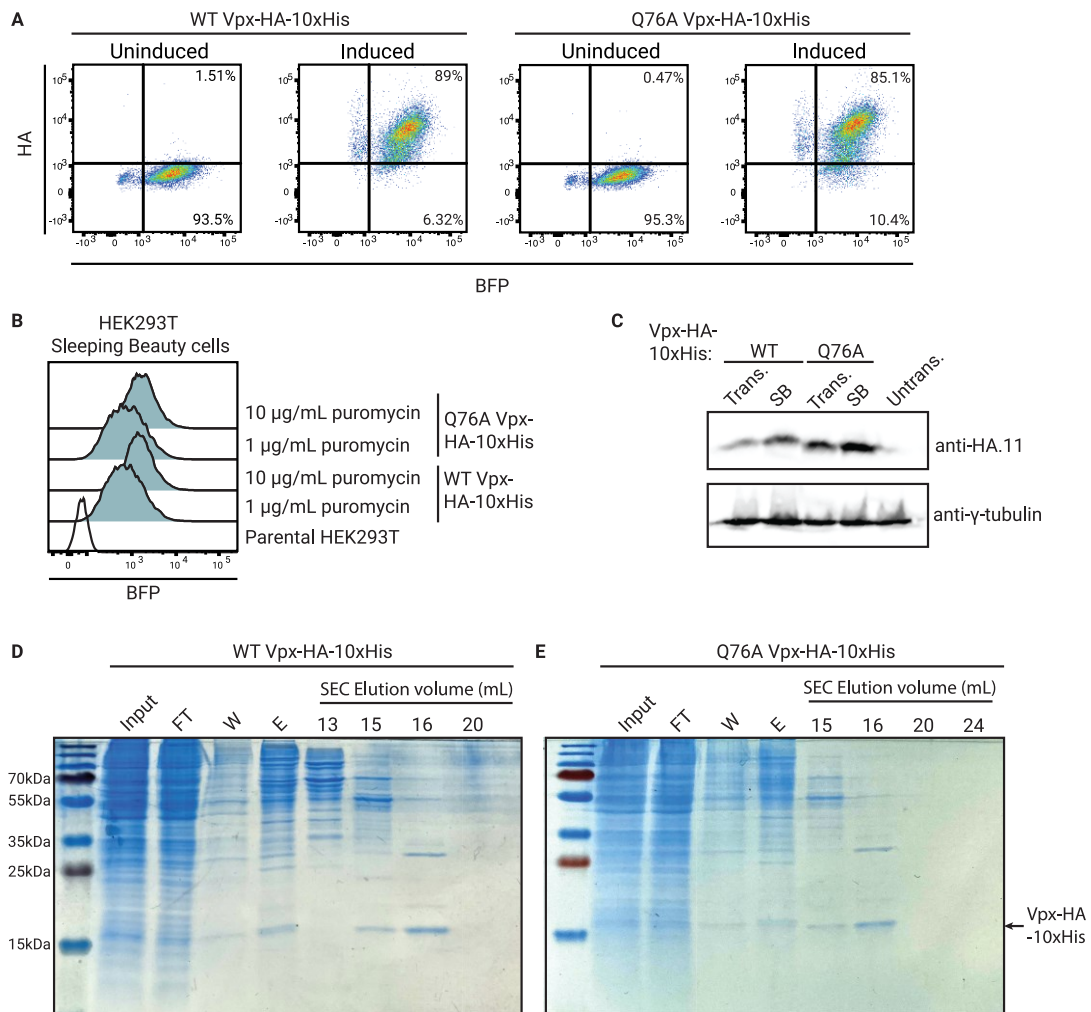


Figure 17: Purification of Vpx-HA-10xHis from HEK293T sleeping beauty cells.

HEK293T sleeping beauty cells encoding Vpx-HA-10xHis were generated, characterized, and used for purification of Vpx-HA-10xHis proteins. **A** HEK293T cells stably expressing WT or Q76A Vpx-HA-10xHis were intracellularly stained for HA and analyzed for BFP and HA (AlexaFluor® 488) expression levels. Puromycin-selected sleeping beauty cells were either induced with 1 µg/mL doxycycline or uninduced. Events shown represent live and single cells. **B** BFP signal histogram of both WT and Q76A Vpx-HA-10xHis sleeping beauty HEK293T cells after further selection with either 1 µg/mL or 10 µg/mL puromycin. Parental HEK293T cells were used as negative control. **C** Immunoblot of total proteins from doxycycline-induced sleeping beauty cells (SB) and pcDNA WT and Q76A Vpx-HA-10xHis-transfected HEK293T cells (Trans.), stained for HA and  $\gamma$ -tubulin (housekeeping control). Total protein from untransfected parental HEK293T (Untrans.) cells was used as control. **D** and **E** InstantBlue Coomassie stained gels with aliquots from the different IMAC purification steps and selected elution volume fractions after SEC of WT (**D**) and Q76A (**E**) Vpx-HA-10xHis purified from sleeping beauty cells. FT: flow-through, W: wash, E: elution. (Parts of this figure are modified and published in Nair *et al.*<sup>280</sup>)

In order to boost the yield of Vpx-HA-10xHis from the sleeping beauty cells, the concentration of puromycin used for selection was increased from 1 µg/mL to 10 µg/mL. This treatment induced an increase in the BFP signal (Figure 17B). Differences between transfected cells and the sleeping beauty cells in terms of the yield of Vpx-HA-10xHis were also tested (Figure 17C). Slightly more intense bands were noticed for the sleeping beauty cells-derived Vpx-HA-10xHis proteins compared to transfected cells, further underscoring the superiority of using the sleeping beauty cells (Figure 17C).



Highly pure Vpx-HA-10xHis proteins, which had an elution volume of 16 mL, could also be obtained after IMAC and SEC purifications from doxycycline-induced sleeping beauty cells (Figure 17D and E). These results collectively showed that Vpx-HA-10xHis expression was easily induced with the low-cost drug doxycycline, and the proteins could be successfully purified from these sleeping beauty HEK293T cells

### 3.2 Establishment of a functionality assay for purified recombinant Vpx

Since the purification procedure of proteins can potentially impact their biological activity, ensuring proper function of the purified recombinant Vpx (i.e., ability to induce SAMHD1 degradation) is important before using them in different delivery systems. Unfortunately, no established *in vitro* functionality protocol for Vpx exists. Some studies that have purified recombinant Vpx have thus far shown SAMHD1 interaction with Vpx and SAMHD1 ubiquitination via co-immunoprecipitation and *in vitro* ubiquitination assays, as summarized in Table 22. However, none have shown the subsequent SAMHD1 degradation by the proteasome complex induced by purified recombinant Vpx.

Table 22: Summary of studies which reported recombinant Vpx interaction with SAMHD1.

Vpx protein construct	Host cell/ expression system	Assays performed with Vpx proteins	Reference
FLAG-HA-Vpx	THP-1	Co-purification of Vpx, SAMHD1, DDB1 and CUL4A	109
HA-FLAG-Vpx	HEK293T	MudPIT interaction and co-IP of Vpx with SAMHD1, DDB1 and DCAF1	108
GST-Vpx	<i>E. coli</i> Rosetta2	Crystallization of complex: Vpx with DCAF1-CtD and SAMHD1-NtD after GST cleavage	163,283
FLAG-Vpx	<i>In vitro</i> translation	Co-IP of Vpx with SAMHD1, <i>in vitro</i> kinase assay	288
NusA-Vpx-6xHis	<i>E. coli</i> Rosetta2	Interaction kinetics of SAMHD1-DDB1-DCAF1-Vpx and <i>in vitro</i> ubiquitination assays	178,289,290

*Co-IP: Co-immunoprecipitation; MudPIT: Multi-dimensional protein identification technology, CtD: C-terminal domain, NtD: N-terminal domain*

In order to determine the functionality of purified Vpx proteins, two strategies were investigated: (1) *in vitro* cell-free, and (2) cell-based degradation assay for SAMHD1.

### 3.2.1 *In vitro* cell-free degradation assay was not successful

Since studies have already shown Vpx interaction and ubiquitination of SAMHD1 with *in vitro* ubiquitination assays, we reasoned that the subsequent proteasomal degradation of SAMHD1 could also be observed via such an assay. Before carrying out *in vitro* degradation assay with the purified Vpx proteins, the proteasome activity of THP-1 lysates was first determined. THP-1 cell lysates were used since THP-1 cells express high levels of SAMHD1. Suc-LLVY-AMC is a common substrate used to measure the chymotrypsin-like activity of the 26S proteasome complex<sup>291</sup>. The protocol by Maher was adapted to determine the activity of the 26S proteasome in THP-1 lysates<sup>282</sup>, as illustrated in Figure 18A and described in subsection 2.7.9. Proteasome activity was efficiently measured in THP-1 lysates and the addition of proteasome inhibitor MG132 was able to completely reduce proteasome activity (Figure 18B).

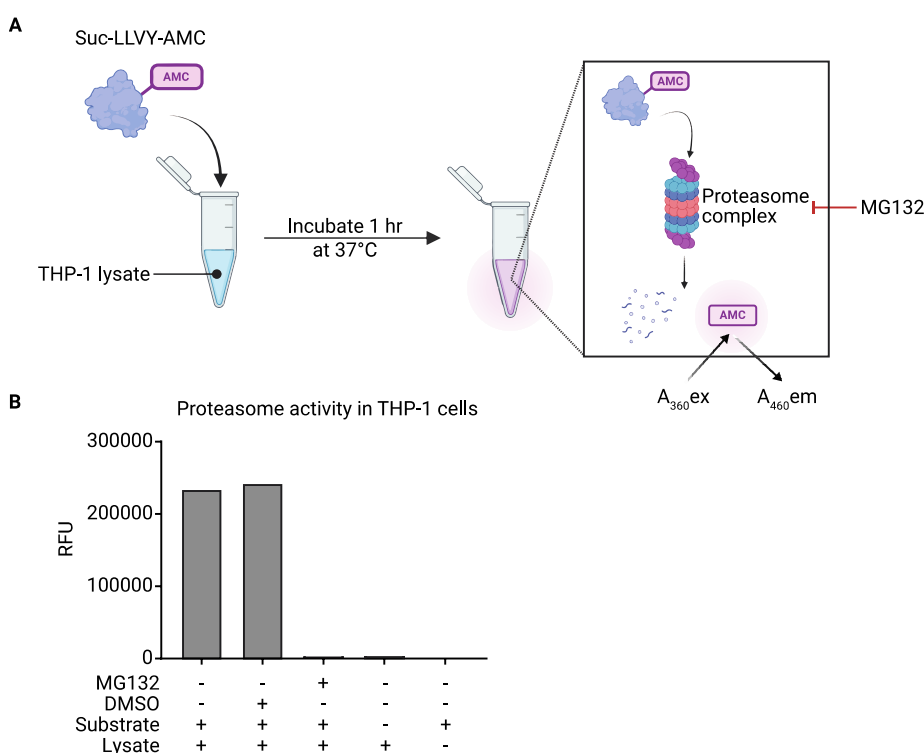


Figure 18: Proteasome activity of THP-1 lysates determined using Suc-LLVY-AMC substrate.

THP-1 cells were lysed and evaluated for proteasome activity. **A** Schematic representation of the proteasome activity assay. Suc-LLVY-AMC was used as a substrate, which upon degradation via the 26S proteasome, released the AMC fluorophore. The fluorescence was measured at 460 nm wavelength. MG132: proteasome inhibitor. **B** Relative fluorescence units (RFU) of the AMC fluorophore released after substrate degradation in THP-1 lysates is shown. Lysate without substrate, and substrate only were used as negative control. 40  $\mu$ M of MG132 were added to inhibit the proteasome. DMSO was added as control.

Next, the impact of lysis buffer composition and imidazole on proteasome activity was investigated, to account for the impact of the purified Vpx protein storage buffer. Three different lysis buffer compositions were tested for THP-1 cells prior to proteasome activity measurement. The buffer compositions are shown in Table 23. THP-1 cells lysed in lysis buffer 2, whose composition was

modified from the protocol by Maher<sup>282</sup>, showed the highest proteasome activity (Figure 19A). The presence of imidazole did not negatively affect the proteasome activity (Figure 19B).

Table 23: Composition of lysis buffers used in THP-1 lysate proteasome activity assay.

Lysis buffer	Composition
1	50 mM HEPES pH 7.5, 150 mM NaCl, 1% NP-40, 5% glycerol, 20 $\mu$ M ZnCl <sub>2</sub> , 5 mM MgCl <sub>2</sub> , 5 mM DTT, 1x PIC (EDTA-free)
2	50 mM HEPES pH 7.5, 10 mM NaCl, 5 mM MgCl <sub>2</sub> , 250 mM sucrose, 5 mM DTT
3	20 mM HEPES pH 7.5, 150 mM NaCl, 15% glycerol, 5 mM MgCl <sub>2</sub> , 1 mM DTT, 1x PIC (EDTA-free)

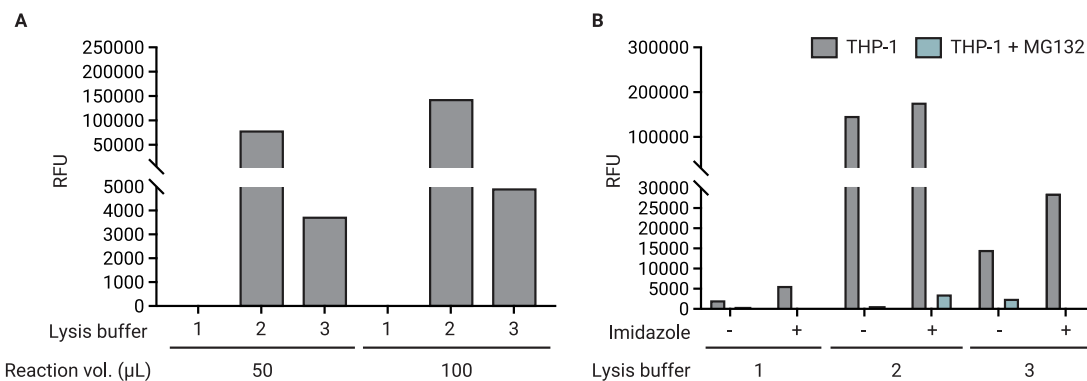


Figure 19: Impact of lysis buffer composition and imidazole on THP-1 lysate proteasome activity.

THP-1 cells were lysed with the indicated lysis buffers. The reaction was carried out in either 50  $\mu$ L or 100  $\mu$ L final volume containing equal amounts of THP-1 lysate and proteasome activity was subsequently measured. **A** Shown are the relative fluorescence units (RFU) of the AMC fluorophore released after substrate degradation in THP-1 lysates. **B** Same as in **A**, but with or without 150 mM imidazole in the reaction mix. THP-1 lysates were either pre-treated with 40  $\mu$ M MG132 or left untreated.

With the optimal lysis buffer conditions, the feasibility of an *in vitro* degradation assay for testing the functionality of purified recombinant Vpx was investigated. For this, the THP-1 lysates (lysed using lysis buffer 2) were mixed with purified recombinant Vpx proteins and incubated for 6 hrs at 37°C (Figure 20A). Subsequently, an aliquot of the reaction was used for western blot analysis. In the initial attempt, the metal chelator EDTA was included in the reaction buffer to prevent protease activity. However, since Vpx is a zinc-binding protein and EDTA chelates divalent ions, EDTA was removed from the reaction buffer. With the removal of EDTA, SAMHD1 degradation was observed using the 6xHis-T7-Vpx proteins purified from *E. coli* (Figure 20B and C). However, the observations were not reproducible (data not shown). A slight reduction in SAMHD1 signal could be observed upon treatment with WT Vpx-HA-10xHis purified from HEK293T cells compared to Q76A Vpx-HA-10xHis (Figure 20D). However, in the case of the Q76A Vpx-HA-10xHis, SAMHD1 was also co-purified, which might explain the stronger SAMHD1 signal (Supplementary Figure 4A). Lysates from THP-1 cells expressing GFP-SAMHD1 were used in order to circumvent this issue, as changes in

the GFP-SAMHD1 levels would be independent of the co-purified WT SAMHD1. Unfortunately, no changes in GFP-SAMHD1 were noticed upon incubation with WT Vpx-HA-10xHis (Supplementary Figure 4B). Due to the non-reproducibility of the *in vitro* degradation assay for SAMHD1, a cell-based degradation assay was attempted to confirm the function of purified recombinant Vpx.

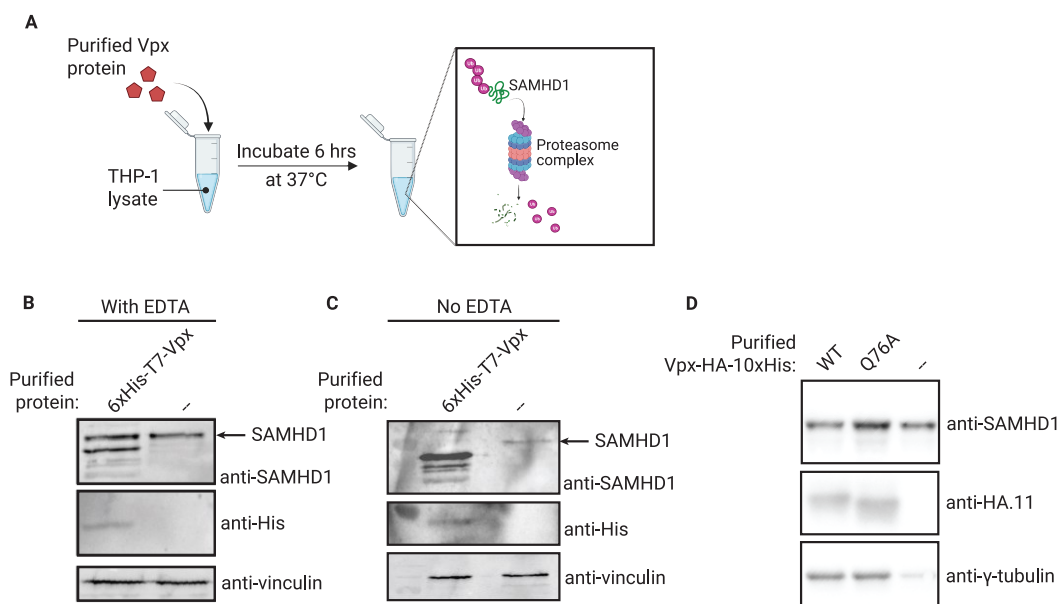


Figure 20: *In vitro* degradation assay with purified recombinant Vpx.

Purified recombinant Vpx proteins were evaluated for their SAMHD1 degradation functionality via an *in vitro* degradation assay. **A** Schematic representation of the *in vitro* degradation assay using purified recombinant Vpx. **B** Immunoblot against SAMHD1, His-tag, and vinculin of degradation assay reactions using 6xHis-T7-Vpx purified from *E. coli* in the presence of EDTA in the reaction mix. Reaction without Vpx protein was used as control. **C** Same as **B**, but in the absence of EDTA in reaction mix. Vinculin was used as loading control. **D** Immunoblot against SAMHD1, HA-tag and  $\gamma$ -tubulin of degradation assay using purified WT and Q76A Vpx-HA-10xHis from HEK293T cells, without EDTA in reaction mix.  $\gamma$ -tubulin was used as loading control. Cell lysates from THP-1 parental cells without Vpx proteins were used as controls.

### 3.2.2 Cell-based degradation assay shows functionality of Vpx-HA-10xHis construct<sub>3</sub>

Since the purified Vpx proteins will be delivered to cells, a cell-based degradation assay might be more appropriate to determine functionality. This way, physiological cellular conditions affecting protein functionality can also be considered. For this purpose, the purified Vpx proteins needed to be introduced into cells. Preliminary tests in THP-1 cells using protein transfection agents such as the Pierce™ Protein Transfection Reagent and TurboFect™ Reagent, which was shown to be effective for protein delivery in HeLa cells<sup>292</sup>, were unsuccessful (data not shown).

<sub>3</sub> Some of the results presented in this subsection have been adapted and published in Nair *et al.*<sup>280</sup>, and indicated in the figure legends, where applicable. Work done by co-authors is indicated in footnotes and figure legends.

Recently, Albanese *et al.* described the successful delivery of Cas9-gRNA ribonucleoproteins (RNPs) into primary resting CD4<sup>+</sup> T cells using nucleofection<sup>278</sup>. Since resting CD4<sup>+</sup> T cells have high endogenous SAMHD1 expression levels and have been used in this work for the nucleofection of plasmids, we decided to investigate this method for the delivery of purified Vpx proteins. Figure 21A illustrates the workflow of the nucleofection reaction. Based on flow cytometry analysis of SAMHD1 protein levels, nucleofection of primary resting CD4<sup>+</sup> T cells with purified WT Vpx-HA-10xHis proteins showed a higher proportion of SAMHD1-negative cells compared to purified Q76A Vpx-HA-10xHis proteins (Figure 21B and C). In addition, MG132-treatment of nucleofected primary resting CD4<sup>+</sup> T cells inhibited the degradation of SAMHD1 by WT Vpx-HA-10xHis compared to DMSO control (Figure 21D)<sup>4</sup>. It needs to be noted that these experiments were conducted using only IMAC-purified Vpx-HA-10xHis before SEC. Proteins that were subjected to SEC did not show any degradation of SAMHD1 (data not shown), likely due to the loss of protein during the SEC run, despite the increased purity. Nevertheless, since the degradation of SAMHD1 observed in this assay was specific to WT Vpx-HA-10xHis and could be inhibited with MG132 treatment, biological activity of WT Vpx-HA-10xHis was confirmed.

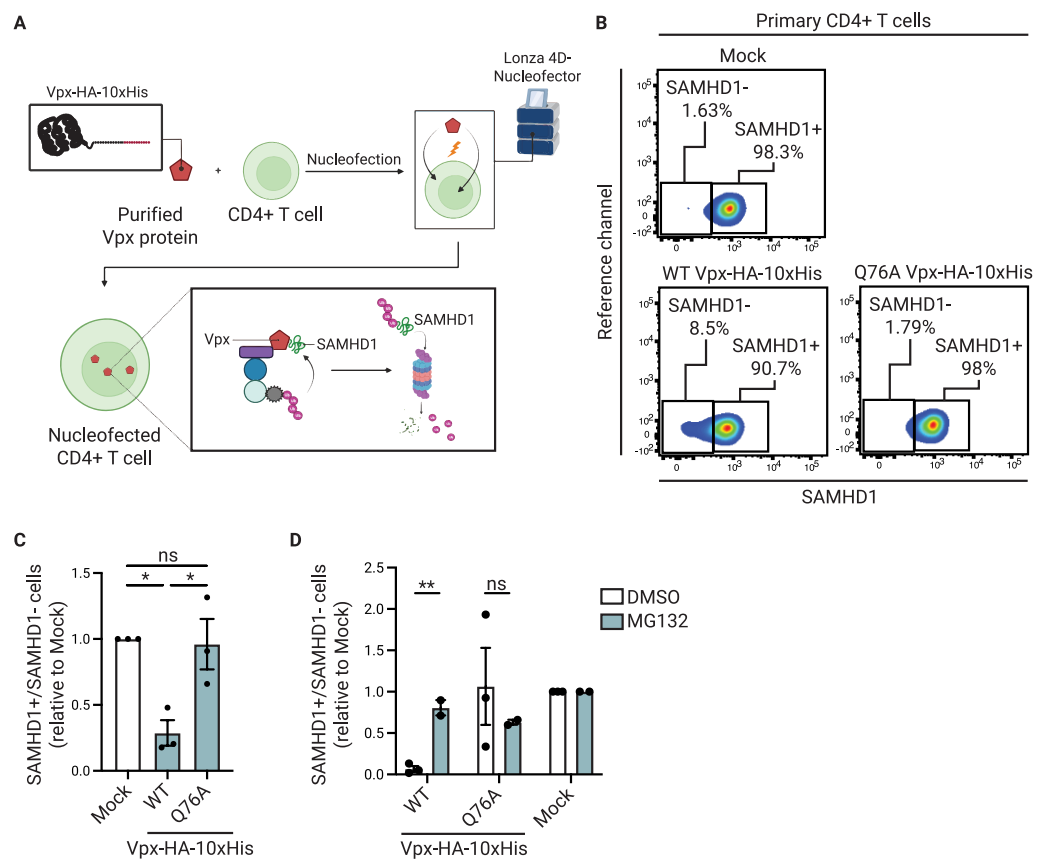


Figure 21: Purified WT Vpx-HA-10xHis proteins degraded SAMHD1 in primary resting CD4<sup>+</sup> T cells. Primary resting CD4<sup>+</sup> T cells were nucleofected with purified Vpx-HA-10xHis proteins. (Continued on next page)

<sup>4</sup> Experiment performed by Yanis Pignot at the Max von Pettenkofer Institute

**A** Schematic representation of Vpx-HA-10xHis protein nucleofection workflow of primary resting CD4<sup>+</sup> T cells isolated from healthy blood using the Lonza 4D-Nucleofector. **B** 24 hrs after protein nucleofection with WT Vpx-HA-10xHis, Q76A Vpx-HA-10xHis or mock nucleofection with buffer, cells were stained for SAMHD1 and analysed via flow cytometry. **C** Ratio of SAMHD1<sup>+</sup> to SAMHD1<sup>-</sup> cells from nucleofected primary resting CD4<sup>+</sup> T cells, as shown in **B**, were calculated and normalized to mock control. Error bars represent the standard error of mean (s.e.m.) from three independent biological replicates. One-way ANOVA was used for statistical analysis: \*:  $p < 0.05$ , ns:  $p > 0.05$ . **D** Vpx-HA-10xHis purified from twice the number of HEK293T cells were used for nucleofection. Nucleofected cells were then either grown in DMSO- or MG132-containing medium for 24 hrs. Bar graph shows ratio of SAMHD1<sup>+</sup> to SAMHD1<sup>-</sup> nucleofected cells based on flow cytometry analysis, normalized to mock control. Experiments represented in **D** were conducted by Yanis Pignot at the Max von Pettenkofer Institute. Error bars represent the standard error of mean (s.e.m.) from two-three independent biological replicates. Unpaired t-test was used for statistical analysis: \*\*:  $p < 0.01$ , ns:  $p > 0.05$ . (Parts of this figure are modified and published in Nair *et al.*<sup>280</sup>).

### 3.3 Production and functionality of Vpx-nanoMOFs

Since the functionality of purified Vpx proteins was confirmed, they could be packaged into different delivery systems. One such delivery system is the nanoMOFs.

#### 3.3.1 Initial characterization of nanoMOFs with 6xHis-GFP

The self-assembly of His-tagged proteins onto nanoMOFs was established by Röder *et al.* and served as the basis for this work<sup>202</sup>. The composition of the nanoMOFs used in this work is described in Table 20, in subsection 2.7.8. Röder *et al.* reported the ability of His-tagged proteins to self-assemble with the nanoMOFs via the binding of the His tag to the metal ions in the nanoMOFs<sup>202</sup>. The nanoMOFs used in this work consisted of three different metal ions for binding the His-tagged proteins: iron ( $\text{Fe}^{3+}$ , MIL88A), zinc ( $\text{Zn}^{2+}$ , ZIF-8), and zirconium ( $\text{Zr}^{4+}$ , Zr-fumarate).

Initially, 6xHis-tagged GFP was used to measure the difference in binding efficiencies of the different nanoMOFs to His-tagged proteins. Refer to subsection 2.7.8 for details on the calculation of nanoMOF binding efficiency of 6xHis-GFP. MIL88A had the highest binding efficiency of 6xHis-GFP, followed by ZIF-8 and Zr-fumarate (Figure 22A). Next, the uptake efficiency of the GFP-bound nanoMOFs was tested in THP-1 cells. The GFP signal was the highest after incubation with MIL88A-bound GFP compared to ZIF-8 and Zr-fumarate (Figure 22B), correlating with the binding efficiencies shown in Figure 22A. The cytotoxicity of the nanoMOFs was also analyzed by staining the THP-1 cells with a viability dye. MIL88A also showed the lowest cytotoxicity compared to ZIF-8 and Zr-fumarate, although MIL88A treatment was toxic to the cells (approx. 73% dead cells) compared to no treatment (approx. 28% dead cells) (Figure 22C). However, since the addition of 6xHis-GFP without nanoMOFs also induced cytotoxicity (approx. 70% dead cells) (Figure 22C), the toxicity observed after MIL88A treatment might have been a result of the 6xHis-GFP and not the nanoMOF itself. From these initial experiments using 6xHis-GFP, MIL88A was chosen as the best nanoMOF candidate for Vpx-HA-10xHis delivery.

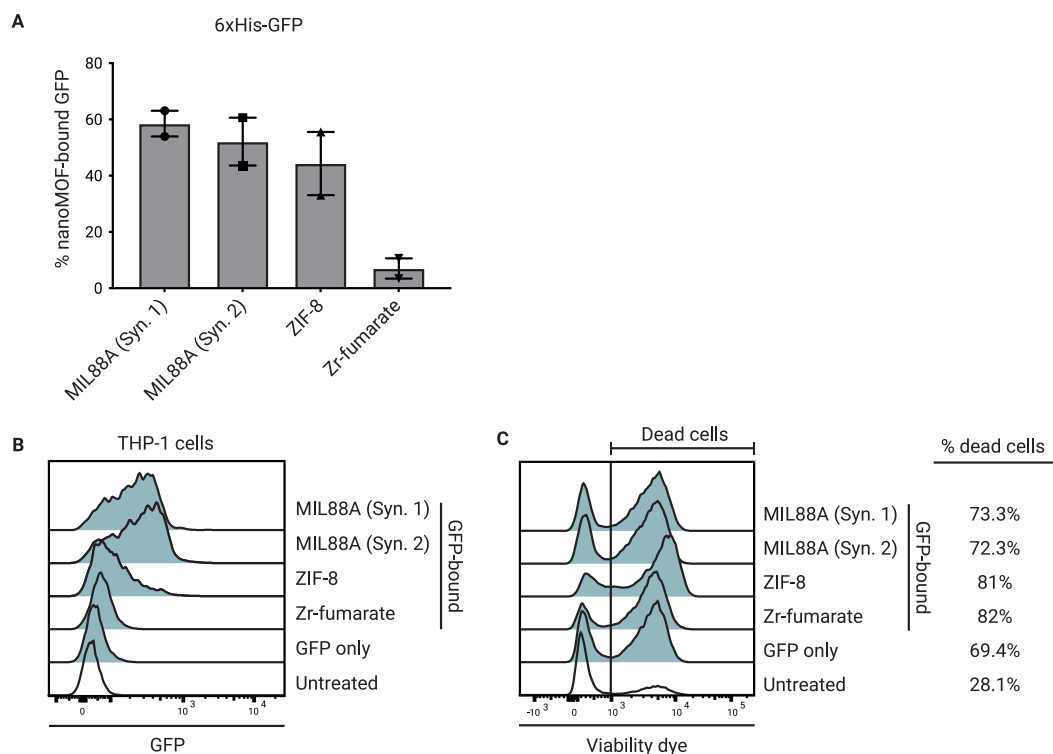


Figure 22: Binding and THP-1 uptake of 6xHis-GFP-nanoMOFs.

Different 6xHis-GFP-nanoMOFs were generated and incubated with THP-1 cells. **A** Percentage of 6xHis-GFP bound to nanoMOFs is shown. Two different syntheses of MIL88A were tested (Syn. 1 and 2). Error bars represent the standard deviation (s.d.) from two independent experiments. **B** THP-1 cells were incubated with 1  $\mu\text{g}/\mu\text{L}$  of GFP-bound nanoMOF for 24 hrs. Histogram shows GFP signal in THP-1 cells compared to untreated cells and cells treated with 6xHis-GFP unbound to nanoMOFs. **C** Same as in **B**, but histogram shows distribution of dead cells after staining with viability dye. The percentages of dead cells are also indicated.

### 3.3.2 Vpx-nanoMOFs were taken up by THP-1 cells

Vpx binding to nanoMOF was determined by analyzing unbound proteins on an SDS-polyacrylamide gel after incubation with nanoMOFs. MIL88A from synthesis 1, which showed the best binding efficiency in the 6xHis-GFP experiment, were able to effectively bind both WT and Q76A Vpx-HA-10xHis proteins, indicated by the lack of Vpx in the unbound fraction (Figure 23A). Zr-fumarate was included as control to confirm the specific and highly effective binding of Vpx by MIL88A. Next, the uptake and functionality of Vpx-bound MIL88A was investigated in THP-1 cells. For this, 25  $\mu\text{g}$  of nanoMOFs were incubated with THP-1 cells for 24 hrs after self-assembly with Vpx-HA-10xHis proteins. Subsequently, HA and SAMHD1 levels were analyzed by flow cytometry. Vpx-bound nanoMOFs were taken up by 16.5% of THP-1 cells, indicated by the increase in HA signal (Figure 23B). However, no degradation of SAMHD1 was observed (Figure 23B).

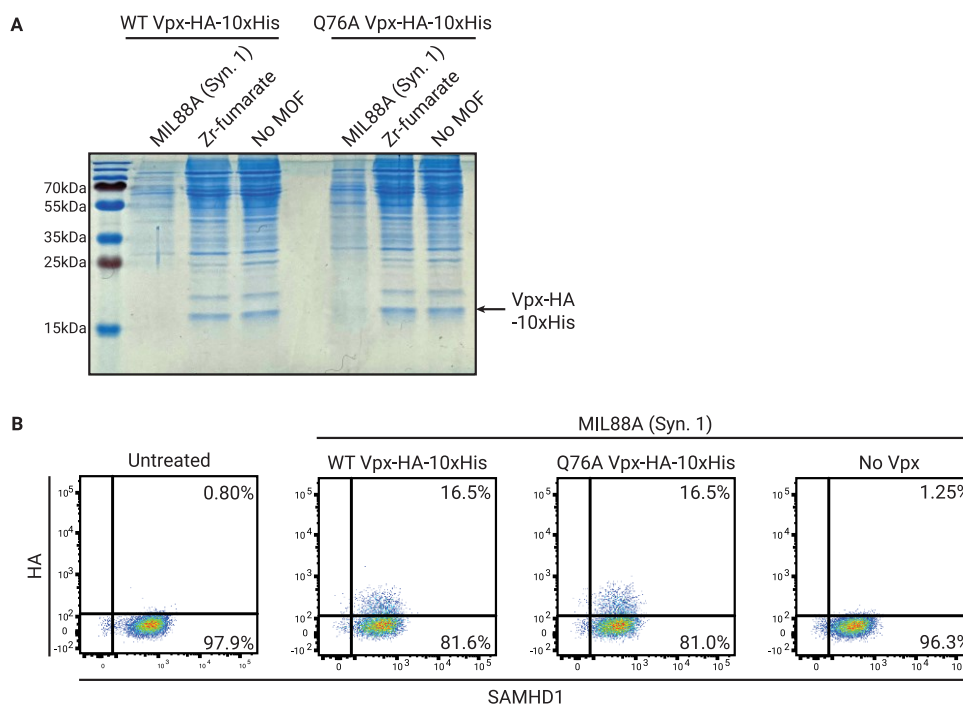


Figure 23: Vpx-HA-10xHis bound to MIL88A nanoMOF were taken up by THP-1 cells but did not induce SAMHD1 degradation.

Purified Vpx-HA-10xHis proteins were incubated with the indicated nanoMOFs for self-assembly. **A** Unbound WT and Q76A Vpx-HA-10xHis proteins after incubation with nanoMOFs were loaded onto SDS-polyacrylamide gels and stained with InstantBlue Coomassie stain. Vpx proteins without nanoMOF co-incubation was included as control (No MOF). **B** THP-1 cells were incubated with 25  $\mu$ g of either WT or Q76A Vpx-MIL88A for 24 hrs. Cells were then stained for HA and SAMHD1 for flow cytometry analysis. MIL88A without Vpx protein was included as control.

A common problem with nanoMOF-based delivery systems is the entrapment of the cargo in endosomal vesicles, as mentioned in subsection 1.4.1.2. In addition, several studies have shown that Vpx induces SAMHD1 degradation in the nucleus, as discussed in subsection 1.3.3. Thus, Vpx needs to be released from the nanoMOF, escape the endosomal vesicles, and translocate to the nucleus. To check whether Vpx reached the nucleus after nanoMOF treatment, THP-1 cells which were incubated with Vpx-bound nanoMOFs were subjected to intracellular HA and nucleus staining, and analyzed by immunofluorescence microscopy (Figure 24). Based on the microscopy images, Vpx did not localize to the nucleus, but rather aggregated in the cell cytoplasm. This so-called “punctate” pattern of aggregation seemed to be similar to previous reports, where authors described a lack of endosomal escape<sup>293,294</sup>. Therefore, the staining pattern of HA observed in Figure 24 suggested that the Vpx was trapped in endosomes.



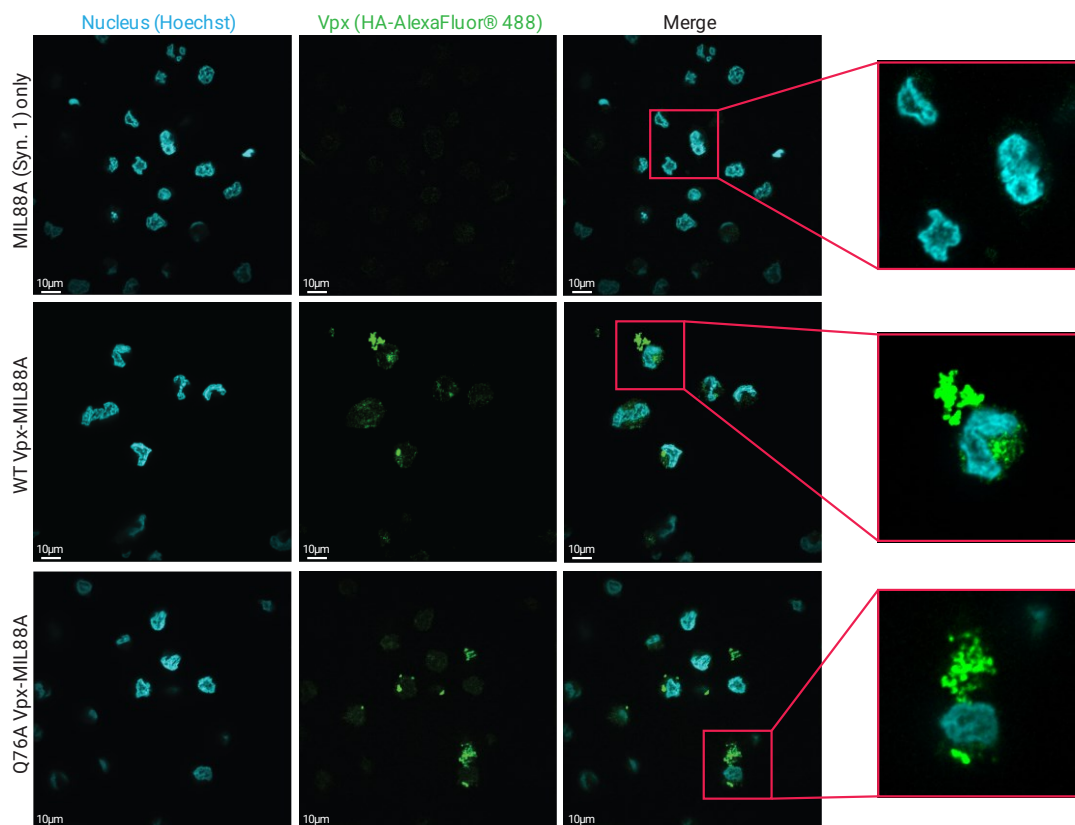


Figure 24: Endosomal entrapment of Vpx in THP-1 cells after uptake of Vpx-bound MIL88A nanoMOF. THP-1 cells which have taken up Vpx-bound MIL88A were subjected to intracellular staining of HA (AlexaFluor® 488; green) and nucleus (Hoechst; blue) for microscopy imaging. Cells treated with nanoMOFs without Vpx was used as control.

To improve endosomal escape of Vpx after nanoMOF treatment, small molecule drugs chloroquine and loperamide were added to THP-1 cells. This strategy is based on work done by Du Rietz *et al.* where they reported increased endosomal escape of cholesterol-conjugated siRNA upon treatment with either chloroquine or loperamide in HeLa and MCF7 cell lines<sup>295</sup>. Unfortunately, neither of the drugs induced SAMHD1 degradation after Vpx-nanoMOF treatment (Figure 25). Several other strategies have been explored by other studies to improve endosomal escape, as described in subsection 1.4.1.2. However, due to time and resource limitations, they were not further pursued in this work.

In summary, although the MIL88A nanoMOFs were able to efficiently bind Vpx and were taken up by THP-1 cells, due to their lack of SAMHD1 degradation functionality possibly caused by endosomal entrapment, the Vpx-nanoMOF-based delivery strategy was not further pursued.

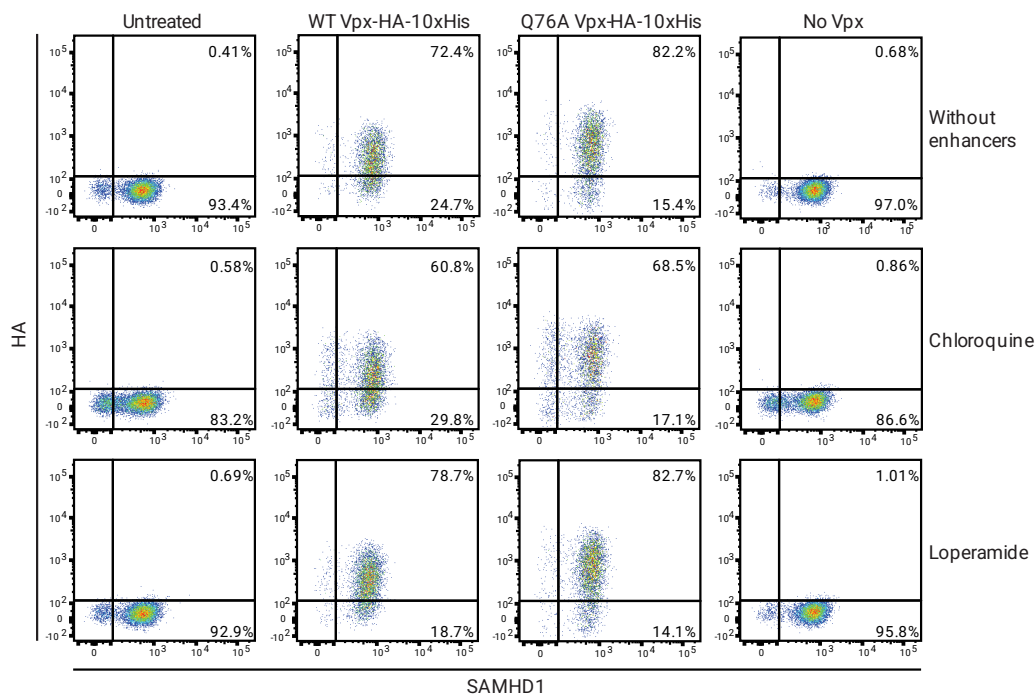


Figure 25: Endosomal escape enhancer treatment of Vpx-MIL88A-treated THP-1 cells did not improve functionality. THP-1 cells were first incubated with WT or Q76A Vpx-HA-10xHis-bound MIL88A for 6 hrs before treatment with either 100  $\mu$ M chloroquine or 20  $\mu$ M loperamide for a further 18 hrs. The cells were then stained for HA and SAMHD1 and analyzed by flow cytometry. Vpx-MIL88A-treated cells without enhancer treatment were used as controls

### 3.4 Production, purification, and functionality of Vpx-CPPs

The next Vpx delivery system to be investigated were CPPs. Vpx-CPPs were either commercially synthesized (subsection 3.4.1) or purified in-house (subsection 3.4.2).

#### 3.4.1 Commercially synthesized CPPs bound to truncated 67aa Vpx were functional

Two CPPs were investigated in this work: TAT and CPP44, as introduced in subsection 1.4.2.2. TAT was chosen due to its popularity as a CPP, whereas CPP44 was chosen due to its leukemic cell-specific uptake properties<sup>241</sup>. The sequence and amino acid properties of each CPP is shown in Figure 26A. Due to the size restrictions of commercial peptide synthesis, the Vpx sequence had to be shortened to 67 amino acids (67aa Vpx). This shortened sequence retained the 3 helices of WT Vpx, the zinc-binding sites and the 2 most essential amino acids involved in inducing SAMHD1 degradation (W24 and Q76). The shortened Vpx, however, did not contain the poly-proline tail. The CPPs also included a HA tag between the CPP and 67aa Vpx for detection (Figure 26A). The initial synthesis of the CPPs was done by Eurogentec with high purity. The obtained CPPs were then re-constituted in PBS containing acetic acid to a final CPP concentration of 1 mg/mL. Despite the shortened Vpx, the CPPs were still taken up by THP-1 cells and induced SAMHD1 degradation in a dose-dependent manner (Figure 26B). CPP44-HA-67aa Vpx performed better than TAT-HA-67aa Vpx, indicated by a greater reduction in SAMHD1 signal upon CPP44-HA-67aa Vpx treatment at 25  $\mu$ M concentration (Figure

26B). These results provided evidence for SAMHD1-degradation capacity of the 67aa Vpx delivered by TAT and CPP44.

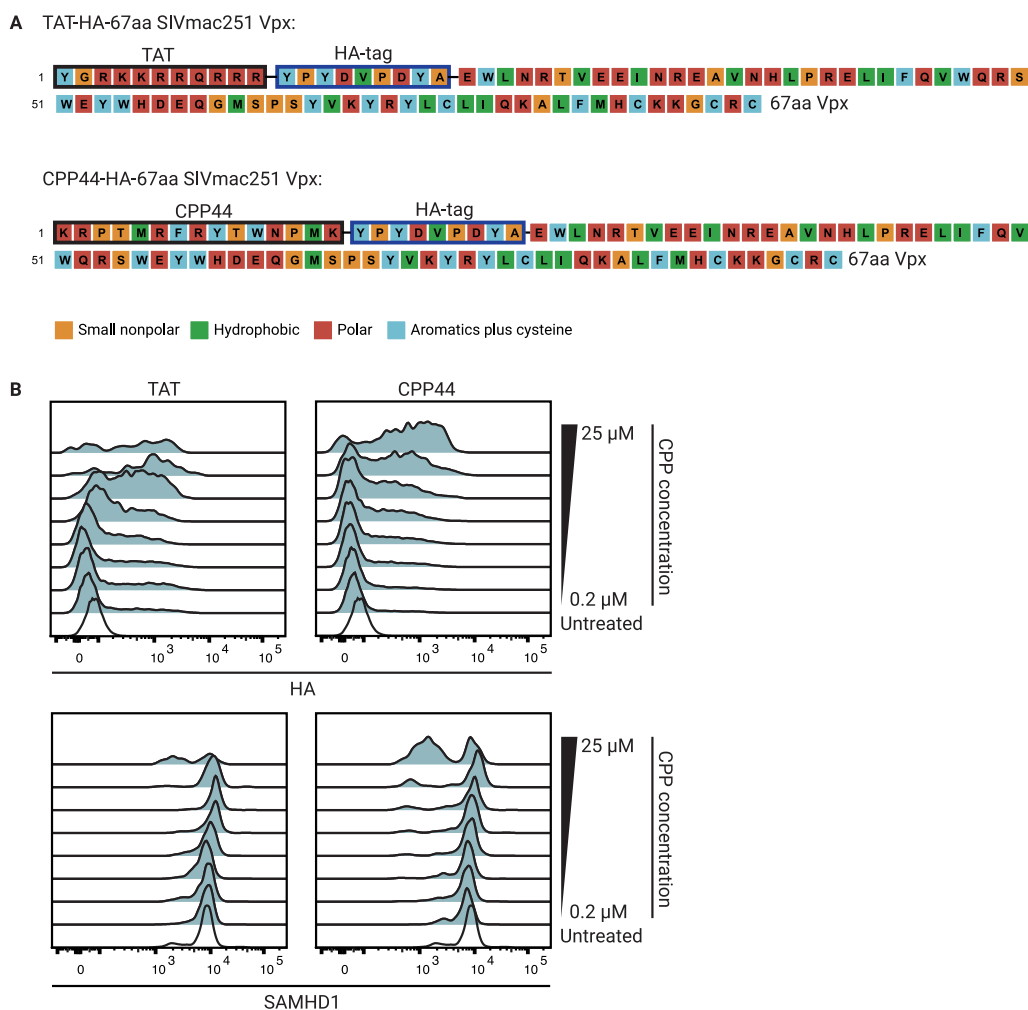


Figure 26: CPP-HA-67aa Vpx synthesized from Eurogentec were taken up and induced SAMHD1 degradation in THP-1 cells.

THP-1 cells were treated with CPP-HA-67aa Vpx synthesized from Eurogentec. **A** Schematic representation of the TAT- and CPP44-HA-67aa Vpx constructs, including their amino acid properties. **B** Uptake and SAMHD1 degradation in THP-1 cells treated with varying concentrations between 0.2  $\mu$ M and 25  $\mu$ M of TAT- and CPP44-HA-67aa Vpx synthesized by Eurogentec for 24 hrs. Cells were stained for HA and SAMHD1 and analyzed via flow cytometry. Histograms of CPP uptake, indicated by HA (top), and SAMHD1 degradation (bottom) is shown, including untreated cells as control.

However, since the amount of peptide received from Eurogentec was limited and a high concentration of CPP was required to degrade SAMHD1 (25  $\mu$ M), a different company (Davids Biotechnologie GmbH) was selected to synthesize the CPPs at a lower cost and slightly lower purity. These CPPs, however, were not soluble in PBS with acetic acid which was used to dissolve the CPPs from Eurogentec. Therefore, they had to be dissolved in DMSO instead. These new CPP-HA-67aa Vpx were also taken up by THP-1 cells and induced SAMHD1 degradation, albeit to a lesser extent than those by Eurogentec, at 25  $\mu$ M CPP concentration (Figure 27A). One possible explanation for this might be the precipitation of the CPPs in medium, observed by the large amounts of debris represented in

the side scatter (SSC) vs forward scatter (FSC) plot (Figure 27B). A low FSC value and large SSC value indicated small, granulated fragments, as indicated in Figure 27B. This precipitation might have reduced the effective concentration of the CPPs in the reaction.

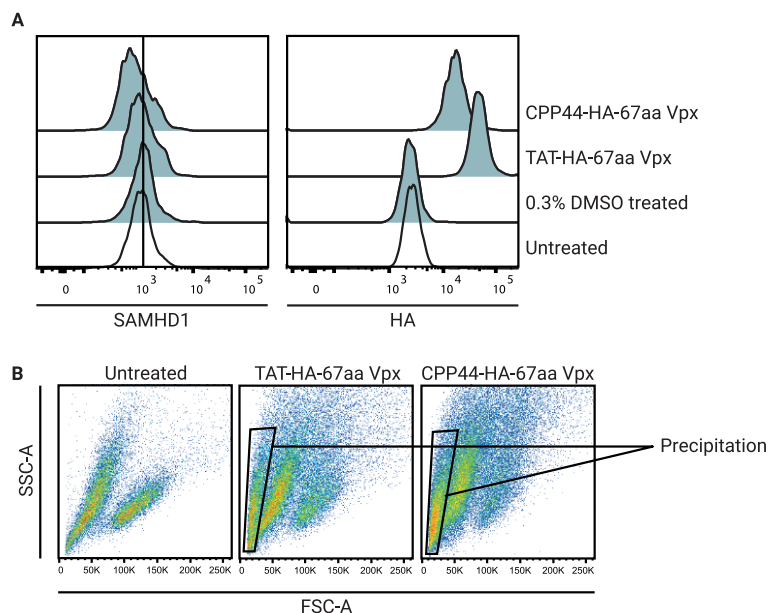


Figure 27: CPP-HA-67aa Vpx synthesized from Davids Biotechnologie were taken up and induced SAMHD1 degradation in THP-1 cells but precipitated in medium.

THP-1 cells were treated with 25  $\mu$ M of CPP-HA-67aa synthesized from Davids Biotechnologie. **A** Cells were stained for HA and SAMHD1 and analyzed via flow cytometry. Histograms of CPP uptake, indicated by HA, and SAMHD1 degradation are shown, including untreated cells as control. **B** Precipitation of the CPPs as indicated by the highly granular and small size of the particles seen in the SSC vs FSC plot, derived from the experiment performed in **A**. The observation of precipitation of the CPPs is indicated.

Despite these issues, we investigated the ability of 67aa Vpx delivered by these CPPs to increase ara-C sensitivity in THP-1 cells, as well as the SAMHD1-low HEL cells (Figure 28A and B). In line with its ability to better induce SAMHD1 degradation compared to TAT-HA-67aa Vpx, CPP44-HA-67aa Vpx also increased the sensitivity of THP-1 cells to ara-C by 4.9-fold compared to 3.2-fold by TAT-HA-67aa Vpx (Figure 28C). As expected, CPP-HA-67aa Vpx treatment of HEL cells did not change the ara-C sensitivity, confirming the SAMHD1-specific activity of the CPP-HA-67aa Vpx treatment (Figure 28B). Although the 67aa Vpx-bound CPPs were able to increase ara-C sensitivity of THP-1 cells, we hypothesized that the improvement of ara-C sensitivity can be further enhanced by using full-length WT Vpx. Since the WT Vpx-bound CPPs could not be commercially synthesized due to their size, they were purified in-house.

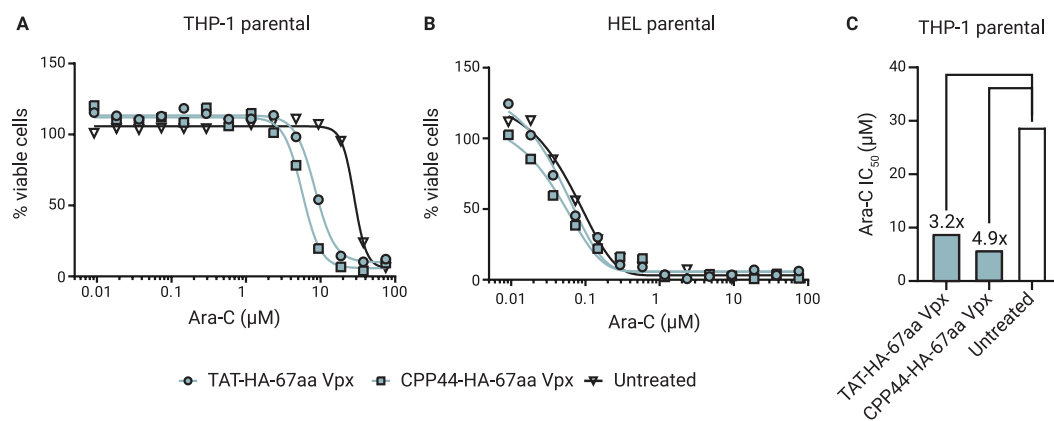


Figure 28: CPP-HA-67aa Vpx synthesized from Davids Biotechnologie improved ara-C sensitivity in THP-1 cells. THP-1 (A) and HEL (B) cells were treated with 25 μM of each CPP-HA-67aa Vpx or untreated for 24 hrs, followed by treatment with varying concentrations of ara-C for 96 hrs. Viability of cells after ara-C treatment was obtained by measuring the reduction of resazurin. Dose-response curves of both THP-1 and HEL cells are shown. C The IC<sub>50</sub> values of the co-treated and untreated cells were calculated using GraphPad Prism. Fold change in IC<sub>50</sub> of CPP-co-treated cells relative to cells without CPP treatment (untreated) is indicated for THP-1 cells.

### 3.4.2 CPP44-HA-WT Vpx constructs purified from HEK293T cells were not functional

Since CPP44-HA-67aa Vpx showed superior functionality compared to TAT-HA-67aa Vpx, only CPP44-HA-WT Vpx was considered for further investigations. Since the purification of recombinant Vpx from HEK293T cells has already been attempted (see section 3.1), similar tags (i.e., 3xFLAG and 10xHis) were used for the purification of CPP44-HA-WT Vpx. In the case of 3xFLAG-CPP44-ha-WT Vpx, the 3xFLAG tag needed to be cleaved off using enterokinase to expose the CPP44 peptide for cell penetration (Figure 29A). The HA tag between the CPP and Vpx remained intact, as shown in Figure 26A. Comparing the band intensities of uncleaved and cleaved CPP44-HA-WT Vpx, based on the FLAG and HA immunoblots, only partial cleavage of the protein was observed (Figure 29A). Nevertheless, varying amounts of the purified and cleaved proteins were added to THP-1 cells to determine the ability of purified CPP44-HA-WT Vpx to induce SAMHD1 degradation (Figure 29B). However, no degradation was observed.

We reasoned that the lack of SAMHD1 degradation was caused by low protein amounts, due to low yields from 3xFLAG purification of recombinant Vpx (Figure 13), and low cleavage efficiencies. Since the WT Vpx-HA-10xHis purification was more successful, we purified CPP44-HA-WT Vpx-10xHis from HEK293T cells (Figure 29C). No tag cleavage was necessary as the 10xHis-tag was at the C-terminus and the CPP was located at the N-terminus. However, this construct was also unable to induce SAMHD1 degradation in THP-1 cells (Figure 29D).

In summary, commercially synthesized CPP-HA-67aa Vpx were able to best degrade SAMHD1 and improve ara-C sensitivity in THP-1 cells at 25 μM concentration, compared to purified CPP44-HA-WT Vpx. Despite the difficulties faced with the CPP precipitation, considering the ability of high quality CPPs synthesized from Eurogentec and the ability of the precipitated CPPs from Davids Biotechnologie to improve ara-C sensitivity up to 4.9-fold, a CPP-based Vpx delivery system shows promise, and should be further investigated in the future.

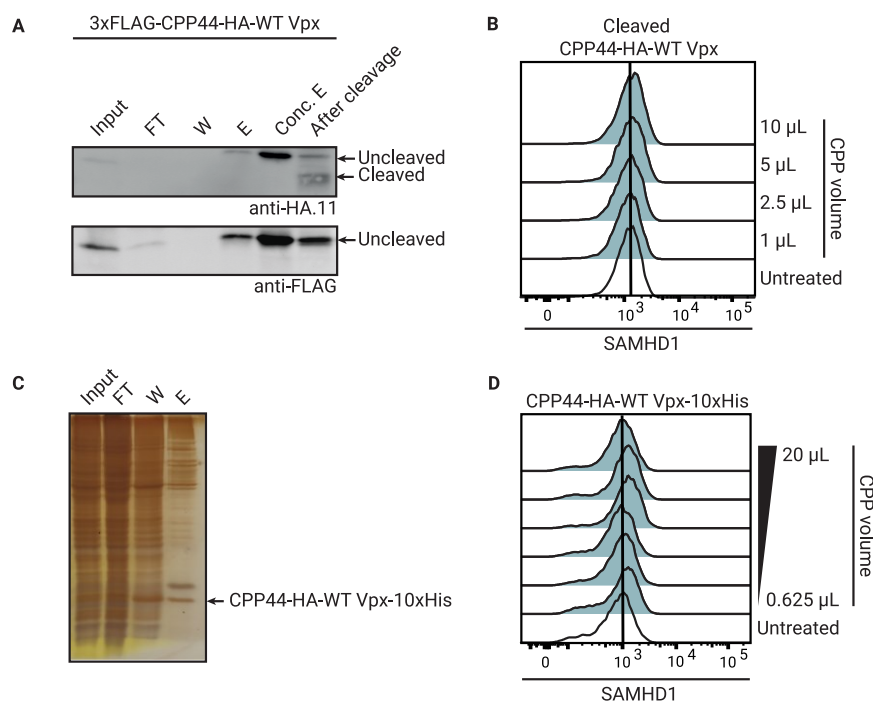


Figure 29: CPP44-HA-WT Vpx could be purified from HEK293T cells but were not functional.

CPP44-HA-WT Vpx proteins were purified from HEK293T cells and evaluated for SAMHD1 degradation functionality in THP-1 cells. **A** Aliquots from various purification steps of 3xFLAG-CPP44-HA-WT Vpx proteins were loaded on an SDS-polyacrylamide gel and immunoblotted against HA and FLAG. Both uncleaved and cleaved CPP44-HA-WT Vpx were detected in the HA immunoblot but only uncleaved 3xFLAG-CPP44-HA-WT Vpx was visualized in the FLAG immunoblot. Conc. E indicates eluted protein after concentration via Amicon ultracentrifugation filters. **B** THP-1 cells were treated with various amounts of purified and cleaved CPP44-HA-WT Vpx for 24 hrs before being stained for SAMHD1 and analyzed via flow cytometry. Histogram of SAMHD1 intensity is shown, with untreated cells as control. **C** CPP44-HA-WT Vpx-10xHis was purified from HEK293T cells. Aliquots from various purification steps were loaded on an SDS-polyacrylamide gel and stained via silver staining. FT: flow-through, W: wash, E: elution. **D** Same as in **B**, but with purified CPP44-HA-WT Vpx-10xHis.

### 3.5 Production, optimization, and functionality of new generation Vpx-VLPs<sub>5</sub>

The final Vpx delivery system investigated in this work was the VLPs. Vpx-VLPs have already been successfully used to induce SAMHD1 degradation and improve ara-C sensitivity in AML cells<sup>145</sup>. However, those VLPs, henceforth referred to as the 1<sup>st</sup> generation VLPs, contained all regulatory and accessory proteins which interact with various other proteins in the cells (described in section 1.3). Therefore, a new generation of VLPs were produced in this work, which only contained Vpx and the necessary structural proteins. This prevents any unwanted side effects caused by the remaining regulatory and accessory proteins.

<sub>5</sub> Some of the results presented in this subsection have been adapted and submitted as an unpublished manuscript, and are indicated in the figure legends, where applicable. Work done by co-authors is indicated in footnotes and figure legends.

### 3.5.1 Characterization of new generation Vpx-VLPs

For the production of the VLPs, the pSIV3+ plasmid was used as a basis, as described by Mangeot *et al.*<sup>296</sup>. This 1<sup>st</sup> generation plasmid encodes all the structural elements of SIVmac251 virus (*gag* and *pol*), all regulatory and accessory proteins, and a polyA tail, under the control of a CMV promoter. Figure 30A shows the various pSIV3+ plasmids used to produce both 1<sup>st</sup> and new generation VLPs. The 1<sup>st</sup> generation pSIV3+ SIVmac251 X+/ R+ plasmids encode either Vpx (X+) or Vpr (R+). For the new generation VLPs, first all the accessory proteins were removed, and unique restriction sites BspI and XhoI were inserted, keeping the Rev responsive element (RRE) intact (pSIV3+ delta). Second, 3xFLAG-tagged Vpx or Vpr from different species were inserted between the *pol* gene and the RRE at the restriction sites (pSIV3+ 3xFLAG-Vpx/Vpr)<sup>6</sup>, since several Vpx and Vpr proteins can induce SAMHD1 degradation (see section 1.3). These Vpx and Vpr proteins originated from SIVmac239 Vpx, HIV-2 7312a Vpx, HIV-2 Rod9 Vpx, SIVdeb Vpr, SIVmus Vpr, and SIVmnd-2 Vpx. Since SIVmnd-2 Vpx is unable to degrade human SAMHD1<sup>161</sup>, it was used as a control in further experiments. Indeed, we confirmed, using pcDNA plasmids encoding the various Vpx and Vpr proteins, that all Vpx and Vpr proteins except for SIVmnd-2 Vpx degraded SAMHD1 in primary resting CD4+ T cells (Figure 30B)<sup>7</sup>. Once the new generation pSIV3+ constructs were generated, they were characterized for their expression. All Vpx and Vpr constructs were expressed in HEK293T cells at varying levels (Figure 30C). Hence, VSV-G pseudotyped new generation VLPs were produced in HEK293T cells and compared to the 1<sup>st</sup> generation VLPs, in terms of yield and SAMHD1 degradation capacity. The VSV-G envelope protein, due to its broad cell tropism, was used to allow for the binding and uptake of the VLPs by various cell types.

The amount of VLP produced was determined by SG-PERT, which measures the RT activity in VLPs (described in subsection 2.5.4). As shown in Figure 31A, the yield of the new generation VLPs was significantly lower than that of the 1<sup>st</sup> generation VLPs. This low yield of the new generation VLPs was in line with the SIV capsid protein p27 levels detected with immunoblotting (Figure 31B). Consequently, the SAMHD1 degradation capacity of the new generation VLPs was also inferior compared to the 1<sup>st</sup> generation VLPs, even at higher VLP volumes (Figure 31C). This prompted the investigation into improving the yield of the new generation VLPs.

---

<sup>6</sup> The pcDNA 3xFLAG Vpx/ Vpr constructs and the new generation pSIV3+ constructs were generated by Lena Stegmann, Helena Lejk, and Hanna-Mari Baldauf.

<sup>7</sup> Experiment was performed by Hanna-Mari Baldauf at the Ruprecht-Karls University in Heidelberg, Germany.

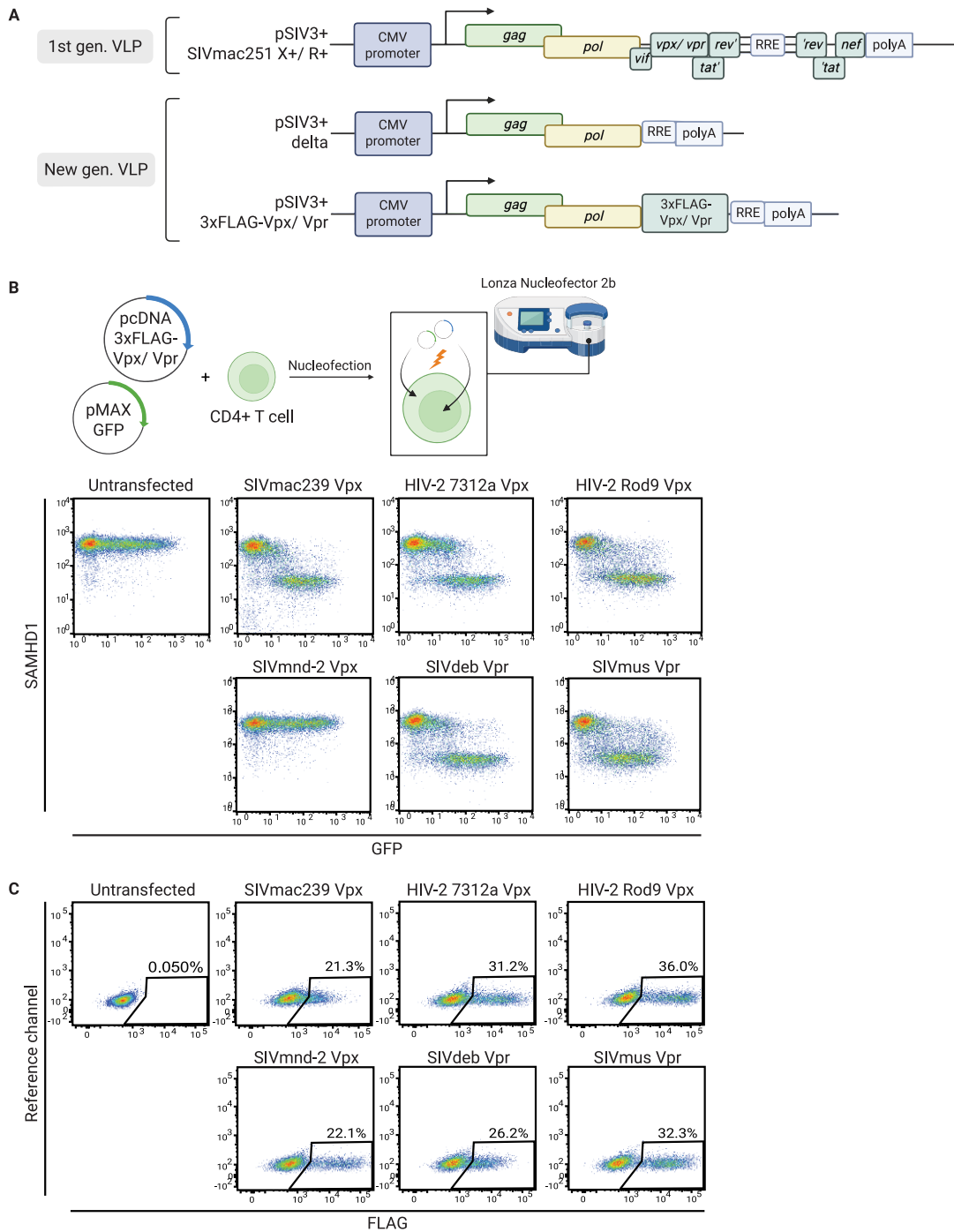


Figure 30: New generation pSIV3+ 3xFLAG-Vpx/Vpr constructs were generated and expressed in HEK293T cells. Plasmids encoding 1<sup>st</sup> and new generation Vpx/Vpr-VLPs were generated and characterized. **A** Schematic representation of the pSIV3+ constructs used to produce both 1<sup>st</sup> generation and new generation VLPs. **B** Primary resting CD4+ T cells were co-nucleofected with pcDNA constructs encoding the various 3xFLAG-Vpx/Vpr constructs and pMAX GFP to identify nucleofected cells. 24 hrs after nucleofection, cells were stained for SAMHD1 and analyzed via flow cytometry. Reduced SAMHD1 levels in GFP positive cells indicate functionality of the various 3xFLAG-Vpx/Vpr constructs. Experiment was performed by Hanna-Mari Baldauf. (Continued on next page)



C HEK293T cells were transfected with the new generation pSIV3+ constructs encoding 3xFLAG-Vpx/Vpr from various species. After 48 hrs, cells were stained for FLAG and analyzed via flow cytometry. The percentage of FLAG-positive cells are indicated. (Parts of this figure are also used in Nair *et al.*, unpublished manuscript)

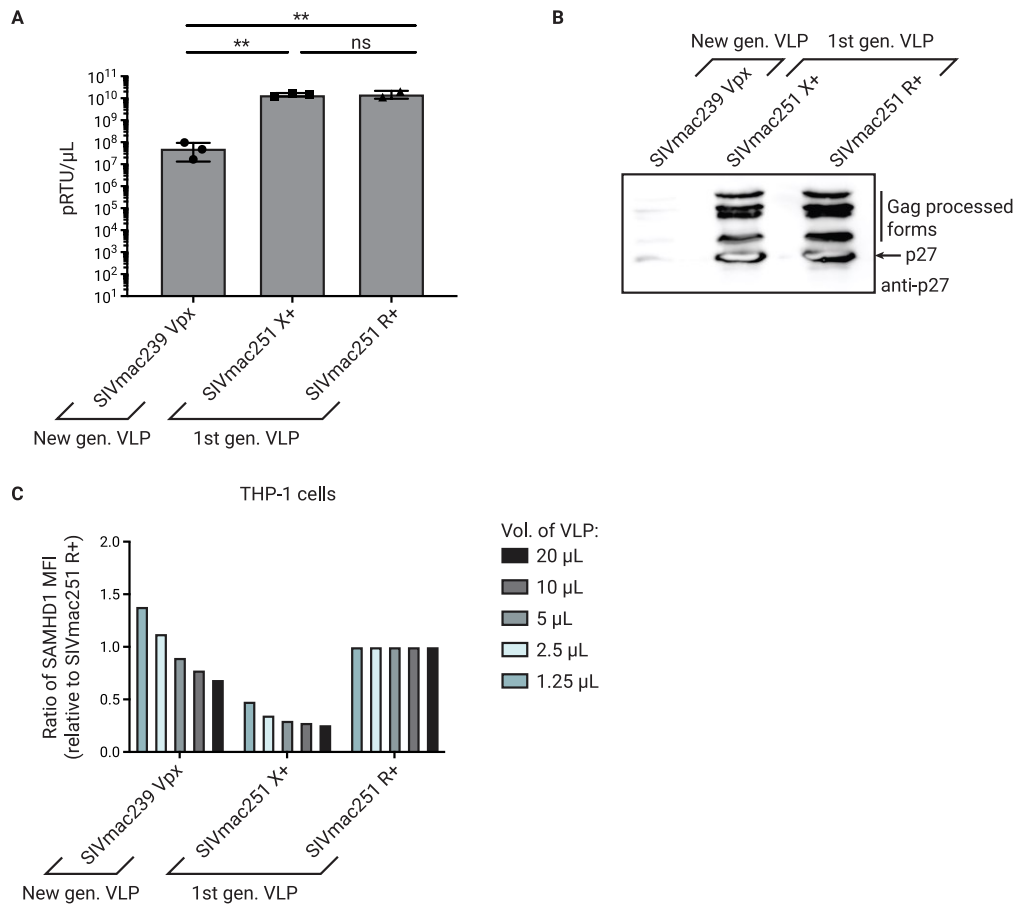


Figure 31: Low yield and functionality of new generation SIVmac239 Vpx-VLP.

VSV-G pseudotyped new and 1<sup>st</sup> generation VLPs were produced in HEK293T cells and harvested via sucrose cushion.

**A** RT activity obtained via SG-PERT assay of new generation SIVmac239 Vpx-VLP and 1<sup>st</sup> generation VLPs. SIVmac251 X+ and R+ refers to VLPs that contained Vpx or Vpr, respectively. Error bars represent the standard error of mean (s.e.m.) from two-three independent biological replicates. One-way ANOVA was used for statistical analyses: \*\*:  $p < 0.01$ , ns:  $p > 0.05$ . **B** Boiled and denatured VLPs were loaded on an SDS-polyacrylamide gel and immunoblotted against p27 SIV capsid protein. The position of p27 on the membrane is indicated. Larger proteins were the various processed forms of the Gag polyprotein. **C** THP-1 cells were titrated with varying amounts of new generation and 1<sup>st</sup> generation VLPs. 24 hrs later, the cells were stained for SAMHD1 and analyzed via flow cytometry. The ratio of the mean fluorescence intensity (MFI) of SAMHD1 relative to the 1<sup>st</sup> generation VLP SIVmac251 R+, which served as negative control, is shown. (Parts of this figure are also used in Nair *et al.*, unpublished manuscript)

### 3.5.2 Improvement of yield and functionality of new generation VLPs produced with HIV-1 Rev protein

Rev is a regulatory protein found in lentiviruses that is involved in the nuclear export of viral RNA<sup>297</sup>. Rev binds to the RRE found in viral RNA and facilitates its export from the nucleus and subsequent translation<sup>298</sup>. Perhaps removal of the Rev protein from the new generation pSIV3+ constructs led

to the reduction in yield caused by insufficient export of viral mRNA from the nucleus. In order to test this, pCMV plasmids encoding HIV-1 Rev protein was co-transfected *in trans* with the pSIV3+ SIVmac239 Vpx plasmids and the VSV-G envelope protein-encoding plasmids into HEK293T cells in different ratios. Based on the RT activity shown in Figure 32A, just a small amount of HIV-1 Rev plasmid was sufficient to enhance the new generation VLP yield by up to 790-fold. This increase coincided with the SIV p27 capsid immunoblot shown in Figure 32B. This increase in yield was also observed for all the new generation Vpx/Vpr-VLPs investigated in this work (Figure 32C). Interestingly, when the new generation VLPs containing the various 3xFLAG-Vpx/Vpr was immunoblotted against FLAG, a large variation in loading between the Vpx and Vpr proteins could be noticed (Figure 32D). SIVdeb and SIVmus Vpr were poorly loaded into the VLPs compared to the remaining Vpx proteins (Figure 32D). In addition, they were unable to induce SAMHD1 degradation after THP-1 transduction (Supplementary Figure 5), despite showing functionality in primary resting CD4+ T cells (Figure 30C). This observation led to the exclusion of these VLPs from further experiments.

The new generation SIVmac239 Vpx-VLPs produced with Rev also reduced SAMHD1 levels in THP-1 cells to a similar extent as the 1<sup>st</sup> generation SIVmac251 X+ VLP, when 15  $\mu$ L of VLPs were used (Figure 32E). HIV-2 7312a Vpx-VLPs were also able to induce SAMHD1 degradation (1.25-fold reduction of SAMHD1), but to a lower extent than SIVmac239 Vpx-VLPs (2-fold reduction of SAMHD1) (Figure 32E). SIVmnd-2 and HIV-2 Rod9 Vpx-VLPs were unable to induce SAMHD1 degradation (Figure 32E). While this observation was expected for SIVmnd-2 Vpx-VLPs, the observation in HIV-2 Rod9 Vpx-VLP was surprising, since large amounts of HIV-2 Rod9 Vpx were loaded into the VLPs (Figure 32D) and SAMHD1 was degraded in primary resting CD4+ T cells (Figure 30B).

Based on these experiments, we showed that the new generation Vpx-VLPs could be successfully produced in high yields and that the new generation SIVmac239 Vpx-VLPs were able to best induce SAMHD1 degradation. In the next steps, the ability of the new generation VLPs to improve ara-C sensitivity was investigated. All new generation VLPs used in experiments performed henceforth were produced with HIV-1 Rev protein.

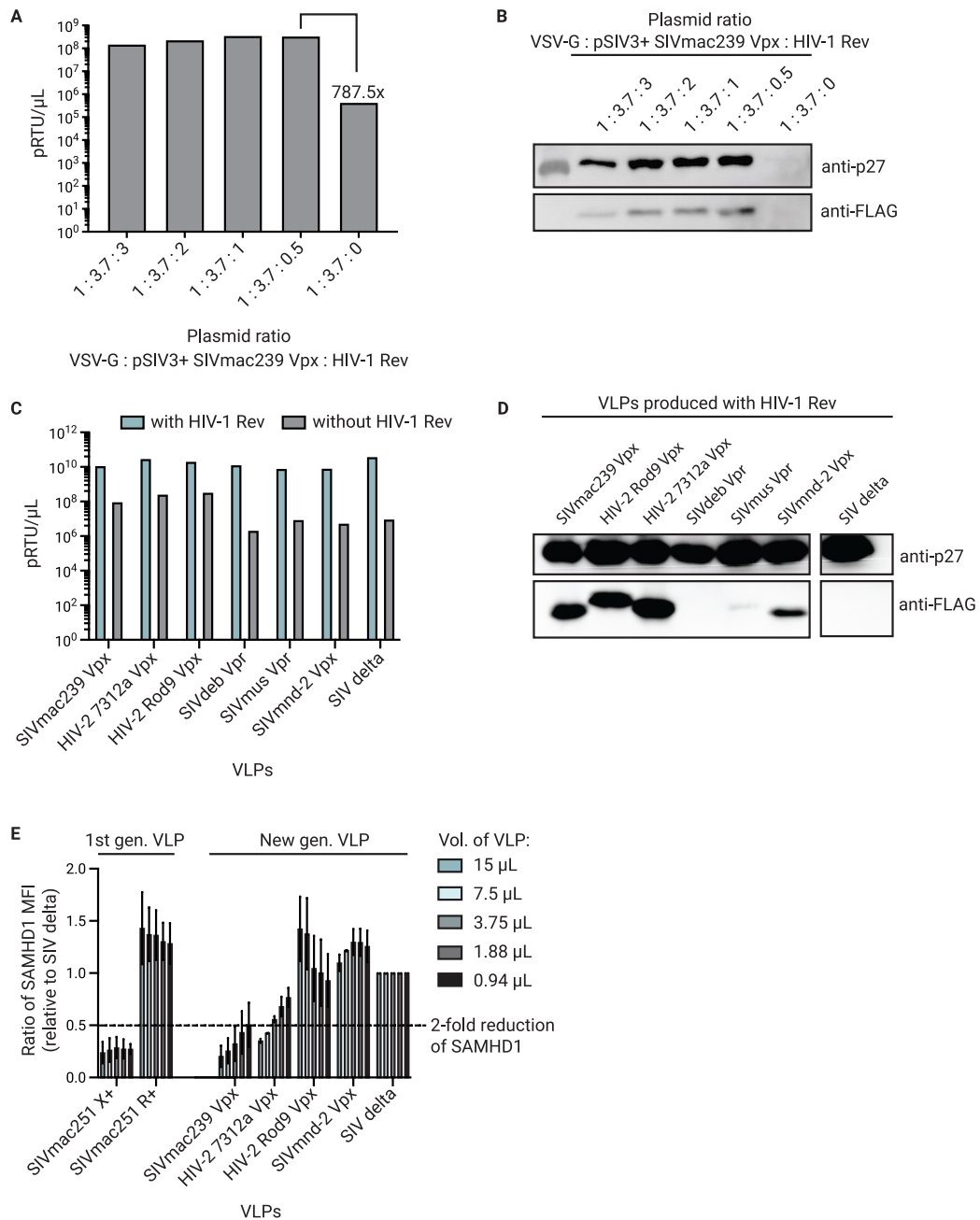


Figure 32: Improvement of yield and functionality of new generation VLPs after using HIV-1 Rev protein.

VSV-G pseudotyped new generation VLPs were produced in HEK293T cells with varying levels of HIV-1 Rev. **A** RT activity obtained via SG-PERT assay of new generation SIVmac239 Vpx-VLP with varying levels of HIV-1 Rev plasmid included during co-transfection of HEK293T cells. Ratio of VSV-G plasmid to pSIV3+ SIVmac239 Vpx plasmid to pCMV HIV-1 Rev plasmid is indicated. **B** VLPs produced from **A** were loaded onto SDS-polyacrylamide gels and immunoblotted against SIV p27 capsid and FLAG. **C** RT activity obtained via SG-PERT assay of the various new generation 3xFLAG-Vpx/Vpr-containing VLPs produced with and without HIV-1 Rev. **D** 3xFLAG-Vpx/Vpr-VLPs generated with HIV-1 Rev were loaded onto an SDS-polyacrylamide gel and immunoblotted against SIV p27 capsid and FLAG. **E** THP-1 cells were titrated with varying amounts of new generation and 1<sup>st</sup> generation VLPs. 24 hrs later, the cells were stained for SAMHD1 and analyzed via flow cytometry. The ratio of mean fluorescence intensity (MFI) of SAMHD1 relative to the new generation SIV delta-VLP, which served as negative control, is shown. Error bars represent the standard deviation (s.d) from two biological replicates. (Parts of this figure are also used in Nair *et al.*, unpublished manuscript)

### 3.6 Ara-C co-treatment of AML cell lines and primary cells with Vpx-VLPs<sub>8</sub>

Thus far, the functionality tests of the delivery systems were performed on THP-1 and HEL cells, which were used as representatives of SAMHD1-high and SAMHD1-low expressing cells, respectively. In order to further confirm the benefits of co-treatment of Vpx-VLPs with ara-C in cells expressing SAMHD1, a range of cell lines with high to low SAMHD1 levels were used. In addition, SAMHD1 knocked-out THP-1 cells (THP-1 SAMHD1<sup>-/-</sup>)<sup>145</sup> and HEL cells overexpressing WT SAMHD1 (HEL WT SAMHD1) were used. The SAMHD1 protein levels in the various cell lines investigated are shown in Figure 33A. As observed, OCI-AML2, OCI-AML3, MonoMac6, and THP-1 SAMHD1<sup>+/+</sup> expressed high levels of SAMHD1, whereas HL60, HEL parental and THP-1 SAMHD1<sup>-/-</sup> expressed low levels of, or in the case of HL60, no SAMHD1 (Figure 33A).

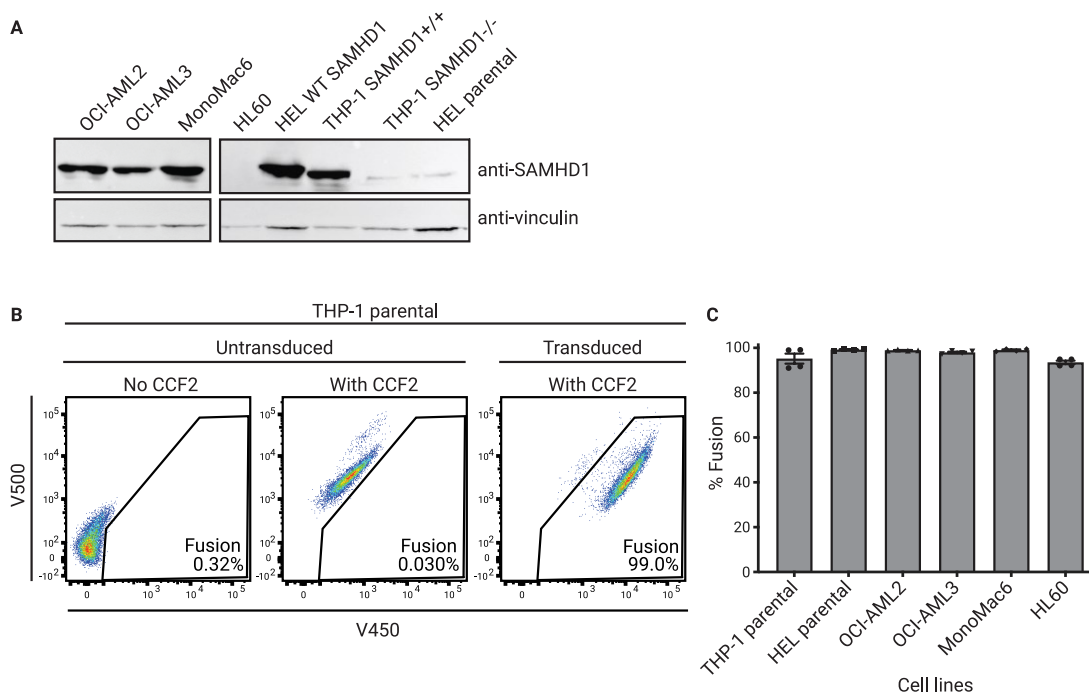


Figure 33: SAMHD1 expression and VSV-G susceptibility of AML cell lines.

Different AML cell lines were lysed and SAMHD1 levels were analyzed. **A** Immunoblot against SAMHD1 and vinculin of AML cell line lysates. Vinculin was used as loading control. THP-1 SAMHD1<sup>+/+</sup> represents THP-1 cells that were used as controls during the production of THP-1 SAMHD1<sup>-/-</sup> cells<sup>145</sup>. **B** Representative blot of VSV-G fusion assay performed in THP-1 cells transduced with VSV-G pseudotyped BlaM-Vpr-VLPs. CCF2 substrate cleavage by the BlaM-Vpr after VLP fusion is shown by the shift of fluorescence intensity in the V450 channel. **C** Percentage virion fusion of VSV-G pseudotyped BlaM-Vpr-VLP, as represented in **B**, of all cell lines tested. Error bars represent the standard deviation (s.d.) from two biological replicates with two technical replicates each. (Parts of this figure are also used in Nair *et al.*, unpublished manuscript)

<sup>8</sup> Some of the results presented in this subsection have been adapted and submitted as an unpublished manuscript, and are indicated in the figure legends, where applicable. Work done by co-authors is indicated in footnotes and figure legends.

To ensure that possible differences in VLP functionality between the cell lines were not caused by differential uptake of the VLPs via VSV-G, a virion fusion assay was performed using VSV-G pseudotyped BlaM-Vpr-VLPs<sup>281</sup>. The experimental set-up and description of the assay can be found in subsection 2.5.5. Figure 33B shows a representative result of such a virion fusion assay in THP-1 cells with 99% fusion. This means that BlaM-Vpr-VLPs were taken up by 99% of THP-1 cells. This high fusion rate was also noticed in all other cell lines tested, as shown in Figure 33C, thereby excluding differences in VSV-G fusion as a factor influencing Vpx-VLP functionality.

Next, the ability of the various Vpx-VLPs to improve ara-C sensitivity in the AML cell lines were investigated. Due to the limited amount of VLPs and volume restrictions of the assay, 2  $\mu$ L of VLPs were used for the co-treatment assays. As shown in Figure 34A, the co-treatment of all SAMHD1-high expressing cell lines with the new generation SIVmac239 Vpx-VLPs resulted in improved ara-C sensitivity, albeit to varying degrees. Co-treatment with the new generation HIV-2 7312a Vpx-VLPs also improved ara-C sensitivity, however to a lower extent than the SIVmac239 Vpx-VLPs. The ara-C sensitivity of THP-1 SAMHD1+/+ and MonoMac6 cell lines were the most improved after SIVmac239 Vpx-VLP treatment, resulting in a 20-fold reduction of IC<sub>50</sub>. VLP treatment in SAMHD1-low cell lines did not show significant differences in ara-C sensitivity (Figure 34A). In any case, the 1<sup>st</sup> generation SIVmac251 X+ VLPs performed better than the new generation SIVmac239 Vpx-VLP, especially in MonoMac6 and HEL WT SAMHD1 cells, where over 50-fold reduction of IC<sub>50</sub> was observed. This was in line with the SAMHD1 protein levels 24 hrs after the VLP treatment of THP-1 SAMHD1+/+ cells. SAMHD1 protein levels were reduced to a larger extent (25-fold) by the 1<sup>st</sup> generation SIVmac251 X+ VLPs compared to the new generation SIVmac239 Vpx-VLPs (2-fold), and to an even larger extent compared to HIV-2 7312a Vpx-VLPs (Figure 34B and C).

Based on the observations from the THP-1 titration (Figure 32E) and the ara-C co-treatment assays (Figure 34A), the 1<sup>st</sup> generation SIVmac251 X+ VLPs were still superior to the new generation SIVmac239 Vpx-VLPs, which was the best performing new generation VLP. Investigations into the difference between the two VLPs were performed next.

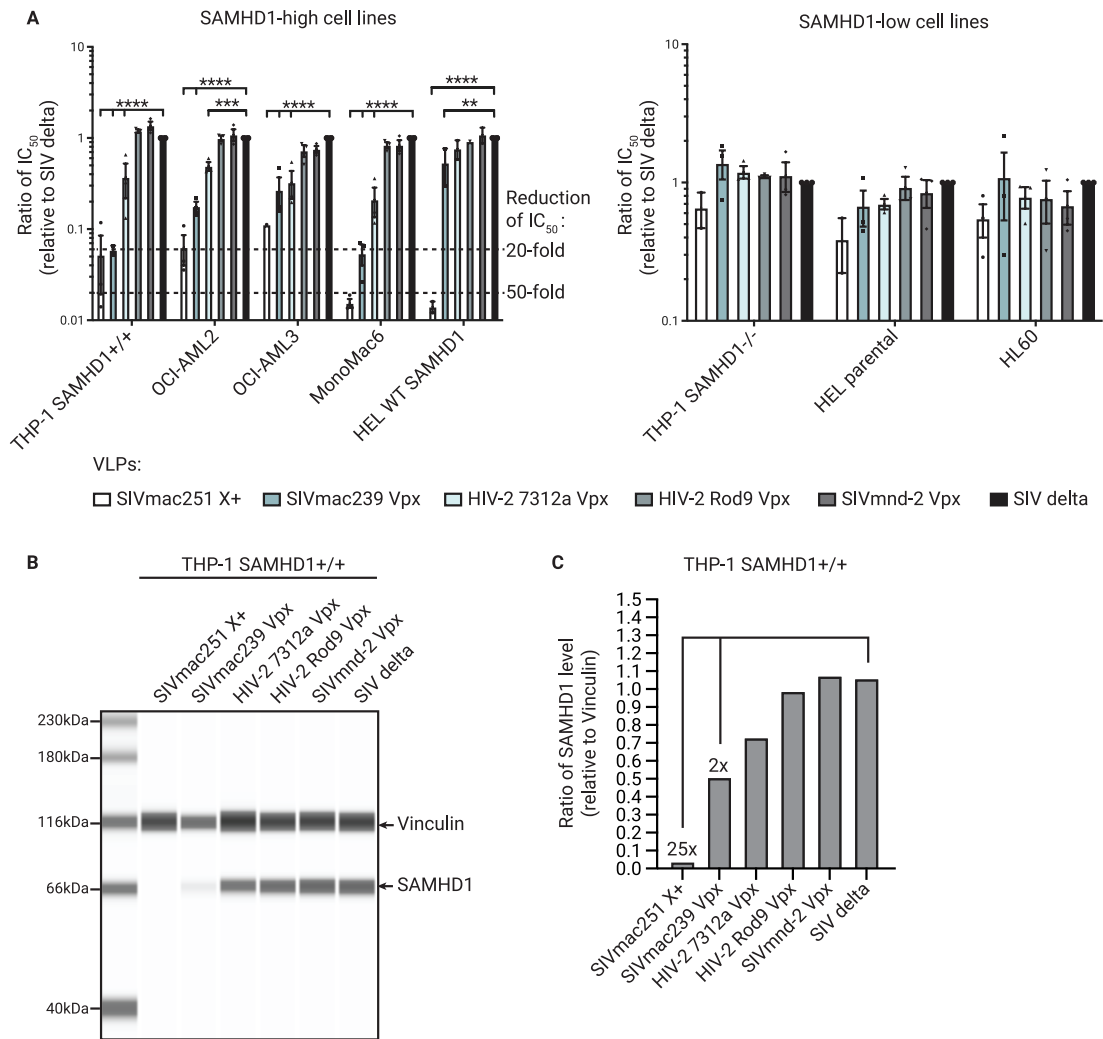


Figure 34: New generation Vpx-VLPs improved ara-C sensitivity of AML cell lines.

AML cell lines were co-treated with 1<sup>st</sup> and new generation VLPs, and ara-C. **A** All AML cell lines indicated were transduced with 2  $\mu$ L of 1<sup>st</sup> generation SIVmac251 X+ VLPs, the new generation Vpx-VLPs, and SIV delta-VLPs for 24 hrs, followed by 96 hrs of ara-C treatment. The ara-C  $IC_{50}$  were calculated and normalized to SIV delta-VLP treatment. The ratio of  $IC_{50}$  relative to SIV delta treatment is shown for both SAMHD1-high (left) and SAMHD1-low (right) expressing cell lines. The fold-reduction of  $IC_{50}$  with respect to SIV delta-VLP treatment is indicated for SAMHD1-high cells. Error bars represent the standard error of mean (s.e.m.) from two-three independent biological replicates. One-way ANOVA was used for statistical analysis: \*\*\*\*:  $p < 0.0001$ , \*\*\*:  $p < 0.001$ , \*\*:  $p < 0.01$ . Non-significant (ns) values are not shown. **B** THP-1 SAMHD1+/+ cells after 24 hr of 2  $\mu$ L VLP treatment were lysed and loaded onto cartridges for Jess analysis. The gel image output from Jess is shown. Vinculin was used as loading control. The ratio of SAMHD1 protein levels relative to vinculin is shown in **C**. (Parts of this figure are also used in Nair *et al.*, unpublished manuscript)

### 3.6.1 New generation SIVmac251 Vpx-VLPs did not improve VLP functionality

One possible reason for the superior functionality of the 1<sup>st</sup> generation VLP might be the selectivity of the Gag protein to load Vpx. In other words, since the Vpx in the 1<sup>st</sup> generation VLP was derived from the SIVmac251 strain, just as the Gag protein, it might be better loaded into or released from the VLP compared to Vpx from the SIVmac239 strain. To investigate this, a stepwise mutagenesis was performed to convert the new generation pSIV3+ 3xFLAG-SIVmac239 Vpx construct into a

3xFLAG-SIVmac251 Vpx construct<sup>o</sup>. Since the two Vpx proteins differed only by two amino acids, three constructs were generated: two with single mutations in each amino acid (P64Q and I75M), and one with both amino acids mutated to form SIVmac251 Vpx (annotated as SIVmac251 Vpx\*). All SIVmac239 Vpx mutant VLPs reached similar yields (Figure 35A). In terms of Vpx loading, a slight reduction in Vpx loading was noticed for the P64Q mutant but not for the other two mutants compared to SIVmac239 WT Vpx (Figure 35B). In terms of their ability to induce SAMHD1 degradation, no major differences could be noticed among the new generation SIVmac239 WT and mutant Vpx-VLPs (Figure 35C). Nevertheless, treatment with 1<sup>st</sup> generation SIVmac251 X+ VLPs resulted in two-fold lower SAMHD1 levels than the new generation VLPs when 0.94  $\mu$ L of VLPs were used (4-fold vs 2-fold SAMHD1 MFI reduction, respectively) (Figure 35C). This was again confirmed in the co-treatment assay in THP-1 cells, where a two-fold reduction in ara-C IC<sub>50</sub>, indicating an improvement in ara-C sensitivity, was observed after treatment with 1<sup>st</sup> generation SIVmac251 X+ VLP (IC<sub>50</sub> 0.13 $\pm$ 0.025  $\mu$ M) compared to both new generation SIVmac239 and 251 Vpx-VLPs (IC<sub>50</sub> 0.36 $\pm$ 0.019  $\mu$ M) (Figure 35D). No differences in ara-C sensitivity could be observed in the SAMHD1-low HEL cells (Figure 35E). Interestingly, the single SIVmac239 Vpx mutants P64Q and I75M performed worse than the SIVmac239 WT and double mutant Vpx (Figure 35D), despite displaying similar SAMHD1 degradation capacities shown in Figure 35C. Thus far, no specific role relating to SAMHD1 functionality have been observed for the amino acids at positions 64 and 75, so these observations were surprising. Further investigation into the importance of these two amino acids was beyond the scope of this work and was, therefore, not performed.

Based on the observations described above, it can be confirmed that the two amino acid difference in composition between SIVmac239 and SIVmac251 Vpx was not responsible for the differences in functionality between 1<sup>st</sup> generation and new generation SIVmac Vpx-VLPs. Despite these differences, the functionality of the new generation SIVmac239 Vpx-VLPs in primary AML blasts was investigated next.

---

<sup>o</sup> Constructs were generated by Alejandro Salinas-Illarena at the Max von Pettenkofer Institute.

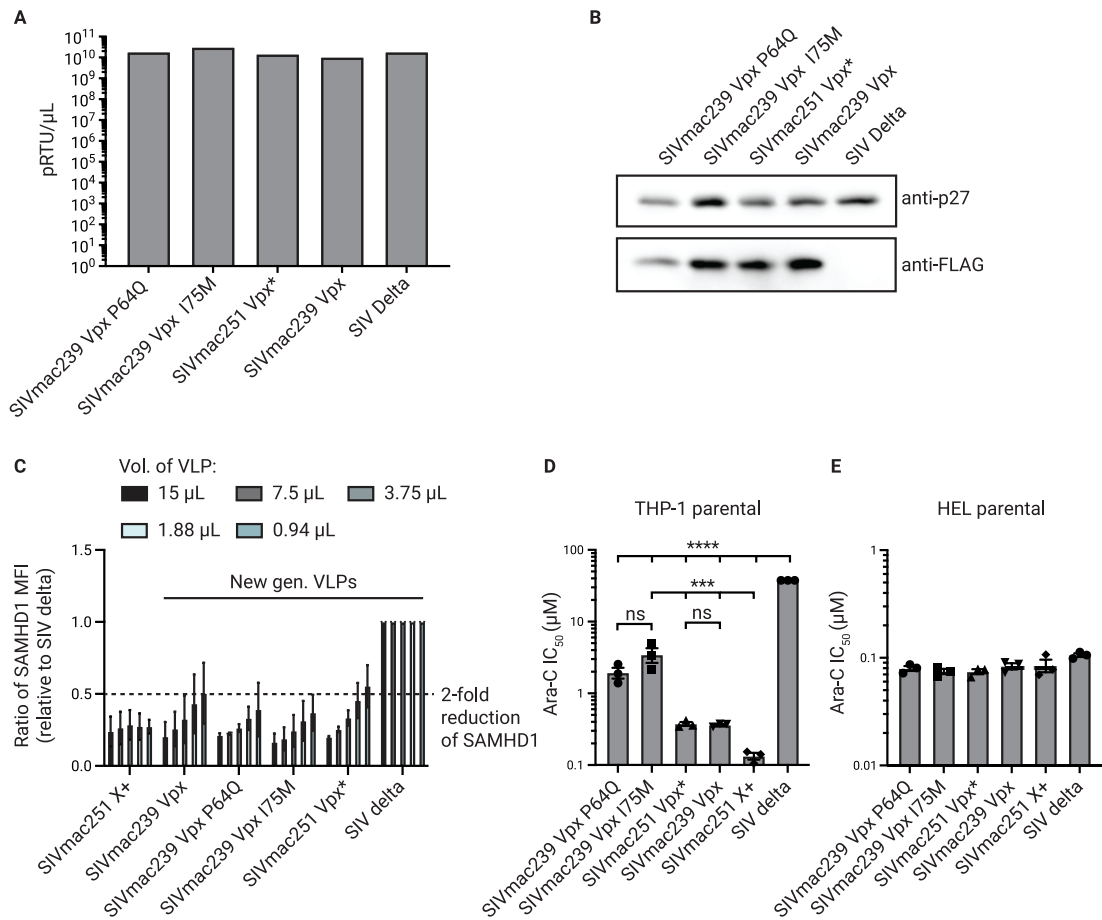


Figure 35: New generation SIVmac251 Vpx-VLPs were not functionally superior to new generation SIVmac239 Vpx-VLPs.

New generation VLPs containing different mutations of SIVmac239 Vpx (P64Q, I75M and double mutant) were generated and characterized. **A** RT activity obtained via SG-PERT assay of new generation VLPs. SIVmac251 Vpx\* represents the SIVmac239 PI64/75QM double mutant which has the same protein sequence as SIVmac251 Vpx. The SIVmac251 Vpx\* has a 3xFLAG-tagged Vpx compared to the 1<sup>st</sup> generation VLP (SIVmac251 X+). **B** 3xFLAG-SIVmac239 WT and mutant Vpx-VLPs were loaded onto an SDS-polyacrylamide gel and immunoblotted against SIV p27 capsid and FLAG. SIV delta-VLPs were used as controls. **C** THP-1 cells were titrated with varying amounts VLPs described in **A**. 24 hrs later, the cells were stained for SAMHD1 and analyzed via flow cytometry. The ratio of mean fluorescence intensity (MFI) of SAMHD1 relative to SIV delta-VLP, which served as negative control, is shown. Error bars represent the standard deviation (s.d.) from two biological replicates. **D** THP-1 cells were transduced with 2 μL of the VLPs described in **A** for 24 hrs, followed by 96 hrs of ara-C treatment. The ara-C IC<sub>50</sub> is shown. Error bars represent the standard error of mean (s.e.m.) from three independent biological replicates. One-way ANOVA was used for statistical analysis: \*\*\*\*:  $p < 0.0001$ , \*\*\*:  $p < 0.001$ , \*\*:  $p < 0.01$ , ns:  $p > 0.05$ . **E** Same as in **D**, but in HEL cells. (Parts of this figure are also used in Nair *et al.*, unpublished manuscript)

### 3.6.2 New generation SIVmac239 Vpx-VLP treatment slightly improved ara-C sensitivity of SAMHD1-high expressing primary AML blast

Investigating the ability of the new generation SIVmac239 Vpx-VLPs to improve ara-C sensitivity of primary AML blast was an important next step to evaluate their potential for clinical usage. The following experiments were conducted in collaboration with Monika Sponheimer from the laboratory of Prof. Dr. Marion Subklewe at the Gene Center Munich. Primary AML blasts were isolated from



peripheral blood or bone marrow collected from AML patients and cultured with irradiated stromal cells at the collaborator's laboratories. Before treating primary AML blasts with the VLPs, a staining workflow was first established to determine the SAMHD1 levels in the blast cells (Figure 36A). First leukocytes were identified using the SSC-A vs FSC-A gating, followed by the identification of single cells in the FSC-H vs FSC-A gating. AML blasts cells were then gated using the SSC vs CD45 blot<sup>299</sup>. These AML blasts cells can be further characterized by their CD33 and CD34 expression, as well as their SAMHD1 expression. Both CD34 and CD33 are markers of leukemic cells, although CD33 expression can vary among CD34-positive cells<sup>300</sup>. With this established gating strategy, SAMHD1 expression in AML blasts was determined.

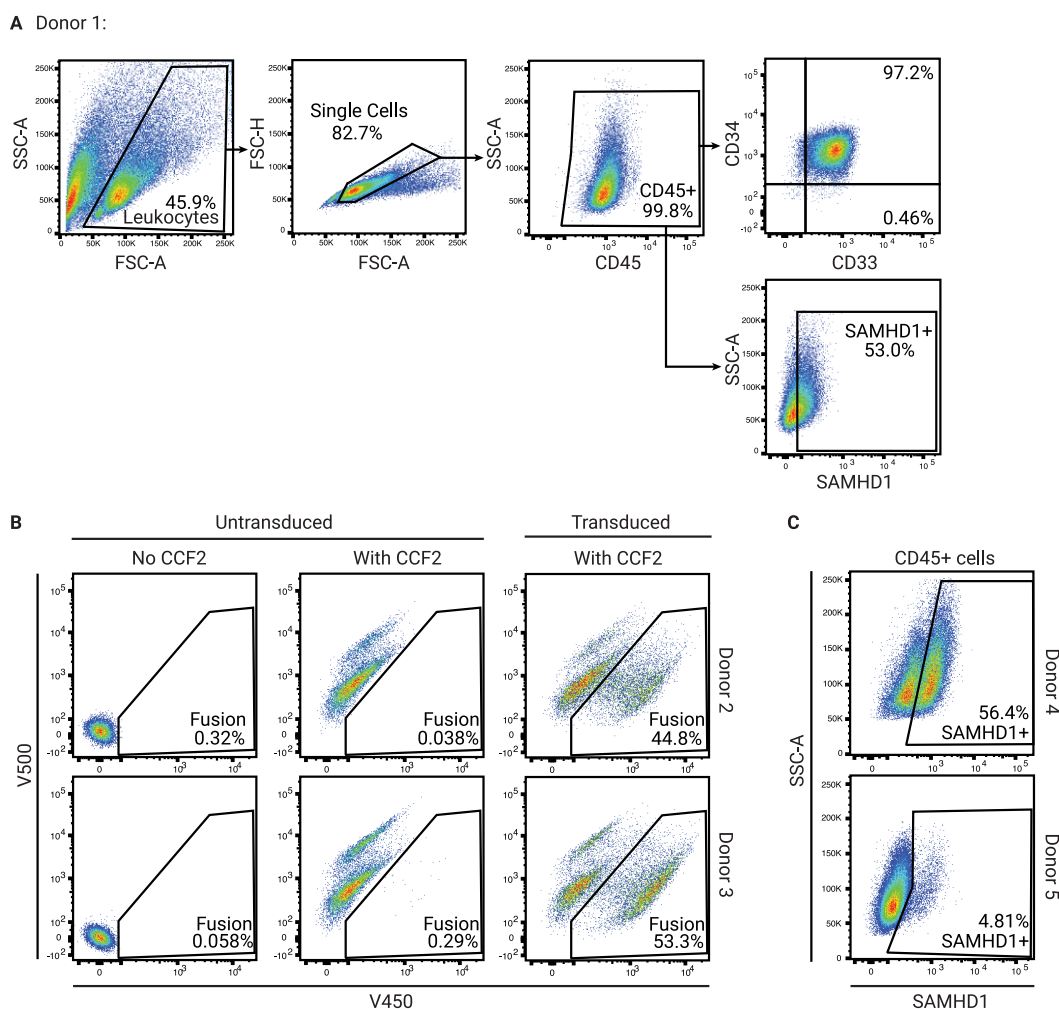


Figure 36: Characterization of primary AML blasts with flow cytometry.

Cultured primary AML blasts cells obtained from the laboratory of Prof. Dr. Marion Subklewe were characterized. **A** The primary blasts were stained for CD45, CD33, CD34 and SAMHD1. A representative of the gating strategy to evaluate the SAMHD1 protein levels in primary AML blasts from one donor is shown. **B** Representative blot of virion fusion assay performed in primary AML blasts from two donors transduced with VSV-G pseudotyped BlaM-Vpr-VLPs. CCF2 substrate was cleaved by the BlaM-Vpr after VLP fusion and led to a shift of fluorescence intensity in the V450 channel. Percentage virion fusion is indicated.

(Continued on next page)

C Percentage of SAMHD1-positive cells from two additional donors of primary AML blasts is shown. Primary blasts from these two donors were used for preliminary studies on new generation VLP co-treatment with ara-C. (Parts of this figure are also used in Nair *et al.*, unpublished manuscript)

Since the new generation VLPs are pseudotyped with the VSV-G envelope protein, the susceptibility of AML blasts to VSV-G mediated virion fusion was also investigated. As shown in Figure 36B, it can be observed that the susceptibility of primary AML blasts was much lower (approximately 44 – 54%) compared to that of the AML cell lines shown in Figure 33C. This difference needs to be considered when evaluating the efficacy of the new generation VLPs on primary AML blasts. To this end, primary AML blasts from two donors – one SAMHD1-high and one SAMHD1-low – were selected to evaluate the ability of the new generation SIVmac239 Vpx-VLPs to improve ara-C sensitivity (Figure 36C).

In an initial trial using 2  $\mu$ L of new generation SIVmac239 Vpx-VLPs during treatment of primary AML blasts, no reduction in SAMHD1 levels was noticed (data not shown). Since the new generation Vpx-VLPs induced SAMHD1 degradation in a dose-dependent manner (Figure 32E), we increased the volume of VLP used for treatment to 10  $\mu$ L. With this increased volume of VLPs, SAMHD1 degradation could be observed 24 hrs after VLP treatment of primary AML blasts from Donor 4 (Figure 37A). However, similar to the observations in AML cell lines, the 1<sup>st</sup> generation SIVmac251 X+ VLPs were able to reduce SAMHD1 levels more efficiently compared to the new generation SIVmac239 Vpx-VLPs (Figure 37A). The SAMHD1 degradation pattern mirrored the ability of the VLPs to improve ara-C sensitivity, as shown in Figure 37B. The 1<sup>st</sup> generation SIVmac251 X+ VLPs were able to improve ara-C sensitivity by 5.4-fold compared to 1.5-fold using the new generation SIVmac239 Vpx-VLPs. In SAMHD1-low primary AML blasts derived from Donor 5, the effect on SAMHD1 degradation and therefore ara-C sensitivity was less pronounced (Figure 37C and D).

Based on these preliminary experiments performed on a single donor for each SAMHD1-high and SAMHD1-low expressing primary AML blasts, the trend observed in AML cell lines was recapitulated. This meant that the 1<sup>st</sup> generation SIVmac251 X+ VLPs were superior in their performance compared to the new generation SIVmac239 Vpx-VLPs. Nevertheless, the ability of the new generation SIVmac239 Vpx-VLPs to improve, albeit only slightly, the ara-C sensitivity of primary AML blasts indicated promise. Further improvements to the new generation VLP could potentially allow for enhancement of ara-C sensitivity in primary AML blasts.

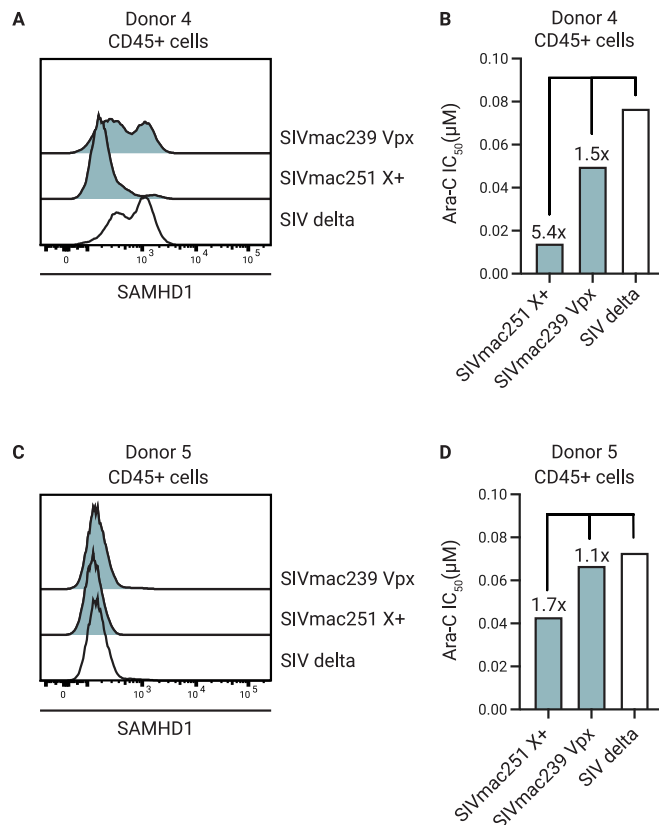


Figure 37: The new generation SIVmac239 Vpx-VLPs only slightly improved ara-C sensitivity of SAMHD1-high expressing primary AML blasts.

Primary AML blasts were co-treated with 1<sup>st</sup> and new generation Vpx-VLPs, and ara-C. All co-treatment assays were performed with Monika Sponheimer from the laboratory of Prof. Dr. Marion Subklewe, at the Gene Center Munich. **A** Primary AML blasts from Donor 4 after 24 hr of 10 μL VLP treatment were stained for CD45, CD33, CD34, and SAMHD1. Change in SAMHD1 protein levels is indicated via the SAMHD1 histogram. Primary AML blasts treated with SIV delta-VLPs were used as control. **B** Primary AML blasts from Donor 4 were transduced with 10 μL of the VLPs described in **A** for 24 hrs, followed by 96 hrs of ara-C treatment. The ara-C IC<sub>50</sub> is shown. Fold change in IC<sub>50</sub> relative to SIV delta-VLP-treatment is indicated. SIVmac251 X+ represents the 1<sup>st</sup> generation VLPs. **C** and **D** Same as **A** and **B**, but with primary AML blasts from Donor 5, expressing low levels of SAMHD1. (Parts of this figure are also used in Nair *et al.*, unpublished manuscript)



## 4. Discussion

In 2017, Schneider *et al.* described the role of SAMHD1 on ara-C resistance in AML cells<sup>145</sup>. This thesis builds on that foundation and shows the potential for using lentiviral accessory protein Vpx-based delivery systems in combination with ara-C chemotherapy to improve ara-C sensitivity in AML cells. Figure 38 illustrates the Vpx delivery systems investigated within this work and their role in improving ara-C sensitivity in AML cells.

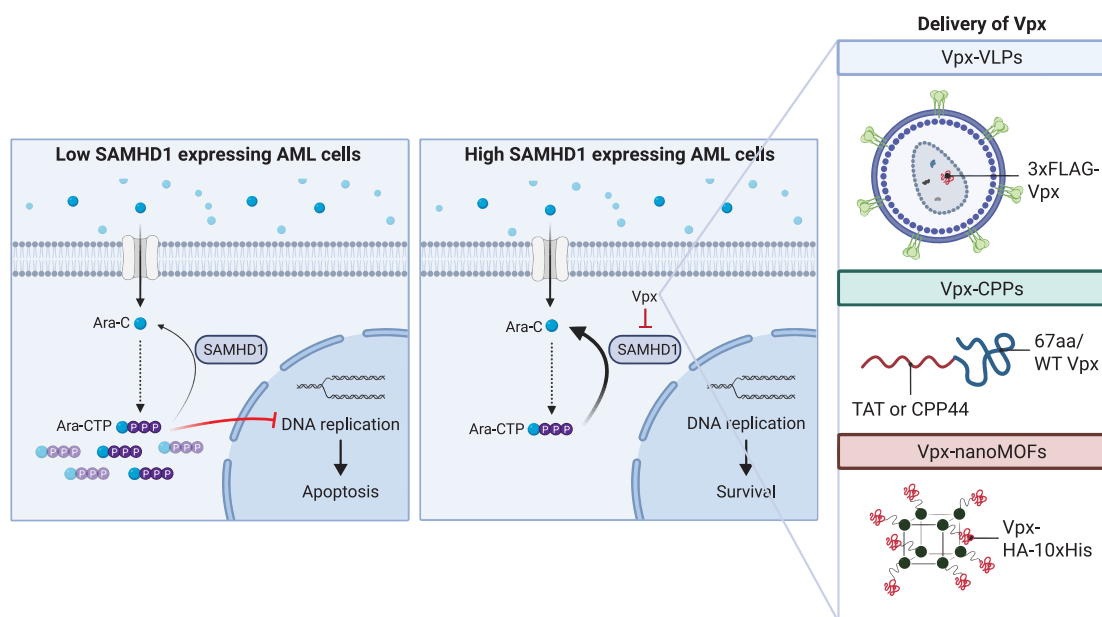


Figure 38: Role of Vpx delivery systems on ara-C metabolism in AML cells.

The illustration shows the three Vpx delivery systems investigated in this work and the role they play in ara-C metabolism and the subsequent improvement of ara-C sensitivity of AML cells via the depletion of SAMHD1 protein.

As mentioned in section 1.5, this work consisted of four main parts:

1. Purification of recombinant Vpx
2. Testing functionality of recombinant Vpx
3. Generating Vpx delivery systems
4. Testing delivery systems in cell lines and primary cells

With regards to parts 1 and 2, this work was able to provide a proof-of-concept for the purification of recombinant Vpx from mammalian HEK293T cells and demonstrated SAMHD1 degradation functionality in primary resting CD4<sup>+</sup> T cells. The results obtained for these two parts will be discussed in further detail in section 4.1. For parts 3 and 4, three different Vpx delivery methods were investigated: nanoMOFs, CPPs, and VLPs. In the upcoming section 4.2, insights into the successes and limitations of the three Vpx delivery systems will be provided.

Since SAMHD1 is involved in many cellular processes, as described in section 1.2, the implications of reducing SAMHD1 levels using Vpx in cells will be discussed in section 4.3. Aside from the three

delivery systems used in this work, there are many other potential protein delivery methods, for instance liposomes, which could also be investigated<sup>301</sup>. This was not done in this work due to time and resource limitations. In addition, since SAMHD1 and Vpx are involved in other cellular pathways aside from ara-C metabolism, there might also be further potential use-cases of the Vpx delivery systems besides AML therapy. Some of these alternative Vpx delivery systems and potential use-cases will be discussed in section 4.4. Finally, some concluding remarks on the implications of this work will be provided in section 4.5.

## **4.1 A functional recombinant Vpx protein could be purified from HEK293T cells**

### **4.1.1 Proof-of-concept for the purification of Vpx-HA-10xHis proteins from HEK293T sleeping beauty cells**

The purification of a functional recombinant Vpx protein was an essential part of this work prior to their subsequent delivery. Initially, a bacterial purification approach was taken due to the advantages of high yield, low cost and ease of scalability<sup>302</sup>. However, during the purification process, many challenges were faced, such as insolubility of the Vpx constructs and lack of activity, which are common issues when purifying proteins from bacterial cells<sup>302</sup>. In addition, when purifying proteins that undergo PTMs, like the Vpx protein, using mammalian cells might be more appropriate to obtain a functional protein. Besides, among the approved protein therapeutics available, majority of them were indeed produced in mammalian cells<sup>303</sup>. Since our final goal with the Vpx proteins is to use them for therapeutic purposes, a mammalian protein purification approach was followed. To this end, we were eventually able to repeatedly purify Vpx-HA-10xHis proteins from HEK293T cells, one of the most widely used mammalian cell lines. The workflow could be further optimized via the generation of the HEK293T sleeping beauty cells to induce Vpx-HA-10xHis expression by using the low cost, readily available drug doxycycline (described in subsection 3.1.3.2). Using the sleeping beauty cells reduced the hands-on time by 24 hrs. This is because the 48 hrs post-transfection incubation time could be replaced by the 24 hrs doxycycline induction time in the HEK293T sleeping beauty cells. In addition, by omitting the plasmid transfection step, the sleeping beauty cells were easily scalable, without the additional need to produce large amounts of plasmid<sup>304</sup>. Since the Vpx protein expression in the sleeping beauty cells was inducible, any potential side-effects on the HEK293T growth by Vpx could be disregarded.

Throughout the optimization process of the purification of Vpx-HA-10xHis, three important observations were made. Firstly, the time required to harvest the HEK293T cells after induction or transfection was very long, since each dish of cells needed to be harvested subsequently. This limitation made it difficult to scale the purification by increasing the number of cells to produce higher yields. Secondly, the detergent used in the lysis buffer played a major role in the yield of the Vpx protein from HEK293T cells, in line with observations made by Ignatoksi *et al.*<sup>305</sup>. This was shown in Figure 15, where a stronger Vpx signal was observed after lysis of HEK293T cells expressing Vpx-HA-10xHis with CHAPS detergent compared to Triton X-100, NP-40, DDM, and Digitonin. However, the CHAPS detergent could not be used for the lysis of HEK293T cells expressing 3xFLAG-Vpx,

since the anti-FLAG affinity resin was incompatible with the CHAPS detergent. This might have been one reason for the low yields observed during the purification of 3xFLAG-Vpx, since Triton X-100 was used in the lysis buffer instead of CHAPS. Thirdly, although Vpx-HA-10xHis was purified with higher yields compared to 3xFLAG-Vpx, the high background impurities is a major limitation of the 10xHis tag purification<sup>306</sup>, despite the reduction of impurities using the Co-NTA resin. Therefore, SEC is an important additional step to significantly increase the purity of the recombinant protein. This was observed in both 3xFLAG-Vpx and Vpx-HA-10xHis purifications. However, in both cases, a very low yield of protein was eluted after SEC, indicated by the low absorption (less than 20 mAU) of the SEC fractions containing the Vpx protein (Figure 13C and Figure 16A).

Based on the three observations mentioned above, several improvements could be made to the purification of recombinant Vpx, going forward. To improve the handling of the mammalian cells, HEK293 cells adapted to suspension growth<sup>307,308</sup>, or other suspension cell lines such as CHO-S could be used to express the recombinant Vpx proteins. In this case, the cells could be grown in roller bottles instead of tissue culture dishes and harvested in a manner similar to bacterial cells (i.e., centrifugation). However, the use of non-human mammalian cell lines for Vpx purification might interfere with functionality since the PTMs, especially glycosylation, is different among mammalian cell lines<sup>305</sup>. This needs to be considered when choosing the host cell type for purification. To determine the best lysis buffer conditions, several lysis methods, including mechanical and chemical lysis, should be investigated depending on the resin used. Perhaps further optimization of sonication conditions could lead to higher yields without the use of detergents, which can interfere with protein binding to resin. Alternatively, the Vpx protein could also be secreted into the growth medium via secretory peptides to avoid cell lysis altogether. To obtain high purity after affinity chromatography, a different tag such as the Strep tag could be used to purify the Vpx protein. The Strep tag has been shown to yield high purity proteins from mammalian cells just after affinity chromatography, making it an attractive tag to investigate for further optimization<sup>309</sup>.

#### **4.1.2 Cell-based nucleofection assay confirmed the functionality of purified Vpx-HA-10xHis**

A crucial and challenging step after purification of any protein is to ensure that they retain biological activity<sup>310</sup>. In the case of Vpx, majority of the studies so far have shown biological activity *in vitro* using co-immunoprecipitation assays, as outlined in Table 22. However, no study has directly observed a reduction in intracellular SAMHD1 protein levels induced by purified recombinant Vpx in their assays. For this work, it was important to show that the Vpx-HA-10xHis construct was able to degrade SAMHD1 inside the cells (i.e., via cell-based assays). This way, the efficacy of Vpx-conjugated delivery systems, like the nanoMOFs, in AML cells can be judged based on the performance of the delivery system itself and not be hindered by the lack of activity of purified Vpx. Cell-based activity assays also provide an important advantage since the protein activity is measured in a physiological environment compared to the synthetic environment in cell-free assays<sup>311</sup>. In addition, since the antagonism of SAMHD1 by Vpx seems to be dependent on cellular localization<sup>79,122,180,181</sup>, cell-based assays might be more appropriate to allow for Vpx to properly localize to the nucleus to degrade SAMHD1. Cell-free assays, in contrast, involve the use of total protein lysate without any compartmentalization. This might explain the challenges faced during the optimization of the cell-free

degradation assay in this work (see subsection 3.2.1). SAMHD1 degradation could only be observed in isolated trials and was not reproducible, even though the proteasome was active, as indicated by the proteasome functionality assay in Figure 18 and Figure 19.

We could successfully show the cellular degradation of SAMHD1 induced by purified WT Vpx-HA-10xHis protein in primary resting CD4+ T cells, compared to Q76A Vpx-HA-10xHis. Even though the purified proteins contained impurities, the WT Vpx protein still demonstrated biological activity. The effect caused by impurities could be disregarded since the Q76A Vpx-HA-10xHis construct was also purified under the exact conditions as the WT Vpx-HA-10xHis construct, and also contained impurities. We also showed that nucleofection of WT Vpx-HA-10xHis protein purified from twice the amount of cells resulted in a greater reduction of SAMHD1 level (shown in Figure 21), further confirming the specificity of this observation. Although the activity of the impure WT Vpx-HA-10xHis construct could be confirmed, this process needs to be repeated to confirm the functionality of WT Vpx-HA-10xHis proteins after SEC. Since the yields of Vpx-HA-10xHis after SEC were so low, no activity could be measured after nucleofection in this work (data not shown). Furthermore, with highly purified Vpx proteins, a more accurate Vpx concentration could be measured, with which the effect of Vpx concentration on SAMHD1 degradation can be determined. This would then provide more information on an effective Vpx dosage required in delivery systems to induce high enough SAMHD1 degradation to improve ara-C sensitivity.

Besides nucleofection, other methods of Vpx transfection were tested, using reagents such as Pierce™ Protein Transfection Reagent and TurboFect™ from Thermo Fisher Scientific (data not shown). However, none of the other methods were successful in delivering Vpx and inducing SAMHD1 degradation. This was perhaps because these methods primarily relied on endosomal uptake of protein-lipid complexes<sup>312</sup>. A common challenge in such a delivery method is entrapment in the endosomes<sup>312</sup>, resulting in the inability of Vpx to enter the nucleus and induce SAMHD1 degradation. Therefore, the success of the nucleofection of the Vpx protein could be attributed to the fact that during nucleofection, biological materials are delivered directly to the nucleus<sup>313</sup>, thereby circumventing the need to escape endosomes. The successful delivery of Vpx via nucleofection could also be expanded to other cell lines or primary cells, which might be difficult to transfect. This can then provide insights into, for example, HIV or SIV pathology since specific effects of the Vpx protein without additional viral components can be observed.

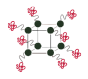



## 4.2 New generation SIVmac Vpx-VLPs showed superior performance compared to the other Vpx delivery systems

Table 24 summarizes the key take-aways obtained for each of the Vpx delivery system based on 4 features: production, the capacity for SAMHD1 degradation, the ability of the delivery system to improve ara-C sensitivity in AML cell lines and in primary AML blasts. Out of the three Vpx delivery systems investigated, the new generation VLPs have thus far shown the best results with ease of production, high SAMHD1 degradation efficiency, and the ability to improve ara-C sensitivity in AML cell lines and partially in primary AML blasts. The Vpx-CPPs have also shown potential based on the results from the commercially synthesized CPPs, albeit to a lesser extent than the Vpx-VLPs.



The Vpx-nanoMOFs, unfortunately, did not show any SAMHD1 degradation functionality even though they could be easily generated using purified Vpx-HA-10xHis.

Table 24: Summary of key take-aways obtained for each Vpx delivery system.

Vpx delivery systems	Production	SAMHD1 degradation	Ara-C sensitivity improvement	
			AML cell lines	Primary AML blasts
 Vpx-nanoMOF	✓	✗	🔄	🔄
 Commercial 67aa Vpx-CPP	✓	✓	✓	🔄
 In-house purified WT Vpx-CPP	✓	✗	✗	🔄
 Vpx-VLP	✓	✓	✓	🔄

✓ Successful ✗ Unsuccessful 🔄 Optimization required

#### 4.2.1 The Vpx homolog SIVmac Vpx was the most effective at improving ara-C sensitivity

The new generation Vpx-VLPs produced in this work are first-of-its-kind, while the 1<sup>st</sup> generation Vpx-VLPs (i.e., SIVmac251 X+ VLPs) have been used previously in many publications. In particular, the 1<sup>st</sup> generation VLP was also used in the study by Schneider *et al.* to reduce SAMHD1 levels in the context of AML<sup>145</sup>. However, in order to be considered for therapy, improvements needed to be made to the 1<sup>st</sup> generation VLPs. One such improvement was to remove all unnecessary regulatory and accessory viral proteins from the 1<sup>st</sup> generation VLPs. Since the remaining viral proteins (i.e., Vif, Nef, Vpu, Tat) antagonize other proteins in the host cells which are irrelevant for SAMHD1 degradation<sup>151</sup>, they needed to be removed to improve safety of the VLPs. This led to the production of the new generation VLPs which only carry the Vpx accessory protein and the essential structural proteins (via the Gag polyprotein). The polymerase (Pol) was kept in the VLP to allow for quantification via SG-PERT. Perhaps the Pol protein could also be removed when a suitable alternative VLP quantification method has been established, resulting in a minimal functional Vpx-VLP. Nevertheless, in this work we showed that removing the additional accessory proteins did not interfere with the VLP production and Vpx could still be packaged. In addition, in line with previous publication by Nègre *et al.*, co-transfecting HIV-1 Rev significantly increased the yield of the VLPs produced (Figure 32)<sup>314</sup>, and enhanced the activity of the new generation VLPs (Figure 31 and Figure 32).

The next improvement was to identify the optimal Vpx homolog to induce SAMHD1 degradation in AML cells. Among the various Vpx homologs tested, SIVmac Vpx (SIVmac239 and SIVmac251) were the most effective at reducing SAMHD1 levels, followed by HIV-2 7312a Vpx. Interestingly, we observed that the various Vpx homologs we tested were differentially loaded into the SIVmac-based VLPs. There could be two main reasons for this observation. First, the Vpx/ Vpr protein might only have weakly interacted with the Gag protein, since interaction with the Gag protein is required for the loading of Vpx and Vpr into the VLPs<sup>165</sup>. In fact, Sunseri *et al.* reported a high packaging efficiency of SIVmac Vpx when using SIV p6 motif for packaging but not when using the HIV-1 p6 motif<sup>315</sup>. Even though this observation was not reported for SIVdeb and SIVmus Vpr, differences in the p6 motif between their homologous and the SIVmac251 Gag proteins might be a reason for their low packaging in the VLPs. Second, variable inherent expression levels of the various Vpx/ Vpr homologs could have led to reduced packaging into the VLPs. A comprehensive expression study by Sakai *et al.* revealed highly variable expression levels of various Vpx and Vpr proteins from different species, including HIV-2, SIVmac and SIVmnd-2<sup>162</sup>. In line with this, a small-scale expression analysis in our lab also revealed expression differences of the various Vpx and Vpr homologs in HEK293T cells (data not shown), which could explain differences in loading of Vpx/ Vpr homologs into the VLPs.

An unexpected observation, however, was that HIV-2 Rod9 Vpx-VLPs, despite the high loading of HIV-2 Rod9 Vpx protein into the VLPs (Figure 32), were unable to induce SAMHD1 degradation. A study in 2017 by Baldauf *et al.* reported increases in HIV-1 infection when the virions contained SIVmac239 and HIV-2 Rod9 Vpx<sup>123</sup>. In their study, HIV-2 7312a Vpx-incorporated HIV-1 virions were not as effective as the incorporation of SIVmac239 and HIV-2 Rod9 Vpx<sup>123</sup>. In contrast, in this work, we showed that HIV-2 7312a Vpx-VLPs were better able to induce SAMHD1 degradation compared to HIV-2 Rod9 Vpx-VLPs. During our VLP production, we incorporated all Vpx proteins into the VLPs *in cis*, meaning that the Vpx proteins were encoded in the same plasmid as the VLP structural proteins. In line with our observations, a study by Sunseri *et al.* has reported a lack of activity of HIV-2 Rod9 Vpx, when it was incorporated *in cis* into HIV-1 virions via a SIVmac p6 motif, compared to virions incorporating SIVmac239 Vpx<sup>315</sup>. Interestingly, their study also reported that HIV-2 Rod9 Vpx was more functional when it was incorporated into HIV-1 virions *in trans*, meaning that the Vpx protein was encoded in a separate plasmid which is then co-transfected with HIV-1 proviral DNA during production<sup>315</sup>. In addition, another study by Baldauf *et al.* reported that HIV-2 Rod9 Vpx retained its activity when incorporated *in cis* into its native HIV-2 Rod9 virions<sup>81</sup>. Since the HIV-2 Rod9 Vpx proteins in this study were incorporated into SIVmac251-based VLPs, this might provide an additional explanation for the lack of activity of the HIV-2 Rod9 Vpx, despite being packaged into the VLPs.

In summary, based on the optimizations conducted, we identified both SIVmac239 and SIVmac251 Vpx-VLPs to be the most effective at inducing SAMHD1 degradation and inducing ara-C sensitivity in AML cells, followed by HIV-2 7312a Vpx-VLPs.

#### 4.2.2 New generation Vpx-VLPs need to be optimized to perform as well as 1<sup>st</sup> generation Vpx-VLPs

On one hand, the new generation SIVmac Vpx-VLPs were able to induce SAMHD1 degradation and significantly improve the sensitivity of AML cells to ara-C. On the other hand, the 1<sup>st</sup> generation Vpx-VLPs still showed superior performance compared to the new generation VLPs, both in AML cell lines and primary AML blasts (Figure 34 and Figure 37). The reason for this difference is currently unclear. Based on our initial investigations, any potential differences between the SAMHD1 degradation activities of SIVmac239 Vpx and SIVmac251 Vpx could be ruled out (Figure 35). Two further possibilities are differences in Vpx loading between the 1<sup>st</sup> and new generation VLPs and possible additive effects of the remaining accessory proteins in the 1<sup>st</sup> generation VLPs. Since the Vpx loaded into the 1<sup>st</sup> generation VLPs could not be visualized via immunoblotting, due to a lack of functional antibodies, the amount of Vpx present in the 1<sup>st</sup> generation VLPs could not be determined. A possible method would be to measure the amount Vpx mRNA transcribed from the 1<sup>st</sup> generation and new generation VLP plasmids via qPCR. Meanwhile, the effect of the remaining accessory proteins on improving ara-C sensitivity can be determined by possibly incorporating each accessory protein individually in *trans* during VLP production and observing their effects on ara-C sensitivity. Interestingly, a study investigating the effects of knocking down certain genes on ara-C sensitivity has reported that the knockdown of APOBEC3G increased the sensitivity of THP-1 cells to ara-C<sup>316</sup>. APOBEC3G is a target of the accessory protein Vif<sup>157</sup>. Although this needs to be experimentally confirmed, the degradation of APOBEC3G induced by Vif present in the 1<sup>st</sup> generation VLPs might have, in addition to SAMHD1 degradation by Vpx, enhanced the ara-C sensitivity of AML cell lines. Nevertheless, since no further studies reported the effect of APOBEC3G on ara-C sensitivity or on cancer progression in general, this might be an interesting line of investigation for future research.

Even though both new generation and 1<sup>st</sup> generation VLPs were able to significantly improve ara-C sensitivity in AML cell lines (Figure 34A), their efficiency in primary AML blasts were much less pronounced (Figure 37). A possible reason for this might be the reduced VSV-G fusion observed in primary AML blasts, between 45-50% as shown in Figure 36B, compared to almost 100% fusion in AML cell lines (Figure 33C). This may have resulted in fewer cells receiving the Vpx protein, therefore remaining resistant to ara-C treatment. Nevertheless, the 1<sup>st</sup> generation VLPs were still able to improve ara-C sensitivity of SAMHD1-high primary AML blasts by 5.4-fold. Therefore, by further optimizing the new generation VLPs as mentioned above, they could improve ara-C sensitivity in primary AML blasts to similar levels as the 1<sup>st</sup> generation VLPs. In any case, primary AML blasts from more donors need to be investigated before drawing any conclusions on Vpx-VLP efficiency *ex vivo*.

#### 4.2.3 Vpx-CPPs and -nanoMOFs require further optimization

Aside from the virus-based carrier for Vpx (VLPs), two chemical carriers were investigated for the delivery of the Vpx protein (Figure 4). These were the nanoMOFs and the CPPs, as introduced in subsections 1.4.1 and 1.4.2, respectively. Although they are very promising potential carriers with many advantages, such as biocompatibility and versatility, in our investigations with Vpx they were not as successful as the VLPs.

In the case of the CPPs, while the commercially synthesized 67aa Vpx-CPPs induced SAMHD1 degradation and increased ara-C sensitivity (Figure 26, Figure 27 and Figure 28), albeit to a smaller extent than the Vpx-VLPs, the in-house purified WT Vpx-CPPs were not successful. The likely reason for this is the low yield achieved during the purification steps. To improve yields of the purified CPPs, the same optimization suggestions discussed for the Vpx protein in subsection 4.1.1 could be implemented. Even though the commercially synthesized 67aa Vpx-CPPs were able to slightly improve ara-C sensitivity, there is room for improvement. Firstly, a high concentration of 25  $\mu$ M was needed to induce SAMHD1 degradation, which was not achieved during the purification of the WT Vpx-CPP. This high concentration might have allowed for a more efficient uptake and intracellular release of the Vpx-CPPs, since it has been reported that peptide concentration is an important factor for uptake<sup>213,317</sup>. Strategies to improve intracellular release of CPPs at lower concentrations could be investigated to reduce the need to use large amounts of Vpx-CPPs. These strategies include the addition of pH-dependent peptides to the CPPs or photosensitizers to damage the endosomal membranes<sup>244</sup>. Secondly, the quality of the CPP was highly dependent on the company which synthesized it. Even though the CPP sequences were identical, the one from Eurogentec was better soluble and did not precipitate upon addition to cell growth media, in contrast to the one from Davids Biotechnologie. The reason for the difference in solubility is unclear. It could be attributed to either the purity grade of the CPPs or to the method used for peptide synthesis, which come with their own challenges<sup>318</sup>. Since a detailed discussion of these challenges of peptide synthesis is beyond the scope of this work, it will not be addressed. Nevertheless, it is important to keep the differences of CPP quality between companies in mind when further investigating commercially synthesized Vpx-CPPs. Thirdly, the Vpx used for commercial synthesis was truncated to 67 amino acids to accommodate the size restrictions for peptide synthesis. This 67 amino acid Vpx, although it contained the essential amino acids required for SAMHD1 (W24) and DCAF1 (Q76) binding according to Schaller *et al.*<sup>179</sup>, some of the amino acids close to the C-terminus which are in close vicinity to the SAMHD1 binding interface were removed<sup>163</sup>. This might have accounted for the inferior performance of the 67aa Vpx-CPP compared to the Vpx-VLPs, in terms of ara-C sensitivity improvement. To confirm this speculation, WT Vpx-CPPs need to be investigated.

In the case of the Vpx-nanoMOFs, despite the ease of production of Vpx-loaded nanoMOFs, no SAMHD1 degradation could be noticed after treatment of THP-1 cells with the nanoMOFs. Based on further investigation, we noticed that the Vpx-nanoMOFs were likely trapped in endosomes (Figure 24). This entrapment in endosomes is a common problem associated with nanoMOFs<sup>199</sup> and CPPs<sup>244</sup>. Perhaps treating the cells with a higher concentration of the Vpx-nanoMOFs might have resulted in a more efficient uptake and release, similar to the CPPs. However, this might have led to increased toxicity caused by the nanoMOFs. Instead, strategies to improve endosomal escape could be pursued. Although the addition of endosomal escape enhancers (i.e., chloroquine and looperamide) were attempted in this work, the concentrations used were based on investigations in HeLa cells<sup>295</sup>. Therefore, further optimizations of the concentration of the enhancers could perhaps improve endosomal escape of the Vpx-nanoMOFs in AML cells. In addition, another study generated siRNA-nanoMOFs complexed with co-factors such as a proton sponge, a CPP KALA, or ammonium chloride, which allowed for a more efficient release of the siRNA from the endosomes and subsequent knockdown of the target gene<sup>319</sup>. This approach could also be investigated for the release of Vpx-

nanoMOFs from the endosomes. It is important to consider that the method of cargo entrapment into the nanoMOF differs between siRNA and the Vpx protein. In our case, the Vpx protein is bound to the surface of the nanoMOFs through interactions between the His tag and the metal ion on the nanoMOFs<sup>202</sup>. In the case of the siRNA-nanoMOFs, the siRNA is encapsulated in the pores of the nanoMOFs<sup>319</sup>. Therefore, methods that change the pH of the endosomes allowing for the His tag to dissociate from the metal ion might be more successful than, for example, using a CPP to penetrate out of the endosome.

All in all, although CPPs and nanoMOFs are attractive candidates for the delivery of Vpx, more optimization is required before they can be investigated for therapeutic use in the AML context.

### 4.3 Implications of Vpx-ara-C combination treatment for AML

As shown in the study by Schneider *et al.* and in this work (Figure 28, Figure 34, and Figure 37), combining Vpx delivery and ara-C treatment of AML cells is a very attractive strategy to improve the outcome of the treatment. However, many factors need to be considered before the strategy can be implemented in pre-clinical and clinical trials. Aside from evaluating the efficacy of the combination treatment in patient cells *ex vivo*, the potential side-effects and the kinetics of the treatment need to be carefully examined. Since SAMHD1 is involved in many important cellular processes (see section 1.2), the impact of reducing SAMHD1 levels in a systemic manner must be considered. Additionally, strategies such as specific targeting of Vpx delivery systems to AML cells and careful tuning of ara-C and Vpx concentrations in the combination setting could be pursued to reduce side effects caused by off-target activities.

As discussed in detail in section 1.2, the functions of SAMHD1 in the cell are multi-faceted. In the context of cancer, SAMHD1 has been shown to have both tumor-suppressing and tumor-inducing roles<sup>125,135</sup>. By depleting SAMHD1, cancer cells have the potential to accumulate mutations through genomic instability, which can then lead to cancer progression<sup>135,320</sup>. At the same time, this depletion also makes the cancer cells more sensitive to DNA damaging agents<sup>125,145,146</sup>. In order to prevent the cancer cells from overcoming the drug sensitivity and continue dividing following SAMHD1 depletion, the kinetics of Vpx depletion of SAMHD1 and changes in dNTP levels need to be determined. With this information, the time frame between Vpx treatment and ara-C treatment, the length of Vpx treatment, and the optimal combinatory concentrations of Vpx and ara-C can be set. The availability of extensive studies into the mechanism and kinetics of SAMHD1 degradation by Vpx is an advantage of using Vpx for SAMHD1 depletion, compared to using small molecules where the mechanisms are often unknown. As mentioned in subsection 1.3.3, studies by Hollenbaugh *et al.* and Kim *et al.* in monocyte-derived macrophages (MDMs) reported lower SAMHD1 levels already 2 hrs after Vpx treatment<sup>182,183</sup>. This low level of SAMHD1 was maintained up to 7 days, after which the SAMHD1 levels started to rise<sup>183</sup>. Although the SAMHD1 levels were low for 7 days, the dNTP levels only rose for 2 days after Vpx treatment and reached normal levels by day 6 after Vpx treatment<sup>182,183</sup>. Specifically, only dATP and dGTP levels were significantly increased<sup>183</sup>. No significant changes in dCTP and dTTP levels have been reported<sup>183</sup>. dCTP competes with ara-CTP to integrate into the DNA during replication<sup>321</sup>. Therefore, the lack of rise in dCTP levels after Vpx treatment provides further evidence for the effect of SAMHD1 depletion on improving ara-C sensitivity. In

addition, the 7-day time frame, where SAMHD1 levels are maintained at low levels while dNTP levels return to normal, presents an optimal time frame for ara-C treatment, since ara-C is typically administered over 7 days to patients<sup>15</sup>. This hypothesis, however, needs to be tested in the AML context and subsequently in animal models as the kinetic studies so far were conducted *in vitro* in healthy MDMs.

In addition to determining the kinetics of SAMHD1 depletion by Vpx in the context of AML, another strategy to circumvent possible side-effects would be to specifically target Vpx to AML cells. For example, CPP44 was chosen as a CPP candidate to deliver Vpx since it was reported to specifically enter AML cells and not healthy blood cells or other cancer cells<sup>241</sup>. In the case of VLPs and nanoMOFs, targeting agents could be adsorbed onto their surface to allow for specific uptake in AML cells. For example, folic acid, which is primarily overexpressed in some cancer cells, were added to surfaces of nanoMOFs to allow for targeted uptake in some solid cancer cell lines<sup>199</sup>. In addition, nanoMOFs were also coated with trastuzumab (anti-HER2 antibody) to support selected delivery into HER-2-positive breast cancer cells<sup>322</sup>. Such modifications have also been made on VLPs to improve targeting, as summarized by Rohovie, Nagasawa and Swartz<sup>260</sup>. In the case of AML, functionalizing nanocarrier surfaces with anti-CD33 antibodies have shown to be a potential strategy for targeted delivery into AML cells<sup>323</sup>. Such a strategy could also be pursued for the delivery of Vpx to prevent off-target effects of SAMHD1 depletion.

## 4.4 Future directions

### 4.4.1 Other potential Vpx delivery systems

Besides the delivery systems investigated in this work, Vpx could also be delivered to AML cells using other well-studied delivery systems<sup>301</sup>. One such delivery system is liposomes. Some liposomes carrying therapeutic proteins have already entered the clinics, while others are undergoing clinical trials and have shown promising results<sup>301</sup>. The use of liposomes was initially considered for the delivery of Vpx in this work. However, due to the challenges of obtaining a high yield purified protein for efficient packaging into the liposomes, this strategy was paused. Liposomes are also attractive carriers for Vpx in the context of AML, since a liposomal formulation of ara-C and daunorubicin (CPX-351 or Vyxeos) is already commercially available<sup>324</sup>. Vpx could, therefore, theoretically be combined with the existing CPX-351 formulation for delivery into AML cells. Another advantage of using liposomes is the ease of surface functionalization for targeted delivery<sup>301</sup>, similar to the VLPs.

An alternative method for Vpx delivery would be the conjugation with polymers. A popular polymer used in many investigations is PEG. This polymer confers many attractive properties to the protein cargo such as low immunogenicity, better solubility, and longer half-life<sup>325</sup>. Many PEGylated proteins have also been approved for clinical use<sup>325</sup>. In fact, a PEGylated enzyme, L-asparaginase, under the brand name Oncaspar, is currently being used in the front-line treatment of acute lymphoblastic leukemia (ALL) and has shown efficiency<sup>326</sup>. In addition to direct PEGylation of therapeutic proteins, PEGylation of nanocarriers such as liposomes have also been investigated and have shown to improve efficiency and reduce toxicity of the delivery systems<sup>325</sup>.

In addition to liposomes and polymers, other protein delivery systems are currently being investigated for their therapeutic potential. These include exosomes, micelles, and polymer networks such as hydrogel<sup>325</sup>. However, due to their complex formulations and inherent toxic properties, their application in protein delivery is currently limited<sup>327</sup>.

Aside from delivery of protein, another delivery method that holds great potential is the delivery of mRNA. Over the last years, many challenges that faced the advancement of RNA therapeutics, such as low stability and high immunogenicity, have been overcome<sup>328</sup>. Since then, a large number of clinical trials have been investigating the use of RNA therapeutics in cancer and infectious diseases<sup>328</sup>. Besides its use as vaccines, mRNA encoding therapeutic proteins could also be delivered. A big advantage of using this method over protein delivery is that, since the proteins are produced directly inside the target cell, there is a higher likelihood of proper protein folding and PTMs which contribute to protein functionality<sup>329</sup>. In addition, existing manufacturing processes do not need to be drastically adjusted for each mRNA<sup>329</sup>. This is not the case for proteins, where each protein manufacturing process need to be optimized due to varying biochemical properties.

The delivery of Vpx via liposomes, PEG polymers or mRNA could be investigated in addition to the delivery systems used in this work. Eventually, the optimal Vpx delivery method which has the highest probability for success in pre-clinical and clinical trials, as a result of low toxicity and high efficiency, can then be determined.

#### 4.4.2 Further applications of Vpx delivery systems

The Vpx delivery systems investigated in this work were primarily evaluated for their functionality in AML cells. However, these delivery systems carrying Vpx could also be applied to other diseases or conditions where SAMHD1 depletion may be beneficial.

SAMHD1's role in drug resistance is not only described in the context of AML, but also in other cancer types such as glioblastoma<sup>330</sup>. A recent study reported that depleting SAMHD1 in glioblastoma cells led to increased sensitivity to irradiation, as well as temozolomide, which induces DNA damage. This observation is in line with many studies indicating SAMHD1's role in causing resistance to DNA damage inducers<sup>125</sup>. In these cancers where DNA damage inducers are primarily used in treatment and where SAMHD1 has been implicated in drug response, combining Vpx delivery systems with the drug treatment might help improve response.

In addition to increasing sensitivity to DNA damage inducers, combining SAMHD1 depletion with radiation has also recently been shown to enhance anti-tumor immunity against lung adenocarcinoma cells via the STING pathway<sup>331</sup>. The relationship between SAMHD1 and the STING pathway was discussed in subsection 1.2.3. A similar observation was also made in the context of ovarian cancer, where the authors alluded to the depletion of SAMHD1 as a potential therapeutic strategy<sup>332</sup>. Interestingly, a recent non-published abstract has also hinted at SAMHD1's role in suppressing anti-tumor immunity in AML<sup>333</sup>. These reports suggest that Vpx delivery systems to deplete SAMHD1 could even be used as monotherapy to enhance anti-tumor immunity.

Another disease where SAMHD1 is extensively studied is in the context of HIV, where it has been shown to restrict HIV infection. Aside from reducing dNTP levels to prevent reverse transcription

of viral RNA, SAMHD1 also represses the reactivation of HIV proviral DNA<sup>334</sup>. The proviral DNA is integrated into the host cell genome after HIV infection and contributes to the latent viral reservoir in HIV-infected patients<sup>335</sup>. The current anti-retroviral therapy (ART) available against HIV stops viral replication but do not target the latent reservoir, which can later reactivate and result in persistent infection<sup>335</sup>. As a solution to target these latent reservoirs, a new strategy called “shock-and-kill” is under development. With this strategy, the HIV proviral DNA is reactivated or “shocked”, making the infected cells more vulnerable to attack by the immune system or by medical interventions<sup>336</sup>. In addition to SAMHD1, the HUSH complex was also reported to repress HIV proviral DNA<sup>176</sup>. The HUSH complex is also targeted for degradation by Vpx<sup>176</sup>. Since SAMHD1 and the HUSH complex help keep the HIV proviral DNA inactive, depleting SAMHD1 and HUSH can reactivate the proviral DNA, facilitating the first step in the “shock-and-kill” treatment strategy<sup>176,334</sup>. In this case, delivering Vpx could be beneficial to deplete both SAMHD1 and the HUSH complex.

All in all, the applications of Vpx delivery systems goes beyond combination with ara-C to improve chemotherapy response in AML. They could be used in a variety of cancers where SAMHD1 has been reported to play a role in therapy response or potentially in HIV treatment. In addition, since SAMHD1 has been shown to induce drug resistance against many DNA damage inducers, Vpx delivery systems can be combined with a variety of drugs to improve their efficiency.

## **4.5 Conclusion**

This work provides some key insights into the application of lentiviral accessory protein Vpx as a potential therapeutic protein. Based on the results obtained, VLPs were shown to be the most effective at delivering Vpx to AML cells to increase their sensitivity to the chemotherapeutic drug ara-C. Considering the additional use-cases of such Vpx therapies, as discussed in subsection 4.4.2, future research and optimizations of current and potential Vpx delivery systems will certainly be beneficial in bringing Vpx-based therapies into the clinics. Furthermore, since the role of SAMHD1 in AML therapy response has been previously established and confirmed in this work, the possibility of including SAMHD1 as a marker for patient stratification should be investigated for the benefit of AML patients.



## References

1. Shallis RM, Wang R, Davidoff A, Ma X, Zeidan AM. Epidemiology of acute myeloid leukemia: Recent progress and enduring challenges. *Blood Rev.* 2019 Jul 1;36:70–87.
2. Noone A, Howlander N, Krapcho M, Miller D, Brest A, Yu M, et al. SEER Cancer Statistics Review, 1975-2018, National Cancer Institute. <https://Seer.Cancer.Gov/>. 2018.
3. Döhner H, Weisdorf DJ, Bloomfield CD. Acute Myeloid Leukemia. Longo DL, editor. *N Engl J Med.* 2015 Sep 17;373(12):1136–52.
4. Weiskopf K, Schnorr PJ, Pang WW, Chao MP, Chhabra A, Seita J, et al. Myeloid cell origins, differentiation, and clinical implications. *Microbiol Spectr.* 2016 Oct 14;4(5).
5. American Cancer Society. Key Statistics for Acute Myeloid Leukemia (AML) [Internet]. About Acute Myeloid Leukemia (Aml). 2020 [cited 2022 Mar 29]. Available from: <https://www.cancer.org/cancer/acute-myeloid-leukemia/about/key-statistics.html>
6. Adithya C, Varun L, Alex S. Leukemia - StatPearls - NCBI Bookshelf. Treasure Island (FL): StatPearls Publishing. 2021.
7. Emadi A, Law JY. Acute Myeloid Leukemia (AML) - Hematology and Oncology [Internet]. MSD Manual Professional Version. 2020 [cited 2022 Jan 18]. Available from: <https://www.msmanuals.com/professional/hematology-and-oncology/leukemias/acute-myeloid-leukemia-aml#v41357234>
8. Arber DA, Erba HP. Diagnosis and Treatment of Patients With Acute Myeloid Leukemia With Myelodysplasia-Related Changes (AML-MRC). *Am J Clin Pathol.* 2020 Dec 1;154(6):731.
9. Briot T, Roger E, Thépot S, Lagarce F. Advances in treatment formulations for acute myeloid leukemia. *Drug Discov Today.* 2018 Dec 1;23(12):1936–49.
10. Short NJ, Rytting ME, Cortes JE. Acute myeloid leukaemia. *Lancet.* 2018 Aug 18;392(10147):593–606.
11. Stone RM, Lindsley C. Older adults with acute myeloid leukemia treated with intensive chemotherapy: “old” prognostic algorithms may not apply. *Haematologica.* 2018 Oct 31;103(11):1758.
12. Ozaki T, Nakagawara A. Role of p53 in Cell Death and Human Cancers. *Cancers (Basel).* 2011 Mar;3(1):994.
13. Nair R, Salinas-Illarena A, Baldauf HM. New strategies to treat AML: novel insights into AML survival pathways and combination therapies. *Leukemia.* 2021;35(2):299–311.
14. Hassan C, Afshinnekoo E, Li S, Wu S, Mason CE. Genetic and epigenetic heterogeneity and the impact on cancer relapse. *Exp Hematol.* 2017 Oct 1;54:26–30.
15. American Cancer Society. Typical Treatment of Acute Myeloid Leukemia (Except APL). 2022.
16. Eleni LD, Nicholas ZC, Alexandros S. Challenges in treating older patients with acute Myeloid Leukemia. *J Oncol.* 2010;2010:11.
17. Estey EH. Acute myeloid leukemia: 2021 update on risk-stratification and management. *Am J Hematol.* 2020 Nov 1;95(11):1368–98.
18. Bazinet A, Assouline S. A review of FDA-approved acute myeloid leukemia therapies beyond “7 + 3.” *Expert Rev Hematol.* 2021;14(2):185–97.
19. Baudino T. Targeted Cancer Therapy: The Next Generation of Cancer Treatment. *Curr Drug Discov Technol.* 2015 Aug 4;12(1):3–20.
20. Tiong IS, Wei AH. New drugs creating new challenges in acute myeloid leukemia. *Genes Chromosom Cancer.* 2019 Dec 11;58(12):903–14.
21. Desikan SP, Daver N, DiNardo C, Kadia T, Konopleva M, Ravandi F. Resistance to targeted therapies: delving into FLT3 and IDH. *Blood Cancer J* 2022 126. 2022 Jun 9;12(6):1–8.
22. Short NJ, Konopleva M, Kadia TM, Borthakur G, Ravandi F, DiNardo CD, et al. Advances in the treatment of acute myeloid leukemia: New drugs and new challenges. *Cancer Discov.* 2020 Apr 1;10(4):506–25.

23. Zhang J, Gu Y, Chen B. Mechanisms of drug resistance in acute myeloid leukemia. *Onco Targets Ther.* 2019;12:1937–45.
24. Yue XY, Chen Q, He JS. Combination strategies to overcome resistance to the BCL2 inhibitor venetoclax in hematologic malignancies. *Cancer Cell Int* 2020 201. 2020 Oct 29;20(1):1–14.
25. Ramsey HE, Fischer MA, Lee T, Gorska AE, Arrate MP, Fuller L, et al. A novel MCL1 inhibitor combined with venetoclax rescues venetoclax-resistant acute myelogenous Leukemia. *Cancer Discov.* 2018 Dec 1;8(12):1566–81.
26. Scholl S, Fleischmann M, Schnetzke U, Heidel FH. Molecular Mechanisms of Resistance to FLT3 Inhibitors in Acute Myeloid Leukemia: Ongoing Challenges and Future Treatments. *Cells.* 2020 Nov 17;9(11).
27. Rechkoblit O, Choudhury JR, Buku A, Prakash L, Prakash S, Aggarwal AK. Structural basis for polymerase  $\eta$ -promoted resistance to the anticancer nucleoside analog cytarabine. *Sci Reports* 2018 81. 2018 Aug 23;8(1):1–9.
28. Li Z, Guo JR, Chen QQ, Wang CY, Zhang WJ, Yao MC, et al. Exploring the Antitumor Mechanism of High-Dose Cytarabine through the Metabolic Perturbations of Ribonucleotide and Deoxyribonucleotide in Human Promyelocytic Leukemia HL-60 Cells. *Mol A J Synth Chem Nat Prod Chem.* 2017 Mar 1;22(3).
29. Lamba JK. Genetic factors influencing cytarabine therapy. *Pharmacogenomics.* 2009;10(10):1657–74.
30. Candelaria M, Corrales-Alfaro C, Gutiérrez-Hernández O, Díaz-Chavez J, Labardini-Méndez J, Vidal-Millán S, et al. Expression Levels of Human Equilibrative Nucleoside Transporter 1 and Deoxycytidine Kinase Enzyme as Prognostic Factors in Patients with Acute Myeloid Leukemia Treated with Cytarabine. *Chemotherapy.* 2016 Apr 13;61(6):313–8.
31. Hubeek I, Stam RW, Peters GJ, Broekhuizen R, Meijerink JPPP, Wering ER Van, et al. The human equilibrative nucleoside transporter 1 mediates in vitro cytarabine sensitivity in childhood acute myeloid leukaemia. *Br J Cancer.* 2005 Dec 12;93(12):1388–94.
32. Abraham A, Varatharajan S, Karathedath S, Philip C, Lakshmi KM, Jayavelu AK, et al. RNA expression of genes involved in cytarabine metabolism and transport predicts cytarabine response in acute myeloid leukemia. *Pharmacogenomics.* 2015 Jul 1;16(8):877–90.
33. Hopper-Borge E, Xu X, Shen T, Shi Z, Chen ZS, Kruh GD. Human multidrug resistance protein 7 (ABCC10) is a resistance factor for nucleoside analogues and epothilone B. *Cancer Res.* 2009 Jan 1;69(1):178.
34. Guo Y, Kock K, Ritter CA, Chen ZS, Grube M, Jedlitschky G, et al. Expression of ABCC-type nucleotide exporters in blasts of adult acute myeloid leukemia: relation to long-term survival. *Clin Cancer Res.* 2009 Mar 1;15(5):1762–9.
35. Giles F, Rizzieri D, Ravandi F, Swords R, Jacobsen TF, O'Brien S. Elacytarabine, a novel 5'-elaidic acid derivative of cytarabine, and idarubicin combination is active in refractory acute myeloid leukemia. *Leuk Res.* 2012 Apr;36(4):e71.
36. Anderson E, Mehta P, Heywood J, Rees B, Bone H, Robinson G, et al. CPX-351 exhibits hENT-independent uptake and can be potentiated by fludarabine in leukaemic cells lines and primary refractory AML. *Leuk Res.* 2018 Nov 1;74:121–9.
37. Voso MT, Larson RA, Jones D, Marcucci G, Prior T, Krauter J, et al. Midostaurin in patients with acute myeloid leukemia and FLT3-TKD mutations: a subanalysis from the RATIFY trial. *Blood Adv.* 2020 Oct 1;4(19):4945–54.
38. Hu S, Niu H, Inaba H, Orwick S, Rose C, Panetta JC, et al. Activity of the Multikinase Inhibitor Sorafenib in Combination With Cytarabine in Acute Myeloid Leukemia. *JNCI J Natl Cancer Inst.* 2011 Jun 6;103(11):893.
39. Deng W, Dai CL, Chen JJ, Kathawala RJ, Sun YL, Chen HF, et al. Tandutinib (MLN518) reverses multidrug resistance by inhibiting the efflux activity of the multidrug resistance protein 7 (ABCC10). *Oncol Rep.* 2013 Jun;29(6):2479.
40. Fajardo-Orduña GR, Ledesma-Martínez E, Aguiñiga-Sánchez I, Mora-García M de L, Weiss-Steider B, Santiago-Osorio E. Inhibitors of Chemoresistance Pathways in Combination with Ara-C to Overcome Multidrug Resistance in AML. A Mini Review. *Int J Mol Sci.* 2021 May 1;22(9).

41. Fulda S, Debatin KM. Apoptosis signaling in tumor therapy. *Ann N Y Acad Sci.* 2004;1028:150–6.
42. Xu Q, Simpson SE, Scialla TJ, Bagg A, Carroll M. Survival of acute myeloid leukemia cells requires PI3 kinase activation. *Blood.* 2003 Aug 1;102(3):972–80.
43. Grandage VL, Gale RE, Lich DC, Khwaja A. PI3-kinase/Akt is constitutively active in primary acute myeloid leukaemia cells and regulates survival and chemoresistance via NF-kappaB, Mapkinase and p53 pathways. *Leukemia.* 2005;19(4):586–94.
44. Brunet A, Bonni A, Zigmond MJ, Lin MZ, Juo P, Hu LS, et al. Akt promotes cell survival by phosphorylating and inhibiting a Forkhead transcription factor. *Cell.* 1999 Mar 19;96(6):857–68.
45. Chen Y, Gan D, Huang Q, Luo X, Lin D, Hu J, et al. Emodin and Its Combination with Cytarabine Induce Apoptosis in Resistant Acute Myeloid Leukemia Cells in Vitro and in Vivo. *Cell Physiol Biochem.* 2018 Aug 1;48(5):2061–73.
46. Kim EK, Jin Kang H, Kim HJ, Lee JW, Kim H, Park KD, et al. Dual PI3K/Akt/mTOR Pathway Inhibitor Potentiate Cytarabine Cytotoxicity For Acute Myeloid Leukemia. *Blood.* 2013 Nov 15;122(21):1289–1289.
47. Sklarz LM, Gladbach YS, Ernst M, Hamed M, Roof C, Sender S, et al. Combination of the PI3K inhibitor Idelalisib with the conventional cytostatics cytarabine and dexamethasone leads to changes in pathway activation that induce anti-proliferative effects in B lymphoblastic leukaemia cell lines. *Cancer Cell Int.* 2020 Aug 12;20(1):1–14.
48. Sampath D, Cortes J, Estrov Z, Du M, Shi Z, Andreeff M, et al. Pharmacodynamics of cytarabine alone and in combination with 7-hydroxystaurosporine (UCN-01) in AML blasts in vitro and during a clinical trial. *Blood.* 2006 Mar 3;107(6):2517.
49. Mesa RA, Loegering D, Powell HL, Flatten K, Arlander SJH, Dai NT, et al. Heat shock protein 90 inhibition sensitizes acute myelogenous leukemia cells to cytarabine. *Blood.* 2005 Jul 1;106(1):318–27.
50. Woods D, Turchi JJ. Chemotherapy induced DNA damage response: convergence of drugs and pathways. *Cancer Biol Ther.* 2013 May;14(5):379–89.
51. Ma J, Li X, Su Y, Zhao J, Luedtke DA, Epshteyn V, et al. Mechanisms responsible for the synergistic antileukemic interactions between ATR inhibition and cytarabine in acute myeloid leukemia cells. *Sci Rep.* 2017 Feb 8;7:41950.
52. Yang C, Boyson CA, Di Liberto M, Huang X, Hannah J, Dorn DC, et al. CDK4/6 Inhibitor PD 0332991 Sensitizes Acute Myeloid Leukemia to Cytarabine-Mediated Cytotoxicity. *Cancer Res.* 2015 May 1;75(9):1838–45.
53. Zhang J, Wang Y, Yin C, Gong P, Zhang Z, Zhao L, et al. Artesunate improves venetoclax plus cytarabine AML cell targeting by regulating the Noxa/Bim/Mcl-1/p-Chk1 axis. *Cell Death Dis* 2022 134. 2022 Apr 20;13(4):1–11.
54. Xie C, Edwards H, Caldwell JT, Wang G, Taub JW, Ge Y. Obatoclax potentiates the cytotoxic effect of cytarabine on acute myeloid leukemia cells by enhancing DNA damage. *Mol Oncol.* 2015 Feb 1;9(2):409–21.
55. Yamauchi T, Negoro E, Kishi S, Takagi K, Yoshida A, Urasaki Y, et al. Intracellular cytarabine triphosphate production correlates to deoxycytidine kinase/cytosolic 5'-nucleotidase II expression ratio in primary acute myeloid leukemia cells. *Biochem Pharmacol.* 2009 Jun 15;77(12):1780–6.
56. Galmarini CM, Thomas X, Graham K, El Jafaari A, Cros E, Jordheim L, et al. Deoxycytidine kinase and cN-II nucleotidase expression in blast cells predict survival in acute myeloid leukaemia patients treated with cytarabine. *Br J Haematol.* 2003;122(1):53–60.
57. Galmarini CM, Graham K, Thomas X, Calvo F, Rousselot P, Jafaari A El, et al. Expression of high Km 5'-nucleotidase in leukemic blasts is an independent prognostic factor in adults with acute myeloid leukemia. *Blood.* 2001 Sep 15;98(6):1922–6.
58. Song JH, Kim SH, Kweon SH, Lee TH, Kim HJHJ, Kim HJHJ, et al. Defective expression of deoxycytidine kinase in cytarabine-resistant acute myeloid leukemia cells. *Int J Oncol.* 2009;34(4):1165–71.
59. Veuger MJT, Heemskerk MHM, Willy Honders M, Willemze R, Barge RMY. Functional role of alternatively spliced deoxycytidine kinase in sensitivity to cytarabine of acute myeloid leukemic cells.

- Blood. 2002 Feb 15;99(4):1373–80.
60. Degwert N, Latuske E, Vohwinkel G, Stamm H, Klokow M, Bokemeyer C, et al. Deoxycytidine kinase is downregulated under hypoxic conditions and confers resistance against cytarabine in acute myeloid leukaemia. *Eur J Haematol*. 2016 Sep 1;97(3):239–44.
  61. Galmarini CM, Thomas X, Calvo F, Rousselot P, Jafaari A El, Cros E, et al. Potential mechanisms of resistance to cytarabine in AML patients. *Leuk Res*. 2002 Jul 1;26(7):621–9.
  62. Levin M, Stark M, Berman B, Assaraf YG. Surmounting Cytarabine-resistance in acute myeloblastic leukemia cells and specimens with a synergistic combination of hydroxyurea and azidothymidine. *Cell Death Dis*. 2019 Jun 1;10(6).
  63. Colly LP, Richel DJ, Arentsen-Honders MW, Kester MGD, ter Riet PM, Willemze R. Increase in Ara-C sensitivity in Ara-C sensitive and -resistant leukemia by stimulation of the salvage and inhibition of the de novo pathway. *Ann Hematol* 1992 651. 1992 Jul;65(1):26–32.
  64. Gao WY, Johns DG, Chokekijchai S, Mitsuya H. Disparate actions of hydroxyurea in potentiation of purine and pyrimidine 2',3'-dideoxynucleoside activities against replication of human immunodeficiency virus. *Proc Natl Acad Sci U S A*. 1995 Aug 8;92(18):8333.
  65. Jädersten M, Lilienthal I, Tsesmetzis N, Lourda M, Bengtzén S, Bohlin A, et al. Targeting SAMHD1 with hydroxyurea in first-line cytarabine-based therapy of newly diagnosed acute myeloid leukaemia: Results from the HEAT-AML trial. *J Intern Med*. 2022 Aug 18;12:18.
  66. Klisovic RB, Blum W, Wei X, Liu S, Liu Z, Xie Z, et al. Phase I Study of GTI-2040, an Antisense to Ribonucleotide Reductase, in Combination with High-Dose Cytarabine in Patients with Acute Myeloid Leukemia. *Clin Cancer Res*. 2008 Jun 15;14(12):3889–95.
  67. Reglero C, Dieck CL, Zask A, Forouhar F, Laurent AP, Lin W-HW, et al. Pharmacological inhibition of NT5C2 reverses genetic and non-genetic drivers of 6-MP resistance in acute lymphoblastic leukemia. *Cancer Discov*. 2022 Aug 19;
  68. Moriyama T, Liu S, Li J, Meyer J, Zhao X, Yang W, et al. Mechanisms of NT5C2-Mediated Thiopurine Resistance in Acute Lymphoblastic Leukemia. *Mol Cancer Ther*. 2019;18(10):1887–95.
  69. Schröder JK, Kirch C, Seeber S, Schütte J. Structural and functional analysis of the cytidine deaminase gene in patients with acute myeloid leukaemia. *Br J Haematol*. 1998;103(4):1096–103.
  70. Schröder JK, Seidelmann M, Kirch HC, Seeber S, Schütte J. Assessment of resistance induction to cytosine arabinoside following transfer and overexpression of the deoxycytidylate deaminase gene in vitro. *Leuk Res*. 1998 Jul;22(7):619–24.
  71. Fanciullino R, Farnault L, Donnette M, Imbs DC, Roche C, Venton G, et al. CDA as a predictive marker for life-threatening toxicities in patients with AML treated with cytarabine. *Blood Adv*. 2018 Mar 13;2(5):462–9.
  72. Bhatla D, Gerbing RB, Alonzo TA, Conner H, Ross JA, Meshinchi S, et al. Cytidine Deaminase Genotype and Toxicity of Cytosine Arabinoside Therapy in Children with Acute Myeloid Leukemia. *Br J Haematol*. 2009 Feb;144(3):388.
  73. Coggins SA, Mahboubi B, Schinazi RF, Kim B. SAMHD1 Functions and Human Diseases. *Viruses* 2020, Vol 12, Page 382. 2020 Mar 31;12(4):382.
  74. Buzovetsky O, Tang C, Knecht KM, Antonucci JM, Wu L, Ji X, et al. The SAM domain of mouse SAMHD1 is critical for its activation and regulation. *Nat Commun*. 2017 Dec 1;9(1).
  75. Kim CA, Bowie JU. SAM domains: uniform structure, diversity of function. *Trends Biochem Sci*. 2003;28(12):625–8.
  76. White TE, Brandariz-Nuñez A, Carlos Valle-Casuso J, Amie S, Nguyen L, Kim B, et al. Contribution of SAM and HD domains to retroviral restriction mediated by human SAMHD1. *Virology*. 2013 Feb 2;436(1):81.
  77. Aravind L, Koonin E V. The HD domain defines a new superfamily of metal-dependent phosphohydrolases. *Trends Biochem Sci*. 1998 Dec 1;23(12):469–72.
  78. Rice GI, Bond J, Asipu A, Brunette RL, Manfield IW, Carr IM, et al. Mutations involved in Aicardi-Goutières syndrome implicate SAMHD1 as regulator of the innate immune response. *Nat Genet*. 2009 Jul 14;41(7):829.

79. Schaller T, Pollpeter D, Apolonia L, Goujon C, Malim MH. Nuclear import of SAMHD1 is mediated by a classical karyopherin  $\alpha/\beta$ 1 dependent pathway and confers sensitivity to VpxMAC induced ubiquitination and proteasomal degradation. *Retrovirology*. 2014 Apr 8;11(1):1–16.
80. Batalis S, Rogers LAC, Hemphill WO, Mauney CH, Ornelles DA, Hollis T. SAMHD1 Phosphorylation at T592 Regulates Cellular Localization and S-phase Progression. *Front Mol Biosci*. 2021 Aug 26;8:832.
81. Baldauf H-M, Pan X, Erikson E, Schmidt S, Daddacha W, Burggraf M, et al. SAMHD1 restricts HIV-1 infection in resting CD4+ T cells. *Nat Med*. 2012 Nov 1;18(11):1682–8.
82. Ryoo J, Choi J, Oh C, Kim S, Seo M, Kim SY, et al. The ribonuclease activity of SAMHD1 is required for HIV-1 restriction. *Nat Med* 2014 208. 2014 Jul 20;20(8):936–41.
83. Schmidt S, Schenkova K, Adam T, Erikson E, Lehmann-Koch J, Sertel S, et al. SAMHD1's protein expression profile in humans. *J Leukoc Biol*. 2015;98:5–14.
84. Franzolin E, Pontarin G, Rampazzo C, Miazzi C, Ferraro P, Palumbo E, et al. The deoxynucleotide triphosphohydrolase SAMHD1 is a major regulator of DNA precursor pools in mammalian cells. *Proc Natl Acad Sci*. 2013 Aug 27;110(35):14272–7.
85. Moore LD, Le T, Fan G. DNA Methylation and Its Basic Function. *Neuropsychopharmacol* 2013 381. 2012 Jul 11;38(1):23–38.
86. De Silva S, Hoy H, Hake TS, Wong HK, Porcu P, Wu L. Promoter methylation regulates SAMHD1 gene expression in human CD4+ T cells. *J Biol Chem*. 2013 Mar 29;288(13):9284–92.
87. Li N, Zhang W, Cao X. Identification of human homologue of mouse IFN-g induced protein from human dendritic cells. *Immunol Lett*. 2000;74:221–4.
88. St Gelais C, de Silva S, Amie SM, Coleman CM, Hoy H, Hollenbaugh JA, et al. SAMHD1 restricts HIV-1 infection in dendritic cells (DCs) by dNTP depletion, but its expression in DCs and primary CD4+ T-lymphocytes cannot be upregulated by interferons. *Retrovirology*. 2012 Dec 11;9:105.
89. Riess M, Fuchs N V., Idica A, Hamdorf M, Flory E, Pedersen IM, et al. Interferons Induce Expression of SAMHD1 in Monocytes through Down-regulation of miR-181a and miR-30a. *J Biol Chem*. 2017 Jan 1;292(1):264.
90. Pilakka-Kanthikeel S, Raymond A, Atluri VSR, Sagar V, Saxena SK, Diaz P, et al. Sterile alpha motif and histidine/aspartic acid domain-containing protein 1 (SAMHD1)-facilitated HIV restriction in astrocytes is regulated by miRNA-181a. *J Neuroinflammation*. 2015 Apr 8;12(1).
91. Jin C, Peng X, Liu F, Cheng L, Lu X, Yao H, et al. MicroRNA-181 expression regulates specific post-transcriptional level of SAMHD1 expression in vitro. *Biochem Biophys Res Commun*. 2014 Sep 26;452(3):760–7.
92. Pauls E, Jimenez E, Ruiz A, Permanyer M, Ballana E, Costa H, et al. Restriction of HIV-1 Replication in Primary Macrophages by IL-12 and IL-18 through the Upregulation of SAMHD1. *J Immunol*. 2013 May 1;190(9):4736–41.
93. Yang S, Zhan Y, Zhou Y, Jiang Y, Zheng X, Yu L, et al. Interferon regulatory factor 3 is a key regulation factor for inducing the expression of SAMHD1 in antiviral innate immunity. *Sci Rep*. 2016 Jul 14;6.
94. Ramos HJ, Gale M. RIG-I like receptors and their signaling crosstalk in the regulation of antiviral immunity. *Curr Opin Virol*. 2011;1(3):167.
95. Buj R, Aird KM. Deoxyribonucleotide Triphosphate Metabolism in Cancer and Metabolic Disease. *Front Endocrinol (Lausanne)*. 2018 Apr 18;9(APR):177.
96. Mauney CH, Hollis T. SAMHD1: Recurring roles in cell cycle, viral restriction, cancer, and innate immunity. *Autoimmunity*. 2018 Apr 3;51(3):96.
97. Goldstone DC, Ennis-Adeniran V, Hedden JJ, Groom HCT, Rice GI, Christodoulou E, et al. HIV-1 restriction factor SAMHD1 is a deoxynucleoside triphosphate triphosphohydrolase. *Nature*. 2011 Dec 6;480(7377):379–82.
98. Lee EJ, Seo JH, Park J-H, Vo TTL, An S, Bae S-J, et al. SAMHD1 acetylation enhances its deoxynucleotide triphosphohydrolase activity and promotes cancer cell proliferation. *Oncotarget*. 2017 Sep 9;8(40):68517.
99. Chabes A, Stillman B. Constitutively high dNTP concentration inhibits cell cycle progression and the

- DNA damage checkpoint in yeast *Saccharomyces cerevisiae*. *Proc Natl Acad Sci U S A*. 2007 Jan 23;104(4):1183–8.
100. Bonifati S, Daly MB, St. Gelais C, Kim SH, Hollenbaugh JA, Shepard C, et al. SAMHD1 controls cell cycle status, apoptosis and HIV-1 infection in monocytic THP-1 cells. *Virology*. 2016 Aug 1;495:92–100.
  101. Pauls E, Ruiz A, Badia R, Permanyer M, Gubern A, Riveira-Muñoz E, et al. Cell cycle control and HIV-1 susceptibility are linked by CDK6-dependent CDK2 phosphorylation of SAMHD1 in myeloid and lymphoid cells. *J Immunol*. 2014 Aug 15;193(4):1988–97.
  102. Arnold LH, Groom HCT, Kunzelmann S, Schwefel D, Caswell SJ, Ordonez P, et al. Phospho-dependent Regulation of SAMHD1 Oligomerisation Couples Catalysis and Restriction. *PLoS Pathog*. 2015;11(10).
  103. Tang C, Ji X, Wu L, Xiong Y. Impaired dNTPase Activity of SAMHD1 by Phosphomimetic Mutation of Thr-592. *J Biol Chem*. 2015 Oct 10;290(44):26352–9.
  104. Patra KK, Bhattacharya A, Bhattacharya S. Uncovering allostery and regulation in SAMHD1 through molecular dynamics simulations. *Proteins*. 2017 Jul 1;85(7):1266–75.
  105. Welbourn S, Dutta SM, Semmes OJ, Strebel K. Restriction of Virus Infection but Not Catalytic dNTPase Activity Is Regulated by Phosphorylation of SAMHD1. *J Virol*. 2013 Nov;87(21):11516.
  106. Bhattacharya A, Wang Z, White T, Buffone C, Nguyen LA, Shepard CN, et al. Effects of T592 phosphomimetic mutations on tetramer stability and dNTPase activity of SAMHD1 can not explain the retroviral restriction defect. *Sci Rep*. 2016 Aug 11;6.
  107. Kretschmer S, Wolf C, König N, Staroske W, Guck J, Häusler M, et al. SAMHD1 prevents autoimmunity by maintaining genome stability. *Ann Rheum Dis*. 2015 Mar 1;74(3):e17–e17.
  108. Hrecka K, Hao C, Gierszewska M, Swanson SK, Kesik-Brodacka M, Srivastava S, et al. Vpx relieves inhibition of HIV-1 infection of macrophages mediated by the SAMHD1 protein. *Nature*. 2011 Jun 30;474(7353):658–61.
  109. Laguette N, Sobhian B, Casartelli N, Ringeard M, Chable-Bessia C, Ségéral E, et al. SAMHD1 is the dendritic- and myeloid-cell-specific HIV-1 restriction factor counteracted by Vpx. *Nature*. 2011 Jun 30;474(7353):654–7.
  110. Gramberg T, Kahle T, Bloch N, Wittmann S, Müllers E, Daddacha W, et al. Restriction of diverse retroviruses by SAMHD1. *Retrovirology*. 2013 Mar 5;10(1):26.
  111. Kim ET, White TE, Brandariz-Núñez A, Diaz-Griffero F, Weitzman MD. SAMHD1 Restricts Herpes Simplex Virus 1 in Macrophages by Limiting DNA Replication. *J Virol*. 2013 Dec;87(23):12949–56.
  112. Zhang K, Lv DW, Li R. Conserved Herpesvirus Protein Kinases Target SAMHD1 to Facilitate Virus Replication. *Cell Rep*. 2019 Jul 7;28(2):449.
  113. Hollenbaugh JA, Gee P, Baker J, Daly MB, Amie SM, Tate J, et al. Host Factor SAMHD1 Restricts DNA Viruses in Non-Dividing Myeloid Cells. *PLOS Pathog*. 2013 Jun;9(6):e1003481.
  114. Saiada F, Zhang K, Li R. PIAS1 potentiates the anti-EBV activity of SAMHD1 through SUMOylation. *Cell Biosci*. 2021 Dec 1;11(1).
  115. Zhang K, Lv D-W, Correspondence RL. Conserved Herpesvirus Protein Kinases Target SAMHD1 to Facilitate Virus Replication. *CellReports*. 2019;28:449-459.e5.
  116. Businger R, Deutschmann J, Gruska I, Milbradt J, Wiebusch L, Gramberg T, et al. Human cytomegalovirus overcomes SAMHD1 restriction in macrophages via pUL97. *Nat Microbiol* 2019 412. 2019 Sep 23;4(12):2260–72.
  117. Kim ET, Roche KL, Kulej K, Spruce LA, Seeholzer SH, Coen DM, et al. SAMHD1 Modulates Early Steps during Human Cytomegalovirus Infection by Limiting NF- $\kappa$ B Activation. *Cell Rep*. 2019 Jul 7;28(2):434.
  118. Lahouassa H, Daddacha W, Hofmann H, Ayinde D, Logue EC, Dragin L, et al. SAMHD1 restricts the replication of human immunodeficiency virus type 1 by depleting the intracellular pool of deoxynucleoside triphosphates. *Nat Immunol*. 2012 Mar;13(3):223–8.
  119. De Meo S, Dell'Oste V, Molfetta R, Tassinari V, Lotti LV, Vespa S, et al. SAMHD1 phosphorylation

- and cytoplasmic relocalization after human cytomegalovirus infection limits its antiviral activity. *PLoS Pathog.* 2020 Sep 1;16(9).
120. Martinat C, Cormier A, Tobaly-Tapiero J, Palmic N, Casartelli N, Coggins SA, et al. SUMOylation of SAMHD1 at Lysine 595 is required for HIV-1 restriction in non-cycling cells. *bioRxiv.* 2020 Jun 5;2020.06.04.133439.
  121. Hyeon S, Lee MK, Kim YE, Lee GM, Ahn JH. Degradation of SAMHD1 Restriction Factor Through Cullin-Ring E3 Ligase Complexes During Human Cytomegalovirus Infection. *Front Cell Infect Microbiol.* 2020 Jul 30;10:391.
  122. Hofmann H, Logue EC, Bloch N, Daddacha W, Polsky SB, Schultz ML, et al. The Vpx lentiviral accessory protein targets SAMHD1 for degradation in the nucleus. *J Virol.* 2012 Dec;86(23):12552–60.
  123. Baldauf HM, Stegmann L, Schwarz SM, Ambiel I, Trotard M, Martin M, et al. Vpx overcomes a SAMHD1-independent block to HIV reverse transcription that is specific to resting CD4 T cells. *Proc Natl Acad Sci U S A.* 2017 Mar 7;114(10):2729–34.
  124. Daddacha W, Koyen AE, Bastien AJ, Head PESE, Dhere VR, Nabeta GN, et al. SAMHD1 Promotes DNA End Resection to Facilitate DNA Repair by Homologous Recombination. *Cell Rep.* 2017 Aug 8;20 8(8):1921.
  125. Felip E, Gutiérrez-Chamorro L, Gómez M, Garcia-Vidal E, Romeo M, Morán T, et al. Modulation of DNA Damage Response by SAM and HD Domain Containing Deoxynucleoside Triphosphate Triphosphohydrolase (SAMHD1) Determines Prognosis and Treatment Efficacy in Different Solid Tumor Types. *Cancers (Basel).* 2022 Feb 1;14(3).
  126. Akimova E, Gassner FJ, Schubert M, Rebhandl S, Arzt C, Rauscher S, et al. SAMHD1 restrains aberrant nucleotide insertions at repair junctions generated by DNA end joining. *Nucleic Acids Res.* 2021 Mar 18;49(5):2598–608.
  127. Husain A, Xu J, Fujii H, Nakata M, Kobayashi M, Wang J, et al. SAMHD1-mediated dNTP degradation is required for efficient DNA repair during antibody class switch recombination. *EMBO J.* 2020 Aug 3;39(15).
  128. Dewannieux M, Heidmann T. Endogenous retroviruses: acquisition, amplification and taming of genome invaders. *Curr Opin Virol.* 2013;3(6):646–56.
  129. Cordaux R, Batzer MA. The impact of retrotransposons on human genome evolution. *Nat Rev Genet.* 2009 Oct;10(10):691.
  130. Zhao K, Du J, Han X, Goodier JL, Li P, Zhou X, et al. Modulation of LINE-1 and Alu/SVA Retrotransposition by Aicardi-Goutières Syndrome-Related SAMHD1. *Cell Rep.* 2013 Sep 9;4(6):1108.
  131. Herrmann A, Wittmann S, Thomas D, Shepard CN, Kim B, Ferreirós N, et al. The SAMHD1-mediated block of LINE-1 retroelements is regulated by phosphorylation. *Mob DNA.* 2018 Mar 28;9(1).
  132. Hu S, Li J, Xu F, Mei S, Le Duff Y, Yin L, et al. SAMHD1 Inhibits LINE-1 Retrotransposition by Promoting Stress Granule Formation. *PLoS Genet.* 2015 Jul 1;11(7).
  133. Chen Z, Hu J, Ying S, Xu A. Dual roles of SAMHD1 in tumor development and chemoresistance to anticancer drugs (Review). *Oncol Lett.* 2021 Jun 1;21(6):1–10.
  134. Zhang X, Zhang R, Yu J. New Understanding of the Relevant Role of LINE-1 Retrotransposition in Human Disease and Immune Modulation. *Front Cell Dev Biol.* 2020 Aug 7;8:657.
  135. Schott K, Majer C, Bulashevskaya A, Childs L, Schmidt MHH, Rajalingam K, et al. SAMHD1 in cancer: curse or cure? *J Mol Med (Berl).* 2022 Mar 1;100(3):351.
  136. Reisländer T, Groelly FJ, Tarsounas M. DNA Damage and Cancer Immunotherapy: A STING in the Tale. *Mol Cell.* 2020 Oct 1;80(1):21–8.
  137. Coquel F, Silva MJ, Técher H, Zadorozhny K, Sharma S, Nieminuszczy J, et al. SAMHD1 acts at stalled replication forks to prevent interferon induction. *Nat* 2018 5577703. 2018 Apr 18;557(7703):57–61.
  138. Yu R, Zhu B, Chen D. Type I interferon-mediated tumor immunity and its role in immunotherapy. *Cell Mol Life Sci.* 2022 Mar 1;79(3):1–24.
  139. Goodman AM, Kato S, Bazhenova L, Patel SP, Frampton GM, Miller V, et al. Tumor mutational

- burden as an independent predictor of response to immunotherapy in diverse cancers. *Mol Cancer Ther.* 2017 Nov 1;16(11):2598–608.
140. Chen M, Linstra R, van Vugt MATM. Genomic instability, inflammatory signaling and response to cancer immunotherapy. *Biochim Biophys Acta - Rev Cancer.* 2022 Jan 1;1877(1):188661.
  141. Galmarini CM, Mackey JR, Dumontet C. Nucleoside analogues and nucleobases in cancer treatment. *Lancet Oncol.* 2002 Jul 1;3(7):415–24.
  142. Knecht KM, Buzovetsky O, Schneider C, Thomas D, Srikanth V, Kaderali L, et al. The structural basis for cancer drug interactions with the catalytic and allosteric sites of SAMHD1. *Proc Natl Acad Sci U S A.* 2018 Oct 23;115(43):E10022–31.
  143. Herold N, Rudd SG, Sanjiv K, Kutzner J, Bladh J, Paulin CBJ, et al. SAMHD1 protects cancer cells from various nucleoside-based antimetabolites. *Cell Cycle.* 2017;16:1029–38.
  144. Rothenburger T, McLaughlin KM, Herold T, Schneider C, Oellerich T, Rothweiler F, et al. SAMHD1 is a key regulator of the lineage-specific response of acute lymphoblastic leukaemias to nelarabine. *Commun Biol* 2020 31. 2020 Jun 24;3(1):1–10.
  145. Schneider C, Oellerich T, Baldauf H-MM, Schwarz SM, Thomas D, Flick R, et al. SAMHD1 is a biomarker for cytarabine response and a therapeutic target in acute myeloid leukemia. *Nat Med.* 2017 Feb 1;23(2):250–5.
  146. Oellerich T, Schneider C, Thomas D, Knecht KM, Buzovetsky O, Kaderali L, et al. Selective inactivation of hypomethylating agents by SAMHD1 provides a rationale for therapeutic stratification in AML. *Nat Commun.* 2019 Dec 1;10(1):3475.
  147. Rassidakis GZ, Herold N, Myrberg IH, Tsesmetzis N, Rudd SG, Henter JI, et al. Low-level expression of SAMHD1 in acute myeloid leukemia (AML) blasts correlates with improved outcome upon consolidation chemotherapy with high-dose cytarabine-based regimens. *Blood Cancer J* 2018 811. 2018 Oct 19;8(11):1–10.
  148. Rudd SG, Tsesmetzis N, Sanjiv K, Paulin CB, Sandhow L, Kutzner J, et al. Ribonucleotide reductase inhibitors suppress SAMHD1 ara-CTPase activity enhancing cytarabine efficacy. *EMBO Mol Med.* 2020 Mar 6;12(3):e10419.
  149. Mauney CH, Perrino FW, Hollis T. Identification of Inhibitors of the dNTP Triphosphohydrolase SAMHD1 Using a Novel and Direct High-Throughput Assay. *Biochemistry.* 2018 Nov 11;57(47):6624.
  150. Coffin J, Hughes S, Varmus H. Overview of Retroviral Assembly. In: *Retroviruses.* Cold Spring Harbor Laboratory Press; 1997.
  151. Malim MH, Emerman M. HIV-1 accessory proteins--ensuring viral survival in a hostile environment. *Cell Host Microbe.* 2008 Jun 12;3(6):388–98.
  152. Cooray S, Howe SJ, Thrasher AJ. Retrovirus and Lentivirus Vector Design and Methods of Cell Conditioning. *Methods Enzymol.* 2012 Jan 1;507:29–57.
  153. Escors D, Breckpot K. Lentiviral vectors in gene therapy: their current status and future potential. *Arch Immunol Ther Exp (Warsz).* 2010 Apr;58(2):107.
  154. Bukrinsky MI, Haggerty S, Dempsey MP, Sharova N, Adzhubei A, Spitz L, et al. A nuclear localization signal within HIV-1 matrix protein that governs infection of non-dividing cells. *Nature.* 1993 Oct 10;365(6447):666.
  155. Boso G, Kozak CA. Retroviral Restriction Factors and Their Viral Targets: Restriction Strategies and Evolutionary Adaptations. *Microorganisms.* 2020 Dec 1;8(12):1–34.
  156. Neil SJD, Zang T, Bieniasz PD. Tetherin inhibits retrovirus release and is antagonized by HIV-1 Vpu. *Nature.* 2008 Jan 24;451(7177):425–30.
  157. Yu X, Yu Y, Liu B, Luo K, Kong W, Mao P, et al. Induction of APOBEC3G ubiquitination and degradation by an HIV-1 Vif-Cul5-SCF complex. *Science.* 2003 Nov 7;302(5647):1056–60.
  158. Berger G, Durand S, Fargier G, Nguyen XN, Cordeil S, Bouaziz S, et al. APOBEC3A Is a Specific Inhibitor of the Early Phases of HIV-1 Infection in Myeloid Cells. *PLOS Pathog.* 2011 Sep;7(9):e1002221.
  159. Rosa A, Chande A, Ziglio S, De Sanctis V, Bertorelli R, Goh SL, et al. HIV-1 Nef promotes infection



- by excluding SERINC5 from virion incorporation. *Nature*. 2015 Oct 10;526(7572):212.
160. Lim ES, Fregoso OI, McCoy CO, Matsen FA, Malik HS, Emerman M. The ability of primate lentiviruses to degrade the monocyte restriction factor SAMHD1 preceded the birth of the viral accessory protein Vpx. *Cell Host Microbe*. 2012;11(2):194.
  161. Laguette N, Rahm N, Sobhian B, Chable-Bessia C, Münch J, Snoeck J, et al. Evolutionary and Functional Analyses of the Interaction between the Myeloid Restriction Factor SAMHD1 and the Lentiviral Vpx Protein. *Cell Host Microbe*. 2012 Feb 2;11(2):205.
  162. Sakai Y, Miyake A, Doi N, Sasada H, Miyazaki Y, Adachi A, et al. Expression profiles of Vpx/Vpr proteins are co-related with the primate lentiviral lineage. *Front Microbiol*. 2016 Aug 3;7(AUG):1211.
  163. Schwefel D, Groom HCT, Boucherit VC, Christodoulou E, Walker PA, Stoye JP, et al. Structural basis of lentiviral subversion of a cellular protein degradation pathway. *Nature*. 2014 Dec 15;505(7482):234–8.
  164. Miyake A, Fujita M, Fujino H, Koga R, Kawamura S, Otsuka M, et al. Poly-proline motif in HIV-2 Vpx is critical for its efficient translation. *J Gen Virol*. 2014 Jan 1;95(PART 1):179–89.
  165. Selig L, Pages J-C, Tanchou V, Prévéral S, Berlioz-Torrent C, Liu LX, et al. Interaction with the p6 Domain of the Gag Precursor Mediates Incorporation into Virions of Vpr and Vpx Proteins from Primate Lentiviruses. *J Virol*. 1999 Jan;73(1):592–600.
  166. Mahalingam S, Van Tine B, Santiago ML, Gao F, Shaw GM, Hahn BH. Functional Analysis of the Simian Immunodeficiency Virus Vpx Protein: Identification of Packaging Determinants and a Novel Nuclear Targeting Domain. *J Virol*. 2001 Jan;75(1):362–74.
  167. Berger G, Turpin J, Cordeil S, Tartour K, Nguyen XN, Mahieux R, et al. Functional Analysis of the Relationship between Vpx and the Restriction Factor SAMHD1. *J Biol Chem*. 2012 Nov 30;287(49):41210–7.
  168. Kumar PR, Singhal PK, Vinod SS, Mahalingam S. A non-canonical transferable signal mediates nuclear import of simian immunodeficiency virus Vpx protein. *J Mol Biol*. 2003 Aug 29;331(5):1141–56.
  169. Belshan M, Ratner L. Identification of the nuclear localization signal of human immunodeficiency virus type 2 Vpx. *Virology*. 2003 Jun 20;311(1):7–15.
  170. Belshan M, Mahnke LA, Ratner L. Conserved amino acids of the human immunodeficiency virus type 2 Vpx nuclear localization signal are critical for nuclear targeting of the viral preintegration complex in non-dividing cells. *Virology*. 2006 Mar 1;346(1):118–26.
  171. Singh SP, Raja S, Mahalingam S. Viral protein X unlocks the nuclear pore complex through a human Nup153-dependent pathway to promote nuclear translocation of the lentiviral genome. *Mol Biol Cell*. 2020 Feb 15;31(4):304–17.
  172. Kumar PR, Singhal PK, Subba Rao MRK, Mahalingam S. Phosphorylation by MAPK regulates simian immunodeficiency virus Vpx protein nuclear import and virus infectivity. *J Biol Chem*. 2005 Mar 4;280(9):8553–63.
  173. Peng G, Greenwell-Wild T, Nares S, Jin W, Ke JL, Rangel ZG, et al. Myeloid differentiation and susceptibility to HIV-1 are linked to APOBEC3 expression. *Blood*. 2007 Jul 7;110(1):393.
  174. Berger A, Münk C, Schweizer M, Cichutek K, Schüle S, Flory E. Interaction of Vpx and Apolipoprotein B mRNA-editing Catalytic Polypeptide 3 Family Member A (APOBEC3A) Correlates with Efficient Lentivirus Infection of Monocytes. *J Biol Chem*. 2010 Apr 4;285(16):12248–54.
  175. Tchasovnikarova IA, Timms RT, Matheson NJ, Wals K, Antrobus R, Göttgens B, et al. Epigenetic silencing by the HUSH complex mediates position-effect variegation in human cells. *Science*. 2015 Jun 6;348(6242):1481.
  176. Yurkovetskiy L, Guney MH, Kim K, Goh SL, McCauley S, Dauphin A, et al. Primate immunodeficiency virus proteins Vpx and Vpr counteract transcriptional repression of proviruses by the HUSH complex. *Nat Microbiol* 2018 312. 2018 Oct 8;3(12):1354–61.
  177. Chougui G, Munir-Matloob S, Matkovic R, Martin MM, Morel M, Lahouassa H, et al. HIV-2/SIV viral protein X counteracts HUSH repressor complex. *Nat Microbiol*. 2018 Aug 1;3(8):891–7.
  178. Ahn J, Hao C, Yan J, DeLucia M, Mehrens J, Wang C, et al. HIV/simian immunodeficiency virus (SIV) accessory virulence factor Vpx loads the host cell restriction factor SAMHD1 onto the E3 ubiquitin

- ligase complex CRL4DCAF1. *J Biol Chem.* 2012 Apr 6;287(15):12550–8.
179. Schaller T, Bauby H, Hué S, Malim MH, Goujon C. New insights into an X-traordinary viral protein. *Front Microbiol.* 2014;5(APR):1–14.
180. Brandariz-Nuñez A, Valle-Casuso JC, White TE, Laguette N, Benkirane M, Brojatsch J, et al. Role of SAMHD1 nuclear localization in restriction of HIV-1 and SIVmac. *Retrovirology.* 2012 Jun 12;9(1):1–12.
181. Jáuregui P, Logue EC, Schultz ML, Fung S, Landau NR. Degradation of SAMHD1 by Vpx Is Independent of Uncoating. *J Virol.* 2015 May 5;89(10):5701.
182. Kim B, Nguyen LA, Daddacha W, Hollenbaugh JA. Tight interplay among SAMHD1 protein level, cellular dNTP levels, and HIV-1 proviral DNA synthesis kinetics in human primary monocyte-derived macrophages. *J Biol Chem.* 2012 Jun 22;287(26):21570–4.
183. Hollenbaugh J, Tao S, Lenzi G, Ryu S, Kim D, Diaz-Griffero F, et al. dNTP pool modulation dynamics by SAMHD1 protein in monocyte-derived macrophages. *Retrovirology.* 2014;11(63).
184. Miyakawa K, Matsunaga S, Yokoyama M, Nomaguchi M, Kimura Y, Nishi M, et al. PIM kinases facilitate lentiviral evasion from SAMHD1 restriction via Vpx phosphorylation. *Nat Commun.* 2019 Dec 1;10(1).
185. Sun Y, Zheng L, Yang Y, Qian X, Fu T, Li X, et al. Metal–Organic Framework Nanocarriers for Drug Delivery in Biomedical Applications. *Nano-Micro Lett* 2020 121. 2020 May 2;12(1):1–29.
186. Zhou HC, Long JR, Yaghi OM. Introduction to metal-organic frameworks. *Chem Rev.* 2012 Feb 8;112(2):673–4.
187. Huxford RC, Della Rocca J, Lin W. Metal–organic frameworks as potential drug carriers. *Curr Opin Chem Biol.* 2010 Apr 1;14(2):262–8.
188. Bunzen H, Grzywa M, Hambach M, Spirkl S, Volkmer D. From Micro to Nano: A Toolbox for Tuning Crystal Size and Morphology of Benzotriazolate-Based Metal-Organic Frameworks. *Cryst Growth Des.* 2016 Jun 1;16(6):3190–7.
189. Sun CY, Qin C, Wang XL, Su ZM. Metal-organic frameworks as potential drug delivery systems. *Expert Opin Drug Deliv.* 2012 Jan;10(1):89–101.
190. Horcajada P, Gref R, Baati T, Allan PK, Maurin G, Couvreur P, et al. Metal-organic frameworks in biomedicine. *Chem Rev.* 2012 Feb 8;112(2):1232–68.
191. Sharabati M Al, Sabouni R, Hussein GA. Biomedical Applications of Metal–Organic Frameworks for Disease Diagnosis and Drug Delivery: A Review. *Nanomaterials.* 2022 Jan 1;12(2):277.
192. Lu K, He C, Guo N, Chan C, Ni K, Lan G, et al. Low-dose X-ray radiotherapy–radiodynamic therapy via nanoscale metal–organic frameworks enhances checkpoint blockade immunotherapy. *Nat Biomed Eng* 2018 28. 2018 Mar 26;2(8):600–10.
193. Zhang H, Jiang W, Liu R, Zhang J, Zhang D, Li Z, et al. Rational Design of Metal Organic Framework Nanocarrier-Based Codelivery System of Doxorubicin Hydrochloride/Verapamil Hydrochloride for Overcoming Multidrug Resistance with Efficient Targeted Cancer Therapy. *ACS Appl Mater Interfaces.* 2017 Jun 14;9(23):19687–97.
194. Wang XG, Dong ZY, Cheng H, Wan SS, Chen WH, Zou MZ, et al. A multifunctional metal–organic framework based tumor targeting drug delivery system for cancer therapy. *Nanoscale.* 2015 Sep 24;7(38):16061–70.
195. Cai W, Gao H, Chu C, Wang X, Wang J, Zhang P, et al. Engineering phototheranostic nanoscale metal-organic frameworks for multimodal imaging-guided cancer therapy. *ACS Appl Mater Interfaces.* 2017 Jan 25;9(3):2040–51.
196. Mao D, Hu F, Kenry, Ji S, Wu W, Ding D, et al. Metal–Organic-Framework-Assisted In Vivo Bacterial Metabolic Labeling and Precise Antibacterial Therapy. *Adv Mater.* 2018 May 1;30(18):1706831.
197. Li Y, Zhang K, Liu P, Chen M, Zhong Y, Ye Q, et al. Encapsulation of Plasmid DNA by Nanoscale Metal–Organic Frameworks for Efficient Gene Transportation and Expression. *Adv Mater.* 2019 Jul 1;31(29):1901570.
198. Chen Q, Xu M, Zheng W, Xu T, Deng H, Liu J. Se/Ru-Decorated Porous Metal-Organic Framework

- Nanoparticles for the Delivery of Pooled siRNAs to Reversing Multidrug Resistance in Taxol-Resistant Breast Cancer Cells. *ACS Appl Mater Interfaces*. 2017 Mar 1;9(8):6712–24.
199. Linnane E, Haddad S, Melle F, Mei Z, Fairen-Jimenez D. The uptake of metal–organic frameworks: a journey into the cell. *Chem Soc Rev*. 2022 Jul 7;51(14):6065–86.
200. Fu A, Tang R, Hardie J, Farkas ME, Rotello VM. Promises and Pitfalls of Intracellular Delivery of Proteins. *Bioconjug Chem*. 2014 Sep 9;25(9):1602–8.
201. Guo Y, Li Y, Zhou S, Ye Q, Zan X, He Y. Metal-Organic Framework-Based Composites for Protein Delivery and Therapeutics. *ACS Biomater Sci Eng*. 2021 Oct 10;8(10):4028–38.
202. Röder R, Preiß T, Hirschle P, Steinborn B, Zimpel A, Höhn M, et al. Multifunctional Nanoparticles by Coordinative Self-Assembly of His-Tagged Units with Metal-Organic Frameworks. *J Am Chem Soc*. 2017 Feb 15;139(6):2359–68.
203. Zhou Y, Liu L, Cao Y, Yu S, He C, Chen X. A Nanocomposite Vehicle Based on Metal-Organic Framework Nanoparticle Incorporated Biodegradable Microspheres for Enhanced Oral Insulin Delivery. *ACS Appl Mater Interfaces*. 2020 May 20;12(20):22581–92.
204. Ernsting MJ, Murakami M, Roy A, Li SD. Factors controlling the pharmacokinetics, biodistribution and intratumoral penetration of nanoparticles. *J Control Release*. 2013;172(3):782–94.
205. Orellana-Tavra C, Mercado SA, Fairen-Jimenez D, Orellana-Tavra C, Mercado SA, Fairen-Jimenez D. Endocytosis Mechanism of Nano Metal-Organic Frameworks for Drug Delivery. *Adv Healthc Mater*. 2016 Sep 1;5(17):2261–70.
206. Abánades Lázaro I, Haddad S, Sacca S, Orellana-Tavra C, Fairen-Jimenez D, Forgan RS. Selective Surface PEGylation of UiO-66 Nanoparticles for Enhanced Stability, Cell Uptake, and pH-Responsive Drug Delivery. *Chem*. 2017 Apr 13;2(4):561–78.
207. Petrak K. Essential properties of drug-targeting delivery systems. *Drug Discov Today*. 2005 Dec 1;10(23–24):1667–73.
208. Abánades Lázaro I, Haddad S, Rodrigo-Muñoz JM, Orellana-Tavra C, Del Pozo V, Fairen-Jimenez D, et al. Mechanistic Investigation into the Selective Anticancer Cytotoxicity and Immune System Response of Surface-Functionalized, Dichloroacetate-Loaded, UiO-66 Nanoparticles. *ACS Appl Mater Interfaces*. 2018 Feb 14;10(6):5255–68.
209. Lindgren M, Hällbrink M, Prochiantz A, Langel Ü. Cell-penetrating peptides. *Trends Pharmacol Sci*. 2000 Mar 1;21(3):99–103.
210. Reissmann S. Cell penetration: scope and limitations by the application of cell-penetrating peptides. *J Pept Sci*. 2014 Oct 1;20(10):760–84.
211. Järver P, Langel Ü. Cell-penetrating peptides—A brief introduction. *Biochim Biophys Acta - Biomembr*. 2006 Mar 1;1758(3):260–3.
212. Gräslund A, Madani F, Lindberg S, Langel Ü, Futaki S. Mechanisms of Cellular Uptake of Cell-Penetrating Peptides. *J Biophys*. 2011;2011(414729).
213. Duchardt F, Fotin-Mleczek M, Schwarz H, Fischer R, Brock R. A Comprehensive Model for the Cellular Uptake of Cationic Cell-penetrating Peptides. *Traffic*. 2007 Jul 1;8(7):848–66.
214. Ziegler A. Thermodynamic studies and binding mechanisms of cell-penetrating peptides with lipids and glycosaminoglycans. *Adv Drug Deliv Rev*. 2008 Mar 1;60(4–5):580–97.
215. Subrizi A, Tuominen E, Bunker A, Róg T, Antopolsky M, Urtti A. Tat(48-60) peptide amino acid sequence is not unique in its cell penetrating properties and cell-surface glycosaminoglycans inhibit its cellular uptake. *J Control Release*. 2012 Mar 10;158(2):277–85.
216. Kalafatovic D, Giralt E. Cell-Penetrating Peptides: Design Strategies beyond Primary Structure and Amphipathicity. *Mol* 2017, Vol 22, Page 1929. 2017 Nov 8;22(11):1929.
217. Console S, Marty C, García-Echeverría C, Schwendener R, Ballmer-Hofer K. Antennapedia and HIV Transactivator of Transcription (TAT) “Protein Transduction Domains” Promote Endocytosis of High Molecular Weight Cargo upon Binding to Cell Surface Glycosaminoglycans. *J Biol Chem*. 2003 Sep 12;278(37):35109–14.
218. Foged C, Nielsen HM. Cell-penetrating peptides for drug delivery across membrane barriers. *Expert*

- Opin Drug Deliv. 2007 Jan;5(1):105–17.
219. Lee JY, Choi YS, Suh JS, Kwon YM, Yang VC, Lee SJ, et al. Cell-penetrating chitosan/doxorubicin/TAT conjugates for efficient cancer therapy. *Int J Cancer*. 2011 May 15;128(10):2470–80.
220. Dubikovskaya EA, Thorne SH, Pillow TH, Contag CH, Wender PA. Overcoming multidrug resistance of small-molecule therapeutics through conjugation with releasable octaarginine transporters. *Proc Natl Acad Sci U S A*. 2008 Aug 26;105(34):12128–33.
221. Dietz GPH, Kilic E, Bähr M. Inhibition of Neuronal Apoptosis in Vitro and in Vivo Using TAT-Mediated Protein Transduction. *Mol Cell Neurosci*. 2002 Sep 1;21(1):29–37.
222. Shin MC, Zhao J, Zhang J, Huang Y, He H, Wang M, et al. Recombinant TAT–gelonin fusion toxin: Synthesis and characterization of heparin/protamine-regulated cell transduction. *J Biomed Mater Res Part A*. 2015 Jan 1;103(1):409–19.
223. Davé SH, Tilstra JS, Matsuoka K, Li F, Karrasch T, Uno JK, et al. Amelioration of Chronic Murine Colitis by Peptide-Mediated Transduction of the I $\kappa$ B Kinase Inhibitor NEMO Binding Domain Peptide. *J Immunol*. 2007 Dec 1;179(11):7852–9.
224. Eguchi A, Dowdy SF. siRNA delivery using peptide transduction domains. *Trends Pharmacol Sci*. 2009 Jul 1;30(7):341–5.
225. Davidson TJ, Harel S, Arboleda VA, Prunell GF, Shelanski ML, Greene LA, et al. Highly Efficient Small Interfering RNA Delivery to Primary Mammalian Neurons Induces MicroRNA-Like Effects before mRNA Degradation. *J Neurosci*. 2004 Nov 10;24(45):10040–6.
226. Koshkaryev A, Piroyan A, Torchilin VP. Bleomycin in octaarginine-modified fusogenic liposomes results in improved tumor growth inhibition. *Cancer Lett*. 2013 Jul 1;334(2):293–301.
227. Chen Y, Xie X, Wu A, Wang L, Hu Y, Zhang H, et al. A synthetic cell-penetrating peptide derived from nuclear localization signal of EPS8 exerts anticancer activity against acute myeloid leukemia. *J Exp Clin Cancer Res*. 2018 Jan 22;37(1):1–15.
228. Shah KK, Whitaker RH, Busby T, Hu J, Shi B, Wang Z, et al. Specific inhibition of DPY30 activity by ASH2L-derived peptides suppresses blood cancer cell growth. *Exp Cell Res*. 2019 Sep 15;382(2):111485.
229. Matijass M, Neundorff I. Cell-penetrating peptides as part of therapeutics used in cancer research. *Med Drug Discov*. 2021 Jun 1;10:100092.
230. Xie J, Bi Y, Zhang H, Dong S, Teng L, Lee RJ, et al. Cell-Penetrating Peptides in Diagnosis and Treatment of Human Diseases: From Preclinical Research to Clinical Application. *Front Pharmacol*. 2020 May 20;11.
231. Kim GC, Cheon DH, Lee Y. Challenge to overcome current limitations of cell-penetrating peptides. *Biochim Biophys Acta - Proteins Proteomics*. 2021 Apr 1;1869(4):140604.
232. Kilk K, Mahlapuu R, Soomets U, Langel Ü. Analysis of in vitro toxicity of five cell-penetrating peptides by metabolic profiling. *Toxicology*. 2009 Nov 30;265(3):87–95.
233. Shin MC, Zhang J, Min KA, Lee K, Byun Y, David AE, et al. Cell-penetrating peptides: achievements and challenges in application for cancer treatment. *J Biomed Mater Res A*. 2014 Feb;102(2):575.
234. Schwarze SR, Ho A, Vocero-Akbani A, Dowdy SF. In vivo protein transduction: Delivery of a biologically active protein into the mouse. *Science (80- )*. 1999 Sep 3;285(5433):1569–72.
235. Foerg C, Weller KM, Rechsteiner H, Nielsen HM, Fernández-Carneado J, Brunisholz R, et al. Metabolic Cleavage and Translocation Efficiency of Selected Cell Penetrating Peptides: A Comparative Study with Epithelial Cell Cultures. *AAPS J*. 2008 Jun;10(2):349.
236. Elmquist A, Langel Ü. In vitro uptake and stability study of pVEC and its all-D analog. *Biol Chem*. 2003 Mar 1;384(3):387–93.
237. Lindgren ME, H MM, Elmquist AM, Langel U. Passage of cell-penetrating peptides across a human epithelial cell layer in vitro. *Biochem J*. 2004;377:69–76.
238. Patel SG, Sayers EJ, He L, Narayan R, Williams TL, Mills EM, et al. Cell-penetrating peptide sequence and modification dependent uptake and subcellular distribution of green florescent protein in different

- cell lines. *Sci Reports* 2019 91. 2019 Apr 18;9(1):1–9.
239. He Y, Li F, Huang Y. Smart Cell-Penetrating Peptide-Based Techniques for Intracellular Delivery of Therapeutic Macromolecules. *Adv Protein Chem Struct Biol.* 2018 Jan 1;112:183–220.
240. Kondo E, Iioka H, Saito K. Tumor-homing peptide and its utility for advanced cancer medicine. *Cancer Sci.* 2021 Jun 1;112(6):2118.
241. Kondo E, Saito K, Tashiro Y, Kamide K, Uno S, Furuya T, et al. Tumour lineage-homing cell-penetrating peptides as anticancer molecular delivery systems. *Nat Commun.* 2012 Jan 17;3(1):951.
242. Fominaya J, Bravo J, Rebollo A. Strategies to stabilize cell penetrating peptides for in vivo applications. *Ther Deliv.* 2015 Oct 1;6(10):1171–94.
243. Mueller J, Kretzschmar I, Volkmer R, Boisguerin P. Comparison of cellular uptake using 22 CPPs in 4 different cell lines. *Bioconjug Chem.* 2008 Dec 17;19(12):2363–74.
244. Erazo-Oliveras A, Muthukrishnan N, Baker R, Wang TY, Pellois JP. Improving the Endosomal Escape of Cell-Penetrating Peptides and Their Cargos: Strategies and Challenges. *Pharmaceuticals.* 2012 Nov 1;5(11):1177.
245. Tagliamonte M, Tornesello ML, Buonaguro FM, Buonaguro L. Virus-Like Particles. In: *Micro- and Nanotechnology in Vaccine Development.* William Andrew Publishing; 2017. p. 205–19.
246. Rodríguez-Limas WA, Tyo KEJ, Nielsen J, Ramírez OT, Palomares LA. Molecular and process design for rotavirus-like particle production in *Saccharomyces cerevisiae*. *Microb Cell Fact.* 2011 May 14;10(1):1–10.
247. Uma M, Rao PP, Nagalekshmi K, Hegde NR. Expression and purification of polioviral proteins in *E. coli*, and production of antisera as reagents for immunological assays. *Protein Expr Purif.* 2016;128:115–22.
248. Muratori C, Bona R, Federico M. Lentivirus-based virus-like particles as a new protein delivery tool. *Methods Mol Biol.* 2010;614:111–24.
249. Wu DT, Roth MJ. MLV based viral-like-particles for delivery of toxic proteins and nuclear transcription factors. *Biomaterials.* 2014;35(29):8416.
250. Mortola E, Roy P. Efficient assembly and release of SARS coronavirus-like particles by a heterologous expression system. *FEBS Lett.* 2004 Oct 8;576(1–2):174–8.
251. Krol E, Brzuska G, Szewczyk B. Production and Biomedical Application of Flavivirus-like Particles. *Trends Biotechnol.* 2019 Nov 1;37(11):1202–16.
252. Xu YF, Zhang YQ, Xu XM, Song GX. Papillomavirus virus-like particles as vehicles for the delivery of epitopes or genes. *Arch Virol.* 2006 Nov;151(11):2133–48.
253. Neukirch L, Nielsen TK, Laursen H, Daradoumis J, Thirion C, Holst PJ. Adenovirus based virus-like-vaccines targeting endogenous retroviruses can eliminate growing colorectal cancers in mice. *Oncotarget.* 2019 Feb 2;10(14):1458.
254. Nooraei S, Bahrulolum H, Hoseini ZS, Katalani C, Hajizade A, Easton AJ, et al. Virus-like particles: preparation, immunogenicity and their roles as nanovaccines and drug nanocarriers. *J Nanobiotechnology* 2021 191. 2021 Feb 25;19(1):1–27.
255. Chung YH, Cai H, Steinmetz NF. Viral nanoparticles for drug delivery, imaging, immunotherapy, and theranostic applications. *Adv Drug Deliv Rev.* 2020 Jan 1;156:214–35.
256. Fuenmayor J, Gòdia F, Cervera L. Production of virus-like particles for vaccines. *N Biotechnol.* 2017 Oct 25;39:174–80.
257. Mohsen MO, Bachmann MF. Virus-like particle vaccinology, from bench to bedside. *Cell Mol Immunol* 2022 199. 2022 Aug 12;19(9):993–1011.
258. Mejía-Méndez JL, Vazquez-Duhalt R, Hernández LR, Sánchez-Arreola E, Bach H. Virus-like Particles: Fundamentals and Biomedical Applications. *Int J Mol Sci.* 2022 Aug 1;23(15).
259. Lee KW, Tan WS. Recombinant hepatitis B virus core particles: association, dissociation and encapsidation of green fluorescent protein. *J Virol Methods.* 2008 Aug;151(2):172–80.
260. Rohovie MJ, Nagasawa M, Swartz JR. Virus-like particles: Next-generation nanoparticles for targeted

- therapeutic delivery. *Bioeng Transl Med.* 2017 Mar;2(1):43–57.
261. Beterams G, Böttcher B, Nassal M. Packaging of up to 240 subunits of a 17 kDa nuclease into the interior of recombinant hepatitis B virus capsids. *FEBS Lett.* 2000 Sep 15;481(2):169–76.
262. Ikwuagwu B, Tullman-Ercek D. Virus-like particles for drug delivery: a review of methods and applications. *Curr Opin Biotechnol.* 2022 Dec 1;78:102785.
263. He J, Yu L, Lin X, Liu X, Zhang Y, Yang F, et al. Virus-like Particles as Nanocarriers for Intracellular Delivery of Biomolecules and Compounds. *Viruses* 2022, Vol 14, Page 1905. 2022 Aug 28;14(9):1905.
264. Kaczmarczyk SJ, Sitaraman K, Young HA, Hughes SH, Chatterjee DK. Protein delivery using engineered virus-like particles. *Proc Natl Acad Sci U S A.* 2011 Oct 11;108(41):16998–7003.
265. Weldon RA, Wills JW. Characterization of a small (25-kilodalton) derivative of the Rous sarcoma virus Gag protein competent for particle release. *J Virol.* 1993 Sep;67(9):5550–61.
266. Voelkel C, Galla M, Maetzig T, Warlich E, Kuehle J, Zychlinski D, et al. Protein transduction from retroviral Gag precursors. *Proc Natl Acad Sci U S A.* 2010 Apr 27;107(17):7805–10.
267. Banskota S, Raguram A, Suh S, Du SW, Davis JR, Choi EH, et al. Engineered virus-like particles for efficient in vivo delivery of therapeutic proteins. *Cell.* 2022 Jan 20;185(2):250–265.e16.
268. Suk JS, Xu Q, Kim N, Hanes J, Ensign LM. PEGylation as a strategy for improving nanoparticle-based drug and gene delivery. *Adv Drug Deliv Rev.* 2016 Apr 4;99(Pt A):28.
269. Rodriguez PL, Harada T, Christian DA, Pantano DA, Tsai RK, Discher DE. Minimal “Self” Peptides That Inhibit Phagocytic Clearance and Enhance Delivery of Nanoparticles. *Science.* 2013 Feb 2;339(6122):971.
270. Cronin J, Zhang X-Y, Reiser J. Altering the Tropism of Lentiviral Vectors through Pseudotyping. *Curr Gene Ther.* 2005 Jul 27;5(4):387–98.
271. Kitai Y, Fukuda H, Enomoto T, Asakawa Y, Suzuki T, Inouye S, et al. Cell selective targeting of a simian virus 40 virus-like particle conjugated to epidermal growth factor. *J Biotechnol.* 2011 Sep 10;155(2):251–6.
272. Hastie E, Cataldi M, Marriott I, Grdzlishvili VZ. Understanding and altering cell tropism of vesicular stomatitis virus. *Virus Res.* 2013 Sep;176(0):16–32.
273. Zdanowicz M, Chroboczek J. Virus-like particles as drug delivery vectors. *Acta Biochim Pol.* 2016 Jul 30;63(3):469–73.
274. Thong QX, Biabanikhankahdani R, Ho KL, Alitheen NB, Tan WS. Thermally-responsive Virus-like Particle for Targeted Delivery of Cancer Drug. *Sci Reports* 2019 91. 2019 Mar 8;9(1):1–14.
275. Hu H, Steinmetz NF. Doxorubicin-Loaded Physalis Mottle Virus Particles Function as a pH-Responsive Prodrug Enabling Cancer Therapy. *Biotechnol J.* 2020 Dec 1;15(12).
276. Robinson SA, Hartman EC, Ikwuagwu BC, Francis MB, Tullman-Ercek D. Engineering a Virus-like Particle to Display Peptide Insertions Using an Apparent Fitness Landscape. *Biomacromolecules.* 2020 Jan 1;21(10):4194–204.
277. Vermeire J, Naessens E, Vanderstraeten H, Landi A, Iannucci V, van Nuffel A, et al. Quantification of reverse transcriptase activity by real-time PCR as a fast and accurate method for titration of HIV, lenti- and retroviral vectors. *PLoS One.* 2012 Dec 5;7(12).
278. Albanese M, Ruhle A, Mittermaier J, Mejías-Pérez E, Gapp M, Linder A, et al. Rapid, efficient and activation-neutral gene editing of polyclonal primary human resting CD4+ T cells allows complex functional analyses. *Nat Methods* 2021 191. 2021 Dec 23;19(1):81–9.
279. Kowarz E, Löscher D, Marschalek R. Optimized Sleeping Beauty transposons rapidly generate stable transgenic cell lines. *Biotechnol J.* 2015 Apr 1;10(4):647–53.
280. Nair R, Pignot Y, Salinas-Illarena A, Bärreiter VA, Wratil PR, Keppler OT, et al. Purified recombinant lentiviral Vpx proteins maintain their SAMHD1 degradation efficiency in resting CD4+ T cells. *Anal Biochem.* 2023 Jun;670:115153.
281. Cavrois M, De Noronha C, Greene WC. A sensitive and specific enzyme-based assay detecting HIV-1 virion fusion in primary T lymphocytes. *Nat Biotechnol.* 2002 Nov 1;20(11):1151–4.

282. Maher P. Proteasome Assay in Cell Lysates. *Bio-protocol*. 2014 Jan 1;4(2).
283. Schwefel D, Boucherit VC, Christodoulou E, Walker PA, Stoye JP, Bishop KN, et al. Molecular Determinants for Recognition of Divergent SAMHD1 Proteins by the Lentiviral Accessory Protein Vpx. *Cell Host Microbe*. 2015 Apr 8;17(4):489–99.
284. Schwarz H, Schmittner M, Duschl A, Horejs-Hoeck J. Residual Endotoxin Contaminations in Recombinant Proteins Are Sufficient to Activate Human CD1c+ Dendritic Cells. *PLoS One*. 2014 Dec 5;9(12).
285. Wingfield PT. Overview of the Purification of Recombinant Proteins. *Curr Protoc Protein Sci*. 2015;80:6.1.1.
286. Dumont J, Euwart D, Mei B, Estes S, Kshirsagar R. Human cell lines for biopharmaceutical manufacturing: history, status, and future perspectives. *Crit Rev Biotechnol*. 2016 Nov 11;36(6):1110.
287. Bornhorst JA, Falke JJ. Purification of Proteins Using Polyhistidine Affinity Tags. *Methods Enzymol*. 2000;326:245.
288. Kudoh A, Miyakawa K, Matsunaga S, Matsushima Y, Kosugi I, Kimura H, et al. H11/HSPB8 restricts HIV-2 Vpx to restore the anti-viral activity of SAMHD1. *Front Microbiol*. 2016;7(JUN):883.
289. DeLucia M, Mehrens J, Wu Y, Ahn J. HIV-2 and SIVmac accessory virulence factor Vpx down-regulates SAMHD1 enzyme catalysis prior to proteasome-dependent degradation. *J Biol Chem*. 2013 Jun 28;288(26):19116–26.
290. Fregoso OI, Ahn J, Wang C, Mehrens J, Skowronski J, Emerman M. Evolutionary Toggling of Vpx/Vpr Specificity Results in Divergent Recognition of the Restriction Factor SAMHD1. *PLOS Pathog*. 2013 Jul;9(7):e1003496.
291. Kisselev AF, Goldberg AL. Monitoring Activity and Inhibition of 26S Proteasomes with Fluorogenic Peptide Substrates. *Methods Enzymol*. 2005 Jan 1;398:364–78.
292. Oba M, Tanaka M. Intracellular internalization mechanism of protein transfection reagents. *Biol Pharm Bull*. 2012 Jul;35(7):1064–8.
293. Boeneman K, Delehanty JB, Blanco-Canosa JB, Susumu K, Stewart MH, Oh E, et al. Selecting improved peptidyl motifs for cytosolic delivery of disparate protein and nanoparticle materials. *ACS Nano*. 2013 May 28;7(5):3778–96.
294. Teo SLY, Rennick JJ, Yuen D, Al-Wassiti H, Johnston APR, Pouton CW. Unravelling cytosolic delivery of cell penetrating peptides with a quantitative endosomal escape assay. *Nat Commun*. 2021 Dec 1;12(1).
295. Du Rietz H, Hedlund H, Wilhelmson S, Nordenfelt P, Wittrup A. Imaging small molecule-induced endosomal escape of siRNA. *Nat Commun* 2020 111. 2020 Apr 14;11(1):1–17.
296. Mangeot P-E, Nègre D, Dubois B, Winter AJ, Leissner P, Mehtali M, et al. Development of Minimal Lentivirus Vectors Derived from Simian Immunodeficiency Virus (SIVmac251) and Their Use for Gene Transfer into Human Dendritic Cells. *J Virol*. 2000 Sep 15;74(18):8307.
297. Pollard VW, Malim MH. The HIV-1 Rev protein. *Annu Rev Microbiol*. 1998;52:491–532.
298. Fernandes JD, Jayaraman B, Frankel AD. The HIV-1 Rev response element: An RNA scaffold that directs the cooperative assembly of a homo-oligomeric ribonucleoprotein complex. *RNA Biol*. 2012 Jan 1;9(1):6.
299. Lacombe F, Durrieu F, Briais A, Dumain P, Belloc F, Bascans E, et al. Flow cytometry CD45 gating for immunophenotyping of acute myeloid leukemia. *Leuk* 1997 1111. 1997;11(11):1878–86.
300. Weeda V, Mestrum SGC, Leers MPG. Flow Cytometric Identification of Hematopoietic and Leukemic Blast Cells for Tailored Clinical Follow-Up of Acute Myeloid Leukemia. *Int J Mol Sci*. 2022 Sep 1;23(18).
301. Moncalvo F, Martinez Espinoza MI, Cellesi F. Nanosized Delivery Systems for Therapeutic Proteins: Clinically Validated Technologies and Advanced Development Strategies. *Front Bioeng Biotechnol*. 2020 Feb 14;8:89.
302. Rosano GL, Ceccarelli EA. Recombinant protein expression in *Escherichia coli*: Advances and challenges. *Front Microbiol*. 2014 Apr 17;5(APR):172.

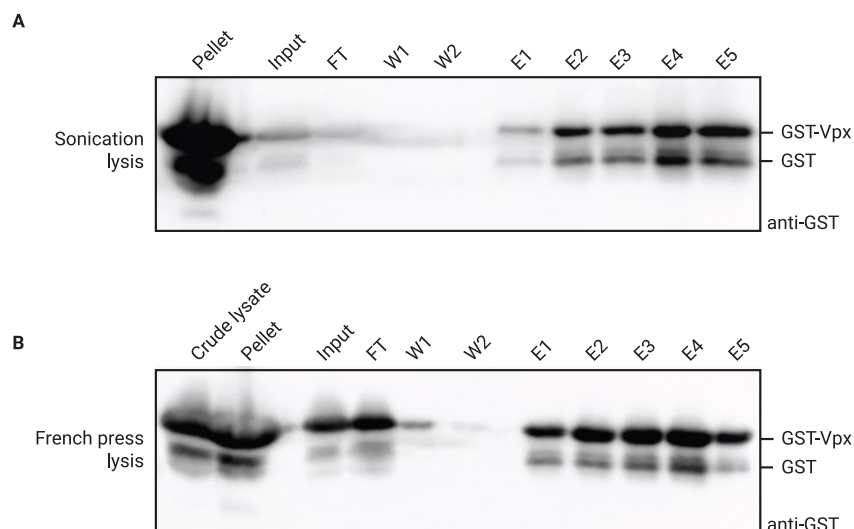
303. Tripathi NK, Shrivastava A. Recent Developments in Bioprocessing of Recombinant Proteins: Expression Hosts and Process Development. *Front Bioeng Biotechnol.* 2019 Dec 20;7:420.
304. Izsvák Z, Ivics Z. Sleeping Beauty Transposition: Biology and Applications for Molecular Therapy. *Mol Ther.* 2004 Feb 1;9(2):147–56.
305. Ignatoski KMW, Verderame MF. Lysis buffer composition dramatically affects extraction of phosphotyrosine-containing proteins. *Biotechniques.* 1996;20(5):794–6.
306. Kimple ME, Sondek J. Overview of affinity tags for protein purification. *Curr Protoc protein Sci.* 2004;Chapter 9.
307. Swiech K, Kamen A, Ansorge S, Durocher Y, Picanço-Castro V, Russo-Carbolante EMS, et al. Transient transfection of serum-free suspension HEK 293 cell culture for efficient production of human rFVIII. *BMC Biotechnol.* 2011 Nov 24;11(1):1–10.
308. Portolano N, Watson PJ, Fairall L, Millard CJ, Milano CP, Song Y, et al. Recombinant Protein Expression for Structural Biology in HEK 293F Suspension Cells: A Novel and Accessible Approach. *J Vis Exp.* 2014 Oct 16;(92):51897.
309. Schmidt T, Skerra A. The Strep-tag system for one-step affinity purification of proteins from mammalian cell culture. *Methods Mol Biol.* 2015;1286:83–95.
310. Du M, Hou Z, Liu L, Xuan Y, Chen X, Fan L, et al. Progress, applications, challenges and prospects of protein purification technology. *Front Bioeng Biotechnol.* 2022 Dec 6;10:2227.
311. Nierode G, Kwon PS, Dordick JS, Kwon SJ. Cell-Based Assay Design for High-Content Screening of Drug Candidates. *J Microbiol Biotechnol.* 2016 Oct 2;26(2):213.
312. Ray M, Lee YW, Scaletti F, Yu R, Rotello VM. Intracellular delivery of proteins by nanocarriers. *Nanomedicine.* 2017 Apr 1;12(8):941.
313. Hohenstein KA, Pyle AD, Chern JY, Lock LF, Donovan PJ. Nucleofection Mediates High-Efficiency Stable Gene Knockdown and Transgene Expression in Human Embryonic Stem Cells. *Stem Cells.* 2008 Jun 1;26(6):1436–43.
314. Nègre D, Mangeot PE, Duisit G, Blanchard S, Vidalain PO, Leissner P, et al. Characterization of novel safe lentiviral vectors derived from simian immunodeficiency virus (SIVmac251) that efficiently transduce mature human dendritic cells. *Gene Ther* 2000 719. 2000 Oct 2;7(19):1613–23.
315. Sunseri N, O'Brien M, Bhardwaj N, Landau NR. Human immunodeficiency virus type 1 modified to package Simian immunodeficiency virus Vpx efficiently infects macrophages and dendritic cells. *J Virol.* 2011 Apr 20;85(13):6263–74.
316. Lamba JK, Pounds S, Cao X, Crews KR, Cogle CR, Bhise N, et al. Clinical significance of In vivo Cytarabine Induced Gene Expression Signature in AML. *Leuk Lymphoma.* 2016 Apr 2;57(4):909.
317. Kosuge M, Takeuchi T, Nakase I, Jones AT, Futaki S. Cellular internalization and distribution of arginine-rich peptides as a function of extracellular peptide concentration, serum, and plasma membrane associated proteoglycans. *Bioconjug Chem.* 2008 Mar 1;19(3):656–64.
318. Chandrudu S, Simerska P, Toth I. Chemical Methods for Peptide and Protein Production. *Molecules.* 2013 Apr;18(4):4373.
319. Teplensky MH, Fantham M, Poudel C, Hockings C, Lu M, Guna A, et al. A Highly Porous Metal-Organic Framework System to Deliver Payloads for Gene Knockdown. *Chem.* 2019 Nov 14;5(11):2926–41.
320. Park K, Ryoo J, Jeong H, Kim M, Lee S, Hwang SY, et al. Aicardi-Goutières syndrome-associated gene SAMHD1 preserves genome integrity by preventing R-loop formation at transcription–replication conflict regions. *PLoS Genet.* 2021 Apr 15;17(4 April 2021).
321. Grant S. Ara-C: Cellular and Molecular Pharmacology. *Adv Cancer Res.* 1997 Jan 1;72:197–233.
322. Cherkasov VR, Mochalova EN, Babenyshev A V., Rozenberg JM, Sokolov IL, Nikitin MP. Antibody-directed metal-organic framework nanoparticles for targeted drug delivery. *Acta Biomater.* 2020 Feb 1;103:223–36.
323. Štefík P, Anušová A, Lakatoš B, Elefantová K, Čepcová L, Hofbauerová M, et al. Targeting acute myeloid leukemia cells by CD33 receptor-specific MoS<sub>2</sub>-based nanoconjugates. *Biomed Mater.* 2021



- Sep 1;16(5):055009.
324. Alfayez M, Kantarjian H, Kadia T, Ravandi-Kashani F, Daver N. CPX-351 (vyxeos) in AML. *Leuk Lymphoma*. 2020 Jan 28;61(2):288–97.
  325. Gupta V, Bhavanasi S, Quadir M, Singh K, Ghosh G, Vasamreddy K, et al. Protein PEGylation for cancer therapy: bench to bedside. *J Cell Commun Signal*. 2019 Sep 1;13(3):319.
  326. Maese L, Rau RE. Current Use of Asparaginase in Acute Lymphoblastic Leukemia/Lymphoblastic Lymphoma. *Front Pediatr*. 2022 Jun 30;10:1030.
  327. Soares S, Sousa J, Pais A, Vitorino C. Nanomedicine: Principles, properties, and regulatory issues. *Front Chem*. 2018 Aug 1;6(AUG):360.
  328. Damase TR, Sukhovshin R, Boada C, Taraballi F, Pettigrew RI, Cooke JP. The Limitless Future of RNA Therapeutics. *Front Bioeng Biotechnol*. 2021 Mar 18;9:161.
  329. Bhat B, Karve S, Anderson DG. mRNA therapeutics: beyond vaccine applications. *Trends Mol Med*. 2021 Sep 1;27(9):923–4.
  330. Daddacha W, Monroe D, Carver K, Usoro ER, Alptekin A, Xu H, et al. Viral Particle-Mediated SAMHD1 Depletion Sensitizes Refractory Glioblastoma to DNA-Damaging Therapeutics by Impairing Homologous Recombination. *Cancers (Basel)*. 2022 Sep 1;14(18):4490.
  331. Li Y, Gao Y, Jiang X, Cheng Y, Zhang J, Xu L, et al. SAMHD1 silencing cooperates with radiotherapy to enhance anti-tumor immunity through IFI16-STING pathway in lung adenocarcinoma. *J Transl Med*. 2022 Dec 1;20(1):1–16.
  332. Gutiérrez-Chamorro L, Felip E, Bernat-Peguera A, Ezeonwumelu IJ, Teruel I, Martínez-Cardús A, et al. SAMHD1 expression modulates innate immune activation and correlates with ovarian cancer prognosis. *Front Immunol*. 2023 Feb 9;14:487.
  333. Zhang L, Dong H, He X, Lin Y, Hu W, Salhotra A, et al. Targeting SAMHD1 Promotes Anti-Tumor Immunity in Acute Myeloid Leukemia. *Blood*. 2022 Nov 15;140(Supplement 1):679–80.
  334. Antonucci JM, Kim SH, Gelais C St., Bonifati S, Li T-W, Buzovetsky O, et al. SAMHD1 Impairs HIV-1 Gene Expression and Negatively Modulates Reactivation of Viral Latency in CD4+ T Cells. *J Virol*. 2018 Aug 8;92(15).
  335. Dahabieh MS, Battivelli E, Verdin E. Understanding HIV Latency: The Road to an HIV Cure. *Annu Rev Med*. 2015 Jan 14;66:407.
  336. Lichterfeld M. Reactivation of latent HIV moves shock-and-kill treatments forward. *Nat* 2021 5787793. 2020 Jan 22;578(7793):42–3.

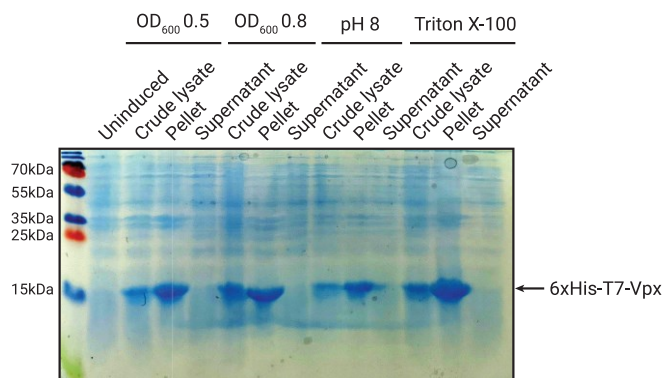


## Supplementary figures



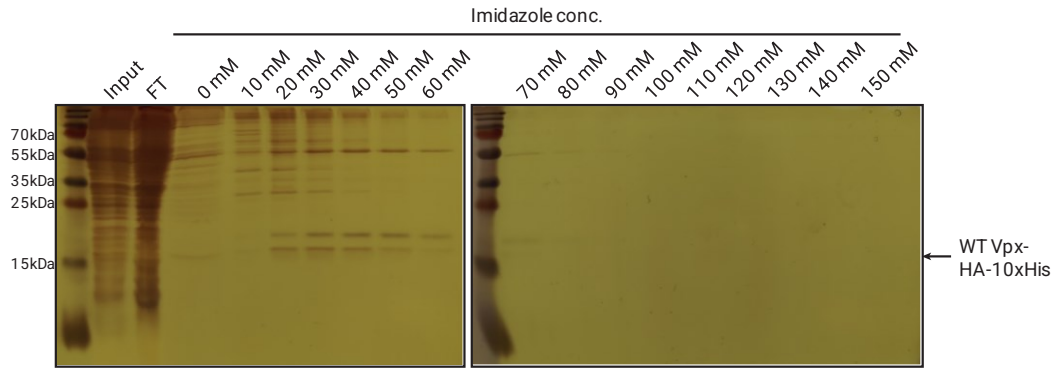
Supplementary Figure 1: Lysis of *E. coli* Rosetta2 GST-Vpx with french press yielded more protein compared to sonication lysis.

**A** *E. coli* Rosetta2 cells encoding GST-Vpx were lysed using sonication. The crude lysate was centrifuged and samples from the pellet and supernatant (Input) were obtained. The GST-Vpx protein from the remaining supernatant was affinity purified. Aliquots from the different GST-Vpx purification steps were loaded onto SDS-polyacrylamide gels and immunoblotted against the GST tag. **B** Same as **A**, but cells were lysed with the french press method. Crude lysate before lysate centrifugation was also included. FT: flow-through, W: wash, E: eluate



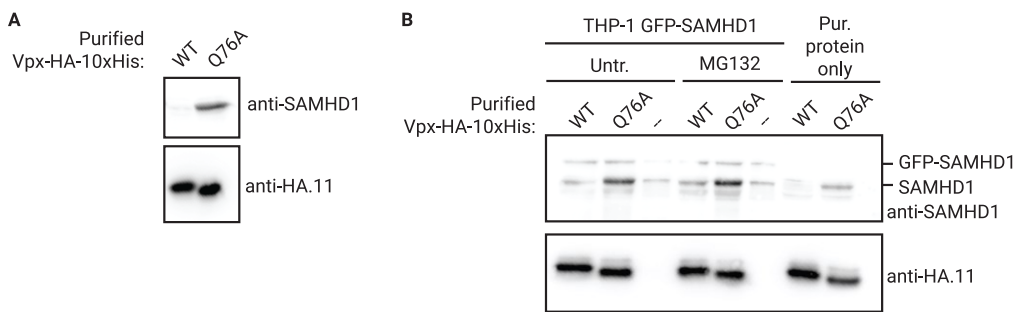
Supplementary Figure 2: The 6xHis-T7-Vpx construct was insoluble and retained in the cell pellet after lysis.

*E. coli* Rosetta2 cells expressing 6xHis-T7-Vpx proteins were subjected to the varying conditions as indicated. Cells were either induced at OD<sub>600</sub> 0.5 or 0.8 with IPTG before lysis and purification or lysed in french press lysis buffer at pH 8 or containing Triton X-100. Crude lysate of uninduced cells were used as control. For each condition, the crude lysate, pellet, and supernatant were loaded onto SDS-polyacrylamide gels and stained with InstantBlue Coomassie stain.



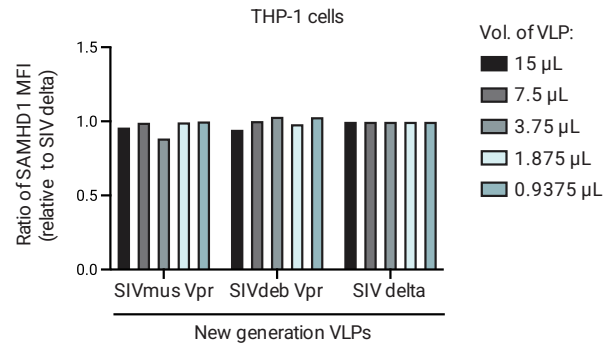
Supplementary Figure 3: Determination of maximum imidazole concentration to be used in wash buffer for Vpx-HA-10xHis purification.

HEK293T cells transfected with pcDNA WT Vpx-HA-10xHis were lysed and subjected to affinity purification using a Co-NTA resin. After loading the lysate (Input) onto the resin, the resin was washed with wash buffer containing various amounts of imidazole, as indicated. Aliquots of input, flow-through (FT) and the various washes were loaded onto SDS-polyacrylamide gels and stained with silver stain. (This figure is modified and used in Nair *et al.*, unpublished manuscript)



Supplementary Figure 4: SAMHD1 was co-purified with Q76A Vpx-HA-10xHis protein from HEK293T cells.

**A** Purified WT and Q76A Vpx-HA-10xHis proteins were loaded onto an SDS-polyacrylamide gel and immunoblotted against the HA tag. SAMHD1 signal indicates co-purification. **B** Lysates of THP-1 GFP-SAMHD1 cells were co-incubated with purified Vpx protein for the *in vitro* degradation assay. 6 hrs after incubation, aliquots from the reaction obtained, loaded onto SDS-polyacrylamide gels, and immunoblotted against SAMHD1 and the HA tag. Aliquots of the purified proteins were also loaded.



Supplementary Figure 5: SIVdeb and SIVmus Vpr-VLPs were unable to induce SAMHD1 degradation in THP-1 cells. THP-1 cells were titrated with varying amounts of new generation SIVdeb and SIVmus Vpr-VLPs, as indicated. 24 hrs later, the cells were stained for SAMHD1 and analyzed via flow cytometry. The ratio of mean fluorescence intensity (MFI) of SAMHD1 relative to the new generation SIV delta-VLP, which served as negative control, is shown.



## Acknowledgements

The successful completion of this thesis would not have been possible without the generous support of my PI, friends, colleagues, collaborators, and family, as well as the financial support by the Wilhelm-Sander-Stiftung and LMU Excellence.

My deepest gratitude goes to my PI and doctoral supervisor PD Dr. Hanna-Mari Baldauf. I want to thank her for her endless support and encouragement to pursue all my ideas, both in the lab and outside. I value every advice and feedback she had given me over the years. Not only was she very engaged in all our projects, but also in our lab activities and social events. Thank you for ensuring a supportive and engaging lab environment for every one of us and for always being there (day and night) to respond to any of our requests or questions. I would also like to extend my heartfelt gratitude towards Prof. Dr. Marion Subklewe and Dr. Christian Schölz for being a part of my thesis advisory committee and providing valuable feedback on my work over the last years. I also want to thank Dr. Hans Nitschko, my former supervisor, for recommending me for the doctoral position, and for all his encouraging words. Thank you also to the examiners of this thesis for taking the time to read through and evaluate it.

A doctoral student's life is never easy. But the strength of the friendships fostered during this time made the journey much sweeter. I'm incredibly grateful to have met Rebecca and Lin at the very beginning of my journey. We shared all the ups and downs of lab life. We drowned our problems and celebrated every little achievement with delicious food and good times together, even after they had graduated. Their friendship will always be cherished. I also want to thank Siva and Grams, two of my dearest friends from Singapore, for always supporting and believing in me, even though we live so far away from each other.

I want to also say a big thank you to all current and former members of the VIIRAL lab for their constant encouragement, conversations, and ideas. I want to especially thank Alejandro for the super productive brainstorming sessions we had, where I really learnt a lot, and for all his support in the lab. My gratitude also goes to João, Luca, and Augusto for keeping the lab environment always positive and for also lending a helping hand in the lab. This also goes for all current and former members of the Keppler, Sewald, and Schölz groups for their willingness to help with any problem I may have had and for contributing to such an uplifting working atmosphere. A special note of thanks goes to Ernesto, Manuel, Robin, Stephi, Madeleine, Marcel, Lisa, and Xaver, who were always open for brainstorming ideas and discussing all kinds of topics. The lunch sessions were especially entertaining!

Some of the projects undertaken in this thesis would not have been possible without the support of collaboration partners. I would like to thank Monika Sponheimer from the Subklewe lab for her incredible support on the primary AML project, and Nagore Barroso García and Dr. Stefan Wuttke from Spain for their work and support on the nanoMOF project.

Finally, I want to thank my whole family for their patience and emotional support throughout this tough time. Their words of encouragement always kept me going no matter how hard things got. A very special thanks goes to Mario for being my rock, encouraging me to step out of my comfort zone, his guidance, and always having my back.





## Affidavit



Nair, Ramya

\_\_\_\_\_  
Surname, first name

\_\_\_\_\_  
Street

\_\_\_\_\_  
Zip code, town, country

I hereby declare, that the submitted thesis entitled:

Manipulation of SAMHD1 using lentiviral protein Vpx to increase sensitivity of AML cells to cytarabine

is my own work. I have only used the sources indicated and have not made unauthorized use of services of a third party. Where the work of others has been quoted or reproduced, the source is always given.

I further declare that the submitted thesis or parts thereof have not been presented as part of an examination degree to any other university.

Munich, 13.04.2024  
place, date

Ramya Nair  
Signature doctoral candidate



## List of publications

**Nair R**, Salinas-Illarena A, Baldauf HM. New strategies to treat AML: novel insights into AML survival pathways and combination therapies. *Leukemia*. 2021;35(2):299–311.

**Nair R**, Pignot Y, Salinas-Illarena A, Bärreiter VA, Wratil PR, Keppler OT, et al. Purified recombinant lentiviral Vpx proteins maintain their SAMHD1 degradation efficiency in resting CD4+ T cells. *Anal Biochem*. 2023 Jun;670:115153.